Roles of Cu^{2+} in the conformational transitions and dimerization of amyloid-β peptide and its implications in Alzheimer's disease

Inaugural-Dissertation

zur Erlangung des Doktorgrades
der Mathematisch-Naturwissenschaftlichen Fakultät
der Heinrich-Heine-Universität Düsseldorf

vorgelegt von

Qinghua Liao
aus Jiangxi, China

Jülich, 22. Januar 2016

aus dem Institute of Complex Systems (ICS-6): Strukturbiochemie des Forschungszentrum Jülich

Gedruckt mit der Genehmigung der
Mathematisch-Naturwissenschaftlichen Fakultät der
Heinrich-Heine-Universität Düsseldorf

Referent: Jun.-Prof. Dr. Birgit Strodel
Korreferent: Prof. Dr. Dieter Willbold

Tag der mündlichen Prüfung: 23. Februar 2016

Statement of Authorship

I, Qinghua Liao, hereby certify that the work presented here is, to the best of my knowledge and belief, original and the result of my own investigations. I have fully acknowledged and referenced the ideas and work of others, whether published or unpublished, in my thesis. My thesis contains no material published elsewhere or extracted in whole or in part from a thesis submitted for a degree at this or any other university. Where the results are produced in collaboration with others, I have clearly mentioned my contributions.

Signed: _____

Dated: _____

Abstract

Alzheimer's disease is associated with the aggregation of amyloid-β (Aβ) peptides into fibrillar β-sheet structures, which eventually aggregate into Aβ plaques. It has been shown experimentally that both metal ions and pH have an important role in the Aβ aggregation. The Cu^{2+} binding increases the neurotoxicity of the Aβ peptides, as Cu^{2+} causes Aβ to become redox active and decreases the lag time associated with Aβ aggregation. Additionally, the pH is also a main factor that influences both the Aβ aggregation rates and the binding of Cu^{2+}. The effects of Cu^{2+} binding and pH on Aβ folding and aggregation have been determined experimentally, but the structural and causal details are still elusive. To investigate the conformational folding of Aβ_{1-42} under Cu^{2+} binding and different pH, we use enhanced sampling methods via the Hamiltonian replica exchange algorithm and we developed a dummy model for Cu^{2+} for a more realistic treatment of this metal ion. First we developed and validated the force field parameters for modelling the interactions between Cu^{2+} and monomeric Aβ_{1-42} using a bonded model for Cu^{2+}–Aβ interactions. We found that both Cu^{2+} binding and a low pH condition accelerate the formation of β-sheet in Aβ_{1-42} and lead to the stabilization of salt bridges, previously shown to promote Aβ aggregation. These results suggest that Cu^{2+} binding and mild acidic conditions can shift the conformational equilibrium towards aggregation-prone conformers of the monomeric Aβ. Furthermore, we developed a nonbonded model for Cu^{2+} including the Jahn-Teller effect, as ligand exchange was suggested to occur in the aggregation of Aβ peptides involving Cu^{2+}. We successfully validated its application by studying the metal binding problem in two biological systems: the Aβ peptide and the mixed-metal enzyme superoxide dismutase. To investigate the effects of Cu^{2+} on the dimerization of Aβ_{1-42}, we performed Hamiltonian replica exchange molecular dynamics simulations of an Aβ_{1-42} dimer bridged by both the bonded and nonbonded models for Cu^{2+}. We found that the bonded Cu^{2+} model greatly decreases the flexibility of the Aβ_{1-42} dimer while the nonbonded Cu^{2+} dummy model has little influence on the flexibility of the Aβ_{1-42} dimer. Ligand exchange was also observed in the dimerization of Aβ_{1-42} with the nonbonded Cu^{2+} dummy model. Moreover, the simulations suggest that the Cu^{2+} enhances the sampling of β-sheet and disrupts the α-helix structures, which is of significant importance to the initialization of the Aβ_{1-42} aggregation.

Zusammenfassung

Die Alzheimersche Demenz steht im Zusammenhang mit der Aggregation des Amyloid-β (Aβ) Peptids zu fibrillaren β-Faltblatt-Strukturen, welche schließlich zu Plaques aggregieren. Experimente haben gezeigt, dass sowohl Metallionen als auch der pH-Wert einen großen Einfluss auf den Aggregationsverlauf haben. Kupfer erhöht die Neurotoxizität des Aβ Peptids, da Kupfer das Redoxpotential von Aβ aktiviert und die Aggregationszeit verkürzt. Darüber hinaus beeinflusst der pH-Wert die Aggregationsrate von Aβ und die Bindung von Kupfer. Während diese Effekte experimentell bewiesen wurden, sind ihre strukturellen und kausalen Details nach wie vor unbekannt. Um den Einfluss von Kupfer und pH-Wert auf die Faltung von Aβ zu untersuchen, haben wir Molekulardynamik-Simulationen (MD-Simulationen) mit Hamiltonian-Replika-Austausch (H-REMD) angewandt, um den Konformationsraum von Aβ effizient abzutasten. Desweiteren haben wir ein nichtbindendes, sogenanntes Dummymodell für Kupfer entwickelt, um eine realistischere Beschreibung dieses Ions in MD-Simulationen zu ermöglichen. Zunächst wurden jedoch Kraftfeldparameter für ein Cu^{2+}-Modell entwickelt und validiert, bei dem kovalente Bindungen zwischen Kupfer und Aβ bestehen. Basierend auf H-REMD-Simulationen konnte dann gezeigt werden, dass sowohl die Bindung von Kupfer als auch ein niedriger pH-Wert die Ausbildung von β-Faltblättern in Aβ beschleunigen und zur Stabilisierung von Salzbrücken beitragen, welche bereits dafür bekannt sind, die Aggregation von Aβ zu begünstigen. Diese Resultate legen den Schluss nahe, dass die Bindung von zweifach positiv geladenen Kupfer(II)-Ionen und ein leicht säuerliches Milieu das Konformationsgleichgewicht von monomerem Aβ in Richtung leicht aggregierender Konformere verschieben. Im zweiten Teil der vorliegenden Arbeit wurde ein Dummymodell ohne kovalente Bindung zwischen Ion und Protein für Kupfer(II)-Ionen entwickelt, welches den Jahn-Teller-Effekt nachbildet und den Austausch von Liganden möglich macht. Das Modell konnte erfolgreich durch die Studie der Metallbindung in zwei biologischen Systemen validiert werden: das Aβ-Peptid und das Metalloenzym Superoxid-Dismutase. Um den Effekt des Kupfers auf die Dimerisierung von Aβ zu untersuchen, haben wir H-REMD-Simulationen des Aβ-Dimers durchgeführt. Hierbei haben wir drei Systeme studiert: das Aβ-Dimer ohne Cu^{2+} und das Dimer, in dem die beiden Peptide entweder durch das gebundene oder durch das ungebundene Dummymodell für Cu^{2+} verbrückt sind. Das gebundene Kupfer(II)-Ionen-Modell vermindert stark die Flexibilität des Aβ-Dimers, während das ungebundene

Modell wenig Einfluss auf die Flexibilität des Dimers hat. Bei Verwendung des ungebundenen Modells konnte dafür Ligandenaustausch während der Simulation beobachtet werden. Schließlich deuten die Simulationsergebnisse darauf hin, dass das den Dimer verbindende Kupfer(II)-Ion die Bildung von β-Faltblättern erleichtert und die von α-Helices stört. Dies ist von großer Wichtigkeit für die Initiierung der Aggregation von Aβ.

Acknowledgements

Foremost, I would like to express my sincere gratitude to my advisor Jun.-Prof. Dr. Birgit Strodel for her continuous support of my Ph.D. study, particularly I appreciate her patience, encouragement throughout my doctoral training. It is my great honour to be under her guidance. Many thanks for her efforts on my thesis, too. I also would like to thank Assoc.-Prof. Dr. Lynn Kamerlin for her collaborations on the copper dummy model and ongoing amyloid projects, and Dr. Paul Strodel for his helpful guiding at the beginning of my Ph.D. study.

I gratefully acknowledge China Scholarship Council for funding me to do the Ph.D. study, and Jülich Supercomputing Center for providing and maintaining the computing resources used in my projects.

I appreciate Dr. OluJide Olubiyi, Dr. Bogdan Barz and Dr. Michael C. Owen for discussions and proof reading in my work. I thank my fellow group members, Dr. Chetan Poojari, Kenneth L. Osborne, Dr. Falk Hoffmann, Philipp Kynast, Oliver Schillinger, Martin Carballo Pacheco, Dusan Petrovic, Marianne Schulte for discussions, sharing experience and spending enjoyable time together.

I thank all my friends, Dr. Peixiang Ma, Dr. Dawei Xu, Dr. Xianwei Kang $\cdots$, in Jülich for their friendships, and great time spending together.

I appreciate my wonderful wife, Qian Yu, for her support and encouragement. I am grateful to my parents, Mr. Liao and Mrs. Zeng, for supporting me throughout my life so far, thanks also go to my younger brother, Chunhua Liao.

Contents

List of abbreviations

Å	Angstrom
AD	Alzheimer's disease
Aβ	amyloid-β
AFM	atomic force microscopy
APP	amyloid precursor protein
CD	circular dichroism
CHC	hydrophobic core
CTH	C-terminal hydrophobic
CuDum	Cu^{2+} dummy model
CW-EPR	continuous-wave electron paramagnetic resonance
EPR	electron paramagnetic resonance
HM	homology modelling
H-REMD	Hamiltonian replica exchange molecular dynamics
ITC	isothermal titration calorimetry
LJ	Lennard-Jones
MD	molecular dynamics
MM	molecular mechanics
NMR	nuclear magnetic resonance
PBC	periodic boundary condition
PCA	principal component analysis
PES	potential energy surface

PME	Particle Mesh Ewald
QM	quantum mechanics
QM/MM	quantum mechanics/molecular mechanics
REMD	replica exchange molecular dynamics
RESP	restrainted electrostatic potential
RMSD	root mean square deviation
RMSF	root mean square fluctuation
ROS	reactive oxygen species
SRP	standard reduction potentials
ss-NMR	solid state nuclear magnetic resonance
vdW	van der Waals
XAS	X-ray absorption spectroscopy
ZnDum	Zn^{2+} dummy model

List of Figures

1 Introduction

1.1 Alzheimer's disease (AD)

As the most common form of dementia (accounting for ∼60-80% of all cases) [1], Alzhermer's disease (AD) is a devastating and fatal neurodegenerative disorder. AD is primarily a disease among elderly people, and it has become a remarkable serious challenge to our society. In US, AD is the sixth most leading cause of death. An estimated 5.3 million of Americans suffered from AD in 2015 according to Alzheimer's Association [1], and the number may be dramatically increased by 13.8 million in 2050 [2]. Meanwhile, the direct costs to American society of caring for those with AD will be an estimated $226 billion in 2015 and $1.1 trillion in 2050 unless effective therapies are developed [1].

The most common AD symptoms are loss of memory, cognitive decline as well as behavioral and physical disability, and eventually leading to death [3,4]. Currently, the cause of AD is poorly understood, and there is no effective treatment to stop or reverse its progression, with some exceptions that may temporarily improve the symptoms[5].

One of the proteins highly associated with brain mass loss and thus AD is the Aβ peptide. Initially found in the cellular membrane as part of the amyloid precursor protein (APP), it is cleaved by the secretase enzymes and once released in the extracellular environment it starts a self-assembly process. This leads to a large variety of aggregates from monomers and small oligomers, to larger protofibrils, fibrils and plaques. Oligomers are thought to be the main toxic species leading to neuronal death, but fibrils have been recently shown to accelerate considerably the oligomer production. External factors, such as the environmental pH or the presence of metal ions have been shown to influence the aggregation process as well. High concentrations of metal ions such as Zn^{2+}, Cu^{2+} and Fe^{2+}/Fe^{3+} have been found in amyloid plaques based on the analysis of postmortem brain tissues, encouraging studies regarding the role of the metal ions in the aggregation process [6–9].

1.2 Amyloid-β (Aβ) peptides

The Aβ peptides are sequentially cleaved from the transmembrane amyloid precursor protein (APP), located in chromosome 21, by β- and γ-secretase enzymes (Fig. 1.1A). The

Aβ peptides are typically 39–43 residues in length, and the most prevalent alloforms of Aβ found in brain plaques are Aβ_{1-40} and Aβ_{1-42}, the only difference being the presence of two extra residues, Ile41 and Ala42, at the latter's C-terminal. The sequence of Aβ_{1-42} is shown in a single-letter code in Fig. 1.1B. There are six negatively charged residues (D1,E3, D7, E11, E22, D23) and three positively charged residues (R5, K16, K28) at physiological conditions, resulting in a net charge of -3e. In general, Aβ peptides can be divided into the metal binding region involving N-terminal residues (D1–K16), central hydrophobic core (CHC, L17–A21) region, central polar region (G22–G29), and C-terminal hydrophobic (CTH) region (A30–V40/A42), as shown in Fig. 1.1B.

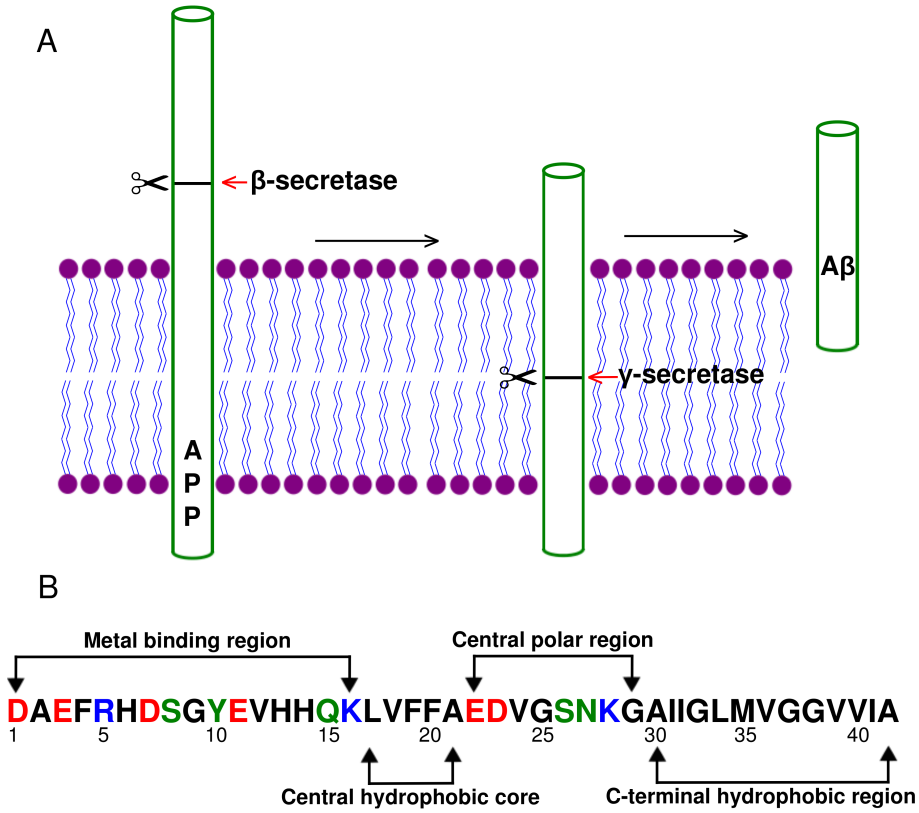

Figure 1.1: (A) shows the production of Aβ peptides which are sequentially cleaved from the amyloid precursor protein (APP) by β- and γ-secretase. (B) shows the sequence of Aβ_{1-42}, which is divided into four regions: metal binding region, central hydrophobic core (CHC) region, central polar region and C-terminal hydrophobic (CTH) region. Residues labelled as red, blue, green and black are negatively charged, positively charged, polar and hydrophobic, respectively.

1.2.1 Aβ monomers

It is highly challenging to identify the structural information of Aβ peptides under physiological conditions because of its rapid aggregation tendency. Various experimental studies

have been carried out focusing on the two main alloforms (Aβ_{1-40} and Aβ_{1-42}) in order to determine their secondary structures and aggregation patterns. Aβ_{1-40} and Aβ_{1-42} monomers are mostly characterized by disordered conformations in solution. There are several NMR models of Aβ peptides determined in membrane-mimicking environments. A three dimensional model of Aβ_{1-40} was reported by using NMR spectroscopy at pH 5.1 in aqueous sodium dodecyl sulfate (SDS) micelles [10], consisting of an α-helix between Gln15 and Val36 as shown in Figure 1.2A. A NMR model of Aβ_{1-42} was also determined in a mixture of hexafluoroisopropanol and water (HFIP/H_2O) [11], which has two helices between residues Tyr10 and Ile32, as shown in Figure 1.2B. Moreover,a second NMR model for Aβ_{1-42} was determined in apolar micro-environment [12] (Figure 1.2C), characterized by two α-helices (Ser8–Gly25 and Lys28–Gly38) connected by a regular β-turn. Generally, the Aβ peptides are typical helices in apolar solvents.

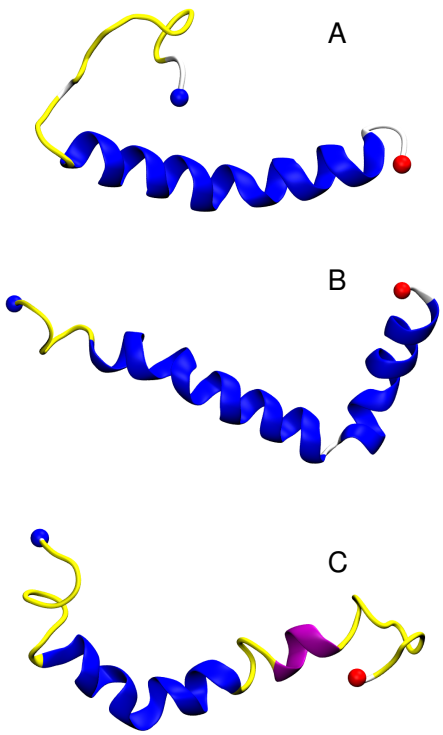

Figure 1.2: The NMR models of Aβ_{1-40} (A, PDB ID: 1BA4) and Aβ_{1-42} (B, PDB ID: 1Z0Q; C, PDB ID: 1IYT) monomers. The figures were generated with VMD [13].

In water, however, β-strands and turns were found at the CHC and CTH regions by solution NMR experiments [14]. Aβ_{1-40} and Aβ_{1-42} were also determined to be dominated by random coil [15], but small contents of β-strand [16] were also suggested by ultraviolet circular dichroism (UV CD) spectra experiments. The population of β-strand is ranging from 12% and 25%, while α-helix is between 3%-9%. Because of the two extra hydropho-

bic residues Ile41 and Ala42, Aβ_{1-42} is more rigid at the CTH region than Aβ_{1-40}, on both side-chain and backbone dynamics [17,18]. Turn structures probably are critical in the aggregation of the Aβ peptides, because it was determined at the central polar region by solution NMR experiments [19], also confirmed by simulations [20,21]. As expected, the Aβ monomer does not have a clearly folded conformation in water, a defining characteristic of intrinsically disordered proteins because of the high aggregation propensity. This however, could play a role in its aggregation into oligomers and fibrils. The investigation of the conformational properties of the Aβ peptides by various computational approaches has been encouraged by the inherent limitations and challenges of current experimental techniques for studying disordered peptides. Currently, computer simulations of the Aβ peptides with implicit and explicit solvent models are able to extend over multiple microseconds as the development of the availability of computational resources. Raffa and Rauk confirmed that the coil structure was the predominant conformation of Aβ_{1-42} with MD simulations [22]. Olubiyi and Strodel found that the formation of β-sheets is enhanced by lowering the pH, i.e., by protonating the three His residues in Aβ_{1-42} investigated by MD simulations [23]. Moreover, advanced sampling techniques like replica exchange molecular dynamics (REMD) simulation [24] are also used to improve the sampling. Rosenman *et al.* sampled β-hairpins between Leu17–Ala21 and Ile31–Val36 regions for Aβ_{1-40} and a second β-hairpin spanning Val39–Ala42 for Aβ_{1-42} from REMD simulations on the microsecond per replica time scale with OPLS-AA/TIP3P [25]. Recently, an excellent review on both experimental and simulation studies of the Aβ peptides were published [26].

1.2.2 Aβ oligomers and fibrils

It is difficult to classify soluble Aβ species systematically without more information about the structure and the assembly pathways. Generally, soluble Aβ aggregates contain protofibrils and oligomers. Protofibrils have molecular masses between 30$\sim$250$\times10^3$ kDa, with high β-sheet content and can seed the growth of fibrils [27]. Oligomers are smaller species, with masses ranging from 9 kDa (dimer) to hundreds of kDa ($\sim$50mers). It is now widely accepted that soluble Aβ species formed at the initial self-assembly step, other than monomers, are the toxic agents [28–31]. For example, dimers are around 3-fold more toxic than monomers, whereas trimers and tetramers are 8- and 13-fold more toxic, respectively [15]. The conformational transition of monomeric Aβ peptides to a β-sheet-rich state resulting in its aggregation, with water-soluble oligomers as intermediates, is crucial for the initiation of Alzheimer's dementia [15,32,33].

A variety of oligomeric species have been identified [34], but the detailed structural information of the Aβ oligomers is still unknown. However, there are several proposed models that describe the intermolecular organization of Aβ oligomers based on experi-

mental data [35–39]. The anti-parallel β-hairpins play an important role in these models. For example, Yu *et al.* proposed a model in which an anti-parallel β-hairpin between β-strands spanning residues 17-23 and residues 28-33 was determined based on solution NMR data [36]. Three twisted β-hairpins in a triangular arrangement were observed for a Aβ_{17-36} trimer based on the X-ray crystallographic technique [39]. Nevertheless, the oligomer structure is still far from being resolved, and a consensus on the toxic oligomer species has yet to be reached [30] in despite of the countless number of experimental and computational studies [40].

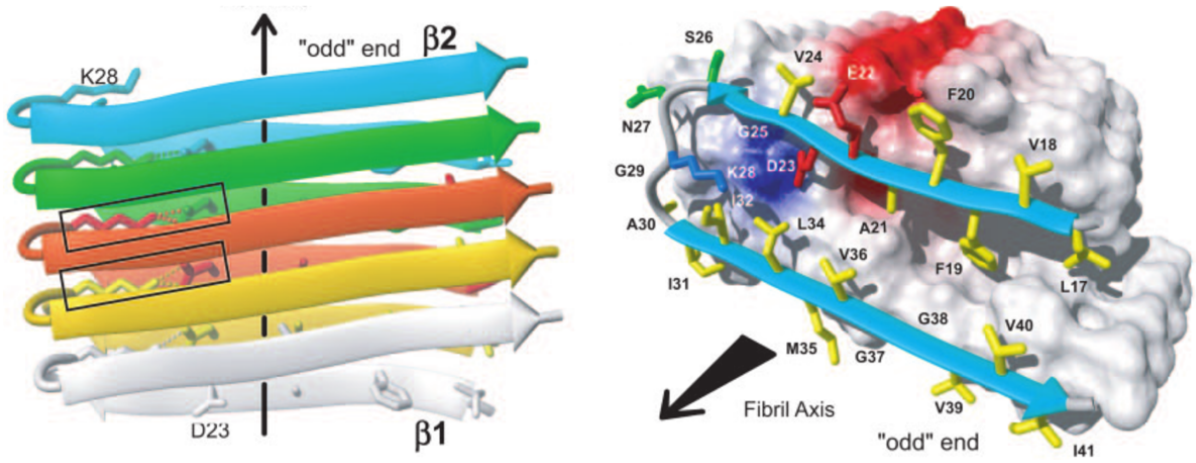

Figure 1.3: A proposed model of the β-sheet amyloid structure based on NMR spectroscopy. Figure reprinted with permission from Lührs *et al.*. **Proceed. Natl. Acad. Sci. U.S.A**, 102(48):17342–17347, 2005. Copyright 2005, National Academy of Sciences, USA.

The amyloid fibrils contain bundles of β-sheets with the backbones orthogonal to the fiber axis called cross-β structure as determined by X-ray diffraction [41]. In spite of difficulties with solubility and crystallization, many groups have determined the fibril structures of Aβ peptides using NMR spectroscopy. Fibrils are composed of parallel or anti-parallel β-sheets being perpendicular to the fibril axis with hydrogen bonds parallel to the fibril axis holding the β-sheets together [42] as shown in Figure 1.3. The Tycko group have studied the fibril of Aβ peptides extensively with NMR techniques [43–49], and they have proposed several fibrillar models, mainly for Aβ_{1-40}. For Aβ_{1-42}, besides the Lührs model [42], there recently have been proposed two more models with considerable different conformations [50,51]. Despite the advances in elucidating the oligomer or fibril structure, the molecular mechanisms involved in the aggregation process are still poorly understood. One important aspect of amyloid aggregation is the interaction of Aβ peptides with metal ions that also makes the focus of this thesis.

1.3 Interactions of amyloid-β with Cu^{2+}

There has been substantial evidence that interactions of Aβ with transition metal ions (especially with Cu^{2+} and Zn^{2+}) may be involved in the process of Aβ aggregation and toxicity, as metal ions like Cu^{2+} and Zn^{2+} are found in amyloid plaques at high concentrations ($\sim$mM) [8]. Therefore, the role of the dysregulation of Cu^{2+} and Zn^{2+} homeostasis as pathogenic factors in AD have been intensively studied, and metal chelation therapy may now be considered as a promising clinical approach to AD [52]. In order to understand the therapeutic potential of the metal chelation approach, we need to understand the role of metal ions (Cu^{2+} and Zn^{2+}) in amyloid aggregation, from monomers and toxic oligomers to fibrils and amyloid plaques.

1.3.1 Stoichiometry of the Cu^{2+}-Aβ complexes

A first question regarding the interactions between Cu^{2+} and Aβ peptide is related to the local chemical interactions between the two. The coordination chemistry of the Cu^{2+}-Aβ complexes has been extensively studied in the past years with both truncated and full-length of Aβ peptides. However, no real consensus has been reached, especially on the exact coordinating ligands until recently. A reason might be the dynamics of the Cu^{2+}-Aβ complexes and the different experimental conditions in various studies.

There are several electron paramagnetic resonance (EPR), circular dichroism (CD) spectroscopy, isothermal titration calorimetry (ITC) studies suggesting that the Aβ peptides could bind two Cu^{2+} ions in a sequential and ratiometric way [53,54], with the first Cu^{2+} indicating $\sim$100 times stronger affinity than the second one [55]. Only one binding site was reported in some studies [56,57], probably the lower affinity of the second Cu^{2+} to Aβ which might prevent its detection.

There were vast majority of studies suggesting the formation of a monomeric $(A\beta)_1Cu_1$ complex prior to aggregation. A cooparative formation of a binuclear species $(A\beta)_2Cu_2$ was reported by Barnham *et al.* [58–60], the two Cu^{2+} centers being bridged via a histidine residue. Moreover, Hane *et al.* [61] proposed another model of $(A\beta)_2Cu_1$ based on the measurement of atomic force microscopy, where Cu^{2+} acts as a bridge between the two monomeric Aβ, increasing the stability of the peptide-peptide complex.

1.3.2 Binding affinity of the Cu^{2+}-Aβ complexes

In biology, the binding affinity between metal ions and protein and peptides is an important parameter. The determination of the metal binding affinity for Aβ peptides helps understanding the physiological significance of metal binding in the pathology of Aβ aggregation. A recent review had extensively discussed the binding affinity of Zn^{2+} and Cu^{2+}

towards Aβ, considering different measurements with different buffers [8]. Normally, the binding affinity is related to the dissociation constant (K_D). The reported K_D values for Aβ-Zn^{2+} complexes vary between 1 and 20 μM, whereas for Aβ-Cu^{2+} complexes between 10 pM and 200 pM [62–64]. Obviously, Cu^{2+} binds to Aβ by a few orders of magnitude stronger than Zn^{2+} as indicated by the K_D coefficients.

It is reported that metal ion chelators, especially for Cu^{2+} and Zn^{2+}, can inhibit or reverse Aβ peptide aggregation *in vitro* [65], thus the metal chelation is proposed as a potential therapeutic intervention in AD. Knowing the detailed information of the K_D of metal ions binding to Aβ peptides is of significance to designing selective metal ion chelators. Taking Cu^{2+} for example, a chelator with a conditional K_D of around 1-10 pM for Cu^{2+} is sufficient to retrieve Cu^{2+} completely from Aβ peptides. Meanwhile, this K_D is still high enough to not compete with Cu^{2+} sites in enzymes [66].

1.3.3 Coordination chemistry of the Cu^{2+}-Aβ complexes

Elucidating the coordination of Cu^{2+} to Aβ is crucial to understand its role in Aβ aggregation and for the rational design of new chelators with potential therapeutic benefits. A lot of progress has been made for the Cu^{2+} binding sites on Aβ peptides in the past years though the exact coordination of Cu^{2+} is still an unresolved issue. Different coordination modes of Cu^{2+} bound to Aβ have been reported depending on different experimental conditions, such as, peptide concentration, pH, ionic strength, or temperature [8,67,68].

So far, the metal binding sites of Zn^{2+} and Cu^{2+} bound to Aβ have been extensively studied. For both Zn^{2+} and Cu^{2+}, the binding sites in Aβ peptides locate at the disordered N-terminal region (Asp1–Lys16). The potential residues at this region which can bind Zn^{2+} and Cu^{2+} are Asp1, Glu3, His6, Aps7, Glu11, His13, and His14. Zirah *et al.* [69] have reported the NMR structural complexes of Aβ_{1-16}/Zn^{2+} with a coordination mode of His6, Glu11, His13 and His14, determined in aqueous solution at pH 6.5 and 7.4. A tetrahedral coordination sphere of Zn^{2+} by Asp1 (amine), His6, Glu11 (COO^-) and His13 at the N-terminal region of rat Aβ_{1-28} was proposed based on an NMR study in sodium dodecyl sulfate (SDS) micelles at temperature 298 K and pH 7.5 [70]. For human Aβ_{1-28}, a different penta-coordination sphere of Zn^{2+} binding with Asp1 (amine), His6, His13, His14, and/or Glu11 (COO^-) was suggested in the same NMR study [70]. Moreover, a coordination sphere of the Aβ/Zn^{2+} complex coordinated by four His residues (His13 and His14 of two different monomers) was reported based on X-ray absorption spectroscopy (XAS) [71], in which Zn^{2+} acted as a bridge between two Aβ monomers.

For Cu^{2+}, the possible coordinating residues in Aβ determined by experiments are almost the same as for Zn^{2+} (Asp1, Glu3, His6, Aps7, Glu11, His13, and His14), loacated at the N-terminal region. The three His residues (His6, His13 and His14) involved in the Cu^{2+} coordination sphere are supported by NMR experiments [55,58,72] and other

experimental studies [71]. Moreover, His13 and His14 were confirmed to be involved in the Cu^{2+} coordination sphere by electrospray ionization mass spectrometry (ESI-MS) [73]. Using homology modelling (HM) and quantum mechanics (QM) approaches, Alí-Torres *et al.* have determined the possible plausible 3D structures of $A\beta_{1-16}/Cu^{2+}$ taking all possible ligands into account with different coordination spheres [74,75].

Drew *et al.* proposed two different 3N1O (three nitrogen and one oxygen atoms) coordination spheres for Cu^{2+}-Aβ complex using continuous-wave electron paramagnetic resonance (CW-EPR) spectra, called component I and II [76–78] (Figure 1.4). At pH 6.3 to 6.9, the Cu^{2+} coordination sphere involves the binding of the amine and the carbonyl groups of Asp1, His6 and His13 (or His14) (component Ia or Ib) in a distorted square planar geometry [78], whereas His6, His13, His14 and the carbonyl group of Ala2 are involved in a distorted square planar coordination sphere at pH 8.0 (component II) [77]. Dorlet *et al.* suggested that a water molecule or a negatively charged residue (Asp or Glu) was also involved in the coordination sphere as a fifth ligand at the axial position [79,80].

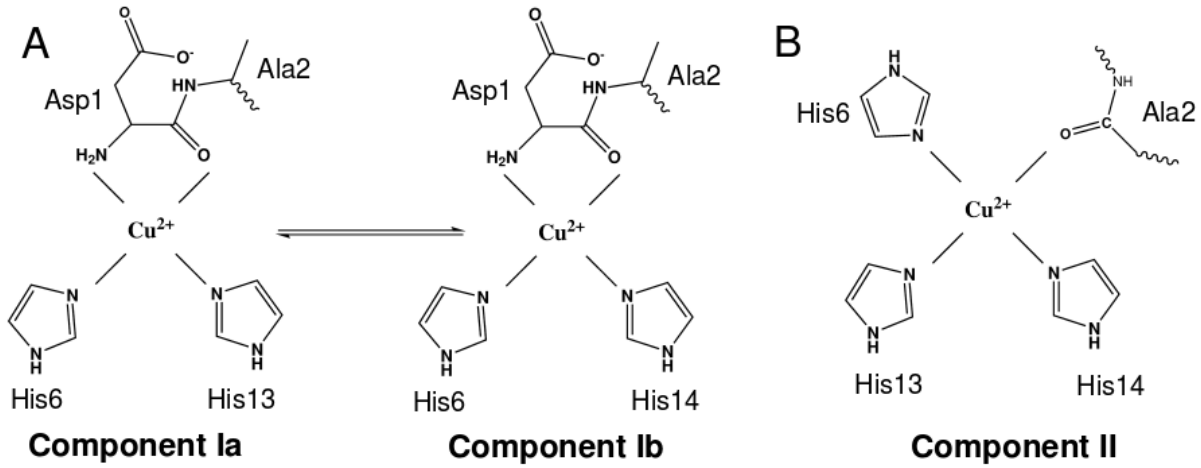

Figure 1.4: Coordination models proposed experimentally for the Cu^{2+}-Aβ_{1-16} complexes from CW-EPR spectroscopy. At low pH, Cu^{2+} is coordinated by NH_2^{D1}, O^{D1}, N^{H6} and N^{H13} (component Ia) or by NH_2^{D1}, O^{D1}, N^{H6} and N^{H14} (component Ib). An equilibrium occurs between component Ia and Ib. At high pH, Cu^{2+} is coordinated by O^{A2}, N^{H6}, N^{H13} and N^{H14}.

1.3.4 The role of Cu^{2+} in Aβ aggregation

Metal ions such as Zn^{2+} and Cu^{2+} have significant influence in the Aβ aggregation process, however, contradictory results about the nature and the direction of these effects were reported. For example, inhibiting [81–86] and enhancing [87–90] fibril formation of the Aβ peptides have been reported for Zn^{2+}, while Cu^{2+} was reported to suppress [81,86,91,92]

and promote [93–95] the aggregation of the Aβ peptides depending on experimental conditions. However, complex effects were also observed [96]. Recently, it was also indicated that small amounts of Cu^{2+} destabilize the Aβ oligomers and inhibit the fibrillation [97]. In the case of Zn^{2+}, the effects on Aβ peptides are mainly dependent on the concentration of Aβ. It has been suggested that Zn^{2+} selectively precipitates oligomers at high Aβ concentrations [98,99]. However, induction of lateral aggregation of Aβ fibrils [100] and enhancement of the formation of fibrillar organization [88,96] by Zn^{2+} were also reported.

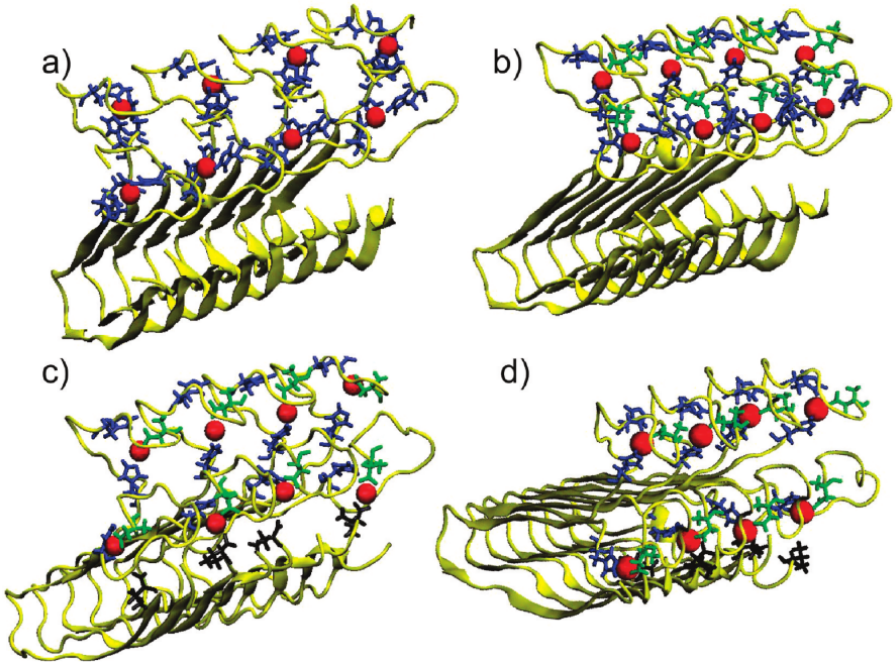

Figure 1.5: Four proposed models for the Aβ_{1-40} fibrils complexed with Cu^{2+}. Figure reprinted with permission from Parthasarathy *et al.* **J. Am. Chem. Soc.**, 133(10): 3390–3400, 2011. Copyright 2011 American Chemical Society.

Cu^{2+} can also modulate Aβ aggregation, but its presence protects Aβ against Zn^{2+}-induced aggregation by competing with Zn^{2+} for histidine residues of Aβ peptides[101, 102], which suggests that the complexes of Cu^{2+}-Aβ are more soluble than the Zn^{2+} counterpart. A consensus has been reached that Cu^{2+} accelerate the aggregation of Aβ peptides into amorphous deposits [82,103,104], but in some cases fibrils were also formed by Cu^{2+}-Aβ [105,106]. The discrepancy between amorphous and fibrillar types of Aβ aggregates is likely to be attributed to the different concentrations of Aβ peptide and Cu^{2+} or to preparation procedures. Pedersen *et al.* [107] suggested that the ratio of Cu^{2+}:Aβ is a major factor in the Aβ aggregation. Together with other researchers, they proposed three different kinetic pathways that Aβ peptides may diffuse under the influences of Cu^{2+}. For the first pathway with $[Cu^{2+}] \ll [A\beta]$, the complexes form rapidly a critical nucleus followed by the slow elongation of the fibril as peptide-metal complexes are added

to the nucleus [106,107]. At equimolar concentrations, the Cu^{2+}-Aβ oligomers slowly bind together resulting in amorphous aggregates [103,107]. For the third pathway with [Cu^{2+}]>[Aβ], both fibrillar and oligomeric formation of the Aβ peptides takes place, with higher proportions of oligomers likely due to a destabilizing effect of Cu^{2+} on the structure of Aβ peptides [107].

It is still unknown how much the structures of Aβ-Cu^{2+} amyloid fibrils differ from the metal-free Aβ fibrils. Mithu *et al.* investigated the conformation of Zn^{2+}-attached fibrils of Aβ_{1-42} by solid-state NMR (ss-NMR) [108]. They found that Zn^{2+} caused major structural changes in the N-terminal and the loop regions connecting the two β-sheets. It disrupted the Asp23-Lys28 salt bridge without altering the fibrillar morphology of aggregates distinctly [108]. Parthasarathy *et al.* examined the molecular details of Cu^{2+} binding to amyloid fibrils using ss-NMR techniques for full-length Aβ_{1-40}. Four models with different coordination modes (Figure 1.5) were proposed based on the experimental data [109], in which the coordination modes agreed with the one proposed by Drew *et al.* [76] partially. And preliminary MD simulations of these model confirmed the stabilities of the models. They also found that no major structural changes upon Cu^{2+} binding in the hydrophobic core regions were found based on the chemical shift analysis [109]. Moreover, there was another model for Aβ_{1-40} fibril in complex with Cu^{2+} [110], of which the coordination mode was consistent with the one proposed for Aβ_{1-16} at pH 6.9 by Drew *et al.* [76]

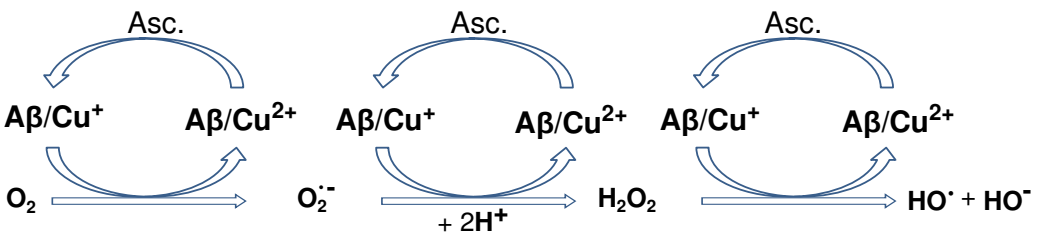

Figure 1.6: Redox chemistry of the production of ROS by ($A\beta/Cu^{2+}$)/($A\beta/Cu^{+}$) in the presence of ascorbate (Asc.) and molecular oxygen. The endogenous antioxidants ascorbate is able to reduce Cu^{2+} to Cu^{+}, and the oxidants O_2, $O_2^{\bullet-}$ and H_2O_2 can oxidize Cu^{2+} to Cu^{+} with the production of $HO^{\bullet}$ and HO^{-}.

1.3.5 Neurotoxicity of Cu^{2+}

In addition to the effects of modulating the aggregation process of Aβ, Cu^{2+} has also been widely accepted to contribute to oxidative stress and inflammation of the brains of Alzheimer's patients [111]. Oxidative stress is known to play a role in normal aging [112]. As one of the initial signs of AD, oxidative stress precedes the presence of inflammation and

amyloid plaques [113]. Oxidative stress includes the production of reactive oxygen species (ROS) (Figure 1.6) [114,115]. Aβ peptides are able to induce the production of ROS in cells [116], while copper ion can exacerbate and facilitate Aβ-mediated oxidative damage in AD [117]. Indeed, it has been reported that complexes of Aβ/Cu^{2+} are able to catalyze the production of ROS like H_2O_2 and $HO^{\bullet}$ in the presence of a biologically relevant reducing agent *in vitro* experiments [118]. Moreover, it was also indicated that oligomers of Aβ_{1-42}/Cu^{2+} produced much more H_2O_2 and $HO^{\bullet}$ than monomeric Aβ_{1-42}/Cu^{2+} [118, 119]. The OH radical is highly reactive and initiates a variety of reactions resulting in post-translational protein modification, DNA damage and lipid peroxidation [120]. A lot of studies have suggested that both the lipid peroxidation and copper at the neuronal synapse promoting the Aβ aggregation contribute to the copper toxicity [121]. Although the brain has a natural defense system for removing excess H_2O_2, it can be overwhelmed with the excessive amount of H_2O_2 and $HO^{\bullet}$ [122,123]. Thus, Cu^{2+} is expected to increase the toxicity of Aβ oligomers and amyloid.

2 Motivation

High concentration of the redox active metal ion Cu^{2+} has been found in senile plaques composed of Aβ peptides. The presence of Cu^{2+} is widely accepted to be involved in Aβ aggregation and toxicity. Experiments have been extensively carried out to investigate the coordination chemistry of Cu^{2+} binding Aβ, the source of toxicity related to Cu^{2+}, and the roles of Cu^{2+} in the process of Aβ aggregation. However, no consensus has been reached on these issues. Computer simulations provide a complementary means of directly accessing these vital information. Various computational studies of Aβ interacting with Cu^{2+} have been performed to investigate these mechanism at different levels including MM and QM approaches. Rauk and co-workers have studied the complex stabilities, ligand preferences and reaction pathways for a series of modelled Aβ/Cu^{2+} and Aβ/Cu^{+} complexes [124–127] using density functional theory with the B3LYP functional [128,129]. QM approaches are useful to study different coordination spheres and to determine some molecular properties such as standard reduction potentials (SRP) or constants of stability of Aβ fragment and Cu^{2+} [74,75,130]. For the full-length Aβ or oligomers, molecular dynamics (MD) simulation has been proved to be a better sampling tool. There are some MD studies focusing on the effects of Cu^{2+} on the binding sites and conformational folding of Aβ peptides [22,131–133], but further study is still necessary as knowledge about the coordination chemistry of Cu^{2+} binding to Aβ is still updating [9,76–80].

Hamiltonian replica exchange molecular dynamics (H-REMD) [134,135] simulation has been proven to be a highly efficient sampling technique [136]. H-REMD is able to be efficiently applied to study the roles of Cu^{2+} in the Aβ aggregation at atomistic level, which can not be obtained by experimental approaches currently. In Chapter 4, we present and discuss the results of our simulations studying the effects of Cu^{2+} on the conformational folding and dimerization of Aβ_{1-42}. The motivation of these simulations is that experimental techniques have so far not been able to interpret the mechanism of how Cu^{2+} modulates Aβ aggregation resulting in an enhanced toxicity. Understanding the mechanism will have significant influences in the field since it will facilitate the finding of potential targets on Aβ peptides and the design of effective drugs against Alzheimer's disease.

3 Methods

3.1 Statistical mechanics

As a branch of theoretical physics, statistical mechanics studies the average behaviour (macrostate) of a very large number of behaviours (microstate) of a mechanical system using probability theory. It provides a framework for relating the microscopic properties of individual atoms and molecules to the macroscopic bulk properties of materials that can be observed in everyday life. Thus, it explains thermodynamics as a result of the classical and quantum mechanical descriptions of statistics and mechanics at the microscopic level. Generally, a number of microstates gives a compatible macrostate in a system with a large number of particles. The dynamical states of the system is a space in which all possible states are represented, called phase space.

Classically, the microscopic state of a system is a function of the momenta and coordinates of its particles. A system containing N particles has $6N$ degrees of freedom due to 3 coordinates (x,y,z) and 3 momenta (P_x, P_y, P_z) for each particle. The possible coordinates and momenta of the particles in the system form the phase space. Each state of the system is represented by a single point in the phase space. Thus, an ensemble is treated as a collection of a huge number of single points in the phase space, satisfying the conditions of a specific thermodynamic state. Some ensembles with different characteristics are described below.

3.1.1 Microcanonical ensemble (NVE)

The microcanonical ensemble [137,138] is used to represent the possible states of a mechanical system which has a constant number of particles (N), a constant volume (V) and a fixed energy (E), thus also called NVE ensemble. It corresponds to a thermally isolated system. In a NVE ensemble, every microstate with energy within a average centered at E is assigned an equal probability. Then if the total number of all possible microstates of the system is denoted as Ω, the probability p_j of finding microstate j of the system is:

$$p_j = \frac{1}{\Omega} \tag{3.1}$$

3.1.2 Canonical ensemble (NVT)

A system in a canonical ensemble [137,138] is allowed to exchange energy with a heat bath , and is also characterized by a constant number of particles (N), a constant volume (V) and a constant temperature (T). The probability p_j of finding a particular microstate j at energy level E_j of the system is expressed as:

$$p_j = \frac{e^{-E_j/k_BT}}{Z} \tag{3.2}$$

$$Z = \sum_j e^{-E_j/k_BT} \tag{3.3}$$

where Z is the partition function of the canonical ensemble. The characteristic state function of this ensemble is the Helmholtz free energy

$$A(N, V, E) = -k_BT\ lnZ \tag{3.4}$$

3.1.3 Isobaric-isothermal ensemble (NPT)

The characteristics of an isobaric-isothermal ensemble [137] is maintaining a constant number of particles (N), a constant pressure (P) and a constant temperature (T) in the system, thus called NPT ensemble, while the system's energy (E) and volume (V) fluctuate around thermal equilibrium. In a NPT ensemble, the system is exchanging volume (or work) with a barostat at pressure P and exchanging energy with a thermostat at temperature T. The NPT ensemble is of significant importance in chemistry since most of the chemical reactions are performed in constant pressure condition. The probability p_j of finding a specific microstate j of the system in a NPT ensemble is:

$$p_j = \frac{e^{-(E_j+pV_j)/k_BT}}{Z} \tag{3.5}$$

$$Z = \sum_j e^{-(E_j+pV_j)/k_BT} \tag{3.6}$$

where Z is the partition function of a NPT ensemble. And the characteristic state function of this ensemble is the Gibbs free energy:

$$G(N, P, T) = -k_BT\ lnZ \tag{3.7}$$

3.1.4 Grand canonical ensemble (μVT)

The grand canonical ensemble is used to describe the possible states of a system of particles, in which the thermodynamic equilibrium (thermal and chemical) is maintained with

a reservoir. The system is open to exchange energy and particles with the reservoir at chemical potential μ. Thus the thermodynamic state of a system in a μVT ensemble is characterized by a constant chemical potential (μ), a constant volume (V) and a constant temperature (T). The probability p_j of determining a microstate j of the system with particle number N_j and energy E_j is:

$$p_j = \frac{e^{-(N_j\mu - E_j)/k_B T}}{Z} \tag{3.8}$$

$$Z = \sum_j e^{-(N_j\mu - E_j)/k_B T} \tag{3.9}$$

where Z is the partition function of μVT ensemble.

3.2 Molecular mechanics

Molecular mechanics (MM) is using classical mechanics methods to describe molecular systems. It is based on a simple model in which the system is treated as a collection of balls (corresponding to atoms) connected together by springs (corresponding to bonds). For this approximated model, the energy of the system changes with changing geometry since the springs resist being deviated away from the natural geometry. The principle behind molecular mechanics is to use a function to express the energy of a system described by energy components corresponding to the bond stretching, bond bending and other terms.

3.2.1 Potential energy functions

The basic function form for the potential energy of a molecular system in molecular mechanics contains bonded and nonbonded terms, as illustrated in Eq. 3.10 [139,140]:

$$E_{total} = E_{bonded} + E_{nonbonded} \tag{3.10}$$

The bonded interactions account for bonds, angles and dihedral angles and improper dihedral angles. The improper dihedrals are used to define the planarity of aromatic groups and to enforce chirality in molecules. Thus, the bonded interaction potential can be written as:

$$E_{bonded} = E_{bonds} + E_{angles} + E_{dihedrals} + E_{impropers} \tag{3.11}$$

The non-bonded interactions originate from interactions of pairs of atoms which are separated by three or more covalent bonds. The nonbonded interactions can be divided into van der Waals and electrostatic terms:

$$E_{nonbonded} = E_{vdW} + E_{elec} \tag{3.12}$$

Usually, the function form used to describe the potential energy of a system is also called force field. Most of the widely used force fields are additive ones, so any additional terms known to affect the energy of a molecular system can be added to the above equations. The most common form of potential energy function used in force fields to model biosystems today is written as follows:

$$\begin{aligned} E_{Total} = E(q^N) = & \sum_{bonds} \frac{K_{ij}}{2}(l_{ij} - l_{ij}^0)^2 \\ & + \sum_{angles} \frac{k_{ijk}}{2}(\theta_{ijk} - \theta_{ijk}^0)^2 \\ & + \sum_{dihedrals} \sum_{n} \frac{V_{ijkl}^n}{2}[1 + \cos(n\phi_{ijkl} - \phi_{ijkl}^0)] \\ & + \sum_{improper} \frac{k_{ijkl}}{2}(\xi_{ijkl} - \xi_{ijkl}^0)^2 \\ & + \sum_{i=1}^{N-1} \sum_{j=i+1}^{N} f_{ij} \left\{ 4\varepsilon_{ij} \left[\left(\frac{\sigma_{ij}}{r_{ij}}\right)^{12} - \left(\frac{\sigma_{ij}}{r_{ij}}\right)^{6} \right] + \frac{Q_i Q_j}{4\pi\varepsilon_0 r_{ij}} \right\} \end{aligned} \tag{3.13}$$

where $E(q^N)$ (E_{Total}) is the potential energy expressed as a function of the system's coordinates q^N. The first four terms in Eq. 3.13 model the covalently bonded interactions the system, whereas the last terms models the nonbonded interactions between atoms in different systems or in the same system separated by at least 3 bonds. The "fudge factor" $f_{ij} = 0.5$ is used to scale down the 1,4 interactions (non-bonded interactions between atoms separated by 3 bonds), otherwise $f_{ij} = 1.0$. In the following, we will describe each term from Eq. 3.13 in detail.

Bond stretching

The bond stretching term describes the interaction between two covalently bonded atoms i and j , such as C-C, C-H, C-O *etc.*. Among many functional forms used for the bond stretching term, the Morse potential (Figure 3.1) is particularly popular, and is described by the following relationship:

$$E(l) = D_e\{1 - exp[-a(l_{ij} - l_{ij}^0)]\}^2 \tag{3.14}$$

$$a = \sqrt{k_e/2D_e} \tag{3.15}$$

where l_{ij} is the bond length, D_e is the well depth of the potential energy minimum, a controls the width of the potential, k_e is the force constant of the bond at the minimum of the potential, and l_{ij}^0 is the reference bond length between atoms i and j. As shown in Figure 3.1, the Morse potential profile fits quite well with the real profile, and it is

still accurate even at large deviation or dissociation. However, it is not widely used in molecular simulations with classical force fields. One of the reasons is that it needs more parameters (3) for each bond than other function forms such as the harmonic potential (2), resulting in computational inefficiency. Furthermore, large bond deviations from the equilibrium value or dissociations rarely occur in simulations.

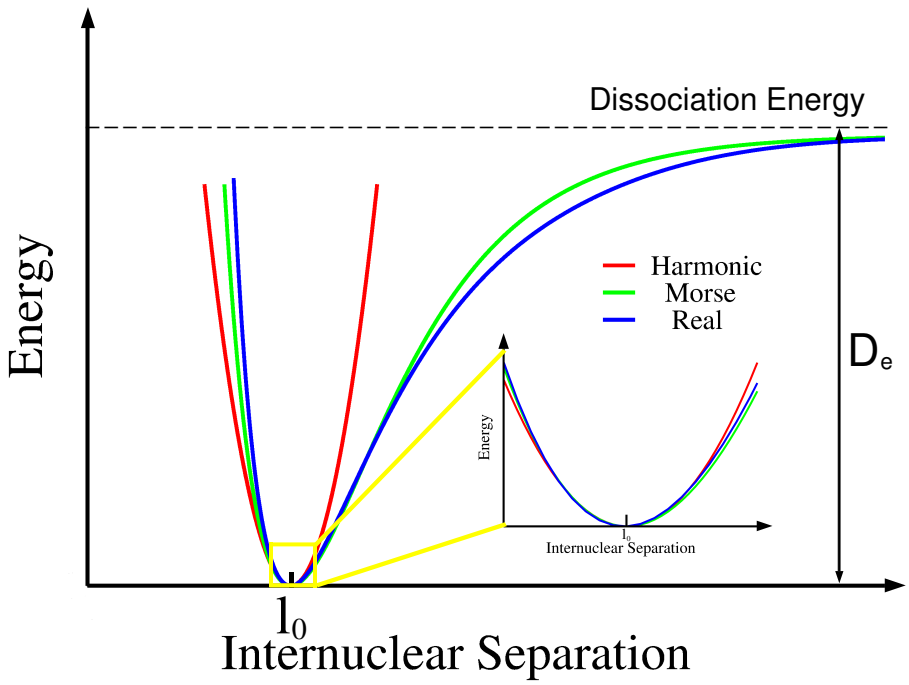

Figure 3.1: Illustration of harmonic (red) and Morse (green) potentials together with the potential profile of a real bond stretching (blue). The potential curves close to the equilibrium bond distance (l_0) are highlighted.

The most used functional form for bond stretching is the harmonic potential, based on the Hooke's law:

$$E_b = \sum_{bonds} \frac{K_{ij}}{2}(l_{ij} - l_{ij}^0)^2 \tag{3.16}$$

The total bond energy E_b of the system is calculated as a summation over all covalent bonds. Each bond is described by a harmonic potential with a unique force constant K_{ij}. Because of the vibrational motions, the bond length l_{ij} of atom i and j deviates from its equilibrium value l_{ij}^0. The harmonic potential is accurate enough to model bond stretching when the deviation from its reference value is around 0.1 Å or less as highlighted in Figure 3.1. More accurate functional forms were also developed [141,142], but they are more computationally expensive.

Angle bending

The harmonic potential or Hooke's law is also widely used for describing the angle bending from its reference value (Eq. 3.17). With this functional form, the angle between three atoms i, j and k (*e.g.* C-C-C, C-N-C, C-O-C *etc.*), in which atoms i and k are covalently bonded to the same atom j, is constrained to the reference angle by the following relationship:

$$E_a = \sum_{angles} \frac{k_{ijk}}{2}(\theta_{ijk} - \theta^0_{ijk})^2 \tag{3.17}$$

or expressed as:

$$E_a = \sum_{angles} \frac{k_{ijk}}{2}[cos(\theta_{ijk}) - cos(\theta^0_{ijk})]^2 \tag{3.18}$$

where k_{ijk} is the force constant, θ^0_{ijk} is the equilibrium value of the angle. In general, the force constants k_{ijk} of angle bending are less than k_{ij} for bond stretching, because less energy is needed to distort an angle than to compress or stretch a bond.

The accuracy of the angle bending term can be improved by adding higher-order terms. For example, there is a quartic term together with a quadratic term in MM2 force field. Then the angle bending form can be expressed as:

$$E_a = \sum_{angles} \frac{k_{ijk}}{2}(\theta_{ijk} - \theta^0_{ijk})^2[1 - k^{'}(\theta_{ijk} - \theta^0_{ijk}) - k^{''}(\theta_{ijk} - \theta^0_{ijk})^2 \cdots] \tag{3.19}$$

Torsional angle potential

A torsion angle is formed by four atoms sequentially bonded and induces rotation about the axis parring through the central bond. The torsional potential is describing the energy change associated with this rotation. The potential of proper dihedral angles is expressed as:

$$E_d = \sum_{dihedrals} \sum_{n} \frac{V^n_{ijkl}}{2} \left[1 + \cos(n\phi_{ijkl} - \phi^0_{ijkl})\right] \tag{3.20}$$

where ϕ_{ijkl} is the torsional angle defined as the angle formed between the two planes of ijk and jkl, and ϕ^0_{ijkl} is the phase factor determining where the torsion angle passes through its minimum energy. The torsional angle may rotate between $[0°, 360°]$ or $[-180°, 180°]$, with $0°$ standing for the *cis* configuration and $180°$ corresponding to the *trans* configuration. V^n_{ijkl} represent the energy barriers and n is the periodicity of the torsion. The energy associated with a $360°$ rotation should remain the same as the energy for $0°$ and thus, for periodicity $n = 1$. In Figure 3.2, it takes the ethane molecule as an example with conformations corresponding to the *cis* and *trans* configurations, and the energy barrier between them is around 2.9 kcal/mol.

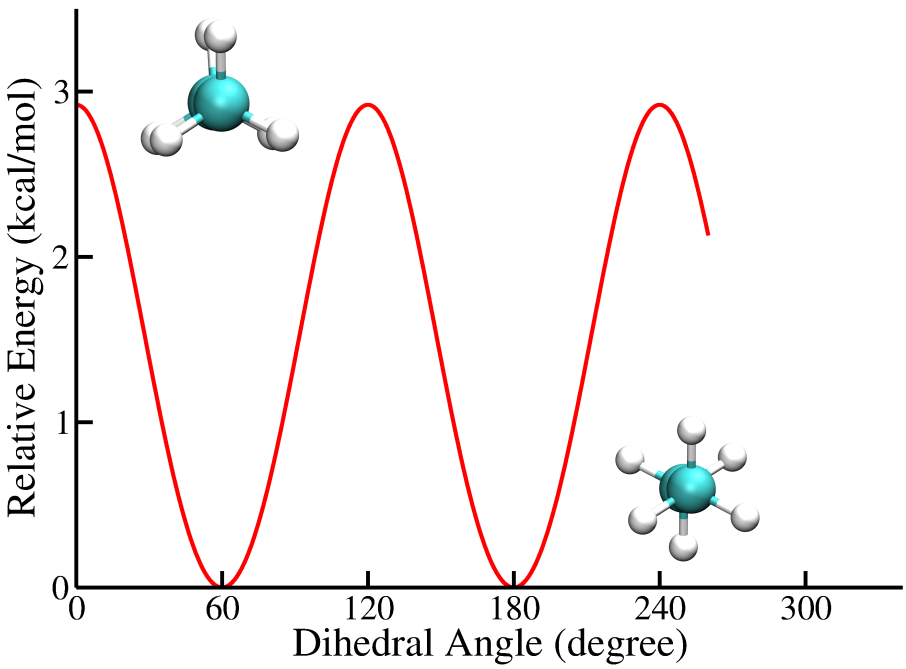

Figure 3.2: The variation of the potential energy of ethane ascribed to the dihedral angle defined by H-C-C-H atoms. The curves can be represented as a typical cosine function

Improper torsion

An improper dihedral angle (out-of-plane) is typically involving a central atom bonded with each of three other atoms. The improper dihedral potential can be incorporated into force fields to achieve specific geometries. The harmonic potential is also used for the improper torsional potential:

$$E_{id} = \sum_{impropers} \frac{k_{ijkl}}{2}(\xi_{ijkl} - \xi^0_{ijkl})^2 \tag{3.21}$$

where k_{ijkl} is the force constant, ξ_{ijkl} is the torsion angle of atoms i, j, k and k, whereas ξ^0_{ijkl} is the reference value. A value of $\xi_{ijkl} = 0°$ corresponds to all the four atoms being in the same plane.

van der Waals interactions

The van der Waals (vdW) energy (E_{vdW}) is defined between atoms i and j which are separated by at least 3 bonds in the same molecule and any atoms from different molecules. Mostly, the 12-6 Lennard-Jones (LJ) potential is used to described the van der Waals

interactions between two atoms:

$$E_{LJ} = \sum_{i=1}^{N-1} \sum_{j=i+1}^{N} 4\varepsilon_{ij} \left[\left(\frac{\sigma_{ij}}{r_{ij}} \right)^{12} - \left(\frac{\sigma_{ij}}{r_{ij}} \right)^{6} \right] \tag{3.22}$$

or is sometimes expressed as

$$E_{LJ} = \sum_{i=1}^{N-1} \sum_{j=i+1}^{N} \varepsilon_{ij} \left[\left(\frac{r_{ij}^{m}}{r_{ij}} \right)^{12} - 2 \left(\frac{r_{ij}^{m}}{r_{ij}} \right)^{6} \right] \tag{3.23}$$

where ε_{ij} is the depth of the potential well between atoms i and j, σ_{ij} is the finite distance at which the interatomic potential of i and j is zero, r_{ij} is the distance between the atoms i and j, r_{ij}^{m} is the distance at which the potential between atoms i and j reaches its minimum (Figure 3.3). The r_{ij}^{m} is related to σ_{ij} as $r_{ij}^{m} = 2^{1/6}\sigma_{ij}$. The first term, proportional to $(r_{ij})^{12}$, is repulsive accounting for the inter-nuclear repulsion and Pauli exclusion, whereas the second one, proportional to $-(r_{ij})^{6}$, is attractive due to dipole-dipole interactions, *etc.*. The parameters in the LJ equation are usually derived from fitting to experimental data or quantum mechanics calculations at high levels. The LJ potential is extensively applied in computer simulations because of its computational simplicity and efficiency even though more accurate potentials exist.

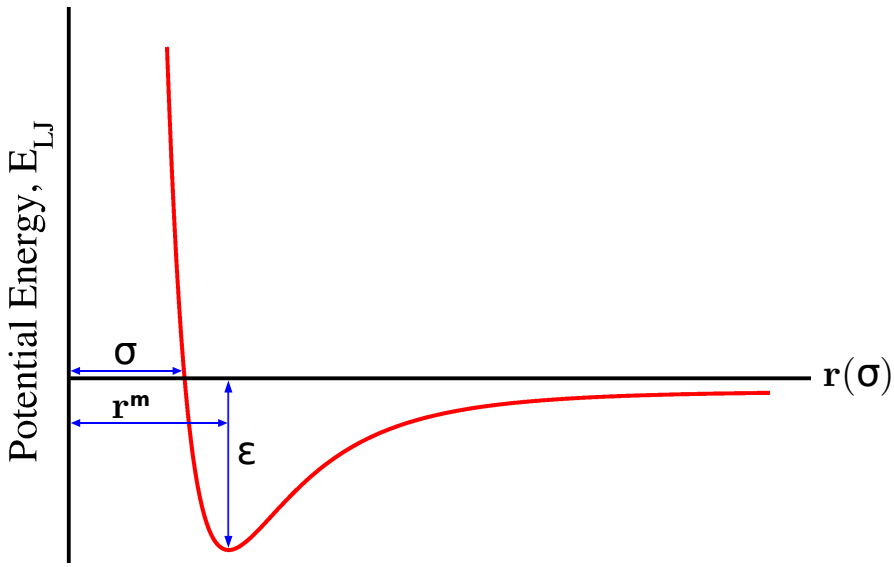

Figure 3.3: The Lennard-Jones potential. The deeper the well depth (ε), the stronger the attraction between the two particles.

The Buckingham potential is another functional form that can be used to model van der Waals interactions, however, it is more computationally expensive. Thus it is not

widely applied in common force fields. It can be expressed as:

$$E_{bh} = \sum_{i>j}^{N} A_{ij} exp(-B_{ij} r_{ij}) - \frac{C_{ij}}{r_{ij}^6} \tag{3.24}$$

where A_{ij}, B_{ij} and C_{ij} are constants, r_{ij} is the interatomic distance between atoms i and j. The two terms on the rights side represent energies of repulsion and attraction, respectively.

Electrostatic interactions

The electrostatic interaction between atoms i and j due to their partial charges (Q_i and Q_j) is often described by the Coulombic potential:

$$U_{elec} = \sum_{i>j}^{N} \frac{Q_i Q_j}{4\pi\varepsilon_0 r_{ij}} \tag{3.25}$$

where r_{ij} is the distance between the two atoms, Q_i and Q_j are their partial charges, and ε_0 is the permittivity of the vacuum. Similar to the LJ potential, the Coulombic interactions are only taken into consideration when atoms i and j are separated by at least 3 bonds.

Since the calculation of the nonbonded interactions is very time-consuming in simulations, predefined cut-offs are usually applied for interatomic distances that can speed up the computations in simulations. The interactions beyond the cut-offs are ignored.

3.2.2 Force field parameterization

In addition to the functional forms of the potentials as mentioned above, a force field includes a large number of parameters needed for the calculation of the potentials for different types of atoms (vdW parameters and partial charges), chemical bonds, angles, dihedral angles, *etc.*. It is not a trivial task to parameterize a force field. A large number of different parameters have to be determined, growing rapidly with increasing number of atom types. A set of targeted data is required to guide the development of a force field, including experimental (e.g. vibrational spectra, density, solvation free energy and X-ray structure $\cdots$) and quantum mechanics (QM) information (e.g. minimum energy geometry, dipole movement, conformational energy barrier, electrostatic potential $\cdots$). Different force fields have different targeted experimental and QM data.

Some popular force fields like CHARMM, AMBER, GROMOS, OPLS-AA have been widely used in the simulations of biological macromolecules such as proteins and DNA [143–149]. There are two typical force fields for small molecules, CHARMM General force

field (CGenFF) [150,151] and General AMBER force field (GAFF) [152]. Unlike force fields for proteins, there is no standard set of force field parameters for the metal ions in metalloproteins, as different metal ions have different coordination spheres and even the same metal ion could have different coordination in different metalloproteins. However, there has been great effort towards the development of force field parameters for metal ions using nonbonded [153,154], cationic dummy [155,156] and bonded models [157,158].

For developing nonbonded or cationic dummy models, the experimental hydration free energy and radius distribution functions of the metal ions are the most common targeted data. For the bonded model, the targeted data is usually the QM data calculated at high level. The minimum requirements for the metal sphere geometry accounts for the reference values of bonds and angles related to the coordination centers of metal ions. The force constants of bonds and angles are derived from QM potential energy surface scan or frequency calculations. The dihedrals involved by metal ions are generally ignored, though there is a study that introduced the dihedral parameters [159]. The restrained electrostatic potential (RESP) [160,161] is widely accepted and chosen for the calculation of the partial charge for each atom of the metal center.

3.3 Molecular dynamics simulation

Molecular dynamics (MD) simulations are among the main tools used in theoretical studies that investigate the behaviours of biological systems at high resolution. In a simulation, the atoms of one or several molecules interact with each other for a limited period of time (femtoseconds to microseconds) and the coordinates, determined by motion, are periodically written into a trajectory to be taken analysed. Newton's second law for a particle i with mass m_i is:

$$\mathbf{F}_i = m_i \mathbf{a}_i \tag{3.26}$$

where $\mathbf{F}_i$ is the force acting on particle i and $\mathbf{a}_i$ is the acceleration of particle i. The acceleration is the second derivative of the coordinates q with respective to time t, or the first derivative of the velocity v with respective to time t:

$$\mathbf{a}_i = \frac{\partial^2 \mathbf{q}_i}{\partial t^2} = \frac{\partial \mathbf{v}_i}{\partial t} \tag{3.27}$$

In a system with N particle, each particle experiences a force acting from all the other particles, therefore the force is a function of the 3N coordinates of the N particles. Thus the Newton's law of motion could be expressed as a set of 3N coupled second order differential equations:

$$\mathbf{F}_i = m_i \frac{\partial^2 q_i}{\partial t^2} \tag{3.28}$$

where F_i can be divided into F_{xi}, F_{yi} and F_{zi} and q_i can be divided into q_{xi}, q_{yi} and q_{zi}. Moreover, the gradient of the potential energy E of the whole system, acting on particle i represents the force $\mathbf{F}_i$ exerted on particle i:

$$\mathbf{F}_i = -\nabla_i E \tag{3.29}$$

Once we combine equations 3.28 and 3.29, we get the relationship between the potential energy and the positions of the particles:

$$-\frac{\partial E}{\partial \mathbf{q}_i} = m_i \frac{\partial^2 \mathbf{q}_i}{\partial t^2} \tag{3.30}$$

where $\mathbf{q}_i$ can be divided into q_{xi}, q_{yi} and q_{zi}.

To start a simulation, the initial coordinates and velocities need to be assigned to all the particles in the system. One also needs to know the potential energy functions (Sec. 3.2.1) that will be used to describe the interactions between particles. The Maxwell-Boltzmann distribution is often used for assigning the initial velocities $\mathbf{v}$. The probability of particle i having velocities $\mathbf{v}_i$ at temperature T is given by:

$$p(\mathbf{v}_i) = \left(\frac{m_i}{2\pi k_B T}\right)^{\frac{3}{2}} exp\left(-\frac{1}{2}\frac{m_i v_{i,x}^2 + m_i v_{i,y}^2 + m_i v_{i,z}^2}{k_B T}\right) \tag{3.31}$$

where $v_{i,x}$, $v_{i,y}$, $v_{i,z}$ are the three components of velocity $\mathbf{v}_i$ along x, y and z axes, respectively, and k_B is the Boltzmann constant.

3.3.1 Integration algorithms

Since it is impossible to solve analytically Eq. 3.30 for a large system, one has to employ numerical integration methods. Thus, integration algorithms are needed to propagate positions, velocities and accelerations of the particles in a very short time interval denoted as time step. On this short time scale, it is assumed that the positions, velocities and accelerations of particles can be approximated by a Taylor expansion [139,162] for all the integration algorithms described below:

$$\mathbf{q}(t+\delta t) = \mathbf{q}(t) + \mathbf{v}(t)\delta t + \frac{1}{2}\mathbf{a}(t)\delta t^2 + \cdots \tag{3.32}$$

$$\mathbf{v}(t+\delta t) = \mathbf{v}(t) + \mathbf{a}(t)\delta t + \frac{1}{2}\mathbf{b}(t)\delta t^2 + \cdots \tag{3.33}$$

$$\mathbf{a}(t+\delta t) = \mathbf{a}(t) + \mathbf{b}(t)\delta t + \frac{1}{2}\mathbf{c}(t)\delta t^2 + \cdots \tag{3.34}$$

where $\mathbf{q}$, $\mathbf{v}$ and $\mathbf{a}$ are the coordinates, velocity and acceleration, respectively. And $\mathbf{b}$ and $\mathbf{c}$ are the third and fourth derivatives of $\mathbf{q}$. Normally, the higher derivatives are ignored

during simulations.

Verlet algorithm

The Verlet algorithm can calculate the new positions $q(t+\delta t)$ at $t+\delta t$ based on the positions $\mathbf{q}(t)$ and accelerations $\mathbf{a}(t)$ at time t as well as the position $\mathbf{q}(t-\delta t)$ at the previous time step $t-\delta t$. As the most frequently used algorithm for integration of the equations of motion, the Verlet algorithm can be written as:

$$\mathbf{q}(t+\delta t) = \mathbf{q}(t) + \mathbf{v}(t)\delta t + \frac{1}{2}\mathbf{a}(t)\delta t^2 + ... \tag{3.35}$$

$$\mathbf{q}(t-\delta t) = \mathbf{q}(t) - \mathbf{v}(t)\delta t + \frac{1}{2}\mathbf{a}(t)\delta t^2 - ... \tag{3.36}$$

Summing up these two Taylor expressions gives:

$$\mathbf{q}(t+\delta t) = 2\mathbf{q}(t) - \mathbf{q}(t-\delta t) + \mathbf{a}(t)\delta t^2 \tag{3.37}$$

As shown in Eq. 3.37, no explicit calculated velocities appear in this algorithm. It is straightforward to implement and has modest storage requirements, but it only has moderate precision. Even though it is very difficult to obtain the velocities due to the lack of an explicit velocity term, they can be calculated in a simple way by:

$$\mathbf{v}(t) = [\mathbf{q}(t+\delta t) - \mathbf{q}(t-\delta t)]/2\delta t \tag{3.38}$$

Alternatively, the velocities can be estimated at the half-step, $t+\frac{1}{2}\delta t$:

$$\mathbf{v}(t+\frac{1}{2}\delta t) = [\mathbf{q}(t+\delta t) - \mathbf{q}(t)]/\delta t \tag{3.39}$$

Leap-Frog algorithm

In order to prevent the disadvantages of the Verlet algorithm, the Leap-Frog algorithm was developed. The following forms are used: [139,163]:

$$\mathbf{q}(t+\delta t) = \mathbf{q}(t) + \mathbf{v}(t+\frac{1}{2}\delta t)\delta t \tag{3.40}$$

$$\mathbf{v}(t+\frac{1}{2}\delta t) = \mathbf{v}(t-\frac{1}{2}\delta t) + \mathbf{a}(t)\delta t \tag{3.41}$$

To apply the leap-frog algorithm, the velocities $\mathbf{v}(t+\frac{1}{2}\delta t)$ are first calculated at time $t+\frac{1}{2}\delta t$ and accelerations $\mathbf{a}(t)$ at time t. Then the new coordinates $\mathbf{q}(t+\delta t)$ can be

calculated with Eq. 3.40 at $t + \delta t$. And the velocities $\mathbf{v}(t)$ can be derived from:

$$\mathbf{v}(t) = \frac{1}{2}[\mathbf{v}(t + \frac{1}{2}\delta t) + \mathbf{v}(t - \frac{1}{2}\delta t)] \tag{3.42}$$

In this way, the velocities 'leap-frog' over the positions to obtain their values at $t + \frac{1}{2}\delta t$, and the positions 'leap-frog' over the velocities to deduce the new values at $t+\delta t$ as well as the velocities at $t + \frac{3}{2}\delta t$. The advantage of the Leap-Frog algorithm is that the velocities are included explicitly compared to the Verlet algorithm. As the velocities and positions are not calculated at the same time, the contribution of the potential energy as a function of the positions and the kinetic energy as a function of the velocities to the total energy cannot be assessed at the same time.

Velocity Verlet algorithm

For the Velocity Verlet algorithm, positions, velocities and accelerations are given at the same time t and no precision is compromised [139,164]:

$$\mathbf{q}(t + \delta t) = \mathbf{q}(t) + \mathbf{v}(t)\delta t + \frac{1}{2}\mathbf{a}(t)\delta t^2 \tag{3.43}$$

$$\mathbf{v}(t + \delta t) = \mathbf{v}(t) + \frac{1}{2}[\mathbf{a}(t) + \mathbf{a}(t + \delta t)]\delta t \tag{3.44}$$

As can be seen from Eq. 3.44, the calculation of the new velocities $v(t + \delta t)$ needs the accelerations at both t and $t + \delta t$. So the new positions at $t + \delta t$ should be computed firstly with Eq. 3.43 using the velocities and accelerations at t.

3.3.2 Thermostats

A thermostat is a component which is used to control the temperature of a system so that it can be maintained close to a targeted point. Controlling temperature in dynamics simulations is of great importance during the equilibration of the system in order to avoid drifting, which might result from integration errors or increased frictional forces due to over-heating. Molecular dynamics simulations at constant temperature are necessary to understand the features of a molecular system related to temperature, such as the binding of a ligand to a protein, or the folding and unfolding of peptides. It is also important for comparing simulations to experiments, since experiments are commonly carried out at constant temperature. In molecular dynamics simulations, the temperature is controlled via the system's kinetic energy using the equipartition theorem:

$$\frac{1}{2}k_B T = \frac{1}{2}m_i v_{i,x}^2 \tag{3.45}$$

A few thermostats widely used in simulations of molecular systems at constant temperature are described below.

Berendsen thermostat

The Berendsen thermostat is a coupling algorithm [165], which is used to couple the system to an external heat bath at fixed temperature T_0. The heat bath is acting as a source of thermal energy for the system by scaling down the velocities of the particles at each time step. The rate of exchange temperature is proportional to the difference of temperature between the heat bath and the system as shown in Eq:3.46.

$$\frac{dT(t)}{dt} = \frac{T_0 - T(t)}{\tau} \tag{3.46}$$

where τ is a coupling parameter (time constant) determining the tightness of coupling between the heat bath and the system. The deviation from the targeted temperature decays exponentially with λ. The difference in temperature between successive time step δt is given:

$$\Delta T = \frac{\delta t}{\tau}[T_0 - T(t)] \tag{3.47}$$

Thus, the scaling factor λ for the velocities is expressed:

$$\lambda^2 = 1 + \frac{\delta t}{\tau}\left(\frac{T_0}{T(t)} - 1\right) \tag{3.48}$$

Generally, large τ results in weak coupling, on the contrary, small τ means strong coupling. When τ is set as the same as the time step ($\tau = \delta t$), the algorithm is corresponding to the simple velocity scaling method. It has been suggested that a coupling parameter τ value of 0.4 ps works properly with time step δt of 1 fs.

Velocity-rescaling thermostat

The advantage of Berendsen thermostat is that the system is efficiently relaxed to the desired temperature. However, it can also generate incorrect sampling and restrict the fluctuations of the kinetic energy of the system. Similar to the Berendsen algorithm, Bussi *et al.* [166] proposed the velocity rescaling thermostat, which produces a reasonable ensemble by adding a stochastic term so that it can generate the correct kinetic energy distribution:

$$dK = (\bar{K} - K)\frac{dt}{\tau} + 2\sqrt{\frac{K\bar{K}}{N_f}}\frac{dW}{\sqrt{\tau}} \tag{3.49}$$

where $\bar{K}$ is the average kinetic energy at target temperature, K denotes the total kinetic energy, N_f is the number of degrees of freedom and dW is the Wiener noise.

Nosé-Hoover thermostat

Because of the extreme efficiency of the Berendsen thermostat, it is widely applied for the initial equilibration of a simulation, while a different thermostat which can generate reasonable kinetic energy distribution has to be chosen for the production run. The Nosé-Hoover thermostat [139] was originally proposed by Nosé [167] and subsequently modified by Hoover [168]. It has been widely applied for constant temperature molecular dynamics simulations as one of the most accurate and efficient methods. It treats the thermal reservoir as an integral part of the system and an additional degree of freedom is assigned to the reservoir. Thus, the thermal reservoir and a friction term are introduced to the modified equation of motion. The friction force is proportional to the velocities of particles and the friction parameter ξ. This parameter is characterized with a fully dynamic quantity with its own momentum p_ξ. Then the equation of motion comes to:

$$\frac{d^2\mathbf{r}_i}{dt^2} = \frac{\mathbf{F}_i}{m_i} - \frac{p_\xi}{Q}\frac{d\mathbf{r}_i}{dt} \tag{3.50}$$

where Q is called the "mass parameter" of the reservoir controlling the strength of the coupling. And the friction parameter ξ of the equation of motion is determined by:

$$\frac{dp_\xi}{dt} = (T - T_0) \tag{3.51}$$

where T_0 is the reference temperature of the heat bath and T is the system's temperature.

3.3.3 Barostats

Similar to thermostats, maintaining the system at a constant pressure is also desirable as it allows the exploration of the the system's behaviours as a function of pressure. Many experimental measurements are done under constant temperature and constant pressure conditions. Thus, simulations in the NPT ensemble are most relevant to experiment comparison. The systems are coupled to barostats that control the pressure of the system. Some of the most used barostats are explained below.

Berendsen barostat

Unlike the Berendsen thermostat's scaling velocities, the Berendsen barostat rescales the coordinates of the particles and the box vectors periodically to control the system's pressure [165]. The rate of pressure change is described by:

$$\frac{dP(t)}{dt} = \frac{P_0 - P(t)}{\tau_P} \tag{3.52}$$

where τ_P is the coupling constant determining how tightly the coupling between the bath and the system is, and $P(t)$ is the pressure at time t. In order to adjust the volume of the system, the atomic coordinates of all the particles are scaled by the factor λ:

$$\lambda = \left\{1 + \frac{\Delta t}{\tau_P}\beta[P(t) - P_0]\right\}^{1/3} \tag{3.53}$$

where β is the experimental isothermal compressibility.

Parrinello-Rahman barostat

The Berendsen barostat algorithm generates the correct average pressure of a simulation, but it does not produce the exact NPT ensemble. If the fluctuations in pressure and volume are important in some particular systems (e.g. protein with lipid bilayer), the Berendsen barostat is not a good choice for the simulation in the NPT ensemble. The Parrinello-Rahman barostat [169,170] can produce the real NPT ensemble in theory. With the Parrinello-Rahman algorithm, the box vectors $\mathbf{b}$ are described as:

$$\frac{d\mathbf{b}^2}{dt^2} = \frac{V}{\mathbf{W}\mathbf{b}'}(P - P_0) \tag{3.54}$$

where V is the volume of the box, W is a parameter used to determine the coupling strength and P and P_0 represent the current and reference pressures, respectively. The combination of the Parrinello-Rahman barostat and the Nosé-Hoover thermostat is widely applied in most studies.

3.3.4 Periodic boundary conditions

Periodic boundary conditions (PBCs) are a set of boundary conditions which are widely used to approximate a system of large (infinite) size by using a small unit cell [140]. PBCs are frequently applied in computer simulations and mathematical models. With PBCs, the unit cell containing the system is multiplicate in all directions to form an infinite lattice. Figure 3.4 illustrates the concept of periodic boundary conditions in two dimensions. The central unit cell is surrounded by 8 neighbouring cells. The coordinates of the image particles found in the surrounding boxes are related to those in the primary box by simple translations. During simulations, when a particle ($\mathbf{A}$ or $\mathbf{B}$ or $\mathbf{C}$) leaves the central unit cell, its periodic image ($\mathbf{A}'$ or $\mathbf{B}'$ or $\mathbf{C}'$) enters at the opposite side with the same velocities. For PBC in three dimensions, the central unit cell has 26 identical adjacent image cells. Thus, whenever a particle leaves the simulation cell, it is replaced by another one with exactly the same velocity, entering from the opposite cell face. Thus, the number of particles in the cell is conserved. For simulations with PBCs, only cells close to the

central cell are necessary for the short-range non-bonded interactions like the truncated Lennard-Jones strategy. However, when interactions extend beyond the box boundary like long-range electrostatic potentials, truncating the interactions at a certain distance (cut-off) will result in non-physical distributions of the molecules with discontinuous forces and energies. Therefore, some lattice sum methods such as Ewald sum [171], Particle Mesh Ewald (PME) [172,173] and particle-particle particle-mesh (PPPM) [172,174,175] are proposed for the calculation of electrostatic interactions under PBC. Meanwhile, an appropriate cut-off is needed so that a particle in the primary box does not see its image in the surrounding boxes.

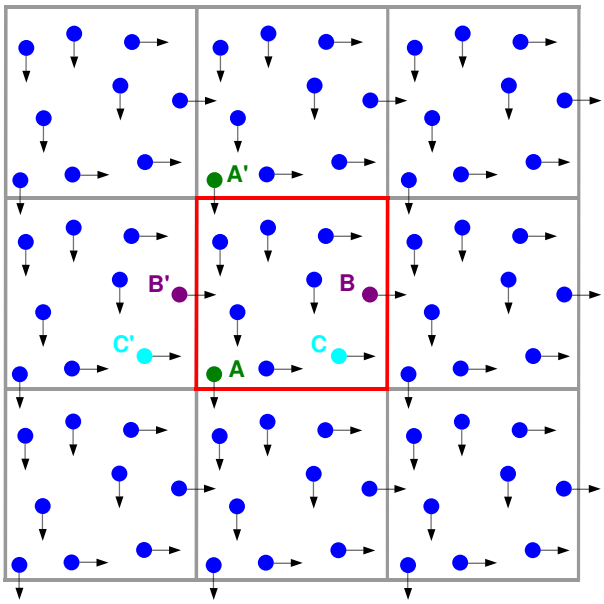

Figure 3.4: Periodic boundary conditions in two dimensions

3.3.5 Solvation

Most of the chemical and biological experiments are carried out in water or buffers. The solvent is very important to molecular properties and its effects depend on the solvent characteristics. It is thus very important to develop accurate models that treat the solvent properly in MD simulations. Currently, there are two types of solvation algorithms widely applied in molecular dynamics simulations. One is the implicit solvation (also called continuum solvation), in which the solvent is represented as a continuous medium. A variety of implicit solvent models have been developed during the past years, and the generalized Born (GB)/surface area (SA) model became very popular. The other type is known as explicit solvation, based on using hundreds or thousands of discrete solvent molecules. There are many types of explicit water models developed and characterized

by: (**i**) the number of interaction points, (**ii**) rigid or flexible, (**iii**) and polarization effects. Moreover, different water models are suggested to work with different force fields, e.g. SPC and SPC/E [176] for GROMOS force fields [146,149], TIP3P [177] for AMBER [147] and CHARMM [143,145] force fields, as well as TIP4P [177] and TIP5P [178] for OPLS-AA [179,180].

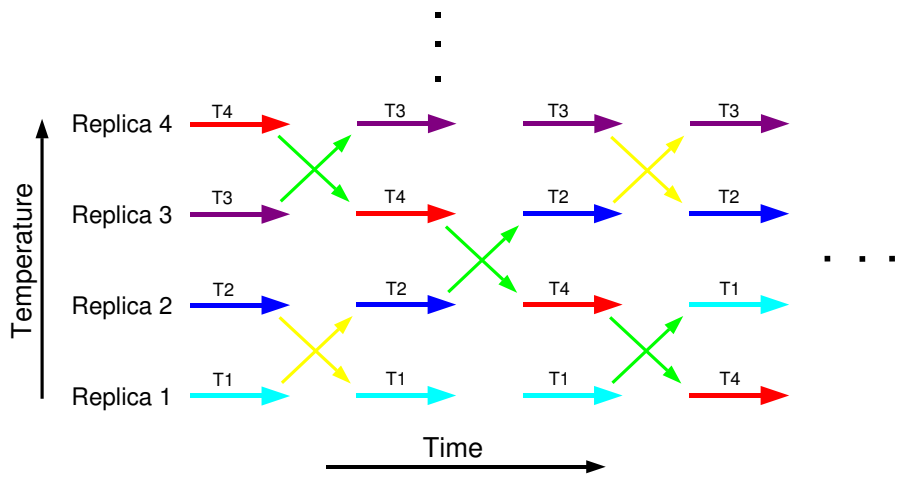

Figure 3.5: An illustration of a REMD simulation. Different colors correspond to different replicas, the exchange of replicas are accepted (green arrows) or rejected (yellow arrows) based on Eq. 3.55

3.3.6 Replica exchange molecular dynamics simulation

With conventional constant-temperature MD simulations, it is often difficult to obtain accurate canonical distributions at room temperature, because these simulations tend to get trapped in local minimum-energy states. However, the replica exchange MD (REMD) method is effective to overcome the multiple-minima problem by running multiple MD simulations of the same system (replicas) simultaneously at different temperatures, as shown in Figure 3.5. At set time intervals, attempts are made to swap temperatures between two different replicas i and j. The exchanges are accepted (green arrows in Figure 3.5) or rejected (yellow arrows in Figure 3.5) according to the Metropolis-Hastings criterion with a probability p:

$$p = min\left(1, e^{\left((E_i - E_j)\left(\frac{1}{k_B T_i} - \frac{1}{k_B T_j}\right)\right)}\right) \tag{3.55}$$

and k_B is the Boltzmann constant, T_i and E_i denote the temperature and potential energy of replica i, respectively, and j is typically replica $i+1$ at the same time step. The temperatures for the replicas are usually exponentially spaced between a minimum value,

T_{min} , and a maximum value, T_{max}. After exchange, the MD simulations resume at the new temperatures. This procedure allows for an improved sampling of the conformational space at low temperatures, since crossing potential energy barriers is facilitated at higher temperatures, and the resulting conformational changes migrate into the lower T replicas. The replica exchange method is thus a high efficiency sampling technique, which was first combined with MD by Sugita and Okamoto [24] and has since then been widely used for studying protein folding and aggregation.

3.4 Analysis

The following analysis methods are particularly useful for MD simulations of protein systems.

3.4.1 Root mean square deviation

The root mean square deviation (RMSD) is frequently used to measure the differences between two protein conformations. Usually, the backbone atoms of two superimposed structures are chosen for the calculations. The formula for the RMSD calculation is:

$$RMSD = \sqrt{\frac{1}{N}\sum_{i=1}^{N}((x_i^A - x_i^B)^2 + (y_i^A - y_i^B)^2 + (z_i^A - z_i^B)^2)} \tag{3.56}$$

where x_i, y_i and z_i are the coordinates of atom i. A and B refer to two different conformations. N is the number of particles or pairs of equivalent atoms. The common unit for RMSD is in Angstrom (Å).

3.4.2 Root mean square fluctuation

The root mean square fluctuation (RMSF) is frequently used to measure the deviation between the position of one particle and some reference position. In MD simulations, Cα atoms are usually chosen for the calculation in order to determine the flexibility of the corresponding residues. It can be calculated with:

$$RMSF = \sqrt{\frac{1}{T}\sum_{t_j=1}^{T}((x_i(t_j) - x_{i_0})^2 + (y_i(t_j) - y_{i_0})^2 + (z_i(t_j) - z_{i_0})^2)} \tag{3.57}$$

where T is the time of the simulation corresponding to the number of conformations, x_i, y_i and z_i are the coordinates of atom i at time t_j, while x_{i_0}, y_{i_0} and z_{i_0} are the reference coordinates of atom i. Typically the reference position is the time-averaged position of the same atom.

3.4.3 Cluster analysis

Cluster analysis is widely used to group a set of objects. The rule is that objects in the same group (also called cluster) are closer (in some property) to each other than those from other groups. In MD simulations, cluster analysis is performed to identify similar conformations based on the mutual RMSD values between all the conformations. A RMSD cut-off is needed for the computing. There are various clustering methods available, and one of the most used clustering algorithms applied to MD trajectories is developed by Daura *et al.* [181].

3.4.4 Free energy surfaces

Biomolecular processes, such as peptide's folding or aggregation, can be described in terms of the system's free energy:

$$\Delta G(R) = -k_B T \; [ln \; P(R) - ln \; P_{max}] \tag{3.58}$$

where k_B is the Boltzmann constant, and P is the probability distribution of the molecular system along some reaction coordinate R, P_{max} is the maximum value, which is a substrate to ensure $\Delta G = 0$ for the lowest free energy minimum.

3.4.5 Principal component analysis

Principal component analysis (PCA), also called covariance analysis or essential dynamics, is a statistical procedure that converts a number of possibly correlated variables into a smaller number of uncorrelated variables called principal components based on an orthogonal transformation. Generally, a vector space transform is used to reduce the dimensionality of large data sets in PCA.

The PCA method uses the covariance matrix $\mathbf{\Sigma}$ of the atomic coordinates:

$$\sigma_{ij} = \langle (q_i - \langle q_i \rangle)(q_j - \langle q_j \rangle) \rangle \quad (1 \leq i, j \leq 3N) \tag{3.59}$$

where q_i and q_j are the mass-weighted Cartesian coordinates, N is the number of particles in the system and $\langle ... \rangle$ denotes the average over all sampled conformations during the simulations. By diagonalizing the $3N \times 3N$ matrix $\mathbf{\Sigma}$ with an orthonormal transformation matrix $\mathbf{V}$ in Eq. 3.60, one obtains $3N$ eigenvectors (columns of $\mathbf{V}$) $\mathbf{v_k}$ and eigenvalues λ_k $(1 \leq k \leq 3N)$ with $\lambda_1 \geq \lambda_2 \geq \lambda_3 \geq \cdots \geq \lambda_{3N}$:

$$\mathbf{V^T \Sigma V} = diag(\lambda_1, \lambda_2, \lambda_3 \cdots \lambda_{3N}) \tag{3.60}$$

where $\mathbf{V^T}$ is the transpose of $\mathbf{V}$. The initial $3N$ coordinates of the system can be projected

onto the $3N$ eigenvectors to give the $3N$ principal components $C_i(t)$, $1 \leq i \leq 3N$:

$$\mathbf{C} = \mathbf{V}^{\mathbf{T}}[\mathbf{q}(t) - \langle \mathbf{q} \rangle] \tag{3.61}$$

where t is the simulation time. The eigenvalues are the mean-square fluctuations in the direction of the corresponding eigenvectors. The first few PCs are typically accounting for collective and global motions within the system.

4 Results

The main aim of this thesis work is to study the interactions between Cu^{2+} and $A\beta_{1-42}$, to investigate the influence of Cu^{2+} and pH values on $A\beta_{1-42}$ folding and dimerization. Thus, we performed MD simulations, which can be divided into three parts.

(1) **Conformational transitions of the amyloid-β peptide upon copper(II) binding and pH changes**

In this study we performed H-REMD simulations with 2 microseconds of total simulation time per simulation to study the influences of Cu^{2+} and pH on $A\beta_{1-42}$ folding. Firstly, we developed OPLS-AA/L force field parameters for describing the interactions between Cu^{2+} and $A\beta_{1-42}$ with a bonded Cu^{2+} model. After validation, these parameters were used for the simulation of the $A\beta_{1-42}/Cu^{2+}$ complex in water. In addition, we simulated $A\beta_{1-42}$ at different pH (5.3, 6.0, 7.4) in water. We found that in all four systems the most abundant secondary structures are turns, bends and random coils. The initial helical structure of $A\beta_{1-42}$ is mostly disrupted in the four systems. We also observed a β-hairpin structure appearing at the C-terminal hydrophobic region upon Cu^{2+} binding. Moreover, less helical and more β-sheet structures were sampled for $A\beta_{1-42}$ at acidic pH. We also obtained that the conformational flexibility of $A\beta_{1-42}$ is greatly enhanced by Cu^{2+} binding and lowering the pH value. Furthermore, principal component analysis and transition networks clearly show the differences in the conformational kinetics induced by Cu^{2+} binding In summary, we concluded that both Cu^{2+} binding and mild acidic conditions shift the conformational equilibrium of the monomeric $A\beta$ towards conformers, which may have a higher tendency to aggregate.

Manuscript to be submitted to PLOS Computational Biology (impact factor (IF) 4.620). Contribution of QL: Development of the force field parameters, complete execution of the simulations and analyses, finishing 85% of the manuscript writing.

(2) **Development and application of a nonbonded Cu^{2+} model that includes the Jahn–Teller effect**

We developed a nonbonded model of Cu^{2+} (CuDum) in this work. It captures both the Jahn-Teller effect and the experimental hydration free energy, and maintains the coordination geometries stably during MD simulations. Moreover, we transferred the parameters of a Zn^{2+} dummy model (ZnDum) previously developed with Q [182] by Duarte *et al.* [183] to GROMACS. We found that our models can reproduce the square planar geometries of Cu^{2+} in Aβ_{1-16} and Cu-Zn superoxide dismutase (CuZnSOD), respectively. We also observed that the interactions between Aβ_{1-16} and ZnDum is lower than those between Aβ_{1-16} and CuDum, which is in agreement with experimental data. Our study also revealed that CuDum and ZnDum can be applied together in CuZnSOD without artificial repulsion between the two metal centers, which is usually a problem when the metal ions are modelled as simple van der Waals spheres with the full charge assigned to this sphere.

This work was published on *The Journal of Physical Chemistry Letters*, 6(13): 2657–2662 (IF 7.458). Contribution of QL: Development of the CuDum model, Complete execution of all simulations, analyses of all the simulations, finishing 90% of the manuscript writing.

(3) **The role of Cu^{2+} in the dimerization of Aβ_{1-42} studied by Hamiltonian replica exchange molecular dynamics simulations**

Here, we focused on the role of the copper ion in the dimerization of Aβ_{1-42} using both a bonded model and a nonbonded model for Cu^{2+}. We found that the bonded Cu^{2+} greatly decreases the flexibility of Aβ_{1-42} in the dimer complex 2Aβ_{1-42}/Cu^{2+} while the nonbonded CuDum only slightly stabilizes Aβ_{1-42} compared to the 2Aβ_{1-42} system without Cu^{2+}. For all three systems, a propensity of around 10-15% for β-sheets and <10% for helices was observed. Cu^{2+} promotes the formation of β-hairpins at the CHC and C-terminal regions of Aβ_{1-42}, which agrees with the observations from our previous study on monomeric Aβ_{1-42} with Cu^{2+}. CuDum was not stable at the coordination center, and ligand exchange was observed in the simulations. Generally, Cu^{2+} binding to Aβ_{1-42} is able to reduce the propensities to form salt bridges in the dimer system. In summary, our simulations reveal that Cu^{2+} promotes β-hairpins at the CHC and C-terminal regions in the Aβ_{1-42} dimer, which probably accounts for the different aggregation behaviours and in turn, toxicity of Aβ_{1-42} in the presence of Cu^{2+}.

Manuscript in preparation. Contribution of QL: Development of the force field parameters, Complete execution of all simulations, analyses of all simulations, finishing 90% of the manuscript writing.

In the following sections, the results of these three studies are presented as manuscripts, which are either published, submitted or in preparation. References referred to the individual manuscripts are given in the following sections (and not the references given at the end of this thesis).

4.1 Conformational transitions of the amyloid-β peptide upon copper(II) binding and pH changes

Conformational Transitions of the Amyloid-β Peptide Upon Copper(II) Binding and pH Changes

Qinghua Liao[1], Olujide O. Olubiyi[1], Michael C. Owen[1], Bogdan Barz[1], Birgit Strodel[1,2],
1 Institute of Complex Systems: Structural Biochemistry, Forschungszentrum Jülich, 52425 Jülich, Germany.
2 Institute of Theoretical and Computational Chemistry, Heinrich Heine University Düsseldorf, Universitätsstrasse 1, 40225 Düsseldorf, Germany.
*** E-mail: b.strodel@fz-juelich.de**

Abstract

Amyloid-β (Aβ) is a natively unfolded peptide found in all Alzheimer's disease patients as the major component of fibrillar plaques, which are recognized as an important pathological hallmark in Alzheimer's disease. The binding of copper to Aβ increases its neurotoxicity, as Cu^{2+} causes Aβ to become redox active and decreases the lag time associated with Aβ aggregation. In addition, the pH is also a major factor that influences both the Aβ aggregation rates and Cu^{2+} binding. Hamiltonian replica exchange molecular dynamics (H-REMD) simulations enable atomistic insights into the effects of pH and Cu^{2+} complexation on the structure and dynamics of Aβ. To study the Aβ_{1-42}/Cu^{2+} complex, we have developed new force field parameters for the divalent copper ion ligated by the two histidine residues, His6 and His13, as well as the amine and carbonyl groups of Asp1 in a distorted square planar geometry. Our comparative simulations reveal that both Cu^{2+} binding and a low pH mimicking acidosis, linked to inflammatory processes *in vivo*, accelerate the formation of β-sheet in Aβ_{1-42} and lead to the stabilization of salt bridges, previously shown to promote Aβ aggregation. The results suggest that Cu^{2+} binding and mild acidic conditions can shift the conformational equilibrium towards aggregation-prone conformers for the monomeric Aβ.

Author Summary

The misfolding and aggregation of amyloid-β (Aβ) is an important event in the etiology of Alzheimer's disease. Cu^{2+} can bind to Aβ and modulate its folding and aggregation, but the molecular details of how Cu^{2+} induces Aβ to be aggregation-prone are still elusive. The pH is also an important factor influencing both Aβ aggregation and Cu^{2+} coordination in Aβ. In this study we developed a set of force field parameters to model the interactions between Cu^{2+} and Aβ_{1-42} (Cu^{2+} coordinated by the amine and carbonyl groups of Asp1, His6 and His13), and subsequently performed H-REMD simulations to investigate the influence of pH and Cu^{2+} on the conformational dynamics of Aβ_{1-42}. We found that both Cu^{2+} binding and moderate acidic pH increase both the flexibility and the β-sheet content of Aβ_{1-42}, which results in a shift of the conformational equilibrium towards aggregation-prone.

PLOS

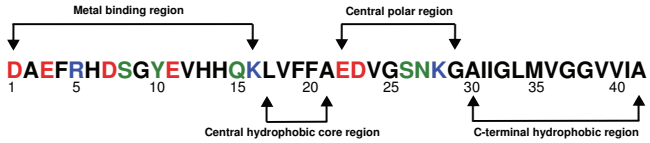

Figure 1. The sequence of Aβ_{1-42}, which can be divided into four regions: the metal binding region, the central hydrophobic core region, the central polar region and the C-terminal hydrophobic region. Residues labelled as red, blue, green and black are negatively charged, positively charged, polar and hydrophobic, respectively.

Introduction

Protein misfolding is an important event in the etiology of neurodegenerative diseases. Some examples of these misfolded proteins are α-synuclein in Parkinson's disease [1], prion protein in Creutzfeldt-Jakob disease [2] and amyloid-β (Aβ) in Alzheimer's disease (AD) [3–5]. AD is characterized by structural changes of Aβ in the brain resulting in neuronal dysfunction, and the extracellular deposition of Aβ peptides in the form of senile plaques is one of its hallmarks. The Aβ peptides are cleaved from the amyloid precursor protein (APP) by β- and γ-secretase and are typically 39–43 residues in length. *In vivo*, the most prevalent alloforms of Aβ found in brain plaques are Aβ_{1-40} and Aβ_{1-42}, the only difference is the presence of two extra residues, Ile41 and Ala42, at the latter's C-terminal. The two extra hydrophobic residues render Aβ_{1-42} more prone to aggregation, and hence more neurotoxic than Aβ_{1-40}. The conformational transition of Aβ peptides to a β-sheet-rich state, with intermediates such as water-soluble oligomers, is crucial for the initiation of AD [3, 6, 7]. In general, the sequence of Aβ peptides can be divided into several regions: the metal binding region involving N-terminal residues (Asp1–Lys16), the central hydrophobic core (CHC) region (Leu17–Ala21), the central polar region (Glu22–Gly29), and the C-terminal hydrophobic region (Ala30–Val40/Ala42), as shown in Fig 1. Different regions play different roles in Aβ aggregation. For example, numerous studies have indicated that the CHC is of great importance during the aggregation and fibril formation of Aβ, therefore considered as a target for aggregation inhibitors [8]. Reverse turns and anti-parallel strands have been reported to appear in the C-terminal hydrophobic region of Aβ_{1-42} [9–11], which could promote fibril formation. Furthermore, the C-termini seem to be of particular importance during the initial oligomer formation [12–14].

High concentrations of metal ions such as Zn^{2+} and Cu^{2+} have been found in senile plaques based on the analysis of postmortem brain tissues, and it has been suggested that the interactions between these ions and Aβ are involved in the Aβ aggregation and toxicity [15, 16]. Indeed, *in vitro* studies revealed that these ions bind to the metal binding region of Aβ and modulate Aβ aggregation [16]. The presence of Cu^{2+} significantly promotes and stabilizes the formation of soluble oligomers [6, 17, 18]. Both disordered amorphous [19–22] and ordered β-sheet-rich amyloid aggregates [6, 23] have been reported for different Cu^{2+} concentrations [16] and other external conditions. Furthermore, the binding of copper to Aβ has been suggested to induce β-sheet formation [24], π-helical destruction [25], increase β-sheet and α-helix contents [26], but also β-sheet structure disruption and increase in random coil [27, 28]. In summary, the reported results for Cu^{2+} binding on the structure and aggregation of Aβ are conflicting. Thus, it is of great importance to further investigate the effects of Cu^{2+} binding on the structure and dynamics of Aβ_{1-42}. Elucidating the coordination of Cu^{2+} to Aβ is crucial to understanding its role in Aβ aggregation and for the rational design

of new chelators with potential therapeutic benefits. To date, little progress has been made in the investigation of interaction and coordination between Cu^{2+} and Aβ. The most accepted coordination mode is 3N1O, involving three nitrogen atoms (3N) from His6, His13 and His14, and one oxygen atom (1O). For possible oxygen-donating ligands, Asp1 [29], Ala2 [30], Glu3 [31], Glu7 [32], Tyr10 [33,34], Glu11 [35] and Val40 [36,37] have been reported. However, Tyr10 is ruled out based on the results of other studies [38–41]. In addition, the pH has a great influence on the coordination of Cu^{2+} binding with Aβ [15]. At pH 6.3–6.9, two competing coordination components in 3N1O have been suggested for Aβ/Cu^{2+} complexes [29,30], while at higher pH (pH 8.0) a different 3N1O coordination involving the carbonyl oxygen of Ala2 ($Ala2_{CO}$) and the three His was determined [30]. Currently, these suggested coordination modes of Cu^{2+} binding Aβ are the most accepted ones [42].

The pH alone is also one of the major factors to affect Aβ aggregation rates as well as the morphologies and toxicity of the aggregates [43,44]. Aβ precipitates more readily at pH values close to the isoelectric point (pI) of around 5.3 [45,46], while aggregation is inhibited at pH values that are much higher or lower than the pI [16]. These phenomena may arise from the structural changes resulting from a redistribution of electrostatic charges caused by the altered the pH values [11]. The pH particularly affects the protonation states of the three histidine residues (His6, His13 and His14), which also influences the coordination modes formed with metal ions. Because of the slightly acidic nature of the inflammatory response in AD, acidic pH-facilitated aggregation has been suggested to play an important role in AD pathology [47]. In line with this hypothesis, brain tissue from patients who died from AD were found to be more acidic than those from non-AD patients who died suddenly without AD pathology [48].

To date, there is no experimental structure of a complex of Aβ with Cu^{2+}. Molecular simulations under physiological conditions provide a complementary means of directly accessing this vital information. There are some theoretical studies that characterize the influence of pH and Cu^{2+} on the structure of Aβ [11,49–54]. Olubiyi and Strodel concluded from their molecular dynamics (MD) simulations that the formation of β-sheets is enhanced by lowering the pH, i.e., by protonating the three His residues in Aβ_{1-42} [11]. Raffa and Rauk performed MD sampling on a Aβ_{1-42}/Cu^{2+} monomer coordination system [49]. They found that the coil structure was the predominant conformation, resulting from the disruption of β-sheet by the binding of Cu^{2+} to Aβ. However, the coordination modes they studied were different from those determined afterwards [29,30,32,36,41], which are currently accepted. Alí-Torres *et al.* [54] studied the 3D structures and redox potentials of various Aβ_{1-16}/Cu^{2+} complexes with different protonation states for the three His residues at different pH values using homology modelling (HM) and quantum mechanics/molecular mechanics (QM/MM) approach, based on the experimental results of Drew *et al.* [29,30,42] and Dorlet *et al.* [55]. Obtaining detailed information of the Cu^{2+}-Aβ complex structure is critical to understand the AD pathology. MD simulations can boost the investigation of the dynamical properties, which may result in a better understanding of the effects of Cu^{2+} on Aβ peptides.

Here we choose a typical Cu^{2+} coordination mode 3N1O involving His6 and His13 as well as the amine and carbonyl groups of Asp1 at physiological pH to investigate the effects of Cu^{2+} on the conformation of Aβ_{1-42} monomer. To this end, we develop a set of new OPLS-AA/L force field parameters to model the interactions between Cu^{2+} and Aβ_{1-42}, and apply them to Hamiltonian replica exchange molecular dynamics (H-REMD) simulations of the Aβ_{1-42}/Cu^{2+} complex. We also perform H-REMD simulations for Aβ_{1-42} at different pH values by considering different protonation states for His6, His13 and His14. This enables us to compare the influence of Cu^{2+} binding and pH on the structure and dynamics of Aβ_{1-42} in an aqueous medium. The key

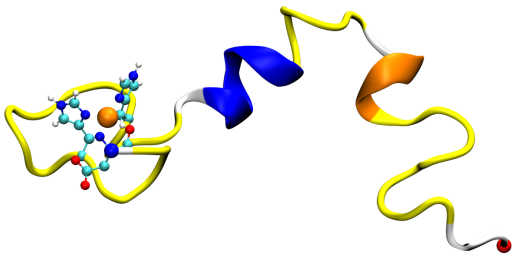

Figure 2. The initial structure of $A\beta_{1-42}/Cu^{2+}$ is shown in new cartoon, and the Cu^{2+} binding residues are shown in Corey-Pauling-Koltun (CPK) and coloured by chemical elements: cyan for carbon (C), blue for nitrogen (N), red for oxygen (O), white for hydrogen (H) and orange for Cu^{2+} atoms. The peptide color is based on secondary structure: blue for α-helix, orange for 3_{10}-helix, yellow for turn and white for coil structures. The N- and C-termini are represented by blue and red beads, respectively.

findings of our study are that (i) both Cu^{2+} binding and mild acidic conditions mimicking inflammatory processes *in vivo* increase the flexibility of $A\beta_{1-42}$, and (ii) both Cu^{2+} binding and acidic pH increase the propensity of β-sheet and salt-bridge formation in monomeric $A\beta_{1-42}$.

Materials and Methods

Structural models

The initial structure of the $A\beta_{1-42}/Cu^{2+}$ complex, shown in Fig 2, was constructed by combining the $A\beta_{1-16}/Cu^{2+}$ model from Alí-Torres *et al.* [54] and the $A\beta_{17-42}$ fragment taken from the solution NMR model of $A\beta_{1-42}$ determined in a hexafluoroisopropyl alcohol/water mixture (PDB entry 1Z0Q) [56]. The coordination mode of the $A\beta_{1-42}/Cu^{2+}$ complex is 3N1O, where Cu^{2+} interacts with NH_2^{D1}, O_C^{D1}, N_δ^{H6} and N_δ^{H13} in a distorted square planar geometry, as suggested by Drew *et al.* [29, 42]. This coordination mode was chosen because it was determined at pH 6.9, which is close to the physiological environment and is the most stable model based on the QM/MM study of Alí-Torres *et al.* [54]. With Cu^{2+} binding, the net charge of the $A\beta_{1-42}/Cu^{2+}$ complex is -2 at pH 6.9, and thus the complex is designated as $A\beta_{1-42}^{6.9,Cu}$. The coordinates for the $A\beta_{1-42}$ monomer were obtained from this complex by removing the copper ion. At the $A\beta$ isoelectric point, the three histidine residues are protonated, $A\beta_{1-42}$ is neutral, and the system is designated as $A\beta_{1-42}^{5.3,0}$. At pH 7.4, the three histine residues are neutral and $A\beta_{1-42}$ has a net charge of -3, leading to $A\beta_{1-42}^{7.4,3-}$. Finally, at pH 6.0, His6 and His14 are positively charged based on the prediction with the pKa predictor, H++ [57, 58], yielding a net charge of -1 for this system labelled $A\beta_{1-42}^{6.0,1-}$. We performed H-REMD simulations for each of the four systems described above.

Parameterization of Cu^{2+}-$A\beta$ interactions

Different approaches exist to incorporate metal ions into force fields. The bonded model, also used here, defines bonds, angles, torsions between the metal ion and its ligands, and van der Waals and electrostatic interactions between the metal ion and ligands are added to the force field. More than twenty years ago, Hancock already used this approach to study systems including copper and nickel [59, 60]. The bonded plus

electrostatics model [61] defines bonds and angles between the metal ion and its ligand as well as electrostatic potential charges. This method attempts to define the correct electrostatic representation of the metal active site because simply assigning a plus two formal charge to a divalent metal ion would not describe the reality of the electronic structure of a metal ion/ligand complex [62]. QM calculations were employed to derive OPLS-AA/L [63, 64] force field parameters for the bonded plus electrostatics model for the Aβ_{1-42}/Cu^{2+} complex. It has been shown that OPLS-AA/L produces results for Aβ in terms of helical and β-strand contents, calculated NMR J-coupling constants and chemical shifts, and radii of gyration that agree well with experimental data [65, 66]. Other force fields (e.g., AMBER03, CHARMM22/CMAP) produce Aβ structures in conflict with experimental findings [65, 67]. The functional form of OPLS/AA-L is given by [64]:

$$E_{MM} = \sum_{bonds} K_r(r - r_{\mathrm{eq}})^2 + \sum_{angles} K_\Theta(\Theta - \Theta_{\mathrm{eq}})^2 + \sum_{dihedrals} \sum_{n=1}^{3} \frac{V_n}{2}\left[1 + \cos(n\phi)\right] + \sum_{i<j} f_{ij}\left[\frac{q_i q_j e^2}{r_{ij}} + 4\epsilon_{ij}\left(\frac{\sigma_{ij}^{12}}{r_{ij}^{12}} - \frac{\sigma_{ij}^{6}}{r_{ij}^{6}}\right)\right] \quad (1)$$

, Where K_r and K_Θ are the stretching and bending force constants, while r_{eq} and Θ_{eq} are the equilibrium bond lengths and angles, respectively. V_n is the torsional (out-of-plane) constant, ϕ is the dihedral angle, q_i and q_j are the partial charges of the interacting atoms i and j with r_{ij} being the distance between them. ϵ_{ij} and σ_{ij} are the geometric mean values ($\epsilon_{ij} = \sqrt{\epsilon_{ii}\epsilon_{jj}}$ and $\sigma_{ij} = \sqrt{\sigma_{ii}\sigma_{jj}}$) of the van der Waals parameters of atoms i and j. Intramolecular nonbonded interactions are counted only for atoms that are separated by three or more bonds ($f_{ij} = 1.0$); 1,4 interactions are considered but scaled down by the factor $f_{ij} = 0.5$. The Cu^{2+} binding site was characterized by Alí-Torres *et al.* [54], which contains Cu^{2+} bound to two His residues (His6 and His13) and the amine and carbonyl groups of Asp1. For the QM calculations, the two imidazole rings of the two His residues and residue Asp1 with a capping group at the C side were kept to conserve the electronic environment of Cu^{2+} whilst bound to these residues (Fig 3, henceforth designated as copper coordination model). This system was optimized at the B3LYP/def2-TZVP level [68–71] with D3 dispersion correction [72] using the Turbomole V6.3 program [73]. The force constants for bonds (K_r) and angles (K_Θ) related to Cu^{2+} were derived from QM potential energy surface (PES) scans based on the fully optimized copper coordination model. To this end, we performed PES scans for the related bonds (Cu^{2+}–X, X is one of the coordinated atoms) and angles (X_i–Cu–X_j and Cu–X–Y, X_i and X_j are two different atoms belonging to X, Y are atoms bound to X.). The equilibrium values correspond to the minima of the PES curves are identical to the corresponding values from the fully optimized geometry. The torsional parameters V_n were neglected as commonly done in the bonded plus electrostatics model [62, 74, 75], as the coordination site with bonded Cu^{2+} is quite rigid and usually devoid of significant torsional freedom. The widely used restrainted electrostatic potential (RESP) [76] was used to derive the atomic partial charges [74, 77]. Based on the fully optimized copper coordination model (Fig 3), the electrostatic potential was calculated at B3LYP/6-31G* level with Gaussian 09 [78], and the fitting was done by antechamber [79] of AmberTools 14.

Finally, we performed molecular mechanics (MM) scanning implemented in GROMACS [81–83] using the derived parameters to reproduce the QM curves, as a validation method [84, 85].

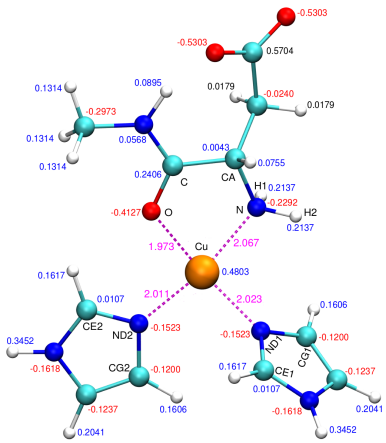

Figure 3. The fully optimized structure of the copper coordination model with the labelled RESP charges, blue and red are for positive and negative charges, respectively. The atoms involved in the bonds and angles with Cu^{2+} are also labelled. The figure was generated with vmd-1.9.1 [80]

Hamiltonian Replica Exchange Molecular Dynamics Simulations

To improve the conformational sampling of Aβ_{1-42}, an enhancing algorithm called Hamiltonian replica exchange molecular dynamics (H-REMD) [86,87] was applied. Such a sampling enhancing algorithm is based on executing simultaneous simulations (replicas) with different Hamiltonians (energies) of the same system and allowing exchanges at a given frequency between replica i and j at neighbouring scales m and n, respectively, with a probability of

$$P(q_i \leftrightarrow q_j) = \ min\left[1, exp\left(\frac{-H_m(q_j) + H_m(q_i)}{k_B T} + \frac{-H_n(q_i) + H_n(q_j)}{k_B T}\right)\right] \tag{2}$$

where H is the Hamiltonian, q are the coordinates, T is the temperature and

$$H_m(q) = \lambda_m H_{pp} + (\lambda_m)^{1/2} H_{ps} + H_{ss}(q) \tag{3}$$

where H_m is the Hamiltonian at scale m, and H_{pp}, H_{ps}, H_{ss} are the protein-protein, protein-solvent, solvent-solvent energies, respectively. λ_m is the scaling factor at scale m ($\lambda_m \leq 1.0$). Previous tests on Trp-Cage and a β-hairpin by H-REMD indicated a significantly lower computational cost and better sampling than the temperature replica exchange algorithm [88].

All the H-REMD simulations [86] were performed using the Gromacs 4.6.7 simulation package [81–83] in combination with the PLUMED plugin (version 2.1) [89]. The peptides were modeled with the OPLS-AA/L force field [63,64]. One peptide was centered in a dodecahedron box with a dimension of 6.5 nm, and periodic boundary conditions were employed for the boundary treatment. The box was solvated with TIP4P explicit water molecules [90]. A sufficient number of sodium and chloride ions were added to achieve system charge neutrality and a NaCl concentration of 0.150 M

simultaneously, which is part of the physiological milieu. Energy minimization was performed on the entire system using both the steepest descent and the conjugate gradient methods. After minimization, 500 ps of each NVT and NPT position-restrained dynamics were performed with a restraining force of 1000 kJ/mol·nm^2 on the non-hydrogen atoms of the peptide, which allowed the water molecules to equilibrate around the restrained peptide, thereby removing bad contacts and bringing the system close to equilibrium.

Then, the final coordinates of the NPT equilibration were used as the initial coordinates for samplings without any position restraints. 16 scaling factors generated by a geometric distribution, 1.000, 0.948 0.899 0.852, 0.808, 0.766, 0.727, 0.689, 0.653, 0.619, 0.587, 0.557, 0.528, 0.501, 0.475 and 0.450, were used in the H-REMD simulation of each system. Each replica was subjected to 130-ns sampling for each of the systems $A\beta_{1-42}^{5.3,0}$, $A\beta_{1-42}^{6.0,1-}$, $A\beta_{1-42}^{6.9,Cu}$ and $A\beta_{1-42}^{7.4,3-}$ in an NPT ensemble. A canonical thermostat with stochastic velocity reassignment [91] and a coupling constant of 0.5 ps was used to keep the system at 300 K during both NVT and NPT simulations. For the NPT simulations a Parrinello-Rahman barostat [92] with 1.0 bar pressure and 1.0 ps coupling constant was employed. Both van der Waals and Coulombic interactions were truncated at 1.2 nm, and the long-range electrostatic interactions were calculated using the Particle Mesh Ewald method [93]. The neighbour-list was updated every 10 steps with a cut-off of 1.2 nm. The LINCS algorithm [94] was used to constrain all bond lengths during the MD simulations. The use of virtual sites for hydrogen atoms allowed the use of a 4-fs time-step. An exchange between neighbouring replicas was attempted every 1 ps, which resulted in an exchange ratio of 20-35%.

Analysis

The analysis was done on the last 100-ns trajectory at λ=1.0 for each system (100,000 frames) unless mentioned otherwise. **Cluster analysis** provides a convenient tool to separate the conformational ensemble into clusters with similar geometry. The trajectory of each system was analyzed every two frames (50,000 frames in total) using the cluster analysis method of Daura *et al.* [95]. A root mean square deviation (RMSD) cut-off of 2.0 Å between backbone atoms was used for the clustering. In order to determine the essential dynamics, **principal component analysis** (PCA) was performed for each system. The trajectories were projected on the first two eigenvectors (also called the first two principal components). The PCA method was employed to investigate the **free energy landscapes** of $A\beta_{1-42}$ under different conditions. The free energy values (kcal/mol) were obtained using the equation $\Delta G = -k_{\mathrm{B}}T(\ln P_i - \ln P_{\max})$, where P_i is the probability distribution along eigenvectors 1 and 2 calculated from the histogram of each trajectory. $P_{\max}$ is the maximum probability for the trajectory in question and $\ln P_i - \ln P_{\max}$ was used to ensure $\Delta G = 0$ for the free energy minimum. The formation of **secondary structures** such as α-helix and β-sheet is crucial in the studies of intrinsically disordered fibrillogenic protein involved in neurodegenerative diseases. A widely used program, the dictionary of protein secondary structure (DSSP) [96] , was applied to determine the secondary structure for each system. The VMD software [80] was used to visualize the peptide structures. **Transition networks** have been shown to successfully describe the kinetics of aggregation for short peptides [13, 97, 98]. Here, we apply a similar analysis to describe the $A\beta_{1-42}$ folding process. For each system, the last 100-ns trajectory at λ=1.0 was used to construct the transition networks. To derive the transition networks, the folding states were defined as a combination of two numbers, $N1|N2$, where each number stands for a structural feature. $N1$ and $N2$ are the number of residues sampled in helix (α-, 3_{10}- and π-helix) and sheet (β-sheet and β-bridge) contents, respectively. Then, all the folding states and pairwise transitions between folding states were identified along the trajectories using a

lag time of 5 ps. An $N \times N$ matrix was built based on these states and transitions, where N is the number of identified folding states. Each element of the matrix corresponds to the population of a specific transition event between two states. Based on the matrix, a new matrix which preserved the maximum flow (max-flow) was derived using the minimum cut (min-cut) algorithm [99–102]. The maximum flow transition matrix was converted into a transition network using the package Gephi 0.8.1 [103] and the minimum stress algorithm together with the link routing procedure.

Results

OPLS-AA/L force field parameters for Aβ_{1-42}/Cu^{2+}

Since MM force fields in general do not model metal–peptide interactions, the first step of this study was to derive force field parameters for Cu^{2+} complexed with Aβ_{1-42} used in the bonded plus electrostatics model. The harmonic potential, already used for metalloproteins [84, 85], is applied to bonds and angles that involve Cu^{2+}, and the force constants are derived by calculating the potential energy profiles with QM methods. The harmonic oscillator approximation is widely applied in the standard force fields of proteins and other biomolecules, but it can only be adopted for bonds and angles close to their equilibrium positions. Therefore, we only computed the potential energy profiles around the corresponding equilibrium positions of bonds and angles involving Cu^{2+}. The force field parameters for bonds and angles fitted to the PES from QM calculations using the least-squares method are summarized in Table 1, while the derived atomic partial charges of the coordinated copper model are shown in Fig 3.

After geometry optimization at the B3LYP/def2-TZVP level with D3 dispersion correction, a distorted square planar geometry for Cu^{2+} coordination sphere was observed (Fig 3), and are in good agreement with experimental [29, 42] and QM/MM studies [54]. The equilibrium values of Cu^{2+}–N and Cu^{2+}–O bonds obtained from the QM optimized structure are around 2.0 Å, which are very similar to previous experimental and theoretical results [36, 51, 54].

Table 1. OPLS-AA/L parameters for bonds and angles of the coordinated copper model[a].

Bonds	r_{eq} (Å)	K_r (kcal/mol·Å^2)	Bonds	r_{eq} (Å)	K_r (kcal/mol·Å^2)
Cu^{2+}–N	2.067	98.5	Cu^{2+}–O	1.973	109.4
Cu^{2+}–NE1	2.023	98.3	Cu^{2+}–NE2	2.011	87.1
Angles	Θ_{eq} (°)	K_Θ (kcal/mol·rad^2)	Angles	Θ_{eq} (°)	K_Θ (kcal/mol·rad^2)
Cu^{2+}–O–C	116.98	80.0	O–Cu^{2+}–N	80.53	80.0
Cu^{2+}–N–CA	111.01	80.0	O–Cu^{2+}–ND1	165.12	14.3
Cu^{2+}–ND1–CG1	127.69	14.7	O–Cu^{2+}–ND2	91.11	58.4
Cu^{2+}–ND1–CE1	125.44	14.7	N–Cu^{2+}–ND1	95.17	23.7
Cu^{2+}–ND2–CG2	129.28	34.6	N–Cu^{2+}–ND2	164.31	18.4
Cu^{2+}–ND2–CE1	123.71	34.6	ND1–Cu^{2+}–ND2	96.10	58.4

a : For atom names, see Fig 3

As validation method we reproduced the QM potential energy curves by using the MM method with the newly developed parameters for bonds and angles. As shown in Fig 4, all QM curves are reproduced within around 0.02 Å or 2° by the MM curves close to equilibrium values of bonds or angles, respectively. The deviations between relative MM and QM energies become larger in some cases, when the bonds and angles are far from their equilibrium values. The reasons for this could be due to the harmonic approximation used. For further validation, we performed a 10-ns MD simulation of the coordinated copper complex with the newly derived parameters. The geometry of the complex was well preserved during the 10-ns simulation: the bond lengths and angles

involving Cu^{2+} remained near their corresponding equilibrium values and the potential energy was conserved (S1 Fig). We concluded that these parameters can be used to model interactions between Cu^{2+} and $A\beta_{1-42}$ in large-scale MD simulations.

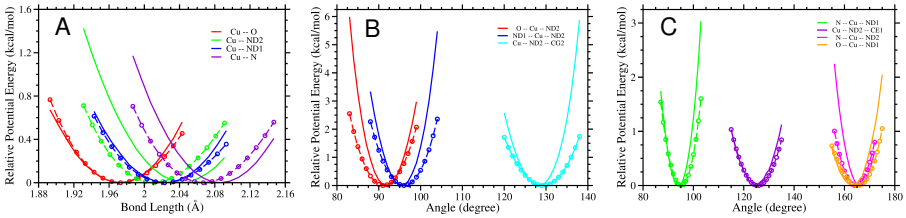

Figure 4. QM and MM potential energy curves for bond stretching (A) and angle bending (B,C). QM curves are shown as dashed lines with circles, whereas MM curves as solid lines. Different colors correspond to different bonds or angles involving Cu^{2+}.

Convergence of the H-REMD simulations

One of the advantages of the H-REMD simulations is that they achieve good conformational sampling in reasonable simulation time compared to conventional MD, and are computationally cheaper and more efficient than stardard temperature REMD. For our simulations, the exchange probabilities are around 30% for all the four systems, which guarantees high sampling quality. In order to further confirm the convergence of the simulations, the secondary structure contents for three time windows [t_{eq}, t_1], [t_{eq}, t_2] and [t_{eq}, t_{full}] were calculated. The equilibration time (t_{eq}) is 30 ns while the full simulation time (t_{full}) is 130 ns for all the four systems, whereas t_1 and t_2 are set at 70 ns and 100 ns, respectively. As shown in Fig 5, the helix and sheet contents obtained for the three windows have no significant differences for the four systems at $\lambda = 1.0$, especially between the two longer time windows (green and blue lines). Similar results were also obtained for bend and turn contents (S2 Fig and S3 Fig), confirming the convergence of the simulations. Thus, the trajectory interval [30-130 ns] at λ=1.0 was used for all the analysis in this study, unless stated otherwise.

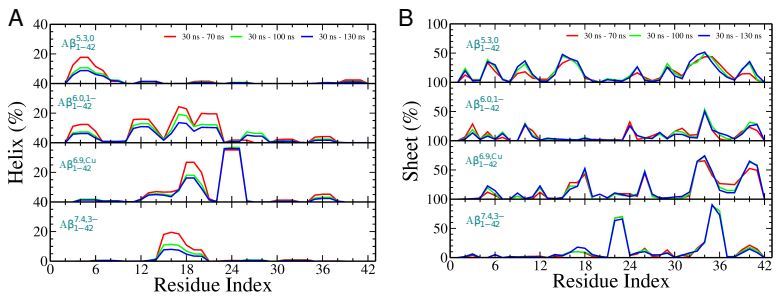

Figure 5. Helix (A) and sheet (B) contents obtained for time windows [30-70 ns], [30-100 ns] and [30-130 ns] for systems $A\beta^{5.3,0}_{1-42}$, $A\beta^{6.0,1-}_{1-42}$, $A\beta^{6.9,Cu}_{1-42}$ and $A\beta^{7.4,3-}_{1-42}$, are shown for the individual residues of the peptide. The helix content includes α-helix, 3_{10}-helix and π-helix, while the sheet content includes β-sheet and β-bridge.

Effects of pH and Cu^{2+} binding on the flexibility of Aβ_{1-42}

In order to assess the conformational flexibility of the Aβ_{1-42} peptide, we performed cluster analysis, computed the root mean square fluctuations (RMSF) of individual residues and derived free energy surfaces via principal component analysis (PCA).

Cluster Analysis The conformations sampled at $\lambda = 1.0$ for each of the four systems are initially clustered considering only the metal binding region (Aβ_{1-16}) of Aβ_{1-42}. The populations of the top ten clusters are shown in Fig 6A. The populations of the largest cluster for the four systems range from 25% to 50%. The most populated A$\beta_{1-42}^{6.9,Cu}$ (48.3%) and A$\beta_{1-42}^{7.4,3-}$ (48.3%) clusters had almost twice of the population of the A$\beta_{1-42}^{5.3,0}$ (25.9%) top cluster, while the system at pH=6.0 fell in between with 38.5% for the top cluster population. A similar situation occurred for the second largest cluster, as shown in Fig 6A. In other words, the metal binding region of Aβ_{1-42} with or without copper at physiological pH is greatly stabilized but more conformationally dynamic at lower pH values. These results are consistent with a recent REMD study of Aβ_{1-16} and Aβ_{1-16}/Cu^{2+} by Xu *et al.* [52].

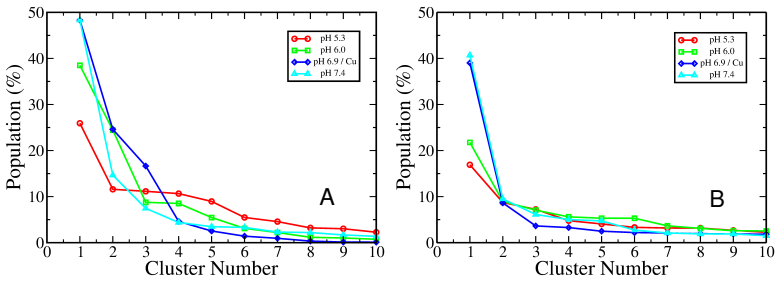

Figure 6. The populations of the top ten clusters for each system, which were calculated based on the backbone atoms of (A) Aβ_{1-16} and (B) Aβ_{1-42}. Different colors correspond to A$\beta_{1-42}^{5.3,0}$ (red), A$\beta_{1-42}^{6.0,1-}$ (green), A$\beta_{1-42}^{6.9,Cu}$ (blue) and A$\beta_{1-42}^{7.4,3-}$ (cyan).

We also clustered the conformations considering the entire Aβ_{1-42} peptide, i.e., including the backbone atoms of all 42 residues. The populations of the top ten clusters are shown in Fig 6B. There are more clusters for A$\beta_{1-42}^{5.3,0}$ (301) than for the other three systems (260, 266 and 189 for A$\beta_{1-42}^{6.0,1-}$, A$\beta_{1-42}^{6.9,Cu}$ and A$\beta_{1-42}^{7.4,3-}$, respectively). The populations of the largest cluster (Cluster One) for A$\beta_{1-42}^{6.9,Cu}$ (39.0%) and A$\beta_{1-42}^{7.4,3-}$ (40.7%) are greater than for A$\beta_{1-42}^{5.3,0}$ (16.9%) and A$\beta_{1-42}^{6.0,1-}$ (21.8%), while the populations of the second largest cluster (Cluster Two) of each system are around 9.0%. Consistent with the clustering results based on the metal binding region, these results indicate more conformational flexibility for the systems at low pH.

The central conformations of the two largest clusters for each system are illustrated in Fig 7. For A$\beta_{1-42}^{5.3,0}$, two β-hairpins (Arg5–His6 and Gly9–Tyr10, Leu34–Met35 and Val39–Val40) and one pair of anti-parallel β-sheet (Gln15–Lys16 and Val24–Gly25) are observed between the metal binding region and the C-terminal hydrophobic region in the central conformation of Cluster One. In Cluster Two, there are two pairs of anti-parallel β-sheet (Phe4–Asp7 and Gly29–Ile32, His14–Lys16 and Leu34–Val36). The central conformation of Cluster One of A$\beta_{1-42}^{6.0,1-}$ is dominated by turn and coil structures, while the central conformation of Cluster Two has one anti-parallel β-sheet pair (Ala2–Glu3 and Gly33–Leu34) and two 3_{10} helices. In the system with Cu^{2+} (A$\beta_{1-42}^{6.9,Cu}$), there is a β-hairpin motif (Gly33–Met35 and Val39–Ile41) at the C-terminal region as well as a 3_{10} helical structure (Asp23–Gly25) at the central polar region in

Cluster One. β-sheet and 3_{10} are also present in Cluster Two. For Aβ_{1-42} at pH 7.4, an anti-parallel β-sheet structure is formed between the central polar region and C-terminal hydrophobic region (Glu22–Val24 and Leu34–Val36) in Cluster One, and an anti-parallel β-sheet (Leu17–Val18 and Leu34–Met35) is observed in Cluter Two with a small shift towards the metal binding region.

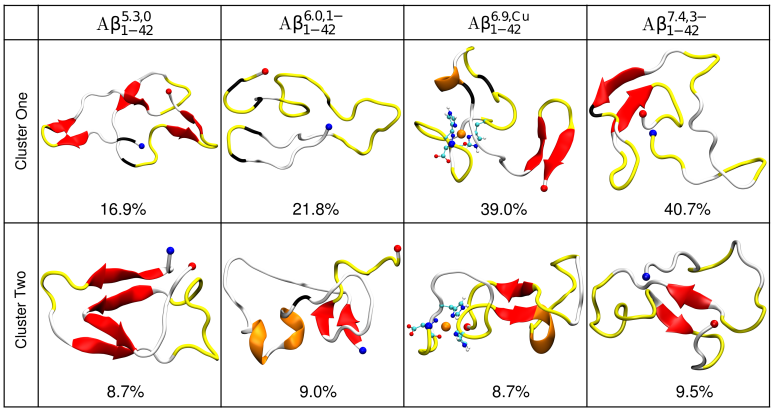

Figure 7. Central structures of the two most populated clusters (Cluster One and Cluster Two) obtained from the trajectories of the four Aβ_{1-42} systems. The percent of the total population of each cluster is given below each structure. The peptide color is based on the secondary structure: red for β-sheet, blue for α-helix, orange for 3_{10}-helix, yellow for turn, black for β-bridge and white for coil structures. The N and C termini are represented by blue and red beads, respectively.

Structural fluctuations As can be seen from the RMSF plots in Fig 8, the N-terminal (Asp1–Ala2) and the central regions (Leu17–Val24) as well as residue Ala30 of Aβ_{1-42} at physiological pH (A$\beta_{1-42}^{7.4,3-}$) are much more flexible than the rest of the peptide. The C-termini is however more rigid. Cu^{2+} stabilizes the metal binding region including the N-termini, but it greatly increases the flexibility of both the central polar and C-terminal hydrophobic regions compared to A$\beta_{1-42}^{7.4,3-}$. At pH 6.0, the two histidines His6 and His14 in A$\beta_{1-42}^{6.0,1-}$ are positively charged, which means that the net charge of Aβ_{1-42} is shifted to -1 from -3 at physiological pH. For this system, the flexibility of the metal binding and the CHC regions of Aβ_{1-42} is increased compared to A$\beta_{1-42}^{6.9,Cu}$. At the C-terminal regions, residues (Glu22–Gly37) are less flexible while residues (Gly38–Ala42) are more flexible than those in A$\beta_{1-42}^{6.9,Cu}$. For Aβ_{1-42} at pH 5.3, the three histidines His6, His13 and His14 are positively charged which lead to a total net charge of 0. Unlike A$\beta_{1-42}^{6.0,1-}$, reducing the net charge increases the flexibility of residues Glu3–Val18 moderately, but remarkably increases the flexibility of residues Asp1–Ala2. Moreover, a much less flexible CHC was observed when compared to A$\beta_{1-42}^{6.0,1-}$, and it was even less flexible than the CHC in A$\beta_{1-42}^{7.4,3-}$. The C-terminal regions (Glu22–Gly37) show more flexibility than A$\beta_{1-42}^{6.0,1-}$, which is similar to the fluctuation pattern in A$\beta_{1-42}^{6.9,Cu}$. Residues Ile41 and Ala42 are, however, more flexible, similar to what was found in A$\beta_{1-42}^{6.9,Cu}$ and A$\beta_{1-42}^{6.0,1-}$.

Free energy surfaces To characterize the free energy landscapes and major conformational motions in each system, we used the PCA method. The projections of the free energy surface on the first two principal components are shown in Fig 9. As can be seen, the different environments influence the free energy profiles of Aβ_{1-42}

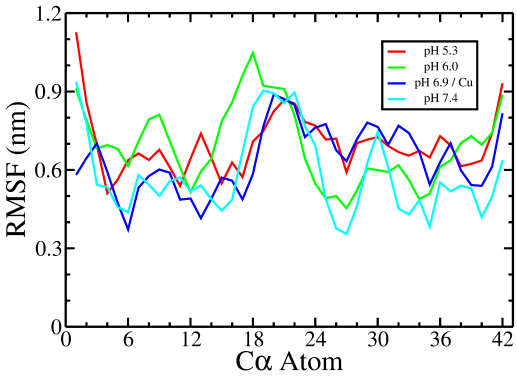

Figure 8. Average RMSF of the C_α atoms for $A\beta^{5.3,0}_{1-42}$ (red), $A\beta^{6.0,1-}_{1-42}$ (green), $A\beta^{6.9,Cu}_{1-42}$ (blue) and $A\beta^{7.4,3-}_{1-42}$ (cyan).

differently. With Cu^{2+} binding at physiological pH, the global minimum (I) along with multiple local minima (II, III $\cdots$) are present. The free energy differences between the global minimum and the local minima II and III are 1.490 kcal/mol and 1.659 kcal/mol, respectively (Fig 9C). At pH 5.3 and 6.0, most of the structures belong to the global minimum (I), which is separated from the other local minima (II, III) by smaller energy differences (0.147 kcal/mol and 0.682 kcal/mol for $A\beta^{5.3,0}_{1-42}$ as well as 0.178 kcal/mol and 0.395 kcal/mol for $A\beta^{6.0,1-}_{1-42}$, respectively) (Fig 9A and 9B). At physiological pH, there is one dominant energy basin (I) with multiple local minima (II, III $\cdots$) (Fig 9D). The energy differences are 0.470 kcal/mol and 0.705 kcal/mol between the global minimum and minima II and III, respectively. The small energy differences between the minima in the systems at low pH reveals more conformational flexibility, in agreement with the clustering and the fluctuation results. The flexibility analysis reveals that the dynamics of an unfolded peptide is largely affected by simply changing the protonation state of a single residue, or by the presence of a Cu^{2+} ion. The aggregation behaviour might also be different due to the modified peptide dynamics. However, the correlation between $A\beta_{1-42}$ dynamics and aggregation needs to be quantitatively assessed in a future aggregation study.

Effects of pH and Cu^{2+} binding on the structure of $A\beta_{1-42}$

Secondary structure The secondary structure transitions, especially the formation of β-sheets play a remarkable role in the aggregation processes and toxicity of $A\beta$ peptides [3, 6, 7]. The propensities for secondary structure elements for the four $A\beta_{1-42}$ systems were calculated and are shown in Table 2 and Fig 10. In general, the most abundant residual secondary structure elements for all the systems are the turn, bend and coil structures, especially at the N- and C-termini. More sheet content is sampled for $A\beta^{5.3,0}_{1-42}$ (17%) and $A\beta^{6.9,Cu}_{1-42}$ (16%) while more coil structure is sampled for $A\beta^{6.0,1-}_{1-42}$ (48%) and $A\beta^{7.4,3-}_{1-42}$ (48%). $A\beta^{7.4,3-}_{1-42}$ is characterized by a small amount of helix and β-sheet ($\sim$10%) at the central region of His14-Phe20, while β-sheet appeared with high probability at the central polar and C-terminal hydrophobic regions [Glu22–Asp23 ($\sim$60%) and Met35–Val36 ($\sim$75%)]. For $A\beta^{6.9,Cu}_{1-42}$, the propensity for helical structure (mostly 3_{10} helix) is increased at the CHC and central polar regions compared to $A\beta^{7.4,3-}_{1-42}$, and more β-sheet is sampled at the C-terminal hydrophobic region (Gly33–Leu34 and Val40–Ile41, β-hairpin) compared to the other three systems. The

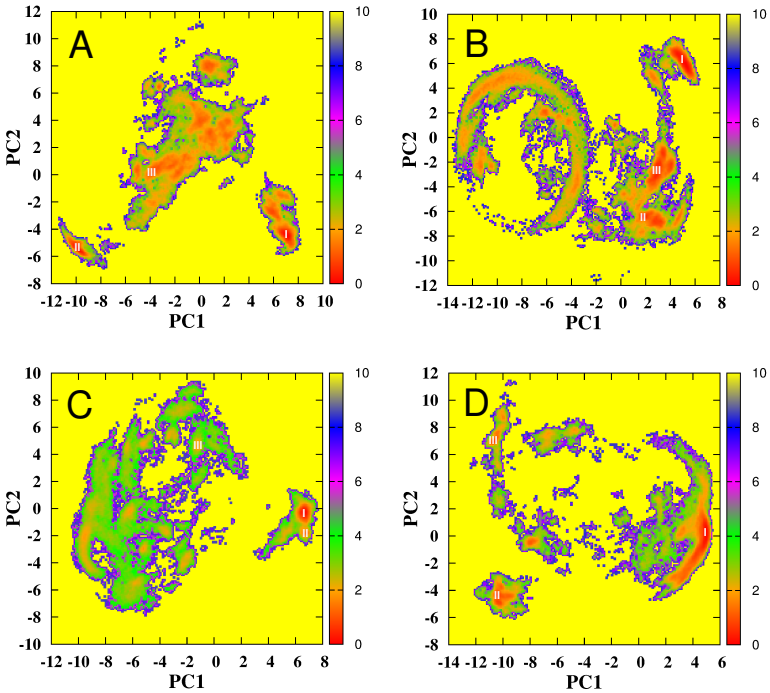

Figure 9. Conformational free energy surfaces (in kcal/mol) for Aβ_{1-42} and Aβ_{1-42}/Cu^{2+} systems, projected onto the first two principal components (PC1 and PC2), A) A$\beta^{5.3,0}_{1-42}$, B) A$\beta^{6.0,1-}_{1-42}$, C) A$\beta^{6.9,Cu}_{1-42}$ and D) A$\beta^{7.4,3-}_{1-42}$.

β-hairpin structure sampled at the C-terminal hydrophobic region was also observed in the A$\beta^{5.3,0}_{1-42}$ and A$\beta^{6.0,1-}_{1-42}$ (∼50%) systems. A$\beta^{5.3,0}_{1-42}$ and A$\beta^{6.0,1-}_{1-42}$ have more β-sheet at the metal binding region (∼25%) and less at the central polar region relative to A$\beta^{7.4,3-}_{1-42}$. Small amounts of helical structures were also determined at the metal binding and CHC regions in A$\beta^{5.3,0}_{1-42}$ and A$\beta^{6.0,1-}_{1-42}$ systems. Finally, A$\beta^{5.3,0}_{1-42}$, A$\beta^{6.0,1-}_{1-42}$ and A$\beta^{6.9,Cu}_{1-42}$ have in general more turn structure throughout the sequence than A$\beta^{7.4,3-}_{1-42}$, while more bend structure is sampled by A$\beta^{7.4,3-}_{1-42}$, as shown in Table 2. These results suggest that Cu^{2+} binding promotes both the helix at the central region and the β-sheet at the C-terminal region. As the net charge of Aβ_{1-42} decreases with pH, intramolecular interactions become more likely, promoting the formation of (temporary) secondary structures. Thus, decreasing the pH stabilizes both helical structures and β-sheets in A$\beta^{5.3,0}_{1-42}$, especially in the metal binding region.

Table 2. Average helix, sheet, bend, turn and coil propensities within the A$\beta^{5.3,0}_{1-42}$, A$\beta^{6.0,1-}_{1-42}$, A$\beta^{6.9,Cu}_{1-42}$ and A$\beta^{7.4,3-}_{1-42}$ systems.

Systems	Helix (%)	Sheet (%)	Bend (%)	Turn (%)	Coil (%)
A$\beta^{5.3,0}_{1-42}$	1.2±3.0	16.4±9.5	23.9±10.0	13.7±5.8	44.8±7.2
A$\beta^{6.0,1-}_{1-42}$	3.8±5.0	8.4±6.9	26.8±7.0	12.9±6.3	48.1±8.1
A$\beta^{6.9,Cu}_{1-42}$	4.6±4.3	16.3±5.8	29.0±6.9	13.6±6.2	36.5±6.3
A$\beta^{7.4,3-}_{1-42}$	1.0±2.6	11.8±4.6	34.2±5.6	4.6±6.5	48.4±7.5

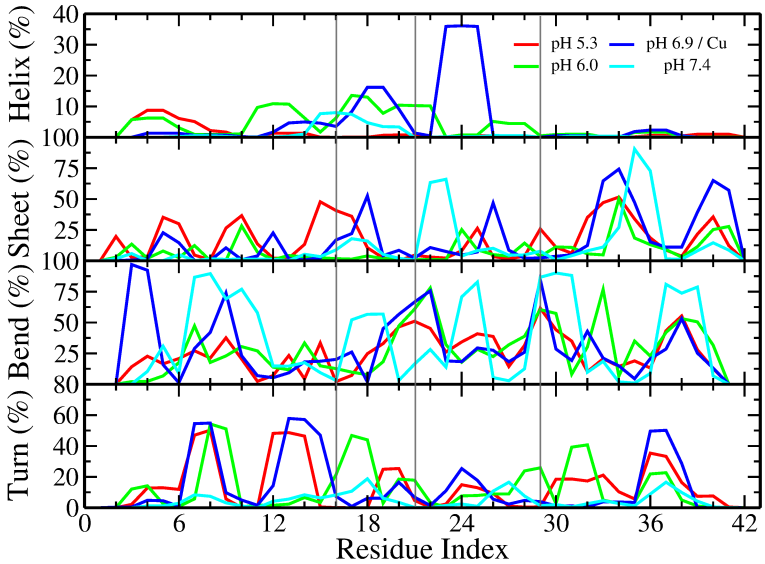

Figure 10. Averaged secondary structure content per residue for $A\beta^{5.3,0}_{1-42}$ (red), $A\beta^{6.0,1-}_{1-42}$ (green), $A\beta^{6.9,Cu}_{1-42}$ (blue) and $A\beta^{7.4,3-}_{1-42}$ (cyan). The helix content contains α-, 3_{10}- and π-helix, while the sheet content includes β-sheet and β-bridge. The coil structure is not shown.

Salt bridges The presence of salt bridges has been suggested to be of great importance in stabilizing the structure of $A\beta_{1-42}$. Arg5 can form stable salt bridges with residues Asp1, Glu11, Glu22, Asp23 and the C-termini [104–106]. Each of these salt bridges was observed in our simulations. The salt bridge between Arg5 and Glu3 is particularly stable in $A\beta^{7.4,3-}_{1-42}$ (99.0%)(Fig 11), yet less prevalent in $A\beta^{5.3,0}_{1-42}$ (72.2%) and $A\beta^{6.0,1-}_{1-42}$ (64.7%) as the metal binding region is more flexible for $A\beta^{5.3,0}_{1-42}$ and $A\beta^{6.0,1-}_{1-42}$ (Fig 8). This salt bridge is disrupted upon Cu^{2+} binding occurring with a much lower probability (8.3%) in $A\beta^{6.9,Cu}_{1-42}$. Coskuner *et al.* also observed a high stability for the Glu3-Arg5 salt bridge, which was present throughout their simulations of $A\beta_{1-40}$ and $A\beta_{1-42}$ [106]. In the same system, two additional salt bridges, namely Glu11-Lys16 (34.1%) and Asp23-Lys28 (44.7%), were sampled with moderate propensities, but were not stable in the other three systems. The salt bridge between Asp23 and Lys28 is very important, as it was previously postulated to nucleate $A\beta$ monomer folding [107] and to play an important role in early $A\beta$ oligomerization [108, 109]. $A\beta_{1-40}$ with Asp23 and Lys28 linked by a lactam bridge has been shown to aggregate very rapidly [110]. Furthermore, the fibrillar structures of both $A\beta_{1-40}$ and $A\beta_{1-42}$ are stabilized by the intermolecular Asp23-Lys28 salt bridge [111]. Thus the prevalence of salt bridge Asp23–Lys28 might add to the higher aggregation propensity of $A\beta_{1-42}$ with Cu^{2+} binding. Moderately stable salt bridges Glu22-Lys16 (22.3%) and C-T–Lys16 (19.8%) can be observed in $A\beta^{5.3,0}_{1-42}$ as well as C-T–Lys16 (59.2%) and C-T–Lys28 (26.4%) in $A\beta^{7.4,3-}_{1-42}$. For $A\beta^{6.0,1-}_{1-42}$, a salt bridge C-T–Lys28 (25.5%) occurred, being a little less stable than the one in $A\beta^{7.4,3-}_{1-42}$.

Contact maps Distance maps for the C_α atoms were generated for the four systems, and are presented in Fig 12. The distance maps reveal the contacts and thus

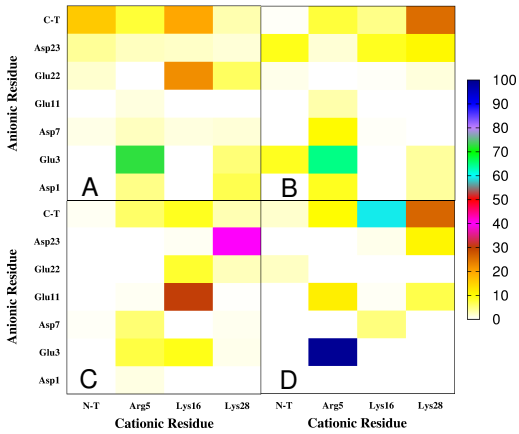

Figure 11. Salt bridge maps formed between all of the cationic and anionic residues for $A\beta_{1-42}^{5.3,0}$ (A), $A\beta_{1-42}^{6.0,1-}$ (B), $A\beta_{1-42}^{6.9,Cu}$ (C) and $A\beta_{1-42}^{7.4,3-}$ (D). N-T and C-T represent the amine and carboxylate groups of N- and C-termini, respectively.

interactions between different regions within $A\beta_{1-42}$, providing relevant information for $A\beta_{1-42}$ folding. For $A\beta_{1-42}$ at physiological pH (Fig 12D), many interactions occur between the residues of the metal binding region as well as between the central polar and the C-terminal hydrophobic regions, which are responsible for the formation of β-sheet as shown in Fig 10. Weaker interactions exist between the metal binding and C-terminal hydrophobic regions. Upon Cu^{2+} binding at physiological pH, the

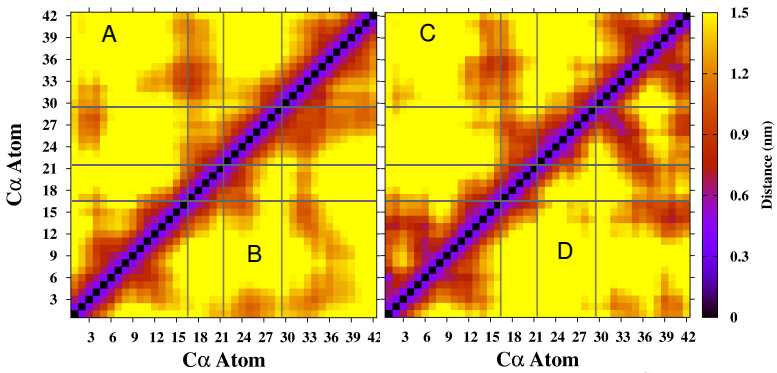

Figure 12. Contact maps for (A) $A\beta_{1-42}^{5.3,0}$, (B) $A\beta_{1-42}^{6.0,1-}$, (C) $A\beta_{1-42}^{6.9,Cu}$ and (D) $A\beta_{1-42}^{7.4,3-}$. The horizontal and vertical gray lines separate the metal binding, central hydrophobic core, central polar and C-terminal hydrophobic regions from each other.

interactions between CHC and C-terminal hydrophobic regions as well as the metal binding and C-terminal hydrophobic regions are decreased compared to $A\beta_{1-42}^{7.4,3-}$. The reduction of intrapeptide interactions is likely to expose $A\beta_{1-42}^{6.9,Cu}$ to more possible interpeptide interactions, which may be critical for facilitating oligomerization and could account for the faster aggregation of $A\beta_{1-42}$ upon Cu^{2+} binding [6, 17, 18]. The

Cu^{2+} binding also showed an increase in the interactions within the metal binding region. The contact maps changed when the pH was lowered, which caused a change to the charge distribution. In $A\beta_{1-42}^{5.3,0}$, the metal binding region (Asp1–Asp7) interacted with the central polar and the C-terminal hydrophobic regions (Val24–Gly33), which also occurred in $A\beta_{1-42}^{6.0,1-}$ but was absent in $A\beta_{1-42}^{6.9,Cu}$ and $A\beta_{1-42}^{7.4,3-}$. Furthermore, $A\beta_{1-42}^{6.0,1-}$ exhibited more interactions between the metal binding and the C-terminal regions and less contacts between the CHC and the C-terminal hydrophobic regions than $A\beta_{1-42}^{5.3,0}$ did.

Transition Networks

The transition network has been widely applied to study the conformational dynamics of peptides or proteins folding [101, 112–114] and recently to peptide aggregation [13, 97] in our group. The transition network for $A\beta_{1-42}^{5.3,0}$, $A\beta_{1-42}^{6.0,1-}$, $A\beta_{1-42}^{6.9,Cu}$ and $A\beta_{1-42}^{7.4,3-}$, based on the definition of folding states (helix|sheet), are shown in S4 Fig. The transition network provided detailed information of the folding process of $A\beta_{1-42}$ under different conditions. For $A\beta_{1-42}$ at physiological pH, there are less nodes (54) and edges (327) than for the other three systems (59 nodes and 468 edges for $A\beta_{1-42}^{5.3,0}$, 84 nodes and 948 edges for $A\beta_{1-42}^{6.0,1-}$, 91 nodes and 924 edges for $A\beta_{1-42}^{6.9,Cu}$). This is consistent with the RMSF results that indicate $A\beta_{1-42}$ as less flexible at physiological pH but more flexible at lower pH values or with copper binding. As the large number of transitions and nodes makes it difficult to see the main pathways in the folding process, the minimum cut method was applied to identify the maximum flow in the transition networks of the four systems, which are illustrated in Fig 13. For all the four systems, the topologies of the MTNs are similar: one central node connected radially to the other states. However, the states and populations of the central nodes are different. All the representative conformations of the central node, except the one for $A\beta_{1-42}^{5.3,0}$, fall into the biggest clusters with similar secondary structure distributions. For $A\beta_{1-42}^{7.4,3-}$, the central node has the highest population (57.3%) with state 0|4, while the second highest population node with state 0|6 is much smaller (9.0%). The largest number of transitions occurs between states 0|4 and 3|4, in which a 3_{10}-helix conversion occurs. The state 3|4 is also connected to other 4 states involving both helix and sheet transitions. Other important transitions occur between state 0|4 and states 0|6, 0|8, 0|10 *etc.* with increasing sheet content. Compared to $A\beta_{1-42}^{7.4,3-}$, the central node of $A\beta_{1-42}^{6.9,Cu}$ has much smaller population (17.5%) and a state (3|8) dominated by 3_{10}-helix and sheet structures. Most of the transitions occur between states 3|8 and states 0|8, 3|6, 0|6 as well as 3|10, with the representative conformations similar to the central conformation of Cluter One as shown in Fig 7. For $A\beta_{1-42}$ at acidic pH values ($A\beta_{1-42}^{5.3,0}$ and $A\beta_{1-42}^{6.0,1-}$), the states of the central nodes are different, 0|4 (21.6%) for $A\beta_{1-42}^{5.3,0}$ and 0|2 (20.4%) for $A\beta_{1-42}^{6.0,1-}$ with equivalent populations. Specifically, the transitions in $A\beta_{1-42}^{5.3,0}$ are mainly between state 0|4 and states 0|8, 0|6 and 0|12, while transitions between state 0|2 and states 0|0, 0|4 and 3|2 were dominant in $A\beta_{1-42}^{6.0,1-}$.

Discussion

MD simulations on a microsecond time-scale of $A\beta_{1-40}$ and $A\beta_{1-42}$ at physiological pH revealed that $A\beta_{1-40}$ and $A\beta_{1-42}$ monomers have crudely similar structural characteristics [115]. Thus, in the following our results are compared to previous studies of both $A\beta_{1-40}$ and $A\beta_{1-42}$. Lin *et al.* [115] concluded that $A\beta_{1-40}$ and $A\beta_{1-42}$ monomers are generally not well structured, and have a tendency to form short α- and 3_{10}-helix segments, especially in the region of residues Tyr10–Phe20, which was

Table 3. The 10 Transistion States with Highest Populations for $\mathbf{A}\beta_{1-42}^{5.3,0}$, $\mathbf{A}\beta_{1-42}^{6.0,1-}$, $\mathbf{A}\beta_{1-42}^{6.9,\mathrm{Cu}}$ and $\mathbf{A}\beta_{1-42}^{7.4,3-}$.

$\mathrm{A}\beta_{1-42}^{5.3,0}$		$\mathrm{A}\beta_{1-42}^{6.0,1-}$		$\mathrm{A}\beta_{1-42}^{6.9,\mathrm{Cu}}$		$\mathrm{A}\beta_{1-42}^{7.4,3-}$	
States	Population (%)	States	Population (%)	States	Population (%)	States	Population (%)
0|4	21.6	0|2	20.4	3|8	17.5	0|4	57.3
0|8	16.1	0|0	10.0	0|8	12.6	0|6	9.0
0|6	9.8	0|4	8.7	3|6	11.4	3|4	6.0
0|12	9.8	3|2	6.4	0|6	9.0	0|8	5.5
0|10	7.9	0|6	5.3	3|10	5.1	0|2	3.7
0|2	7.0	0|8	5.0	0|5	5.0	0|5	3.0
3|4	3.5	3|0	4.3	0|10	3.2	0|10	2.9
3|2	2.8	3|3	4.3	0|4	2.8	0|7	2.7
0|14	2.7	3|4	4.0	0|3	2.7	3|8	2.0
0|0	1.9	3|6	2.9	0|7	2.5	3|6	1.8

consistent with an NMR study of $\mathrm{A}\beta_{1-40}$ [116]. In this partially folded NMR structure of $\mathrm{A}\beta_{1-40}$, a 3_{10}-helix from His13 to Asp23 has been reported, while we observed an averaged helix propensity (α- and 3_{10}-helices) of $\leq$10% in the region of residues His14–Phe20 in our simulations of $\mathrm{A}\beta_{1-42}^{7.4,3-}$. In general, the $\mathrm{A}\beta_{1-42}$ NMR conformation appears to be dominated by unstructured bend, turn, and loop/irregular structures [115]. We also observed a high population of these structural elements in $\mathrm{A}\beta_{1-42}^{7.4,3-}$. The NMR study has further indicated β-hairpin formation near the C-terminus of $\mathrm{A}\beta_{1-42}$ [117]. From previous simulations it was concluded that $\mathrm{A}\beta_{1-42}$ preferentially forms β-hairpins with the turns at the positions of the Gly residues, i.e., residues 25, 29, 30, 33, 37 and 38 [11, 65, 115, 118, 119]. In agreement with previous MD simulations from Olubiyi *et al.* [11] using the GROMOS force fields ffG43a2 [120] and Côté *et al.* [121] using a coarse-grained force field, we observe a β-propensity for $\mathrm{A}\beta_{1-42}^{7.4,3-}$ of 11.8% similar to 11.5% in Olubiyi *et al.* [11] and 10.8% in Côté *et al.* [121], however lower ($\sim$ 3% [115]), higher ($\sim$ 30% [122]) or equivalent ($\sim$ 6 % [123] and $\sim$ 15 % [124]) β-propensities were also reported. These differences results from different force fields used as (i) a previous MD study testing force fields for $\mathrm{A}\beta_{1-40}$ also produced a considerably higher β-propensity for ffG53a6 ($>$ 30%) compared to all other force fields [67], and (ii) a REMD comparing five force fields for $\mathrm{A}\beta_{1-42}$ also produced different α- and β-propensities [125]. However, the different force fields results agree by demonstrating that the helical propensity is the highest between residues 10 and 20 while β-structures are preferentially adopted by C-terminal residues.

In this study, more β-sheet is sampled upon decreasing the pH and with Cu^{2+} binding. The increased β-propensity at the isoelectric point is in agreement with the findings of our earlier simulation study [11]. For the structures at mild acidic conditions we also observed helix formation, while for $\mathrm{A}\beta_{1-42}^{6.9,\mathrm{Cu}}$ the helix content was higher at the CHC and central polar regions. These observations are supported by previous experimental studies reporting β-sheet formation [24, 26] and helix reduction [25] upon Cu^{2+} binding to $\mathrm{A}\beta$. In a previous MD simulation of the $\mathrm{A}\beta_{1-42}/\mathrm{Cu}^{2+}$ complex, it was found that coil structures are the predominant conformation, which is due to the disruption of β-sheet upon Cu^{2+} binding [49]. While we could not reproduce the low β-propensity, our results agree in terms of an increased disorder in $\mathrm{A}\beta_{1-42}^{6.9,\mathrm{Cu}}$.

Experimental studies show that $\mathrm{A}\beta$ peptides aggregate more readily at acidic pH [43, 45, 46], and especially at isoelectric point. The formation of a β-hairpin structure sampled in $\mathrm{A}\beta_{1-42}^{5.3,0}$ with a high propensity at the C-terminal hydrophobic region is thought to be an important factor that promotes the aggregation of $\mathrm{A}\beta_{1-42}$ peptides [65, 108–110]. In $\mathrm{A}\beta_{1-42}^{7.4,3-}$, both the β-hairpin structure at the C-terminal hydrophobic region and the Asp23-Lys28 salt bridge were sampled with low populations.

PLOS

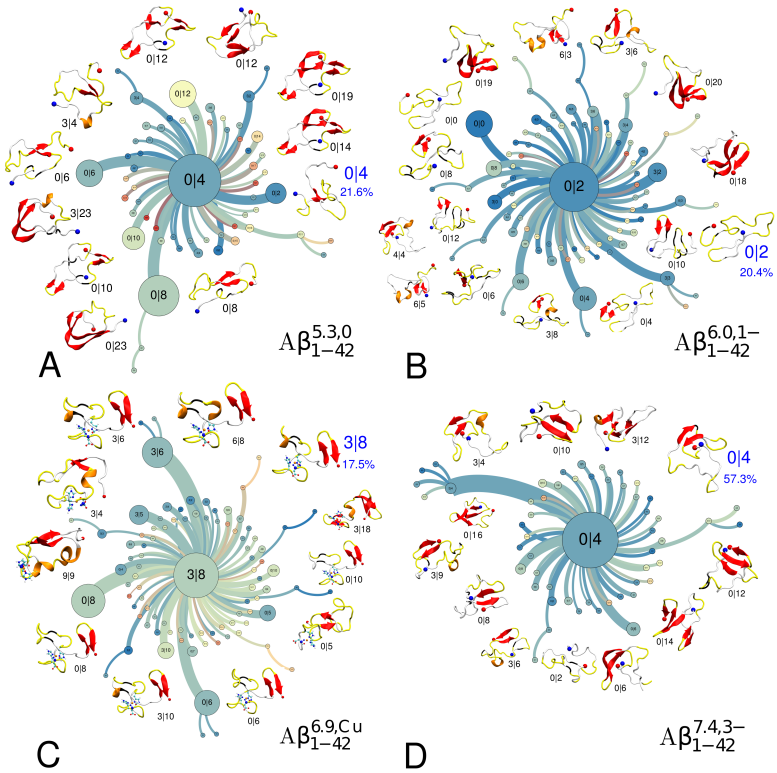

Figure 13. Min-cut transition networks for $A\beta_{1-42}^{5.3,0}$ (A), $A\beta_{1-42}^{6.0,1-}$ (B), $A\beta_{1-42}^{6.9,Cu}$ (C) and $A\beta_{1-42}^{7.4,3-}$ (D). The nodes represent the folding states. The size of each node is proportional to the population of each node, and the colouring of the nodes and edges indicates the number of residues of sheet structure ($N2$). The number of transitions between two folding states is defined by the thickness of the network edge. Representative conformations of nodes with high populations or sheet contents are included. For colouring of secondary structures, see Figure 7.

Salt bridges between C-termini and Lys16 as well as Lys28 were more populated, consistent with the low flexibility of the C-terminal hydrophobic region. These observation might explain the fact that Aβ peptides aggregate faster under acidic condition, rather than under physiological pH conditions [45, 46]. The Glu3–Arg5 salt bridge was formed in the three systems without Cu^{2+} and is especially stable in $A\beta_{1-42}^{7.4,3-}$. In rat Aβ, which has a much lower aggregation tendency than human Aβ [126, 127] and does not show amyloid deposition [128], the Glu3-Arg5 contact cannot be formed as Arg5 is substituted by Gly. Moreover, the key mutation between the human and rat Aβ peptides with regard to Cu^{2+} binding is the Arg5Gly mutation, as it results in deprotonation of the Gly5–His6 bond and coordination of the deprotonated amidyl nitrogen atom [129]. Thus, the Glu3-Arg5 interaction in human Aβ might be of relevance to the aggregation kinetics of this peptide. The interaction of the Cu^{2+} with the N-terminus is also reflected in the transition network analysis that shows a central state for this system that is dominated by the strand-loop-strand motif in the C-terminal region and displays some helical elements. Interestingly, the main transitions occur with states that preserve the above mentioned motif, suggesting its important role

in the structure and kinetics of the $A\beta_{1-42}^{6.9,Cu}$ monomer [65, 108–110].

Summary and Conclusions

In this study, we investigated the effects of Cu^{2+} binding and different pH values (5.3, 6.0, 7.4) on $A\beta_{1-42}$ folding using Hamiltonian replica exchange molecular dynamics (H-REMD) simulations with explicit solvent. First, we developed a set of new OPLS-AA/L force field parameters for modeling the interactions between Cu^{2+} and $A\beta_{1-42}$. We used one of the most widely accepted Cu^{2+} coordination modes of 3N1O involving the amine and carbonyl groups of Asp1, His6 and His13 as ligands [29, 42, 54]. After validation, these newly developed parameters were then applied in H-REMD simulations of $A\beta_{1-42}/Cu^{2+}$. The effects of Cu^{2+} binding on $A\beta_{1-42}$ monomeric conformation were compared to the effects of acidic pH values of 6.0 and 5.3 (the isoelectric point of $A\beta_{1-42}$) on $A\beta_{1-42}$.

For each of the four systems under study, i.e., $A\beta_{1-42}^{7.4,3-}$, $A\beta_{1-42}^{6.9,Cu}$, $A\beta_{1-42}^{5.3,0}$ and $A\beta_{1-42}^{6.0,1-}$, the most abundant secondary structures are turns, bends and coils, especially at the N- and C-termini. At physiological pH 7.4, the initial helical structure of $A\beta_{1-42}$ is mostly disrupted, and anti-parallel β-sheets form mainly between the central polar and C-terminal hydrophobic regions. With Cu^{2+} binding at physiological pH, the helical content (mainly 3_{10}-helix) is increased at the central polar regions, while a β-hairpin structure is observed at the C-terminal hydrophobic region though a small amount of β-sheet also appeared at the other regions (Val18 and Ser26). Moreover, the conformational flexibility of $A\beta$ is greatly enhanced in $A\beta_{1-42}^{6.9,Cu}$ even though the metal binding region is rigidified upon Cu^{2+} binding. The increased peptide dynamics is accompanied by reduced intrapeptide interactions, which is likely to expose $A\beta_{1-42}^{6.9,Cu}$ to more interpeptide interactions that could facilitate aggregation. At acidic pH, less helix and more sheet structures were sampled for $A\beta_{1-42}^{5.3,0}$ than $A\beta_{1-42}^{6.0,1-}$. Similar to Cu^{2+} binding, decreasing pH values increases the conformational flexibility of $A\beta_{1-42}$, which is best demonstrated by the cluster analysis and the free energy surfaces of $A\beta_{1-42}^{5.3,0}$ and $A\beta_{1-42}^{6.0,1-}$. Finally, transition networks clearly show the differences in the conformational kinetics induced by Cu^{2+} binding.

In summary, charge reduction of $A\beta_{1-42}$ brought by Cu^{2+} binding or mild acidic conditions leads to conformational changes compared to uncomplexed $A\beta_{1-42}$ at physiological pH. While complexation with Cu^{2+} increases the conformational flexibility, a pH of 7.4 reduces it. Nonetheless, both Cu^{2+} binding and a mildly acidic pH accelerate the formation of β-sheet in $A\beta_{1-42}$ and also lead to stable salt bridges, which may promote the aggregation. While the current study provides insights into the subtle interplay of pH and Cu^{2+} binding during the $A\beta_{1-42}$ folding, a future study will elucidate the role of these environmental conditions on $A\beta$ aggregation.

Supporting Information

S1 Fig.

The fluctuations of bonds (A) and angles (B) involving Cu^{2+} during a 10-ns MD simulations of the copper coordination model with the newly derived parameters for the Cu^{2+} coordination.
(PDF)

S2 Fig.

Bend content obtained for time windows [30-70 ns], [30-100 ns] and [30-130 ns] for the $\mathbf{A}\beta_{1-42}^{5.3,0}$, $\mathbf{A}\beta_{1-42}^{6.0,1-}$, $\mathbf{A}\beta_{1-42}^{6.9,\mathrm{Cu}}$ and $\mathbf{A}\beta_{1-42}^{7.4,3-}$ systems, are shown for the individual residues in the peptide, respectively.
(PDF)

S3 Fig.

Turn content obtained for time windows [30-70 ns], [30-100 ns] and [30-130 ns] for the $\mathbf{A}\beta_{1-42}^{5.3,0}$, $\mathbf{A}\beta_{1-42}^{6.0,1-}$, $\mathbf{A}\beta_{1-42}^{6.9,\mathrm{Cu}}$ and $\mathbf{A}\beta_{1-42}^{7.4,3-}$ systems, are shown for the individual residues in the peptide, respectively.
(PDF)

S4 Fig.

Transition networks for $\mathbf{A}\beta_{1-42}^{5.3,0}$ (A), $\mathbf{A}\beta_{1-42}^{6.0,1-}$ (B), $\mathbf{A}\beta_{1-42}^{6.9,\mathrm{Cu}}$ (C) and $\mathbf{A}\beta_{1-42}^{7.4,3-}$ (D). The nodes represent the folding states as defined by $N1$ and $N2$. The size of each node is proportional to the population of the node, and the colouring of the nodes and edges indicates the number of residues with β-sheet structure ($N2$). The thickness of the edges is defined by the number of transitions between the folding states.
(PDF)

Acknowledgments

Q.L. gratefully acknowledges the funding received towards his Ph.D. from the China Scholarship Council. M.C.O. thanks the Helmholtz postdoctoral programme for financial support. The authors gratefully acknowledge the computing time granted on the supercomputer JUROPA at Jülich Supercomputing Centre (grant number JICS61) and the HPC cluster of Heinrich-Heine University Düsseldorf.

Author Contributions

Conceived and performed the simulations: BS QL. Analyzed the data: QL BB OO. Wrote the paper: QL OO MO BB BS.

References

1. Stefanis L (2012) α-synuclein in Parkinson's disease. CSH Perspect Med 2: a009399.
2. Collinge J (2001) Prion diseases of humans and animals: Their causes and molecular basis. Annu Rev Neurosci 24: 519–550.
3. Chiti F, Dobson CM (2006) Protein misfolding, functional amyloid, and human disease. Annu Rev Biochem 75: 333-366.
4. Shankar GM, Walsh DM (2009) Alzheimer's disease: synaptic dysfunction and Aβ. Mol Neurodegener 4: 48.
5. Rauk A (2009) The chemistry of Alzheimer's disease. Chem Soc Rev 38: 2698–2715.
6. Tew DJ, Bottomley SP, Smith DP, Ciccotosto GD, Babon J, et al. (2008) Stabilization of neurotoxic soluble β-sheet-rich conformations of the Alzheimer's disease amyloid-β peptide. Biophys J 94: 2752–2766.
7. Ono K, Condron MM, Teplow DB (2009) Structure-neurotoxicity relationships of amyloid β-protein oligomers. Proc Natl Acad Sci USA 106: 14745–14750.
8. Tjernberg LO, Näslund J, Lindqvist F, Johansson J, Karlström AR, et al. (1996) Arrest of β-amyloid fibril formation by a pentapeptide ligand. J Biol Chem 271: 8545–8548.
9. Urbanc B, Cruz L, Yun S, Buldyrev SV, Bitan G, et al. (2004) In silico study of amyloid β-protein folding and oligomerization. Proc Natl Acad Sci USA 101: 17345–17350.
10. Yun S, Urbanc B, Cruz L, Bitan G, Teplow D, et al. (2007) Role of electrostatic interactions in amyloid β-protein (Aβ) oligomer formation: A discrete molecular dynamics study. Biophys J 92: 4064 - 4077.
11. Olubiyi OO, Strodel B (2012) Structures of the amyloid β-peptides Aβ1-40 and Aβ1-42 as influenced by pH and a D-peptide. J Phys Chem B 116: 3280–3291.
12. Ahmed M, Davis J, Aucoin D, Sato T, Ahuja S, et al. (2010) Structural conversion of neurotoxic amyloid-β_{1-42} oligomers to fibrils. Nat Struct Mol Biol 17: 561–567.
13. Barz B, Olubiyi OO, Strodel B (2014) Early amyloid β-protein aggregation precedes conformational change. Chem Commun 50: 5373–5375.
14. Urbanc B, Betnel M, Cruz L, Bitan G, Teplow DB (2010) Elucidation of amyloid β-protein oligomerization mechanisms: Discrete molecular dynamics study. J Am Chem Soc 132: 4266–4280.
15. Faller P, Hureau C (2009) Bioinorganic chemistry of copper and zinc ions coordinated to amyloid-β peptide. Dalton Trans : 1080–1094.
16. Faller P, Hureau C, Berthoumieu O (2013) Role of metal ions in the self-assembly of the Alzheimer's amyloid-β peptide. Inorg Chem 52: 12193–12206.

17. Atwood CS, Moir RD, Huang X, Scarpa RC, Bacarra NME, et al. (1998) Dramatic aggregation of Alzheimer Aβ by Cu(II) is induced by conditions representing physiological acidosis. J Biol Chem 273: 12817–12826.

18. Chen WT, Liao YH, Yu HM, Cheng IH, Chen YR (2011) Distinct effects of Zn^{2+}, Cu^{2+}, Fe^{3+}, and Al^{3+} on amyloid-β stability, oligomerization, and aggregation: Amyloid-β destabilization promotes annular protofibril formation. J Biol Chem 286: 9646–9656.

19. Raman B, Ban T, Yamaguchi Ki, Sakai M, Kawai T, et al. (2005) Metal ion-dependent effects of clioquinol on the fibril growth of an amyloid β peptide. J Biol Chem 280: 16157–16162.

20. Deshpande A, Mina E, Glabe C, Busciglio J (2006) Different conformations of amyloid β induce neurotoxicity by distinct mechanisms in human cortical neurons. J Neurosci 26: 6011–6018.

21. Roychaudhuri R, Yang M, Hoshi MM, Teplow DB (2009) Amyloid β-protein assembly and Alzheimer disease. J Biol Chem 284: 4749–4753.

22. Valensin D, Gabbiani C, Messori L (2012) Metal compounds as inhibitors of β-amyloid aggregation. perspectives for an innovative metallotherapeutics on Alzheimer's disease. Coord Chem Rev 256: 2357–2366.

23. Sarell CJ, Wilkinson SR, Viles JH (2010) Substoichiometric levels of Cu^{2+} ions accelerate the kinetics of fiber formation and promote cell toxicity of amyloid-β from Alzheimer disease. J Biol Chem 285: 41533–41540.

24. Tickler AK, Smith DG, Ciccotosto GD, Tew DJ, Curtain CC, et al. (2005) Methylation of the imidazole side chains of the Alzheimer disease amyloid-β peptide results in abolition of superoxide dismutase-like structures and inhibition of neurotoxicity. J Biol Chem 280: 13355–13363.

25. Danielsson J, Pierattelli R, Banci L, Gräslund A (2007) High-resolution NMR studies of the zinc-binding site of the Alzheimer's amyloid β-peptide. FEBS J 274: 46–59.

26. Dai XL, Sun YX, Jiang ZF (2006) Cu(II) potentiation of Alzheimer Aβ1-40 cytotoxicity and transition on its secondary structure. Acta Bioch Bioph Sin 38: 765–772.

27. Ricchelli F, Drago D, Filippi B, Tognon G, Zatta P (2005) Aluminum-triggered structural modifications and aggregation of β-amyloids. Cell Mol Life Sci 62: 1724–1733.

28. Brzyska M, Trzesniewska K, Wieckowska A, Szczepankiewicz A, Elbaum D (2009) Electrochemical and conformational consequences of copper (CuI and CuII) binding to β-amyloid(1-40). ChemBioChem 10: 1045–1055.

29. Drew SC, Noble CJ, Masters CL, Hanson GR, Barnham KJ (2009) Pleomorphic copper coordination by Alzheimer's disease amyloid-β peptide. J Am Chem Soc 131: 1195–1207.

30. Drew SC, Masters CL, Barnham KJ (2009) Alanine-2 carbonyl is an oxygen ligand in Cu^{2+} coordination of Alzheimer's disease amyloid-β peptide - relevance to N-terminally truncated forms. J Am Chem Soc 131: 8760–8761.

31. Miura T, Mitani S, Takanashi C, Mochizuki N (2004) Copper selectively triggers β-sheet assembly of an N-terminally truncated amyloid β-peptide beginning with Glu3. J Inorg Biochem 98: 10–14.

32. Sarell CJ, Syme CD, Rigby SEJ, Viles JH (2009) Copper(II) binding to amyloid-β fibrils of Alzheimer's disease reveals a picomolar affinity: Stoichiometry and coordination geometry are independent of Aβ oligomeric form. Biochemistry 48: 4388–4402.

33. Curtain CC, Ali F, Volitakis I, Cherny RA, Norton RS, et al. (2001) Alzheimer's disease amyloid-β binds copper and zinc to generate an allosterically ordered membrane-penetrating structure containing superoxide dismutase-like subunits. J Biol Chem 276: 20466–20473.

34. Miura T, Suzuki K, Kohata N, Takeuchi H (2000) Metal binding modes of Alzheimer's amyloid β-peptide in insoluble aggregates and soluble complexes. Biochemistry 39: 7024–7031.

35. Streltsov VA, Titmuss SJ, Epa VC, Barnham KJ, Masters CL, et al. (2008) The structure of the amyloid-β peptide high-affinity copper II binding site in Alzheimer disease. Biophys J 95: 3447–3456.

36. Parthasarathy S, Long F, Miller Y, Xiao Y, McElheny D, et al. (2011) Molecular-level examination of Cu^{2+} binding structure for amyloid fibrils of 40-residue Alzheimer's β by solid-state NMR spectroscopy. J Am Chem Soc 133: 3390–3400.

37. Miller Y, Ma B, Nussinov R (2012) Metal binding sites in amyloid oligomers: Complexes and mechanisms. Coord Chem Rev 256: 2245–2252.

38. Syme CD, Nadal RC, Rigby SEJ, Viles JH (2004) Copper binding to the amyloid-β (aβ) peptide associated with Alzheimer's disease: Folding, coordination geometry, pH dependence, stoichiometry, and affinity of Aβ-(1-28): Insights from a range of complementary spectroscopic techniques. J Biol Chem 279: 18169–18177.

39. Karr JW, Akintoye H, Kaupp LJ, Szalai VA (2005) N-terminal deletions modify the Cu^{2+} binding site in amyloid-β. Biochemistry 44: 5478–5487.

40. Guilloreau L, Damian L, Coppel Y, Mazarguil H, Winterhalter M, et al. (2006) Structural and thermodynamical properties of CuII amyloid-β16/28 complexes associated with Alzheimer's disease. J Biol Inorg Chem 11: 1024–1038.

41. Streltsov V (2008) X-ray absorption and diffraction studies of the metal binding sites in amyloid β-peptide. Eur Biophys J 37: 257–263.

42. Drew SC, Barnham KJ (2011) The heterogeneous nature of Cu^{2+} interactions with Alzheimer's amyloid-β peptide. Acc Chem Res 44: 1146–1155.

43. Su Y, Chang PT (2001) Acidic pH promotes the formation of toxic fibrils from β-amyloid peptide. Brain Res 893: 287–291.

44. Perálvarez-Marín A, Barth A, Gräslund A (2008) Time-resolved infrared spectroscopy of pH-induced aggregation of the Alzheimer Aβ1-28 peptide. J Mol Biol 379: 589–596.

45. Burdick D, Soreghan B, Kwon M, Kosmoski J, Knauer M, et al. (1992) Assembly and aggregation properties of synthetic Alzheimer's A4/β amyloid peptide analogs. J Biol Chem 267: 546–554.

46. Schmittschmitt JP, Scholtz JM (2003) The role of protein stability, solubility, and net charge in amyloid fibril formation. Protein Sci 12: 2374–2378.

47. Ibarreta D, Urcelay E, Parrilla R, Ayuso MS (1998) Distinct pH homeostatic features in lymphoblasts from Alzheimer's disease patients. Ann Neurol 44: 216–222.

48. Yates CM, Butterworth J, Tennant MC, Gordon A (1990) Enzyme activities in relation to pH and lactate in postmortem brain in Alzheimer-type and other dementias. J Neurochem 55: 1624–1630.

49. Raffa DF, Rauk A (2007) Molecular dynamics study of the beta amyloid peptide of Alzheimer's disease and its divalent copper complexes. J Phys Chem B 111: 3789–3799.

50. Minicozzi V, Morante S, Rossi GC, Stellato F, Christian N, et al. (2008) The role of metals in amyloid aggregationexperiments and ab initio simulations. Int J Quantum Chem 108: 1992–2015.

51. Aí-Torres J, Maréchal JD, Rodríguez-Santiago L, Sodupe M (2011) Three dimensional models of Cu^{2+}-Aβ(1-16) complexes from computational approaches. J Am Chem Soc 133: 15008–15014.

52. Xu L, Wang X, Shan S, Wang X (2013) Characterization of the polymorphic states of copper(II)-bound Aβ(1-16) peptides by computational simulations. J Comput Chem 34: 2524–2536.

53. Xu W, Zhang C, Morozova-Roche L, Zhang JZH, Mu Y (2013) pH-dependent conformational ensemble and polymorphism of amyloid-β core fragment. J Phys Chem B 117: 8392–8399.

54. Alí-Torres J, Mirats A, Maréchal JD, Rodríguez-Santiago L, Sodupe M (2014) 3d structures and redox potentials of Cu^{2+}-Aβ(1-16) complexes at different pH: A computational study. J Phys Chem B 118: 4840–4850.

55. Dorlet P, Gambarelli S, Faller P, Hureau C (2009) Pulse EPR spectroscopy reveals the coordination sphere of copper(II) ions in the 1-16 amyloid-β peptide: A key role of the first two N-terminus residues. Angew Chem Int Ed 48: 9273–9276.

56. Tomaselli S, Esposito V, Vangone P, van Nuland NAJ, Bonvin AMJJ, et al. (2006) The α-to-β conformational transition of Alzheimer's Aβ-(1-42) peptide in aqueous media is reversible: A step by step conformational analysis suggests the location of β conformation seeding. ChemBioChem 7: 257–267.

57. Gordon JC, Myers JB, Folta T, Shoja V, Heath LS, et al. (2005) H++: a server for estimating pKas and adding missing hydrogens to macromolecules. Nucleic Acids Res 33: W368–W371.

58. Anandakrishnan R, Aguilar B, Onufriev AV (2012) H++ 3.0: automating pK prediction and the preparation of biomolecular structures for atomistic molecular modeling and simulations. Nucleic Acids Res 40: W537–W541.

59. Hancock RD (1989) Molecular mechanics calculations as a tool in coordination chemistry. Prog Inorg Chem 37: 187–291.

60. Hancock RD (1990) Molecular mechanics calculations and metal ion recognition. Acc Chem Res 23: 253–257.

61. Hoops SC, Anderson KW, Merz KM (1991) Force field design for metalloproteins. J Am Chem Soc 113: 8262–8270.

62. Peters MB, Yang Y, Wang B, Füsti-Molnár L, Weaver MN, et al. (2010) Structural survey of zinc-containing proteins and development of the zinc AMBER force field (ZAFF). J Chem Theory Comput 6: 2935–2947.

63. Jorgensen WL, Maxwell DS, Tirado-Rives J (1996) Development and Testing of the OPLS All-Atom Force Field on Conformational Energetics and Properties of Organic Liquids. J Am Chem Soc 118: 11225–11236.

64. Kaminski GA, Friesner RA, Tirado-Rives J, Jorgensen WL (2001) Evaluation and reparametrization of the OPLS-AA force field for proteins via comparison with accurate quantum chemical calculations on peptides. J Phys Chem B 105: 6474–6487.

65. Sgourakis NG, Yan Y, McCallum SA, Wang C, Garcia AE (2007) The Alzheimer's peptides Aβ40 and 42 adopt distinct conformations in water: A combined MD/NMR study. J Mol Biol 368: 1448–1457.

66. Rosenman DJ, Connors CR, Chen W, Wang C, García AE (2013) Aβ monomers transiently sample oligomer and fibril-like configurations: Ensemble characterization using a combined MD/NMR approach. J Mol Biol 425: 3338–3359.

67. Gerben SR, Lemkulm JA, Brown AM, Bevan DR (2014) Comparing atomistic molecular mechanics force fields for a difficult target: a case study on the Alzheimer's amyloid β-peptide. J Biomol Struct Dyn 32: 1817–1832.

68. Becke AD (1988) Density-functional exchange-energy approximation with correct asymptotic behavior. Phys Rev A 38: 3098–3100.

69. Lee C, Yang W, Parr RG (1988) Development of the colle-salvetti correlation-energy formula into a functional of the electron density. Phys Rev B 37: 785–789.

70. Weigend F, Ahlrichs R (2005) Balanced basis sets of split valence, triple zeta valence and quadruple zeta valence quality for H to Rn: Design and assessment of accuracy. Phys Chem Chem Phys 7: 3297–3305.

71. Weigend F (2006) Accurate coulomb-fitting basis sets for H to Rn. Phys Chem Chem Phys 8: 1057–1065.

72. Grimme S, Antony J, Ehrlich S, Krieg H (2010) A consistent and accurate ab initio parametrization of density functional dispersion correction (DFT-D) for the 94 elements H-Pu. J Chem Phys 132: 154104.

73. TURBOMOLE V6.3 2011, a development of University of Karlsruhe and Forschungszentrum Karlsruhe GmbH, 1989-2007, TURBOMOLE GmbH, since 2007; available from `http://www.turbomole.com`.

74. De Kerpel JO, Ryde U (1999) Protein strain in blue copper proteins studied by free energy perturbations. Proteins: Struc, Func, Bioinf 36: 157–174.

75. Lin F, Wang R (2010) Systematic derivation of AMBER force field parameters applicable to zinc-containing systems. J Chem Theory Comput 6: 1852–1870.

76. Bayly CI, Cieplak P, Cornell W, Kollman PA (1993) A well-behaved electrostatic potential based method using charge restraints for deriving atomic charges: the RESP model. J Phys Chem 97: 10269–10280.

77. Hu L, Ryde U (2011) Comparison of methods to obtain force-field parameters for metal sites. J Chem Theory Comput 7: 2452–2463.

78. Frisch MJ, Trucks GW, Schlegel HB, Scuseria GE, Robb MA, et al. Gaussian 09 Revision A.02. Gaussian Inc. Wallingford CT 2009.

79. Wang J, Wang W, Kollman PA, Case DA (2006) Automatic atom type and bond type perception in molecular mechanical calculations. J Mol Graph Model 25: 247–260.

80. Humphrey W, Dalke A, Schulten K (1996) VMD: Visual molecular dynamics. J Mol Graph 14: 33–38.

81. Van Der Spoel D, Lindahl E, Hess B, Groenhof G, Mark AE, et al. (2005) GROMACS: Fast, flexible, and free. J Comput Chem 26: 1701–1718.

82. Hess B, Kutzner C, van der Spoel D, Lindahl E (2008) GROMACS 4: Algorithms for highly efficient, load-balanced, and scalable molecular simulation. J Chem Theory Comput 4: 435–447.

83. Pronk S, Páll S, Schulz R, Larsson P, Bjelkmar P, et al. (2013) GROMACS 4.5: a high-throughput and highly parallel open source molecular simulation toolkit. Bioinformatics 29: 845–854.

84. Comba P, Remenyi R (2002) A new molecular mechanics force field for the oxidized form of blue copper proteins. J Comput Chem 23: 697–705.

85. Zhu Y, Su Y, Li X, Wang Y, Chen G (2008) Evaluation of amber force field parameters for copper(II) with pyridylmethyl-amine and benzimidazolylmethyl-amine ligands: A quantum chemical study. Chem Phys Lett 455: 354–360.

86. Bussi G (2014) Hamiltonian replica exchange in GROMACS: a flexible implementation. Mol Phys 112: 379–384.

87. Côté S, Binette V, Salnikov ES, Bechinger B, Mousseau N (2015) Probing the huntingtin 1-17 membrane anchor on a phospholipid bilayer by using all-atom simulations. Biophys J 108: 1187–1198.

88. Wang L, Friesner RA, Berne BJ (2011) Replica exchange with solute scaling: A more efficient version of replica exchange with solute tempering (REST2). J Phys Chem B 115: 9431–9438.

89. Tribello GA, Bonomi M, Branduardi D, Camilloni C, Bussi G (2014) PLUMED2: New feathers for an old bird. Comput Phys Commun 185: 604–613.

90. Jorgensen WL, Chandrasekhar J, Madura JD, Impey RW, Klein ML (1983) Comparison of simple potential functions for simulating liquid water. J Chem Phys 79: 926–935.

91. Bussi G, Donadio D, Parrinello M (2007) Canonical sampling through velocity rescaling. J Chem Phys 126: 014101–014101-7.

92. Parrinello M, Rahman A (1981) Polymorphic transitions in single crystals: A new molecular dynamics method. J Appl Phys 52: 7182–7190.

93. Darden T, York D, Pedersen L (1993) Particle mesh Ewald: An N·log(N) method for Ewald sums in large systems. J Chem Phys 98: 10089.

94. Hess B, Bekker H, Berendsen HJC, Fraaije JGEM (1997) LINCS: A linear constraint solver for molecular simulations. J Comput Chem 18: 1463–1472.

95. Daura X, Gademann K, Jaun B, Seebach D, van Gunsteren WF, et al. (1999) Peptide folding: When simulation meets experiment. Angew Chem Int Ed 38: 236–240.

96. Kabsch W, Sander C (1983) Dictionary of protein secondary structure: Pattern recognition of hydrogen-bonded and geometrical features. Biopolymers 22: 2577–2637.

97. Barz B, Wales DJ, Strodel B (2014) A kinetic approach to the sequence-aggregation relationship in disease-related protein assembly. J Phys Chem B 118: 1003–1011.

98. Yang YI, Gao YQ (2015) Computer simulation studies of Aβ_{37-42} aggregation thermodynamics and kinetics in water and salt solution. J Phys Chem B 119: 662–670.

99. Ford LR, Fulkerson DR (1956) Maximal flow through a network. Canad J Math 8: 399–404.

100. Krivov SV, Karplus M (2002) Free energy disconnectivity graphs: Application to peptide models. J Chem Phys 117: 10894–10903.

101. Krivov SV, Karplus M (2004) Hidden complexity of free energy surfaces for peptide (protein) folding. Proc Natl Acad Sci USA 101: 14766–14770.

102. Gomory RE, Hu TC (1961) Multi-terminal network flows. J Soc Ind Appl Math 9: 551–570.

103. Bastian M, Heymann S, Jacomy M (2009) Gephi: An open source software for exploring and manipulating networks. International AAAI Conference on Web and Social Media (ICWSM) .

104. Wise-Scira O, Xu L, Kitahara T, Perry G, Coskuner O (2011) Amyloid-β peptide structure in aqueous solution varies with fragment size. J Chem Phys 135: 205101.

105. Barz B, Urbanc B (2012) Dimer formation enhances structural differences between amyloid β-protein (1-40) and (1-42): An explicit-solvent molecular dynamics study. PLoS ONE 7: e34345.

106. Coskuner O, Wise-Scira O, Perry G, Kitahara T (2013) The structures of the E22Δ mutant-type amyloid-β alloforms and the impact of E22Δ mutation on the structures of the wild-type amyloid-β alloforms. ACS Chem Neurosci 4: 310–320.

107. Lazo ND, Grant MA, Condron MC, Rigby AC, Teplow DB (2005) On the nucleation of amyloid β-protein monomer folding. Protein Sci 14: 1581–1596.

108. Li W, Zhang J, Su Y, Wang J, Qin M, et al. (2007) Effects of zinc binding on the conformational distribution of the amyloid-β peptide based on molecular dynamics simulations. J Phys Chem B 111: 13814–13821.

109. Tarus B, Straub JE, Thirumalai D (2006) Dynamics of Asp23-Lys28 salt-bridge formation in Aβ10-35 monomers. J Am Chem Soc 128: 16159–16168.

110. Sciarretta KL, Gordon DJ, Petkova AT, Tycko R, Meredith SC (2005) Aβ40-lactam (D23/K28) models a conformation highly favorable for nucleation of amyloid. Biochemistry 44: 6003–6014.

111. Petkova AT, Yau WM, Tycko R (2006) Experimental constraints on quaternary structure in Alzheimer's β-amyloid fibrils. Biochemistry 45: 498–512.

112. D G (2007) Complex network analysis of free-energy landscapes. Proc Natl Acad Sci USA 104: 1817–1822.

113. A B (2007) Construction of effective free energy landscape from single-molecule time series. Proc Natl Acad Sci USA 104: 19297–19302.

114. F R (2010) Protein dynamics investigated by inherent structure analysis. Proc Natl Acad Sci USA 107: 9152–9157.

115. Lin YS, Bowman G, Beauchamp K, Pande V (2012) Investigating how peptide length and a pathogenic mutation modify the structural ensemble of amyloid beta monomer. Biophys J 102: 315–324.

116. Vivekanandan S, Brender JR, Lee SY, Ramamoorthy A (2011) A partially folded structure of amyloid-beta(1-40) in an aqueous environment. Biochem Biophys Res Commun 411: 312–316.

117. Hou L, Shao H, Zhang Y, Li H, Menon NK, et al. (2004) Solution NMR studies of the Aβ(1-40) and Aβ(1-42) peptides establish that the Met35 oxidation state affects the mechanism of amyloid formation. J Am Chem Soc 126: 1992–2005.

118. Urbanc B, Cruz L, Yun S, Buldyrev SV, Bitan G, et al. (2004) In silico study of amyloid β-protein folding and oligomerization. Proc. Natl. Acad. Sci. U.S.A. 101: 17345–17350.

119. Sgourakis NG, Merced-Serrano M, Boutsidis C, Drineas P, Du Z, et al. (2011) Atomic-level characterization of the ensemble of the Aβ(1-42) monomer in water using unbiased molecular dynamics simulations and spectral algorithms. J Mol Biol 405: 570–583.

120. van Gunsteren WF, Billeter SR, Eising AA, Hünenberger PH, Krüger P, et al. (1996) Biomolecular Simulation: The GROMOS96 Manual and User Guide. Zürich: Vdf Hochschulverlag AG an der ETH Zürich.

121. Côté S, Laghaei R, Derreumaux P, Mousseau N (2012) Distinct Dimerization for Various Alloforms of the Amyloid-Beta Protein: Aβ1-40, Aβ1-42, and Aβ1-40(D23N). J Phys Chem B 116: 4043–4055.

122. Lam AR, Teplow DB, Stanley HE, Urbanc B (2008) Effects of the arctic ($E^{22} \rightarrow G$) mutation on amyloid β-protein folding: Discrete molecular dynamics study. J Am Chem Soc 130: 17413–17422.

123. Yang M, Teplow DB (2008) Amyloid beta-protein monomer folding: Free-energy surfaces reveal alloform-specific differences. J Mol Biol 384: 450-464.

124. Vitalis A, Caflisch A (2010) Micelle-like architecture of the monomer ensemble of Alzheimer's amyloid-β peptide in aqueous solution and its implications for Aβ aggregation. J Mol Biol 403: 148–165.

125. Carballo-Pacheco M, Strodel B (2015) unpublished work .

126. Liu ST, Howlett G, Barrow CJ (1999) Histidine-13 is a crucial residue in the zinc ion-induced aggregation of the Aβ peptide of Alzheimer's disease. Biochemistry 38: 9373–9378.

127. Huang J, Yao Y, Lin J, Ye YH, Sun WY, et al. (2004) The solution structure of rat Aβ-(1-28) and its interaction with zinc ion: insights into the scarcity of amyloid deposition in aged rat brain. J Biol Inorg Chem 9: 627–635.

128. Duyckaerts C, Potier MC, Delatour B (2008) Alzheimer disease models and human neuropathology: similarities and differences. Acta Neuropathologica 115: 5–38.

129. Eury H, Bijani C, Faller P, Hureau C (2011) Copper(II) coordination to amyloid-β: Murine versus human peptide. Angew Chem Int Ed 50: 901–905.

Supporting Information

Conformational transitions of the amyloid-β peptide upon copper(II) binding and pH changes

Qinghua Liao, Olujide O. Olubiyi, Michael C. Owen, Bogdan Barz

Institute of Complex Systems: Structural Biochemistry (ICS-6),
Forschungszentrum Jülich GmbH,
52425 Jülich, Germany

Birgit Strodel*

Institute of Complex Systems: Structural Biochemistry (ICS-6),
Forschungszentrum Jülich GmbH,
52425 Jülich, Germany

Institute of Theoretical and Computational Chemistry,
Heinrich Heine University Düsseldorf, 40225 Düsseldorf, Germany

*Corresponding Author: b.strodel@fz-juelich.de

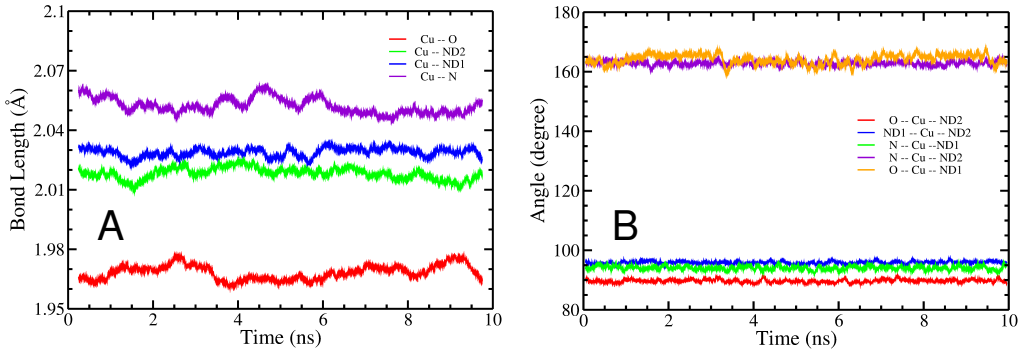

Figure S1: The fluctuations of bonds (A) and angles (B) involving Cu^{2+} during a 10-ns MD simulations of the copper coordination model with the newly derived parameters for the Cu^{2+} coordination.

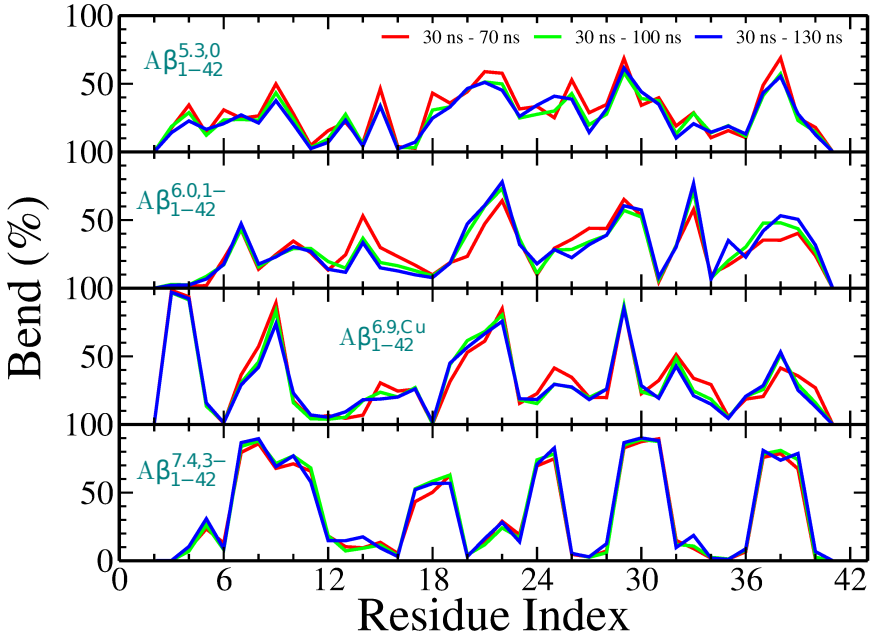

Figure S2: Bend content obtained for time windows [30-70 ns], [30-100 ns] and [30-130 ns] for the $A\beta_{1-42}^{5.3,0}$, $A\beta_{1-42}^{6.0,1-}$, $A\beta_{1-42}^{6.9,Cu}$ and $A\beta_{1-42}^{7.4,3-}$ systems, are shown for the individual residues in the peptide, respectively.

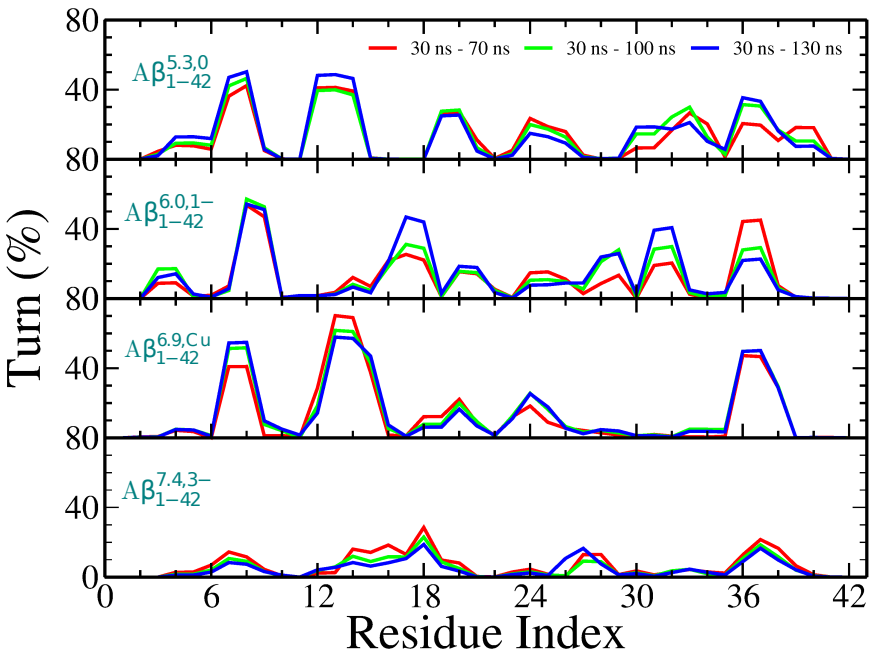

Figure S3: Turn content obtained for time windows [30-70 ns], [30-100 ns] and [30-130 ns] for the $A\beta_{1-42}^{5.3,0}$, $A\beta_{1-42}^{6.0,1-}$, $A\beta_{1-42}^{6.9,Cu}$ and $A\beta_{1-42}^{7.4,3-}$ systems, are shown for the individual residues in the peptide, respectively.

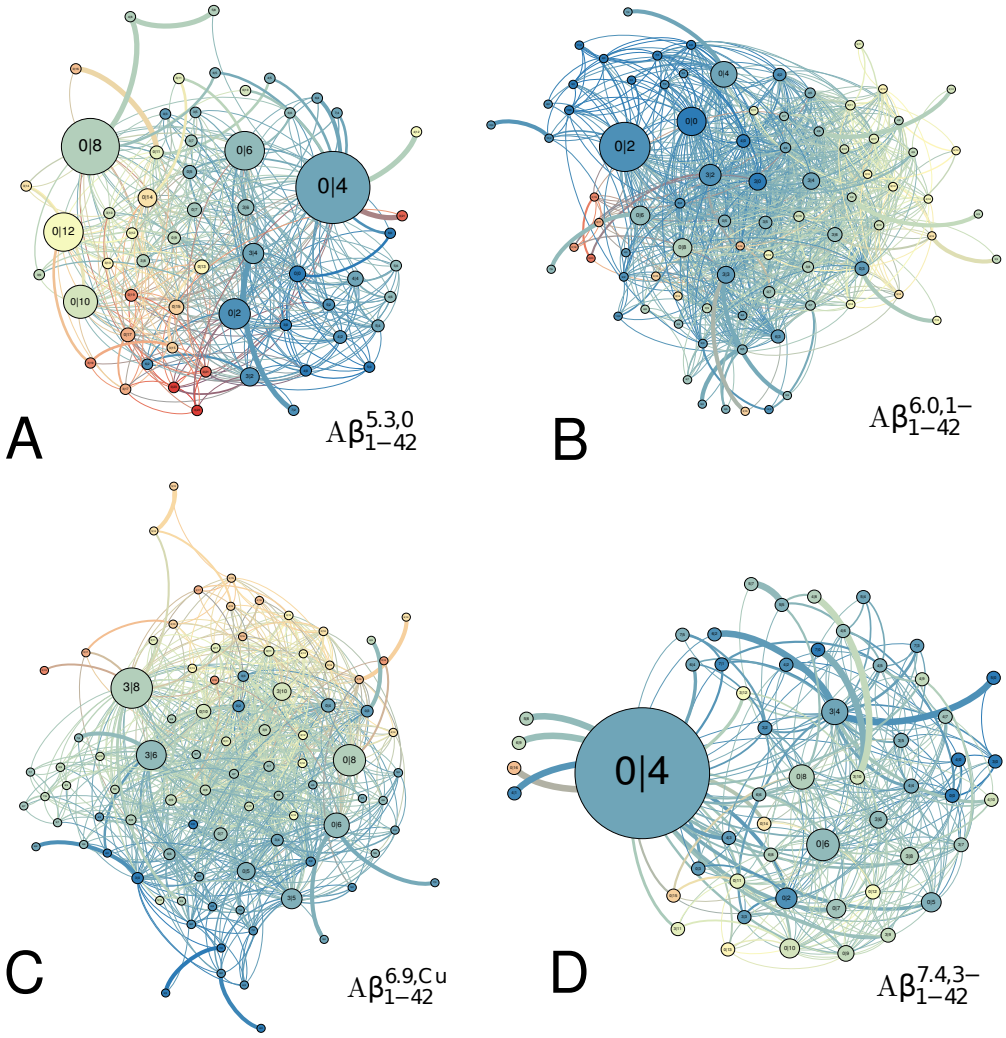

Figure S4: Transition networks for $A\beta_{1-42}^{5.3,0}$ (A), $A\beta_{1-42}^{6.0,1-}$ (B), $A\beta_{1-42}^{6.9,Cu}$ (C) and $A\beta_{1-42}^{7.4,3-}$ (D). The nodes represent the folding states as defined by $N1$ and $N2$. The size of each node is proportional to the population of the node, and the coloring of the nodes and edges indicates the number of residues with β-sheet structure ($N2$). The thickness of the edges is defined by the number of transitions between the folding states.

4.2 Development and application of a nonbonded Cu^{2+} model that includes the Jahn–Teller effect

THE JOURNAL OF PHYSICAL CHEMISTRY Letters

Letter

pubs.acs.org/JPCL

Development and Application of a Nonbonded Cu^{2+} Model That Includes the Jahn–Teller Effect

Qinghua Liao,[†] Shina Caroline Lynn Kamerlin,*[,‡] and Birgit Strodel*[,†,¶]

[†]Institute of Complex Systems: Structural Biochemistry, Forschungszentrum Jülich, 52425 Jülich, Germany

[‡]Department of Cell and Molecular Biology, Uppsala University, BMC Box 596, S-751 24 Uppsala, Sweden

[¶]Institute of Theoretical and Computational Chemistry, Heinrich Heine University Düsseldorf, Universitätsstrasse 1, 40225 Düsseldorf, Germany

Supporting Information

ABSTRACT: Metal ions are both ubiquitous to and crucial in biology. In classical simulations, they are typically described as simple van der Waals spheres, making it difficult to provide reliable force field descriptions for them. An alternative is given by nonbonded dummy models, in which the central metal atom is surrounded by dummy particles that each carry a partial charge. While such dummy models already exist for other metal ions, none is available yet for Cu^{2+} because of the challenge to reproduce the Jahn–Teller distortion. This challenge is addressed in the current study, where, for the first time, a dummy model including a Jahn–Teller effect is developed for Cu^{2+}. We successfully validate its usefulness by studying metal binding in two biological systems: the amyloid-β peptide and the mixed-metal enzyme superoxide dismutase. We believe that our parameters will be of significant value for the computational study of Cu^{2+}-dependent biological systems using classical models.

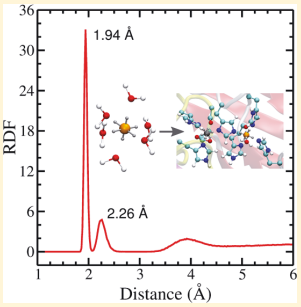

Most proteins function with metal ions such as copper, zinc, iron, calcium and magnesium ions being involved. They form complexes with surrounding residues of proteins and play significant roles including structural, electron transfer, and catalytic functions. For example, Cu–Zn superoxide dismutases (CuZnSODs) in complex with both Cu^{2+} and Zn^{2+} protect cells from oxygen toxicity by catalyzing the dismutaion of superoxide (O_2^-) into molecular oxygen and hydrogen peroxide.[1−3] On the other hand, dysregulation of metal ion homeostasis results in different kinds of diseases. Among these, Alzheimer's disease (AD) is one of the most frequent age-related neurodegenerative pathologies with disorders in Zn^{2+} and Cu^{2+} homeostasis playing a pivotal role in the mechanisms of pathogenesis. The extracellular deposition of fibrils of the amyloid-β peptide (Aβ) is considered as a hallmark of AD, and it has been shown that the presence of substoichiometric levels of Cu^{2+} doubles the rate of production of amyloid fibers and promotes cell death.[4−6] The N-terminal residues Aβ_{1-16} encompass the metal binding region of Aβ.

Molecular dynamics (MD) simulations are commonly applied to investigate the dynamics and structural information of protein systems including metalloproteins. However, most of the widely used force fields do not have appropriate parameters for metal ions, presenting a practical obstacle to MD studies of metalloproteins. Various approaches have been developed to describe the interactions between metal ions and coordinated residues in classical MD simulations. They include representations of metal ions as simple van der Waals spheres,[7,8] nonbonded models with dummy atoms (called "dummy models" henceforth),[9−13] and bonded models where artificial bonds between metal ions and ligands are introduced.[14−17] Each of these methods has its own merits and limitations.[16,18] Modeling metal ions as simple spheres with electrostatic and van der Waals interactions is often successful for the description of alkali and alkaline-earth ions, but appears to be inadequate when it comes to more complex situations such as systems containing multinuclear metal centers with closely located metal ions, or for the correct treatment of transition metals. Bonded models, on the other hand, suffer from the fact that they include predefined covalent bonds between the metal and ligands, thus not allowing for ligand exchange and/or interconversion between different coordination geometries. For a more thorough discussion of the pros and cons of these approaches, the reader is referred to ref 13 and the references therein. The dummy model approach aims at resolving the aforementioned problems by providing a nonbonded description that captures both structural and electrostatic effects via the introduction of dummy atoms surrounding the metal ion. There have been several studies reporting dummy models for Zn^{2+}, Ca^{2+}, Mg^{2+}, Fe^{2+}, Ni^{2+}, Co^{2+}, and Mn^{2+} in tetrahedral, octahedral, or pentagonal bipyramid geometries.[9−13] For the octahedral model shown in Figure 1, originally proposed by Åqvist and Warshel,[12] six dummy atoms with negligible van der Waals parameters and positive charge δ^+ are placed around a central metal ion (n^+)

Received: May 28, 2015
Accepted: June 18, 2015
Published: June 18, 2015

DOI: 10.1021/acs.jpclett.5b01122
J. Phys. Chem. Lett. 2015, 6, 2657−2662

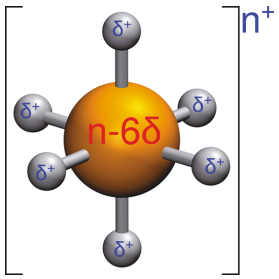

Figure 1. Schematic illustration of the dummy model.[12] Instead of a simple sphere, the point charge of the metal ion is distributed to six dummy atoms with partial charge δ^+.

with a charge of $n - 6\delta$. Such a charge distribution is particularly advantageous in systems with multiple metal centers,[10] since the redistribution of charges reduces the excessive repulsion between metal sites. The dummy atoms are bonded and angled to the central atom, but there are no bonds to the ligands. No dummy model has yet been developed for Cu^{2+}, most likely because of the Jahn−Teller distortion of Cu^{2+} (electron configuration d^9) in water. In the present work, a Cu^{2+} dummy model (CuDum) that includes the Jahn−Teller effect is developed to facilitate computational studies of copper proteins.[19] The major strength of this model is that it allows us to simultaneously reproduce the correct coordination properties of the metal, without the need for higher level quantum chemical calculations, while sampling the conformational properties of the peptide.[20] It should be noted that recently a polarizable force field for transition-metal ions was developed based on AMOEBA and the angular overlap model (AOM).[21] This classical approach, which is similar in idea to previous AOM implementations for Cu^{2+},[22,23] can also handle the Jahn−Teller distortion yet is computationally more costly than the dummy model approach. Our CuDum model is implemented into the MD program Gromacs,[24] together with the previous Zn^{2+} dummy model (ZnDum),[13] which was originally developed for Q.[25]

Full details about the MD simulations performed in this work and the adaptation of ZnDum for its use in Gromacs are given in the Supporting Information (SI). In short, the van der Waals distance σ_{ZnO} was systematically optimized (Table S1) in oder to reproduce both the experimental ion-oxygen distance (Zn−O) and the hydration free energy (ΔG_{hyd}) for Zn^{2+} in water. The calculation of ΔG_{hyd} is divided in two steps, decomposing it into the contributions from van der Waals (ΔG_{LJ}) and electrostatic (ΔG_{elec}) interactions[7,26,27] (Figure S1). For σ_{ZnO} = 2.034 Å, we found a compromise in terms of reproducing both ΔG_{hyd} and Zn−O with good accuracy (Figure S2).

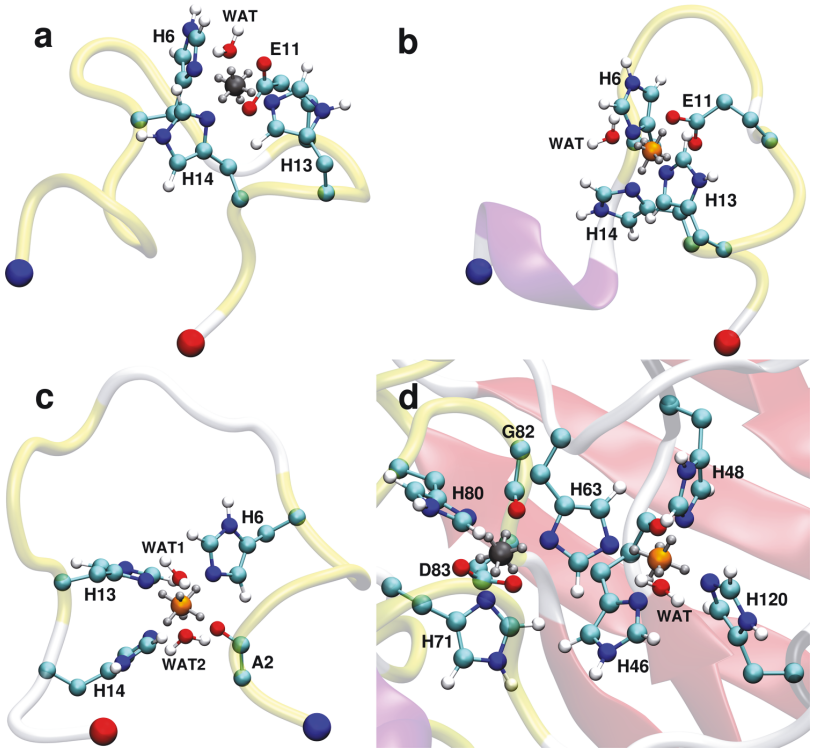

Figure 2. Final snapshots of dummy models in protein systems taken from 100 ns MD simulations of (a) $A\beta^{E11}_{1-16}$/ZnDum, (b) $A\beta^{E11}_{1-16}$/CuDum, (c) $A\beta^{A2}_{1-16}$/CuDum, and (d) CuZnSOD/ZnDum/CuDum. The proteins are shown in cartoon presentation and colored red for β-sheet, purple for 3_{10} helix, yellow for turn, and white for coil. The N- and C-terminus of $A\beta_{1-16}$ is indicated by a blue and red bead, respectively. The metal binding sites are shown in Corey−Pauling−Koltun (CPK) presentation using turquoise for C, blue for N, red for O, and white for H atoms, while Zn^{2+} is shown in gray and Cu^{2+} in orange.

DOI: 10.1021/acs.jpclett.5b01122
J. Phys. Chem. Lett. 2015, 6, 2657−2662

Furthermore, in subsequent 100 ns MD simulations for Aβ_{1-16} in complex with ZnDum the metal binding site was maintained in a distorted square pyrimidal geometry (Figure 2a), in accordance with the NMR structure (PDB ID: 1ZE9).[28]

The results for ZnDum were then taken for the development of CuDum. As Zn−O calculated with σ_{ZnO} = 2.088 Å is quite close to the weighted mean distance between Cu^{2+} and oxygen (Cu−O, 2.07 Å), this σ together with the other ZnDum parameters were used as a starting point and systematically optimized for CuDum. In order to capture both the Jahn−Teller effect (i.e., different Cu−O distances for equatorial and axial ligands) and ΔG_{hyd}, we tested different charge and distance distributions for the dummy atoms (Figures S3 and S4). We found that reducing the charges for the axial and increasing them for the equatorial dummy atoms (based on q = 0.5e for the dummy atoms in ZnDum) is important for reproducing the Jahn−Teller effect (Figure S4). This reflects the fact that equatorial interactions are preferred over axial coordination for Cu^{2+} (d^9) in aqueous solution. In combination with this charge disparity, a compressed octahedron performs better than elongated and regular octahedra. Despite the shorter distances between Cu^{2+} and the axial dummy atoms, due to the larger charges of the equatorial dummy atoms, the resulting Cu−O distances are shorter for the equatorial and not the axial ligands, in agreement with the Jahn−Teller distortion in water. The compressed octahedron combined with axial charges q_{ax} = 0.05e and equatorial charges q_{eq} = 0.725e (Table 1) was identified as being able to reproduce both the Jahn−Teller effect and ΔG_{hyd}. The calculated Cu−O distances (d^{eq}_{Cu-O} = 1.94 Å and d^{ax}_{Cu-O} = 2.26 Å) agree almost perfectly with the corresponding experimental values of 1.96 and 2.28 Å,[29] and also the calculated ΔG_{hyd} = −496.1 kcal/mol deviates by less than 0.1 kcal/mol from the experimental finding (−496.16 kcal/mol)[30] (Figure 3). It should be noted, though, that the metal solvation free energies can largely deviate in different experimental studies. Following our earlier work,[13] we use the data presented by Noyes,[30] which includes thermodynamic parameters for a wide range of metal centers, thus capturing the relative effect of the different metals (for further discussion of this choice, see ref 13). This Cu^{2+} dummy model was further validated using MD simulations of metalloproteins, which are discussed below. The usage of six dummy atoms generally favors hexacoordinated complexes. However, since the current model is a nonbonded model, it has the flexibility to adopt other geometries, such as five- or four-coordinated geometries where relevant. In the latter case, square-planar geometries are favored due to the higher charges on the equatorial dummy atoms, which make them more attractive toward ligands than the axial dummy atoms. An alternative Cu^{2+} dummy model with larger charges on the axial dummy atoms is presented in the SI. As can be seen from the results (Figures S5 and S6) and the associated discussion, this model is also able to produce good results in the MD simulations. Yet, CuDum better reproduces the Jahn−Teller effect and ΔG_{hyd} for Cu^{2+} in water and is therefore our preferred model.

Table 1. Force Field Parameters for the Dummy Model of Cu^{2+} (CuDum)

bond type	b_0 (Å)	K_b (kcal/mol Å^2)		
Cu−D_{eq}	1.000	800.0		
Cu−D_{ax}	0.800	800.0		
angle type	θ_0 (degree)	K_θ (kcal/mol rad^2)		
D_i−Cu−D_i	180.0	250.0		
D_i−Cu−D_j	90.0	250.0		
atom type	mass (au)	charge (e)	σ_{CuO} (Å)	ϵ_{CuO} (kcal/mol)
Cu	45.546	−1.00	2.043	4.1854
D_{eq}	3.000	0.725	σ_D =0	ϵ_D = 0
D_{ax}	3.000	0.050	σ_D =0	ϵ_D = 0

Dummy atoms are denoted by D with D_i being either D_{eq} or D_{ax}. The bond potential is $U_b = K_b(b - b_0)^2$; the angle potential is $U_\theta = K_\theta(\theta - \theta_0)^2$.

We performed MD simulations of both CuDum and ZnDum coordinated to Aβ_{1-16} and tested the interplay of both metal ions in CuZnSOD. We studied Aβ_{1-16} with two different coordination modes for CuDum (denoted Aβ^{A2}_{1-16} and Aβ^{E11}_{1-16}) and only Aβ^{E11}_{1-16} for ZnDum. In Aβ^{E11}_{1-16} residues, H6, E11, H13, H14 act as ligands,[4,28,31] while in Aβ^{A2}_{1-16} the ligands are A2, H6, H13, H14.[32,33] In CuZnSOD, there are one copper and one zinc ion in the active site.[1−3] The copper and zinc ions are bridged by the imidazole ring of H63. Copper is coordinated by another three His residues and a water molecule in a distorted square pyramidal geometry, while zinc is coordinated by two further His residues and an aspartic acid in a distorted tetrahedral geometry.[3] More information about the choice of our starting structure can be found in the SI. For each test case, we performed two independent 100 ns MD simulations.

CuDum produces stable Cu^{2+} binding sites during the MD simulations of the Aβ_{1-16}/Cu^{2+} complex. The root-mean-square deviation (RMSD) of the metal binding site fluctuates around ∼0.42 Å for Aβ^{E11}_{1-16}/CuDum and it is only ∼0.15 Å greater for Aβ^{A2}_{1-16}/CuDum (Table 2). The whole Aβ_{1-16} peptide experiences larger flexibility with RMSD values of up to ∼2.6 Å, which is in agreement with Aβ being an intrinsically disordered peptide. For binding mode Aβ^{E11}_{1-16} the stabilization for the interaction between Aβ_{1-16} and CuDum is by more than 30 kcal/mol larger than for the Aβ^{E11}_{1-16}/ZnDum complex (Table S3). Here the direct interactions between metal ion and Aβ_{1-16} but also the interactions between the ion and solvent are considered. In either case, the main contribution is the Coulomb interaction between the metal center and Aβ_{1-16}, which is substantially stronger for CuDum than for ZnDum. This agrees with the fact that Cu^{2+} has a higher affinity for Aβ than Zn^{2+}.[34,35] CuDum is able to maintain the coordination center of the Aβ^{E11}_{1-16}/Cu^{2+} complex in a distorted square pyramidal geometry (Figure 2b) with shorter distances between Cu^{2+} and the equatorial ligands (H6, atom OE1 of E11, H13, 14) and a longer distance for the single axial ligand (atom OE2 of E11) (Table S2). A water molecule is coordinated at the opposite axial position, that adds to the stability of the coordination center. In the simulations of Aβ^{A2}_{1-16} with CuDum, the four ligands prefer to interact with the equatorial dummy atoms producing a square planar coordination geometry (Figure 2c and Table S4), which agrees with findings from experiments[32,33,36] and other quantum-mechanics based calculations.[37,38] Furthermore, we successfully tested that this coordination geometry can also be obtained when the simulation is not initiated from a "perfect" starting conformation but from a distorted geometry (see Figure S7 and associated discussion). As for Aβ^{E11}_{1-16}, water coordinates to Cu^{2+}. Yet for Aβ^{A2}_{1-16}, there are two water molecules interacting with the two unoccupied axial dummy atoms. Again, the electrostatic interactions between Aβ_{1-16} and ligands is the dominating contribution to the complex stability (Table S5). In

DOI: 10.1021/acs.jpclett.5b01122
J. Phys. Chem. Lett. 2015, 6, 2657−2662

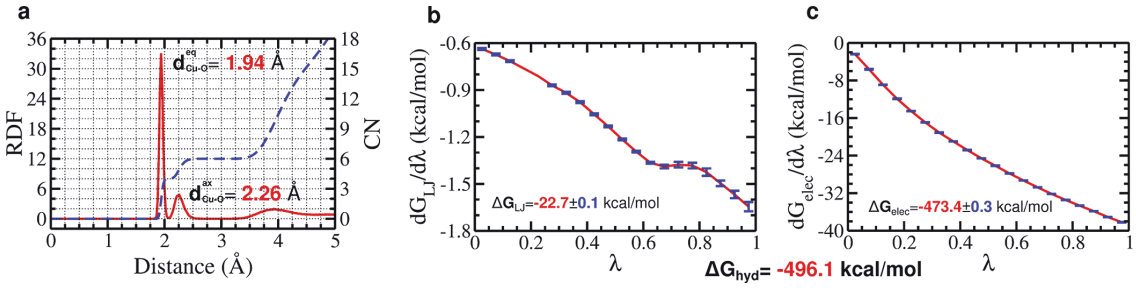

Figure 3. Jahn–Teller effect and ΔG_{hyd} for CuDum in water. (a) Radial distribution function (red, left y axis) and coordination number (blue, right y axis) for water around CuDum. The free energy contributions $dG_{LJ}/d\lambda$ (b) and $dG_{elec}/d\lambda$ (c) as a function of the coupling parameter λ. ΔG_{LJ} and ΔG_{elec} are calculated by summing over the 21 intermediate states ranging from $\lambda = 0$ to $\lambda = 1$ applying eq S7. The standard deviation for each state is shown by a blue bar (for some cases, it is <0.001 kcal/mol and thus not visible) while the interpolation between the states is shown in red. The experimental values are d^{eq}_{Cu-O} = 1.96 Å, d^{ax}_{Cu-O} = 2.28 Å, and ΔG_{hyd} = −496.16 kcal/mol.

Table 2. Time Averages of the RMSDs of the Protein Backbone Atoms and of the Metal Binding Sites of Aβ_{1-16} and CuZnSOD

system	backbone (Å)	metal site (Å)
Aβ^{E11}_{1-16}/ZnDum	1.34 ± 0.39	0.52 ± 0.08
Aβ^{E11}_{1-16}/CuDum	1.26 ± 0.43	0.42 ± 0.11
Aβ^{A2}_{1-16}/CuDum	2.64 ± 0.49	0.67 ± 0.11
CuZnSOD/ZnDum/CuDum	1.54 ± 0.16	0.71 ± 0.03

summary, CuDum and ZnDum work well for modeling metal binding to Aβ_{1-16}.

In the two 100 ns MD simulations of CuZnSOD, ZnDum and CuDum are both stable in the metal binding site (Figure 2d). Both overall structure and coordination geometry are conserved with the average RMSDs of the whole backbone and of the metal binding site being below 2.0 and 1.0 Å, respectively (Table 2). Throughout the simulation, the coordination geometry remains distorted square pyramidal for CuDum with the four His ligands interacting firmly with CuDum through the equatorial dummy atoms at distances of ∼2.0 Å. The distances to H46, H48, H120 are quite close to those in the crystal structure (PDB ID: 1HL5[3]) while the H63–CuDum distance is only 1.98 Å (Table S6), which is 0.48 Å shorter than the one in the crystal structure 1HL5. This discrepancy may be explained by the oxidation state of the copper ion in CuZnSOD. A distance increase for copper–H63 from ∼2.0 Å to ∼3.0 Å was observed when Cu^{2+} was reduced to Cu^{+}.[3] The state of the metal binding site in the crystal structure 1HL5 is considered to represent a mixture of the oxidized (Cu^{2+}) and reduced (Cu^{+}) states of CuZnSOD. Moreover, the distance between Zn^{2+} and Cu^{2+} calculated from our simulations (5.84 Å) is closer to the one in the oxidized (∼6.0 Å) than in the reduced state (∼6.8 Å). Interestingly, the carbonyl group of H46 is found to be close to CuDum and adds to the overall stability of the Cu^{2+} coordination center. Figure 2d shows that this carbonyl group and H48 compete for coordination to Cu^{2+}. A water molecule binds to CuDum via an axial dummy atom as a fifth ligand. The distance Cu^{2+}–O^{water} is 2.35 Å, which is slightly shorter than the one in the crystal structure 1HL5 (2.62 Å) but still falls in a reasonable range based on other crystal structures of CuZnSOD (i.e., PDB ID: 1CB4[1]). The coordination of water to CuDum is in good agreement with the experimental finding that the involvement of a water molecule is necessary for reactions to occur at the metal binding site. For the Zn^{2+} binding site, the distances Zn^{2+}–His are 0.1–0.2 Å larger than the corresponding distances in the crystal structure 1HL5 (Table S6). Our findings are nonetheless satisfactory, as these distances vary upon chemical reactions.[1−3] It should be noted, though, that the tetrahedral Zn^{2+} coordination geometry cannot be maintained in CuZnSOD, as the carbonyl group from G82 coordinates to Zn^{2+} and D83 becomes bidentately coordinated, causing a 6-coordinated distorted octahedral geometry. This observation is not too surprising, as ZnDum was developed for octahedral geometries.[13] This issue could be resolved by developing a tetrahedral Zn^{2+} dummy model,[9] which, however, would have been beyond the scope of the current aim to develop and validate a Cu^{2+} dummy model with Jahn–Teller effect. Furthermore, it is a known fact that zinc coordination is flexible and can adopt multiple binding modes, including tetrahedral, as well as penta- or hexacoordinated geometries.[39] Especially for the zinc coordination to the carboxylate group, it could be either bidentate or monodentate,[40] which is exactly what happens to D83 during the MD simulation of CuZnSOD.

In conclusion, a nonbonded model of Cu^{2+} (CuDum) was developed in this study. This classical Cu^{2+} model captures both the Jahn–Teller effect and the experimental hydration free energy, and maintains stable coordination geometries during MD simulations of metalloproteins without the need for artificial bonds between metal center and ligands. Furthermore, parameters for a Zn^{2+} dummy model (ZnDum) were derived based on a previously reported dummy model.[13] Our parameters can reproduce square planar Cu^{2+} geometries for our two test cases, the metal binding region of the amyloid-β peptide, Aβ_{1-16}, and the Cu–Zn superoxide dismutase (CuZnSOD). The comparison between Aβ_{1-16}/CuDum and Aβ_{1-16}/ZnDum reveals a lower binding affinity for ZnDum. This metal selectivity is in agreement with experimental findings.[34,35] The study of the bimetallo enzyme CuZnSOD further confirms that the two dummy models can be applied together without artificial repulsion between the two metal centers. We therefore believe that the dummy model of Cu^{2+} presented in this work is of great importance for future studies of the dynamics of copper proteins. A clear advantage of such nonbonded over bonded models is that they are able to model ligand exchange on the metal without the need for higher level quantum chemical calculations, while still performing conformational sampling on the peptide. For a peptide such as Aβ, this is of importance as the aggregation of Aβ is believed to be

DOI: 10.1021/acs.jpclett.5b01122
J. Phys. Chem. Lett. 2015, 6, 2657−2662

sped up by the formation of interpeptide coordination modes, which compete with the intrapeptide Cu^{2+} coordination discussed here.[41]

■ ASSOCIATED CONTENT

Supporting Information

Full details of the computational methods and starting structures, results for the parametrization of the Zn^{2+} dummy model (ZnDum) and an alternative Cu^{2+} dummy model, eight tables, and seven figures. The Supporting Information is available free of charge on the ACS Publications website at DOI: 10.1021/acs.jpclett.5b01122.

■ AUTHOR INFORMATION

Corresponding Authors

*Phone: +46 (0)18 471 4423; E-mail: kamerlin@icm.uu.se.
*Phone:+49 (0)2461 613670; Fax:+49 (0)2461 619497; E-mail: b.strodel@fz-juelich.de.

Notes

The authors declare no competing financial interest.

■ ACKNOWLEDGMENTS

Q.L. gratefully acknowledges the funding received towards his Ph.D. from the China Scholarship Council. The authors gratefully acknowledge the computing time granted on the supercomputer JUROPA at Jülich Supercomputing Centre (Grant Number JICS61). The European Research Council has provided financial support under the European Community's Seventh Framework Programme (FP7/2007-2013)/ERC Grant Agreement No. 306474. We thank Paul Bauer and Fernanda Duarte for valuable discussion.

■ REFERENCES

(1) Hough, M. A.; Hasnain, S. Crystallographic Structures of Bovine Copper-Zinc Superoxide Dismutase Reveal Asymmetry in Two Subunits: Functionally Important Three and Five Coordinate Copper Sites Captured in the Same Crystal. *J. Mol. Biol.* **1999**, *287*, 579−592.

(2) Hough, M. A.; Strange, R. W.; Hasnain, S. Conformational Variability of the Cu Site in One Subunit of Bovine CuZn Superoxide Dismutase: The Importance of Mobility in the Glu119-Leu142 Loop Region for Catalytic Function. *J. Mol. Biol.* **2000**, *304*, 231−241.

(3) Strange, R. W.; Antonyuk, S.; Hough, M. A.; Doucette, P. A.; Rodriguez, J. A.; Hart, P.; Hayward, L. J.; Valentine, J. S.; Hasnain, S. The Structure of Holo and Metal-Deficient Wild-Type Human Cu, Zn Superoxide Dismutase and Its Relevance to Familial Amyotrophic Lateral Sclerosis. *J. Mol. Biol.* **2003**, *328*, 877−891.

(4) Faller, P.; Hureau, C. Bioinorganic Chemistry of Copper and Zinc Ions Coordinated to Amyloid-β Peptide. *Dalton Trans.* **2009**, *21*, 1080−1094.

(5) Faller, P.; Hureau, C.; Berthoumieu, O. Role of Metal Ions in the Self-Assembly of the Alzheimer's Amyloid-β Peptide. *Inorg. Chem.* **2013**, *52*, 12193−12206.

(6) Sarell, C. J.; Wilkinson, S. R.; Viles, J. H. Substoichiometric Levels of Cu^{2+} Ions Accelerate the Kinetics of Fiber Formation and Promote Cell Toxicity of Amyloid-β from Alzheimer Disease. *J. Biol. Chem.* **2010**, *285*, 41533−41540.

(7) Li, P.; Roberts, B. P.; Chakravorty, D. K.; Merz, K. M. Rational Design of Particle Mesh Ewald Compatible Lennard-Jones Parameters for +2 Metal Cations in Explicit Solvent. *J. Chem. Theory Comput.* **2013**, *9*, 2733−2748.

(8) Torras, J.; Alemán, C. Determination of New Cu^{+}, Cu^{2+}, and Zn^{2+} Lennard-Jones Ion Parameters in Acetonitrile. *J. Phys. Chem. B* **2013**, *117*, 10513−10522.

(9) Pang, Y.-P. Novel Zinc Protein Molecular Dynamics Simulations: Steps Toward Antiangiogenesis for Cancer Treatment. *J. Mol. Model.* **1999**, *5*, 196−202.

(10) Oelschlaeger, P.; Klahn, M.; Beard, W. A.; Wilson, S. H.; Warshel, A. Magnesium-Cationic Dummy Atom Molecules Enhance Representation of DNA Polymerase β in Molecular Dynamics Simulations: Improved Accuracy in Studies of Structural Features and Mutational Effects. *J. Mol. Biol.* **2007**, *366*, 687−701.

(11) Saxena, A.; Sept, D. Multisite Ion Models That Improve Coordination and Free Energy Calculations in Molecular Dynamics Simulations. *J. Chem. Theory Comput.* **2013**, *9*, 3538−3542.

(12) Åqvist, J.; Warshel, A. Calculations of Free Energy Profiles for the Staphylococcal Nuclease Catalyzed Reaction. *Biochemistry* **1989**, *28*, 4680−4689.

(13) Duarte, F.; Bauer, P.; Barrozo, A.; Amrein, B. A.; Purg, M.; Åqvist, J.; Kamerlin, S. C. L. Force Field Independent Metal Parameters Using a Nonbonded Dummy Model. *J. Phys. Chem. B* **2014**, *118*, 4351−4362.

(14) Hancock, R. D. Molecular Mechanics Calculations as a Tool in Coordination Chemistry. *Prog. Inorg. Chem.* **1989**, *37*, 187−291.

(15) Hancock, R. D. Molecular Mechanics Calculations and Metal Ion Recognition. *Acc. Chem. Res.* **1990**, *23*, 253−257.

(16) Lin, F.; Wang, R. Systematic Derivation of AMBER Force Field Parameters Applicable to Zinc-Containing Systems. *J. Chem. Theory Comput.* **2010**, *6*, 1852−1870.

(17) Peters, M. B.; Yang, Y.; Wang, B.; Füsti-Molnár, L.; Weaver, M. N.; Merz, K. M. Structural Survey of Zinc-Containing Proteins and Development of the Zinc AMBER Force Field (ZAFF). *J. Chem. Theory Comput.* **2010**, *6*, 2935−2947.

(18) Hu, L.; Ryde, U. Comparison of Methods to Obtain Force-Field Parameters for Metal Sites. *J. Chem. Theory Comput.* **2011**, *7*, 2452−2463.

(19) Klinman, J. P. Mechanisms Whereby Mononuclear Copper Proteins Functionalize Organic Substrates. *Chem. Rev.* **1996**, *96*, 2541−2562.

(20) Alí-Torres, J.; Mirats, A.; Maréchal, J.-D.; Rodríguez-Santiago, L.; Sodupe, M. Modeling Cu^{2+}−Aβ Complexes from Computational Approaches. *AIP Advances* **2015**, *5*, 092402.

(21) Xiang, J. X.; Ponder, J. W. An Angular Overlap Model for Cu(II) Ion in the AMOEBA Polarizable Force Field. *J. Chem. Theory Comput.* **2014**, *10*, 298−311.

(22) Piquemal, J.-P.; Williams-Hubbard, B.; Fey, N.; Deeth, R. J.; Gresh, N.; Giessner-Prettre, C. Inclusion of the Ligand Field Contribution in a Polarizable Molecular Mechanics: SIBFA-LF. *J. Comput. Chem.* **2003**, *24*, 1963−1970.

(23) Deeth, R. J.; Anastasi, A.; Diedrich, C.; Randell, K. Molecular Modelling for Transition Metal Complexes: Dealing With d-Electron Effects. *Coord. Chem. Rev.* **2009**, *253*, 795−816.

(24) Hess, B.; Kutzner, C.; van der Spoel, D.; Lindahl, E. GROMACS 4: Algorithms for Highly Efficient, Load-Balanced, and Scalable Molecular Simulation. *J. Chem. Theory Comput.* **2008**, *4*, 435−447.

(25) Marelius, J.; Kolmodin, K.; Feierberg, I.; Åqvist, J. Q. A Molecular Dynamics Program for Free Energy Calculations and Empirical Valence Bond Simulations in Biomolecular Systems. *J. Mol. Graph. Model.* **1998**, *16*, 213−225.

(26) Li, X.; Tu, Y.; Tian, H.; Ågren, H. Computer Simulations of Aqua Metal Ions for Accurate Reproduction of Hydration Free Energies and Structures. *J. Chem. Phys.* **2010**, *132*, 104505.

(27) Li, P.; Merz, K. M. Taking into Account the Ion-Induced Dipole Interaction in the Nonbonded Model of Ions. *J. Chem. Theory Comput.* **2014**, *10*, 289−297.

(28) Zirah, S.; Kozin, S. A.; Mazur, A. K.; Blond, A.; Cheminant, M.; Ségalas-Milazzo, I.; Debey, P.; Rebuffat, S. Structural Changes of Region 1−16 of the Alzheimer Disease Amyloid β-Peptide upon Zinc Binding and in Vitro Aging. *J. Biol. Chem.* **2006**, *281*, 2151−2161.

(29) Nomura, M.; Yamaguchi, T. Concentration Dependence of EXAFS and XANES of Copper(II) Perchlorate Aqueous Solution: Comparison of Solute Structure in Liquid and Glassy States. *J. Phys. Chem.* **1988**, *92*, 6157−6160.

DOI: 10.1021/acs.jpclett.5b01122
J. Phys. Chem. Lett. 2015, 6, 2657−2662

(30) Noyes, R. M. Thermodynamics of Ion Hydration as a Measure of Effective Dielectric Properties of Water. *J. Am. Chem. Soc.* **1962**, *84*, 513−522.
(31) Streltsov, V. A.; Titmuss, S. J.; Epa, V. C.; Barnham, K. J.; Masters, C. L.; Varghese, J. N. The Structure of the Amyloid-β Peptide High-Affinity Copper (II) Binding Site in Alzheimer Disease. *Biophys. J.* **2008**, *95*, 3447−3456.
(32) Drew, S. C.; Masters, C. L.; Barnham, K. J. Alanine-2 Carbonyl is an Oxygen Ligand in Cu^{2+} Coordination of Alzheimer's Disease Amyloid-β Peptide-Relevance to N-Terminally Truncated Forms. *J. Am. Chem. Soc.* **2009**, *131*, 8760−8761.
(33) Drew, S. C.; Barnham, K. J. The Heterogeneous Nature of Cu^{2+} Interactions with Alzheimer's Amyloid-β Peptide. *Acc. Chem. Res.* **2011**, *44*, 1146−1155.
(34) Nair, N. G.; Perry, G.; Smith, M. A.; Reddy, V. P. NMR Studies of Zinc, Copper, and Iron Binding to Histidine, the Principal Metal Ion Complexing Site of Amyloid-β Peptide. *J. Alzheimers Dis.* **2010**, *20*, 57−66.
(35) Kepp, K. P. Bioinorganic Chemistry of Alzheimer's Disease. *Chem. Rev.* **2012**, *112*, 5193−5239.
(36) Dorlet, P.; Gambarelli, S.; Faller, P.; Hureau, C. EPR Pulse Spectroscopy Reveals the Coordination Sphere of Copper(II) Ions in the 1−16 Amyloid-β Peptide: A Key Role of the First Two N-Terminus Residues. *Angew. Chem., Int. Ed.* **2009**, *48*, 9273−9276.
(37) Alí-Torres, J.; Maréchal, J.-D.; Rodríguez-Santiago, L.; Sodupe, M. Three Dimensional Models of Cu^{2+}−Aβ(1−16) Complexes from Computational Approaches. *J. Am. Chem. Soc.* **2011**, *133*, 15008−15014.
(38) Xu, L.; Wang, X.; Shan, S.; Wang, X. Characterization of the Polymorphic States of Copper(II)-Bound Aβ(1−16) Peptides by Computational Simulations. *J. Comput. Chem.* **2013**, *34*, 2524−2536.
(39) Maret, W.; Li, Y. Coordination Dynamics of Zinc in Proteins. *Chem. Rev.* **2009**, *109*, 4682−4707.
(40) Wu, R.; Lu, Z.; Cao, Z.; Zhang, Y. A Transferable Nonbonded Pairwise Force Field to Model Zinc Interactions in Metalloproteins. *J. Chem. Theory Comput* **2011**, *7*, 433−443.
(41) Hane, F.; Tran, G.; Attwood, S. J.; Leonenko, Z. Cu^{2+} Affects Amyloid-β (1−42) Aggregation by Increasing Peptide−Peptide Binding Forces. *PLoS One* **2013**, *8*, e59005.

DOI: 10.1021/acs.jpclett.5b01122
J. Phys. Chem. Lett. 2015, 6, 2657−2662

Supporting Information

Development and Application of a Non-Bonded Cu^{2+} Model That Includes the Jahn-Teller Effect

Qinghua Liao,[†] Shina Caroline Lynn Kamerlin,[*,‡] and Birgit Strodel[*,†,¶]

†*Institute of Complex Systems: Structural Biochemistry, Forschungszentrum Jülich, 52425 Jülich, Germany*

‡*Department of Cell and Molecular Biology, Uppsala University, BMC Box 596, S-751 24 Uppsala, Sweden*

¶*Institute of Theoretical and Computational Chemistry, Heinrich Heine University Düsseldorf, Universitätsstrasse 1, 40225 Düsseldorf, Germany*

E-mail: kamerlin@icm.uu.se; b.strodel@fz-juelich.de

Phone: +49 (0)2461 613670. Fax: +49 (0)2461 619497

This supplementary material contains the details of the computational methods and starting structures, results for the parameterization of the Zn^{2+} dummy model (ZnDum) and an alternative Cu^{2+} dummy model, 8 tables, and 7 figures.

Computational methods

The form of the non-bonded potential function applied for the OPLS-AA/L force field[1,2] in GROMACS[3] is

$$U_{ij} = \sum_{i<j} f_{ij} \left[4\epsilon_{ij} \left(\frac{\sigma_{ij}^{12}}{r_{ij}^{12}} - \frac{\sigma_{ij}^{6}}{r_{ij}^{6}} \right) + \frac{q_i q_j e^2}{4\pi\epsilon_0 r_{ij}} \right] , \tag{S1}$$

where the first term is the standard 12-6 Lennard-Jones (LJ) potential and the second term is the classical Coulomb potential with ϵ_0 being the permittivity of free space. The distance between interacting atoms i and j with partial charges q_i and q_j is given by r_{ij}. For the van der Waals parameters the combining rule is applied: $\epsilon_{ij} = \sqrt{\epsilon_{ii}\epsilon_{jj}}$ and $\sigma_{ij} = \sqrt{\sigma_{ii}\sigma_{jj}}$. Intramolecular non-bonded interactions are counted only for atoms three or more bonds apart ($f_{ij} = 1.0$); 1,4 interactions are considered but scaled down by the factor $f_{ij} = 0.5$.

To determine the hydration free energy, the thermodynamic cycle shown in Figure S1 is employed,

$$\Delta G_{\mathrm{hyd}} = \Delta G_{\mathrm{LJ}} + \Delta G_{\mathrm{elec}} \, . \tag{S2}$$

For the calculation of the free energy difference between the end states A and B, we assume multiple intermediate states. The Hamiltonians for these states are defined by combining the Hamiltonians of the end states, H_A and H_B, and employ a linear mixing

$$H(\lambda) = (1 - \lambda)H_A + \lambda H_B \tag{S3}$$

where λ=0 and λ=1 correspond to a Hamiltonian for state A and B, respectively. For the calculation of the free energy difference between states i and j corresponding to λ_i and λ_j

in Eq. S3 Bennett's acceptance ratio (BAR) method is employed:[4,5]

$$\Delta G_{ji}^{\mathrm{BAR}} = k_{\mathrm{B}}T \left(\ln \frac{\langle f(H_i - H_j + C)\rangle_j}{\langle f(H_j - H_i - C)\rangle_i} \right) + C \tag{S4}$$

where f is the Fermi function

$$f(x) = \frac{1}{1 + \exp\left(\frac{x}{k_{\mathrm{B}}T}\right)} \tag{S5}$$

with k_{B} being the Boltzmann constant and T the temperature. The value for C is determined iteratively to fulfill $\langle f(H_i - H_j + C)\rangle_j = \langle f(H_j - H_i - C)\rangle_i$. The free energy difference is then given as

$$\Delta G_{ji}^{\mathrm{BAR}} = -k_{\mathrm{B}}T \ln \frac{N_j}{N_i} + C \tag{S6}$$

and

$$\Delta G_{BA}^{\mathrm{BAR}} = \sum_{i=1}^{n-1} \Delta G_{i+1,i}^{\mathrm{BAR}} \tag{S7}$$

where n is the number of intermediate states considered and N_i and N_j are the number of coordinate frames at state λ_i and λ_j, respectively. Sufficient overlap between the forward and backward energy differences is necessary for the convergence of this iterative process.[5]

The calculation of the hydration free energy is divided into two steps (Figure S1). First, an uncharged particle in water is created yielding ΔG_{LJ}, followed by the charging process for the calculation of ΔG_{elec}. For the calculation of both energies according to Eq. S7, the BAR method as implemented in GROMACS[5] is employed considering 21 equidistant intermediate states with λ varying from 0 to 1 and $\Delta\lambda = 0.05$. Following earlier work,[6,7] a soft-core potential is used during the calculation of ΔG_{LJ} in order to avoid singularities that might occur near the end states when atoms are being removed or added. As suggested by Shirts,[8] the soft-core parameter α was set to 0.5 while the soft-core power was chosen as 1. For the MD simulations at each λ value, the Cu^{2+} or Zn^{2+} dummy model was immersed in a TIP4P[9] cubic water box with a minimum distance of 1.8 nm from the edge of the box to any dummy atom. Two Cl^- counterions were added to keep the system neutral. The systems were first subjected to energy minimization using 1,000 steps of steepest descent followed

by 1,000 conjugate gradient steps, and then equilibrated during 25-ps NVT and 25-ps NPT MD runs (without position restraints). For the calculation of ΔG_{LJ} and ΔG_{elec} 100-ps MD simulations in the NPT ensemble were performed and the potential energy was saved every 0.01 ps. Another 1-ns MD simulation under NPT conditions was finally performed for the dummy model in water in order to determine the radial distribution function (RDF) and coordination number (CN) of water. For the MD simulations mentioned thus far a time step of 1 fs was used. All other MD parameters are given below.

For the testing of the dummy models in protein systems, Aβ_{1-16} and human Cu-Zn superoxide dismutase (CuZnSOD) were chosen. All MD simulations involving Aβ_{1-16} and CuZnSOD followed the same procedure. The protein-metal complex under study was solvated with TIP4P water[9] in the center of a cubic box with a minimum distance between protein and any box edge of 1.2 nm. Na^+ and Cl^- ions were added at a concentration of 0.150 M while, at the same time, they neutralize the system. The preparatory steps involved 1,000 steps of steepest descent and 1,000 steps of conjugate gradient energy minimizations, followed by 500-ps MD equilibration runs first under NVT and then under NPT conditions with position restraints of 1,000 kJ mol^{-1} nm^{-2} on non-hydrogen protein atoms. Production runs were performed for 100 ns in the NPT ensemble without position restraints. For the MD simulations of the protein systems a time step of 2 fs was applied and coordinates were saved every 5 ps.

All MD simulations in this study were carried out using GROMACS 4.5.5[3] with the OPLS-AA/L force field.[1,2] Periodic boundary conditions in conjunction with the particle mesh Ewald method[10,11] was used for the treatment of electrostatic interactions using a cutoff of 1.2 nm for short-range electrostatic interactions. The cutoff for LJ interactions was also 1.2 nm with a switching function being applied between 1.0 and 1.2 nm, and dispersion correction was employed for long-range LJ contributions. The temperature was kept at 300 K using a Langevin thermostat with a coupling constant of 1.0 ps^{-1} while the pressure was kept at 1 bar (only in NPT simulations) via a Parrinello-Rahman barostat[12] with a coupling constant of 0.5 ps. All bonds were constrained via the LINCS method.[13,14]

Choice of the starting structures

Since there is no crystal or NMR structure of Aβ in complex with Cu^{2+}, a model for the Aβ_{1-16}/Cu^{2+} complex was taken from a quantum mechanics/molecular mechanics (QM/MM) study.[15] In this model, which was identified as the most stable coordination mode,[15] residues A2, H6, H13 and H14 coordinate Cu^{2+} in a square planar geometry. Moreover, this coordination mode was also suggested by continuous-wave electron paramagnetic resonance (CW-EPR) spectroscopy for the Aβ/Cu^{2+} complex at pH 8.7.[16,17] Other studies using x-ray absorption spectroscopy and density functional theory indicated that also residue E11 together with the three His residues are possible ligands for both Zn^{2+} and Cu^{2+} binding to Aβ at pH values between 6.3 and 7.4,[18–20] while the coordination mode A2, H6, H13, H14 has never been suggested for the Aβ/Zn^{2+} complex. Thus we studied Aβ_{1-16} with two different coordination modes for CuDum (denoted as Aβ^{A2}_{1-16} and Aβ^{E11}_{1-16} in the main text) and only Aβ^{E11}_{1-16} for ZnDum. The NMR structure of the Aβ_{1-16}/Zn^{2+} complex in aqueous solution at pH 6.5 (PDB ID: 1ZE9)[19] was used for the initial coordinates of the MD simulations of Aβ^{E11}_{1-16}/ZnDum and Aβ^{E11}_{1-16}/CuDum, while the Aβ^{A2}_{1-16}/CuDum simulations were initiated from the QM/MM structure.[15] In either starting structure, the original metal ion was replaced by CuDum or ZnDum, and the ligating residues were allowed to choose their preferred dummy atom to interact with. In all simulations of Aβ_{1-16}, H6, H13 and H14 were modeled as neutral residues, considering that the pH values in the experiments were above the pK_a value of ~6.0 for the imidazole side chain in histidine. Furthermore, only with at least one of the nitrogens being deprotonated, histidine can coordinate to Cu^{2+} or Zn^{2+}. In the PDB structure 1ZE9, Nδ of H6, Nϵ of H13, and Nδ of H14 are coordinated to Zn^{2+}, which we adapted for our MD simulations of Aβ^{E11}_{1-16}/ZnDum and did not change during the simulations. To warrant comparibility, the assignment was the same for the Aβ_{1-16}/Cu^{2+} complexes.

CuZnSODs have been extensively studied by using crystallographic and spectroscopic techniques.[21–23] The enzymes are functional dimers with one copper and one zinc ion per

subunit. The metal sites play significant roles in the catalytic reaction. For the simulation of CuZnSOD the crystal structure from PDB entry 1HL5[21] with a resolution of 1.80 Å was used. This database entry includes nine dimer models (i.e., 18 subunits) and only subunit A of the first model was selected for our MD simulations. In CuZnSOD Cu^{2+} and Zn^{2+} are bridged by the imidazole ring of H63, which is doubly deprotonated (i.e., negatively charged) and acts as a ligand to both ions. Copper is coordinated by another three His residues (H46, H48 and H120) and a water molecule in a distorted square pyramidal geometry, while zinc is coordinated by two further His residues (H71 and H89) and an aspartic acid (D83) in a distorted tetrahedral geometry.[21] The coordinating His residues (apart from H63) are neutral with the protonation states of Nϵ and Nδ of the imidazole rings taken from the crystal structure.[21] This coordination geometry provides an excellent model to test if two different dummy ion models with two different coordination geometries can be applied together, what, to our knowledge, has not been attempted before.

For each test case (A$\beta^{\mathrm{A2}}_{1-16}$/CuDum, A$\beta^{\mathrm{E11}}_{1-16}$/CuDum, A$\beta^{\mathrm{E11}}_{1-16}$/ZnDum, and CuZnSOD/ZnDum/CuDum) we performed two independent 100-ns MD simulations to investigate the stability of the coordination geometry. In addition, we repeated all simulations using CuDum2 (for more details see below) instead of CuDum.

Results for the Zn^{2+} dummy model

Given the different functional forms of the LJ potential and combining rules in Q and GROMACS, the parameters of the orginal ZnDum model[24] that was used together with the SPC or TIP3P water models were first transformed: $\sigma_{\mathrm{ZnZn}} = (A_{\mathrm{Zn}}/B_{\mathrm{Zn}})^{\frac{1}{3}}$ and $\epsilon_{\mathrm{ZnZn}} = B^4_{\mathrm{Zn}}/4A^2_{\mathrm{Zn}}$. These transformations were used as initial parameters for ZnDum with TIP4P water, to be further optimized for their usage within GROMACS. First, bonds and angles originally defined between dummy atoms were removed so that a larger time step of up to 2 fs can be applied in MD simulations. Then the parameters were systematically optimized in oder to reproduce both the experimental ion-oxygen distance (Zn–O) and the hydration free energy

(ΔG_{hyd}) for Zn^{2+} in water. Previous studies[24–26] were able to simultaneously reproduce both quantities with good accuracy, while others reported that the simultaneous high-accuracy reproduction of both quantities is not obtainable.[27] Here, one has to consider the different simulation techniques applied in Q[28] and GROMACS.[3] In reference 24, spherical boundary conditions were used and a correction of infinite electrostatic interactions using the Born equation applied for the calculation of ΔG_{hyd}.[29] In the current study, periodic boundary conditions with dispersion correction as implemented in GROMACS are used. Furthermore, ΔG_{hyd} is calculated in two steps, decomposing it into the contributions from van der Waals (ΔG_{LJ}) and electrostatic (ΔG_{elec}) interactions[27,30,31] (Figure S1). Finally, Zn–O is determined independently from ΔG_{hyd} in a separate MD simulation.

We tested three different values for σ_{ZnO} (denoted as $\sigma_{\mathrm{ZnO}}^{\mathrm{low}}$, $\sigma_{\mathrm{ZnO}}^{\mathrm{middle}}$ and $\sigma_{\mathrm{ZnO}}^{\mathrm{high}}$) while keeping the other parameters identical (Table S1). With a decrease of σ_{ZnO}, ΔG_{elec} increases significantly while ΔG_{LJ} decreases only marginally. For $\sigma_{\mathrm{ZnO}}^{\mathrm{high}}$, Zn–O agrees exactly with the experimental distance (2.08 Å), but ΔG_{hyd} is ∼40 kcal/mol (8.3%) less than the experimental value (−483.3 kcal/mol).[32,33] For $\sigma_{\mathrm{ZnO}}^{\mathrm{low}}$, the calculated ΔG_{hyd} was quite close to the experimental value, but Zn–O is underestimated by 0.12 Å (5.8%) in this case. This behavior of ZnDum agrees to the findings of Merz and co-workers for divalent metal ions.[27] Nonetheless, with $\sigma_{\mathrm{ZnO}}^{\mathrm{middle}}$ we found a compromise as with this parameter setting Zn–O is only 0.06 Å smaller than the experimental distance and ΔG_{hyd} is underestimated by only 5.2% (∼ 25 kcal/mol) (Figure S2). Two 100-ns MD simulations were performed for $A\beta_{1-16}$ in complex with ZnDum using $\sigma_{\mathrm{ZnO}}^{\mathrm{middle}}$ to test its validity in a protein system. In this MD simulation the system is stable with root mean square deviations (RMSDs) of 1.34 Å and 0.52 Å for all backbone atoms and only the Zn^{2+}-ligating residues, respectively. Furthermore, the distances between Zn^{2+} and coordinated atoms agree well with the NMR results[19] (Table S2). Only the Zn–O distances for both carboxylate atoms of ligand residue E11 are underestimated by ∼0.17 Å due to the stronger electrostatic interactions between the positively charged dummy atoms and the negatively charged carboxylate group. ZnDum is able to maintain the metal binding site in a distorted square pyrimidal geometry (Figure 3a) in

accordance with the NMR structure (PDB ID: 1ZE9). A water molecule helps stabilize the coordination center and the non-bonded interactions between ZnDum and its environment are conserved (Table S3).

Results for the alternative Cu^{2+} dummy model

Despite the fact that all test runs were successful for CuDum, we considered another Cu^{2+} dummy model with larger charges for the axial dummy atoms. This allows for stronger electrostatic interactions between axial ligands and dummy atoms, which may become necessary in future studies of square pyramidal Cu^{2+} coordination geometries. To this end, a CuDum model with $q_{\mathrm{ax}} = 0.2$e and $q_{\mathrm{eq}} = 0.65$e (and keeping all other parameters as in Table 1) was included in our study. With this model, which is denoted CuDum2, we obtained satisfactory results for Cu^{2+} in water with $d^{\mathrm{eq}}_{\mathrm{Cu-O}} = 1.96$ Å and $d^{\mathrm{ax}}_{\mathrm{Cu-O}} = 2.18$ Å and $\Delta G_{\mathrm{hyd}} = -484.3$ kcal/mol (Figure S5). CuDum2 thus represents a compromise between sufficiently reproducing the Jahn-Teller effect while not underestimating the hydration free energy too much.

We repeated all MD simulations presented in the manuscript but using CuDum2 instead of CuDum. Like CuDum, CuDum2 produces stable Cu^{2+} binding sites during the MD simulations of the $A\beta_{1-16}/Cu^{2+}$ complex. The RMSD of the metal binding site fluctuates around 0.46 Å for $A\beta^{\mathrm{E11}}_{1-16}$/CuDum2 and is only ∼0.13 Å larger for $A\beta^{\mathrm{A2}}_{1-16}$/CuDum2. The comparison between CuDum and CuDum2 can be seen in the Table S8. The whole $A\beta_{1-16}$ peptide is quite flexible though to a lesser extent compared to $A\beta_{1-16}$ in complex with CuDum, which results from the larger charges on the axial dummy atoms. This leads to stronger interactions with the axial ligand (atom OE2 of E11) and decreased interactions with the equatorial ligands (H6, atom OE1 of E11, H13, 14), which is mirrored in the shortened axial distance and lengthened equatorial distances between metal center and ligands (Table S2). The Cu–O distance for the water molecule, that like with CuDum is coordinated at the opposite axial position, is also shorter for CuDum2. Nonetheless, the charge distribution for the dummy

atoms of CuDum2 allows the coordination center of A$\beta_{1-16}^{\mathrm{E11}}$/CuDum2 to be maintained in a distorted square pyramidal geometry (Figure S6a). Also the stabilization for the interaction between Aβ_{1-16} and metal center is considerably larger in A$\beta_{1-16}^{\mathrm{E11}}$/CuDum2 than in A$\beta_{1-16}^{\mathrm{E11}}$/ZnDum (Table S3), i.e., also CuDum2 is able to reproduce the higher affinity of Aβ for Cu^{2+} than for Zn^{2+}. In the simulations of A$\beta_{1-16}^{\mathrm{A2}}$/CuDum2, like with CuDum the four ligands prefer to interact with the equatorial dummy atoms (Figure S6b). CuDum2 is also able to maintain the square planar coordination geometry for binding mode A$\beta_{1-16}^{\mathrm{A2}}$, while water molecules coordinate to the two unoccupied axial dummy atoms. Again, CuDum2 produces slightly longer distances for the equatorial ligands A2, H6, H13, 14 and somewhat shorter Cu–water distances compared to CuDum (Table S4). According to the interaction energies (Table S5) the A$\beta_{1-16}^{\mathrm{A2}}$/CuDum2 complex is slightly less stable (by 5.5 kcal/mol) than A$\beta_{1-16}^{\mathrm{A2}}$/CuDum as a result of reduced electrostatic interactions between Aβ_{1-16} and the ligands. For both CuDum and CuDum2 the electrostatic interactions between Aβ_{1-16} and ligands is the dominating contribution to the complex stability. In summary, also CuDum2 works well for modeling metal binding to Aβ_{1-16}. Moreover, from 100-ns MD simulations of CuZnSOD where CuDum2 replaced CuDum, we obtained similar results as before (Tables S7 and S8, Figure S6c). The similarity of the results for CuDum and CuDum2 emphasizes the robustness of our approach for the Cu^{2+} dummy model. Nonetheless, CuDum is our preferred model as it better reproduces the Jahn-Teller effect and ΔG_{hyd} for Cu^{2+} in water.

Supplementary tables

Table S1: Force field parameters for the dummy model of Zn^{2+} (ZnDum) used in this work.

bond type	b_0 (Å)		K_b (kcal/mol Å^2)	
Zn–D	0.900		800.0	
angle type	θ_0 (degree)		K_θ (kcal/mol rad^2)	
D_i–Zn–D_i	180.0		250.0	
D_i–Zn–D_j	90.0		250.0	
atom type	mass	charge (e)	σ_{ZnO} (Å)	ϵ_{ZnO} (kcal/mol)
Zn	47.370	−1.00	2.088 (high)	4.2386
Zn	47.370	−1.00	2.034 (middle)	4.2386
Zn	47.370	−1.00	1.957 (low)	4.2386
D	3.000	0.50	$\sigma_D = 0$	$\epsilon_D = 0$

Dummy atoms are denoted by D with D_i being either D_{eq} or D_{ax}.
The bond potential is $U_b = K_b(b - b_0)^2$, the angle potential $U_\theta = K_\theta(\theta - \theta_0)^2$.

Table S2: Interatomic distances between metal ions (M) and ligands of Aβ_{1-16} (H6, E11, H13 and H14) obtained from MD simulations.

Distance	Aβ_{1-16}/ZnDum (Å) calculated	Aβ_{1-16}/ZnDum (Å) experimental	Aβ_{1-16}/CuDum (Å)	Aβ_{1-16}/CuDum2 (Å)
M–ND1$^{\mathrm{H6}}$	2.15±0.05	2.11	2.05±0.04	2.07±0.04
M–OE1$^{\mathrm{E11}}$	1.94±0.03	2.11	1.84±0.02	1.86±0.03
M–OE2$^{\mathrm{E11}}$	1.94±0.03	2.11	2.18±0.07	2.11±0.06
M–NE2$^{\mathrm{H13}}$	2.19±0.07	2.15	2.08±0.04	2.10±0.05
M–NE2$^{\mathrm{H14}}$	2.11±0.05	2.29	2.03±0.04	2.05±0.04
M–O^{wat}	2.16±0.04	–	2.28±0.09	2.20±0.07

Table S3: Nonbonded interaction energies in the A$\beta^{\mathrm{E11}}_{1-16}$/M systems (M = CuDum(2) or ZnDum) obtained from MD simulations.

Interaction	Aβ_{1-16}/ZnDum	Aβ_{1-16}/CuDum	Aβ_{1-16}/CuDum2
Coulomb: M–Aβ_{1-16}	−329.2±8.3	−408.1±9.6	−385.1±9.2
LJ: M–Aβ_{1-16}	−17.9±4.1	−0.6±5.8	−6.3±5.2
Coulomb: M–water	−64.1±5.1	−30.8±5.2	−37.1±5.2
LJ: M–water	−0.9±2.1	−5.4±0.4	−5.0±0.7
Total:	−412.1	−444.9	−433.5

Table S4: Interatomic distances between Cu^{2+} and ligands of Aβ_{1-16} (A2, H6, H13 and H14) obtained from MD simulations.

Distance	CuDum (Å)	CuDum2 (Å)	QM
Cu^{2+}–O^{A2}	1.94±0.03	1.95±0.03	2.00
Cu^{2+}–$NE2^{H6}$	2.03±0.04	2.05±0.04	1.98
Cu^{2+}–$ND1^{H13}$	2.03±0.04	2.05±0.04	2.03
Cu^{2+}–$NE2^{H14}$	2.03±0.04	2.05±0.04	1.97
Cu^{2+}–O^{wat1}	2.28±0.08	2.20±0.07	–
Cu^{2+}–O^{wat2}	2.25±0.08	2.18±0.06	–

Table S5: Nonbonded interaction energies in the Aβ^{A2}_{1-16}/CuDum(2) systems obtained from MD simulations.

Interaction	CuDum (kcal/mol)	CuDum2 (kcal/mol)
Coulomb: Cu–Aβ_{1-16}	−296.1±7.7	−272.9±7.4
LJ: Cu–Aβ_{1-16}	−3.5±4.8	−8.2±4.3
Coulomb: Cu–water	−66.9±4.3	−80.2±4.4
LJ: Cu–water	−9.2±0.6	−8.3±1.0
Total:	−375.1	−369.6

Table S6: Interatomic distances in CuZnSOD obtained from MD simulations with CuDum.

Distance	Distance (Å)		Distance	Distance (Å)	
	calculated	experimental		calculated	experimental
Zn^{2+}–$ND1^{H63}$	2.14±0.05	2.02	Cu^{2+}–O^{H46}	2.33±0.13	–
Zn^{2+}–$ND1^{H71}$	2.21±0.07	1.99	Cu^{2+}–$ND1^{H46}$	2.03±0.03	2.14
Zn^{2+}–$ND1^{H80}$	2.10±0.05	2.00	Cu^{2+}–$NE2^{H48}$	2.03±0.04	2.13
Zn^{2+}–O^{G82}	2.13±0.15	–	Cu^{2+}–$NE2^{H63}$	1.98±0.03	2.46
Zn^{2+}–$OD1^{D83}$	1.95±0.03	1.90	Cu^{2+}–$NE2^{H120}$	2.05±0.04	2.12
Zn^{2+}–$OD2^{D83}$	1.94±0.03	2.83	Cu^{2+}–O^{wat}	2.35±0.11	2.65
Zn^{2+}–Cu^{2+}	5.84±0.10	6.36	–	–	–

Table S7: Interatomic distances in CuZnSOD calculated from MD simulations with CuDum2.

Distance	Distance (Å)		Distance	Distance (Å)	
	calculated	experimental		calculated	experimental
Zn^{2+}–$ND1^{H63}$	2.13 ± 0.05	2.02	Cu^{2+}–O^{H46}	2.29 ± 0.13	–
Zn^{2+}–$ND1^{H71}$	2.23 ± 0.08	1.99	Cu^{2+}–$ND1^{H46}$	2.05 ± 0.04	2.14
Zn^{2+}–$ND1^{H80}$	2.09 ± 0.05	2.00	Cu^{2+}–$NE2^{H48}$	2.05 ± 0.04	2.13
Zn^{2+}–O^{G82}	2.13 ± 0.09	–	Cu^{2+}–$NE2^{H63}$	2.00 ± 0.03	2.46
Zn^{2+}–$OD1^{D83}$	1.94 ± 0.03	1.90	Cu^{2+}–$NE2^{H120}$	2.08 ± 0.04	2.12
Zn^{2+}–$OD2^{D83}$	1.94 ± 0.03	2.83	Cu^{2+}–O^{wat}	2.25 ± 0.08	2.65
Zn^{2+}–Cu^{2+}	5.87 ± 0.10	6.36	–	–	–

Table S8: Time averages of the RMSDs of the protein backbone atoms and of the metal binding sites of Aβ_{1-16} and CuZnSOD

System	backbone (Å)	metal site (Å)
Aβ^{E11}_{1-16}/ZnDum	1.34±0.39	0.52±0.08
Aβ^{E11}_{1-16}/CuDum	1.26±0.43	0.42±0.11
Aβ^{E11}_{1-16}/CuDum2	1.09±0.45	0.46±0.12
Aβ^{A2}_{1-16}/CuDum	2.64±0.49	0.67±0.11
Aβ^{A2}_{1-16}/CuDum2	1.73±0.83	0.53±0.11
CuZnSOD/ZnDum/CuDum	1.54±0.16	0.71±0.03
CuZnSOD/ZnDum/CuDum2	1.56±0.12	0.81±0.04

Supplementary figures

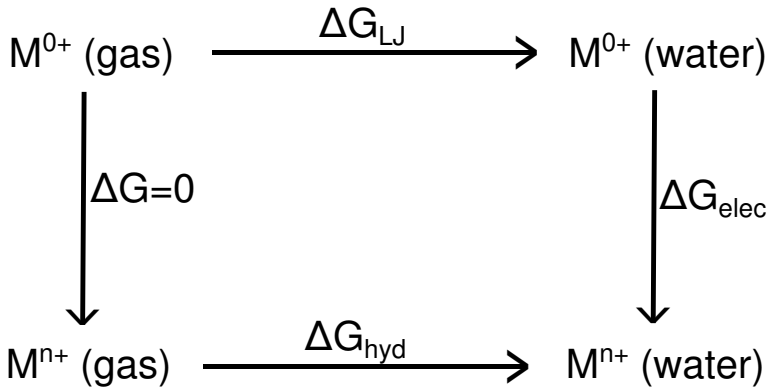

Figure S1: Thermodynamic cycle for the calculation of the hydration free energy, ΔG_{hyd}, which is the sum of ΔG_{LJ} and ΔG_{elec}.

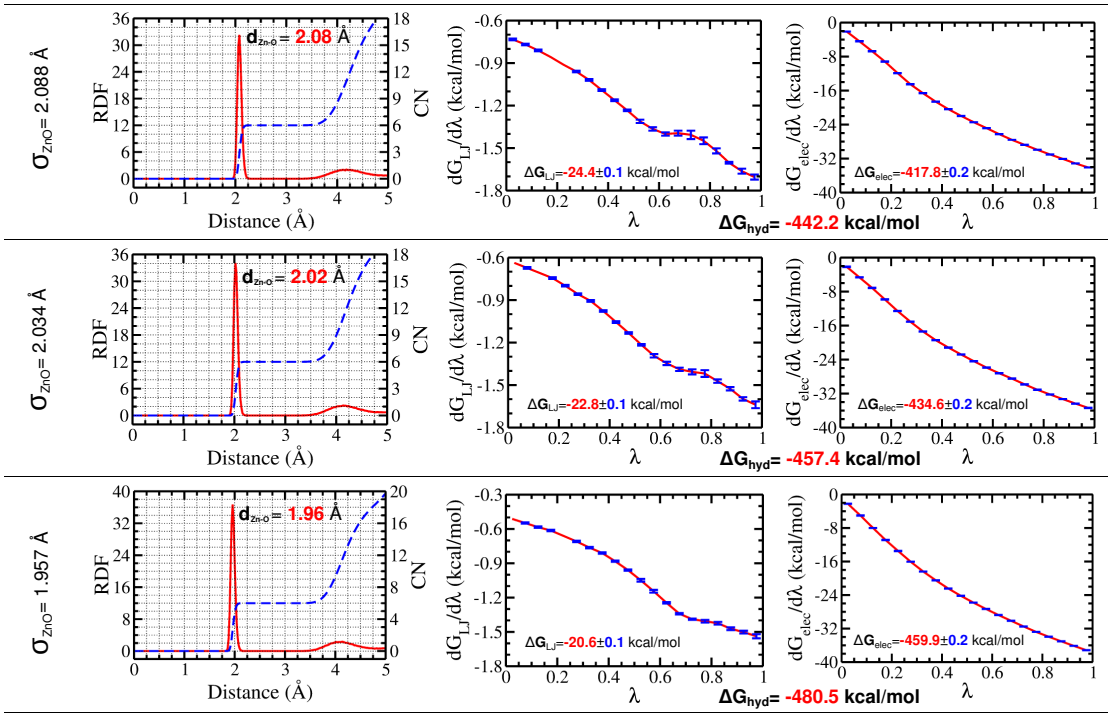

Figure S2: Radial distribution function (RDF, red), coordination number (CN, blue) and $\Delta G_{\mathrm{hyd}} = \Delta G_{\mathrm{LJ}} + \Delta G_{\mathrm{elec}}$ for Zn^{2+} dummy models in water. ΔG_{LJ} and ΔG_{elec} are calculated by summing over the 21 intermediate states ranging from λ=0 and λ=1 applying Eq. S7. Results are shown for $\sigma_{\mathrm{ZnO}}^{\mathrm{high}}$ (top), $\sigma_{\mathrm{ZnO}}^{\mathrm{middle}}$ (middle) and $\sigma_{\mathrm{ZnO}}^{\mathrm{low}}$ (bottom). $\sigma_{\mathrm{ZnO}}^{\mathrm{middle}}$ produces the best results and was thus chosen for the ZnDum model considered in this study. The experimental values are: $d_{\mathrm{Zn-O}} = 2.08$ Å and $\Delta G_{\mathrm{hyd}} = -483.3$ kcal/mol.

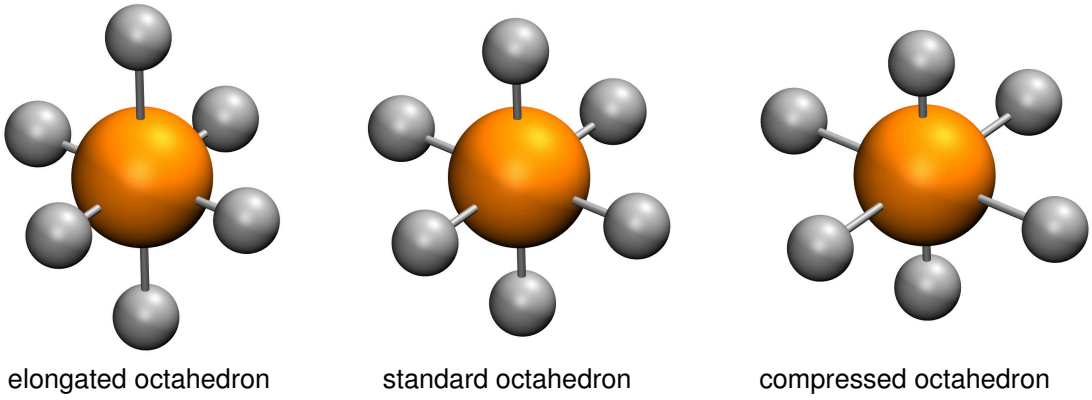

Figure S3: Three different octahedral geometries which were tested in the process of parameterization of CuDum.

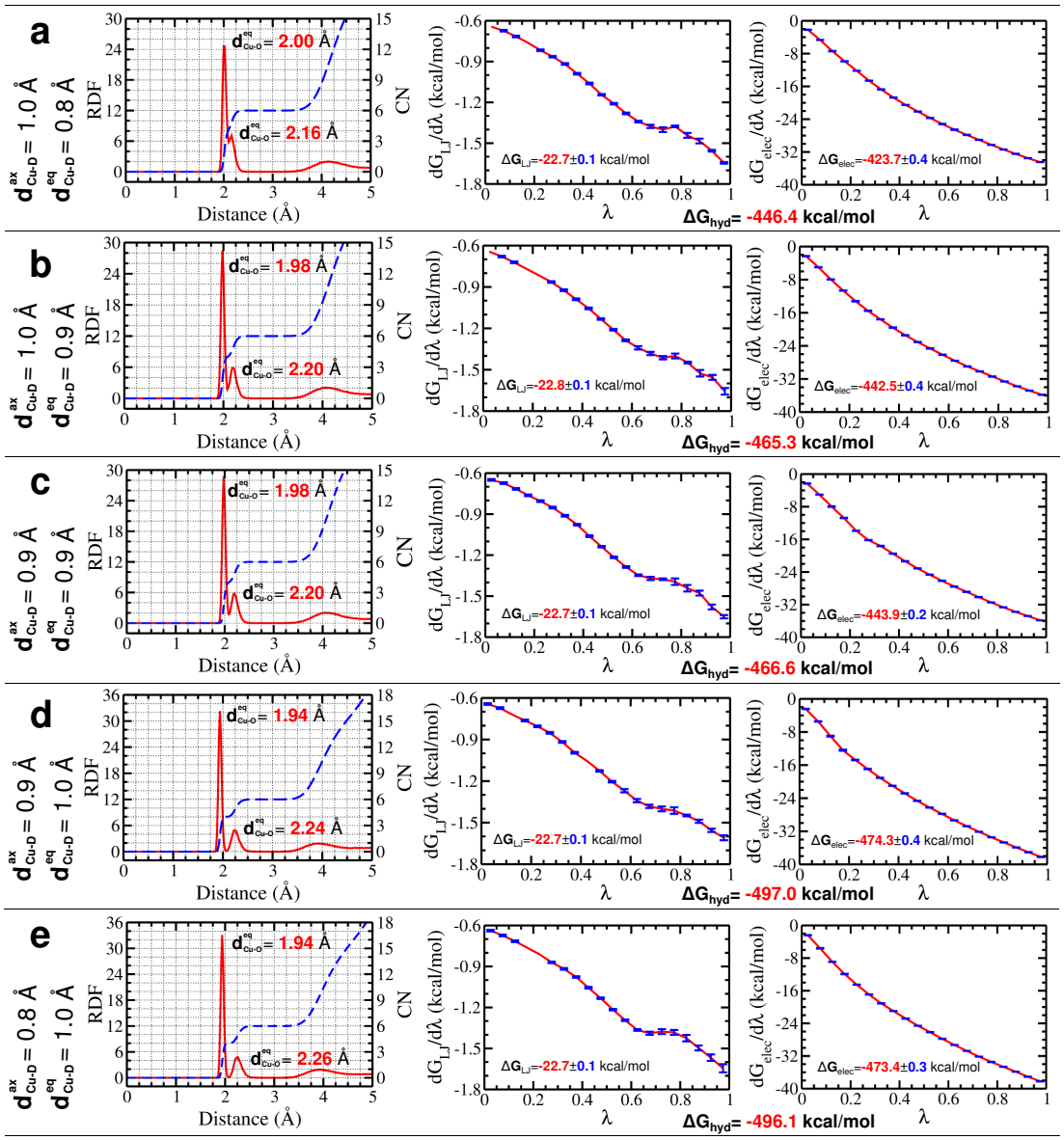

Figure S4: Radial distribution function (RDF, red), coordination number (CN, blue) and $\Delta G_{\mathrm{hyd}} = \Delta G_{\mathrm{LJ}} + \Delta G_{\mathrm{elec}}$ for Cu^{2+} dummy models in water. ΔG_{LJ} and ΔG_{elec} are calculated by summing over the 21 intermediate states ranging from λ=0 and λ=1 applying Eq. S7. Results are shown for different octahedral geometries. The charge distribution was kept constant with axial charges $q_{\mathrm{ax}} = 0.05$e and equatorial charges $q_{\mathrm{eq}} = 0.725$e. Two elongated (a) and (b), the regular (c), and two compressed (d) and (e) octahedra were tested. The compressed octahedron with 1.0 Å for Cu–D_{eq} and 0.8 Å for Cu–D_{ax} produces the best results and was thus chosen for the CuDum model considered in this study. The experimental values are: $d^{\mathrm{eq}}_{\mathrm{Cu-O}} = 1.96$ Å, $d^{\mathrm{ax}}_{\mathrm{Cu-O}} = 2.28$ Å and $\Delta G_{\mathrm{hyd}} = -496.16$ kcal/mol.

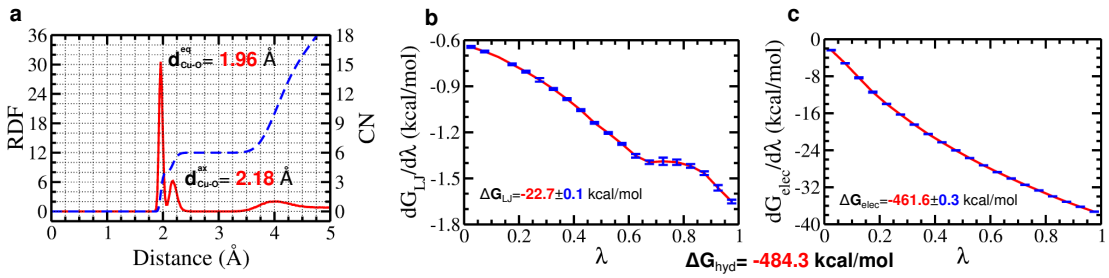

Figure S5: The Jahn-Teller effect and ΔG_{hyd} for CuDum2 in water. (a) Radial distribution function (red, left y axis) and coordination number (blue, right y axis) for water around CuDum2. The free energy contributions $\mathrm{d}G_{\text{LJ}}/d\lambda$ (b) and $\mathrm{d}G_{\text{elec}}/\lambda$ (c) as a function of the coupling parameter λ. ΔG_{LJ} and ΔG_{elec} are calculated by summing over the 21 intermediate states ranging from λ=0 and λ=1 applying Eq. S7. The experimental values are: $d^{\text{eq}}_{\text{Cu-O}} = 1.96$ Å, $d^{\text{ax}}_{\text{Cu-O}} = 2.28$ Å and $\Delta G_{\text{hyd}} = -496.16$ kcal/mol.

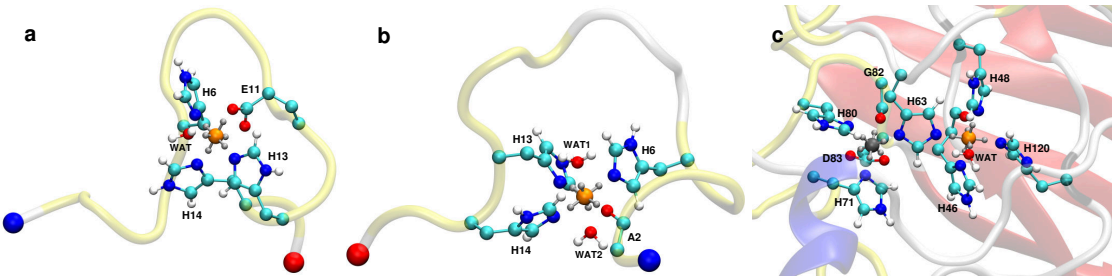

Figure S6: The final snapshots of CuDum2 in protein systems taken from 100-ns MD simulations of (a) $\text{A}\beta^{\text{E11}}_{1-16}$/CuDum2, (b) $\text{A}\beta^{\text{A2}}_{1-16}$/CuDum2, and (c) CuZnSOD/ZnDum/CuDum2. The proteins are shown in cartoon presentation and colored red for β-sheet, purple for 3_{10} helix, yellow for turn, and white for coil. The N- and C-terminus of $\text{A}\beta_{1-16}$ is indicated by a blue and red bead, respectively. The metal binding sites are shown in Corey-Pauling-Koltun (CPK) presentation using turque for C, blue for N, red for O and white for H atoms while Zn^{2+} is shown in grey and Cu^{2+} in orange.

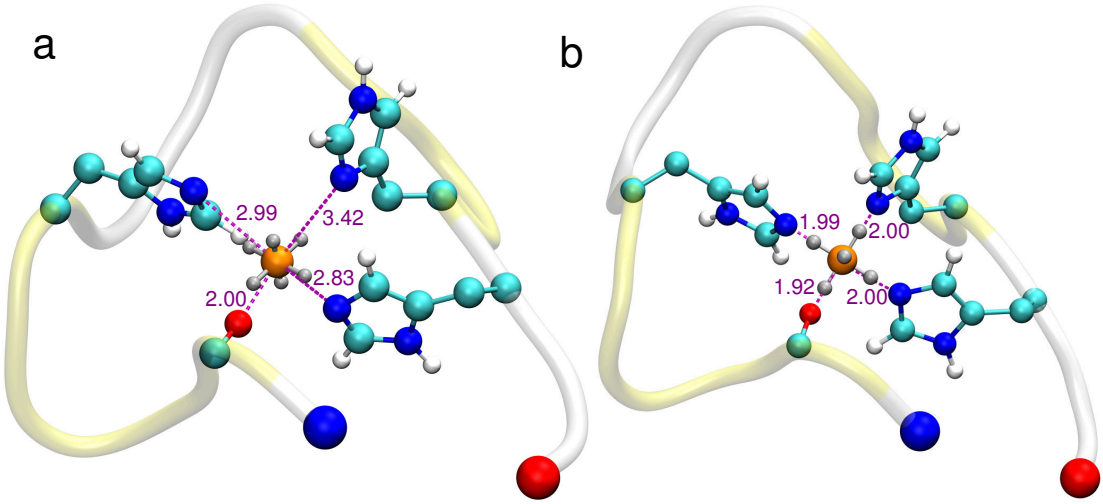

Figure S7: Recovery of the square planar Cu^{2+} geometry for $A\beta^{A2}_{1-16}$/CuDum after distorting the metal binding site. (a) In the distorted structure the His residues have been moved away and also rotated. (b) Energy minimization recovers the square planar binding site with the Cu^{2+}–ligand distances (in Å) being close to the average equilibrium distances (Table S4). For coloring explanation see Figure S6.

References

(1) Jorgensen, W. L.; Maxwell, D. S.; Tirado-Rives, J. Development and Testing of the OPLS All-Atom Force Field on Conformational Energetics and Properties of Organic Liquids. *J. Am. Chem. Soc.* **1996**, *118*, 11225–11236.

(2) Kaminski, G. A.; Friesner, R. A.; Tirado-Rives, J.; Jorgensen, W. L. Evaluation and Reparametrization of the OPLS-AA Force Field for Proteins via Comparison with Accurate Quantum Chemical Calculations on Peptides. *J. Phys. Chem. B* **2001**, *105*, 6474–6487.

(3) Hess, B.; Kutzner, C.; van der Spoel, D.; Lindahl, E. GROMACS 4: Algorithms for Highly Efficient, Load-Balanced, and Scalable Molecular Simulation. *J. Chem. Theory Comput.* **2008**, *4*, 435–447.

(4) Bennett, C. H. Efficient Estimation of Free Energy Differences from Monte Carlo Data. *J. Comput. Phys.* **1976**, *22*, 245–268.

(5) de Ruiter, A.; Boresch, S.; Oostenbrink, C. Comparison of Thermodynamic Integration and Bennett Acceptance Ratio for Calculating Relative Protein-Ligand Binding Free Energies. *J. Comput. Chem.* **2013**, *34*, 1024–1034.

(6) Beutler, T. C.; Mark, A. E.; van Schaik, R. C.; Gerber, P. R.; van Gunsteren, W. F. Avoiding Singularities and Numerical Instabilities in Free Energy Calculations Based on Molecular Simulations. *Chem. Phys. Lett.* **1994**, *222*, 529–539.

(7) Liu, H.; Mark, A. E.; van Gunsteren, W. F. Estimating the Relative Free Energy of Different Molecular States with Respect to a Single Reference State. *J. Phys. Chem.* **1996**, *100*, 9485–9494.

(8) Shirts, M. R.; Pande, V. S. Solvation Free Energies of Amino Acid Side Chain Analogs for Common Molecular Mechanics Water Models. *J. Chem. Phys.* **2005**, *122*, 134508.

(9) Jorgensen, W. L.; Chandrasekhar, J.; Madura, J. D.; Impey, R. W.; Klein, M. L. Comparison of Simple Potential Functions for Simulating Liquid Water. *J. Chem. Phys.* **1983**, *79*, 926–935.

(10) Darden, T.; York, D.; Pedersen, L. Particle Mesh Ewald: An N·log(N) Method for Ewald Sums in Large Systems. *J. Chem. Phys.* **1993**, *98*, 10089.

(11) Essmann, U.; Perera, L.; Berkowitz, M. L.; Darden, T.; Lee, H.; Pedersen, L. G. A Smooth Particle Mesh Ewald Method. *J. Chem. Phys.* **1995**, *103*, 8577–8593.

(12) Parrinello, M.; Rahman, A. Polymorphic Transitions in Single Crystals: A New Molecular Dynamics Method. *J. Appl. Phys.* **1981**, *52*, 7182–7190.

(13) Hess, B.; Bekker, H.; Berendsen, H. J. C.; Fraaije, J. G. E. M. LINCS: A Linear Constraint Solver for Molecular Simulations. *J. Comput. Chem.* **1997**, *18*, 1463–1472.

(14) Hess, B. P-LINCS: A Parallel Linear Constraint Solver for Molecular Simulation. *J. Chem. Theory Comput.* **2008**, *4*, 116–122.

(15) Alí-Torres, J.; Maréchal, J.-D.; Rodríguez-Santiago, L.; Sodupe, M. Three Dimensional Models of Cu^{2+}-Aβ(1-16) Complexes from Computational Approaches. *J. Am. Chem. Soc.* **2011**, *133*, 15008–15014.

(16) Drew, S. C.; Masters, C. L.; Barnham, K. J. Alanine-2 Carbonyl is an Oxygen Ligand in Cu^{2+} Coordination of Alzheimer's Disease Amyloid-β Peptide–Relevance to N-Terminally Truncated Forms. *J. Am. Chem. Soc.* **2009**, *131*, 8760–8761.

(17) Drew, S. C.; Barnham, K. J. The Heterogeneous Nature of Cu^{2+} Interactions with Alzheimer's Amyloid-β Peptide. *Acc. Chem. Res.* **2011**, *44*, 1146–1155.

(18) Faller, P.; Hureau, C. Bioinorganic Chemistry of Copper and Zinc Ions Coordinated to Amyloid-β Peptide. *Dalton Trans.* **2009**, *21*, 1080–1094.

(19) Zirah, S.; Kozin, S. A.; Mazur, A. K.; Blond, A.; Cheminant, M.; Ségalas-Milazzo, I.; Debey, P.; Rebuffat, S. Structural Changes of Region 1-16 of the Alzheimer Disease Amyloid β-Peptide upon Zinc Binding and in Vitro Aging. *J. Biol. Chem.* **2006**, *281*, 2151–2161.

(20) Streltsov, V. A.; Titmuss, S. J.; Epa, V. C.; Barnham, K. J.; Masters, C. L.; Varghese, J. N. The Structure of the Amyloid-β Peptide High-Affinity Copper (II) Binding Site in Alzheimer Disease. *Biophys. J.* **2008**, *95*, 3447–3456.

(21) Strange, R. W.; Antonyuk, S.; Hough, M. A.; Doucette, P. A.; Rodriguez, J. A.; Hart, P.; Hayward, L. J.; Valentine, J. S.; Hasnain, S. The Structure of Holo and Metal-Deficient Wild-type Human Cu, Zn Superoxide Dismutase and its Relevance to Familial Amyotrophic Lateral Sclerosis. *J. Mol. Biol.* **2003**, *328*, 877–891.

(22) Hough, M. A.; Hasnain, S. Crystallographic Structures of Bovine Copper-Zinc Superoxide Dismutase Reveal Asymmetry in Two Subunits: Functionally Important Three and Five Coordinate Copper Sites Captured in the Same Crystal. *J. Mol. Biol.* **1999**, *287*, 579–592.

(23) Hough, M. A.; Strange, R. W.; Hasnain, S. Conformational Variability of the Cu Site in One Subunit of Bovine CuZn Superoxide Dismutase: the Importance of Mobility in the Glu119-Leu142 Loop Region for Catalytic Function. *J. Mol. Biol.* **2000**, *304*, 231–241.

(24) Duarte, F.; Bauer, P.; Barrozo, A.; Amrein, B. A.; Purg, M.; Åqvist, J.; Kamerlin, S. C. L. Force Field Independent Metal Parameters Using a Nonbonded Dummy Model. *J. Phys. Chem. B* **2014**, *118*, 4351–4362.

(25) Åqvist, J.; Warshel, A. Free Energy Relationships in Metalloenzyme-Catalyzed Reactions. Calculations of the Effects of Metal Ion Substitutions in Staphylococcal Nuclease. *J. Am. Chem. Soc.* **1990**, *112*, 2860–2868.

(26) Åqvist, J.; Warshel, A. Computer Simulation of the Initial Proton Transfer Step in Human Carbonic Anhydrase I. *J. Mol. Biol.* **1992**, *224*, 7–14.

(27) Li, P.; Roberts, B. P.; Chakravorty, D. K.; Merz, K. M. Rational Design of Particle Mesh Ewald Compatible Lennard-Jones Parameters for +2 Metal Cations in Explicit Solvent. *J. Chem. Theory Comput.* **2013**, *9*, 2733–2748.

(28) Marelius, J.; Kolmodin, K.; Feierberg, I.; Åqvist, J. Q: A Molecular Dynamics Program for Free Energy Calculations and Empirical Valence Bond Simulations in Biomolecular Systems. *J. Mol. Graph. Model.* **1998**, *16*, 213–225.

(29) Carlsson, J.; Åqvist, J. Absolute Hydration Entropies of Alkali Metal Ions from Molecular Dynamics Simulations. *J. Phys. Chem. B* **2009**, *113*, 10255–10260.

(30) Li, X.; Tu, Y.; Tian, H.; Ågren, H. Computer Simulations of Aqua Metal Ions for Accurate Reproduction of Hydration Free Energies and Structures. *J. Chem. Phys.* **2010**, *132*, 104505.

(31) Li, P.; Merz, K. M. Taking into Account the Ion-Induced Dipole Interaction in the Nonbonded Model of Ions. *J. Chem. Theory Comput.* **2014**, *10*, 289–297.

(32) Noyes, R. M. Thermodynamics of Ion Hydration as a Measure of Effective Dielectric Properties of Water. *J. Am. Chem. Soc.* **1962**, *84*, 513–522.

(33) Rosseinsky, D. R. Electrode Potentials and Hydration Energies. Theories and Correlations. *Chem. Rev.* **1965**, *65*, 467–490.

4.3 The role of Cu^{2+} in the dimerization of Aβ_{1-42} studied by Hamiltonian replica exchange molecular dynamics simulations

The role of Cu^{2+} in the dimerization of $A\beta_{1-42}$ studied by Hamiltonian replica exchange molecular dynamics simulations

Qinghua Liao
Institute of Complex Systems: Structural Biochemistry (ICS-6),
Forschungszentrum Jülich GmbH,
52425 Jülich, Germany

Birgit Strodel*
Institute of Complex Systems: Structural Biochemistry (ICS-6),
Forschungszentrum Jülich GmbH,
52425 Jülich, Germany

Institute of Theoretical and Computational Chemistry,
Heinrich Heine University Düsseldorf, 40225 Düsseldorf, Germany

*Corresponding Author: b.strodel@fz-juelich.de

1 Introduction

Alzheimer's disease (AD) is the most common form of dementia and a progressive irreversible neurodegenerative disorder, which results in neuronal dysfunction, cognitive disability and finally death [1–3]. It is characterized by the abnormal deposition of extracellular senile plaques, of which the primary component is amyloid-β (Aβ) peptides ranging from 39 to 43 residues. The Aβ peptides are cleaved from the amyloid precursor protein (APP) by β- and γ-secretase, and the 40-residue (Aβ_{1-40}) and 42-residue (Aβ_{1-42}) peptides are the most two prevalent alloforms found in plaques [3]. With two additional residues Ile41-Ala42, Aβ_{1-42} is reported to be more toxic than Aβ_{1-40} *in vitro* [4] and *in vivo* [5]. The Aβ monomers are mostly determined to be random coil in physiological buffer, but readily aggregate to form fibrils with a cross-β-sheet pattern. There is strong evidence suggesting that the small-size oligomers rather than mature fibrils are the most neurotoxic species [6, 7].

Thus, it is essential to characterize the Aβ dimer and small-size oligomers for understanding the first stage of Aβ aggregation. Because of the high aggregation propensity of Aβ, only low-resolution experimental data on the dimers and oligomers is available [8]. Using a combination of different experimental techniques (CD spectroscopy, Thioflavin T fluorescence, atomic force microscopy (AFM) *etc.*), Teplow *et al.* [9] reported that the Aβ oligomers exhibit an order-dependent increase in β-strand content, and thus suggested that dimerization and subsequent monomer addition were processes in which significant and asymmetric monomer conformational changes occur. Walsh *et al.* [10] have confirmed the potential synaptotoxicity of the Aβ dimer *in vivo*. Recently, Aβ dimers isolated directly from Alzheimer's brains have been suggested to be the smallest synaptotoxic species that damage the synaptic plasticity and memory [11]. A collision cross section (CCS) of 1256 Å^2 for Aβ_{1-42} dimers was reported by Bernstein *et al.* [12] using ion-mobility mass spectrometry. However, it is still extremely difficult to determine high resolution structures for the Aβ oligomers because of the fast rate of aggregation in aqueous solution.

Molecular dynamics (MD) simulations have been extensively applied to study the conformational dynamics of Aβ_{1-40} and Aβ_{1-42} monomers at atomistic level in explicit solvents [13–16], more details were reviewed by Nasica-Labouze *et al.* [17]. Several MD simulations have been performed on Aβ_{1-40} and Aβ_{1-42} dimers using various coarse-grained (CG) models [18–20] and all-atom force fields with explicit solvents [20–25]. Moreover, the Aβ_{1-42} dimer was also studied by all-atom Monte Carlo simulations with an implicit solvent model [26, 27]. It has been suggested that the interface of Aβ_{1-42} dimer primarily consists of the central hydrophobic core (CHC, Leu17-Ala21) and the C-terminal hydrophobic region (CHT, Gly29-Ala42) with predominant inter-chain contacts of CHC-CHC, CHT-CHT

and CHC-CHT, though the contact probabilities vary depending on the force fields and the sampling approaches applied [19,20,22,24,27]. Similar binding interfaces were also reported by other simulations of larger Aβ oligomers [28–30]. Furthermore, the β-strand content was mainly sampled at the CHC and CHT regions [20,22–24], though much higher probabilities of β-strand was also found at the N-terminal region in the study of Mousseau *et al.* [19].

Metal ions such as Cu^{2+} and Zn^{2+} have been indicated to be involved in the Aβ aggregation and toxicity [31,32] as high concentrations of these ions were found in senile plaques composed of the Aβ peptides. A lot of studies with experimental [33–39] and theoretical [13, 40–42] techniques have been performed to investigate the coordination chemistry of Cu^{2+} with Aβ monomers. Currently, the coordination modes for Cu^{2+} binding the Aβ monomers as suggested by Drew *et al.* [38,39] and Faller *et al.* [43–45] are mostly accepted though contradicting results exist [31, 32, 46, 47]. Fewer studies have focused on the coordination chemistry of Cu^{2+} and Aβ oligomers and its roles involved in the aggregation of Aβ. Three aggregation pathways have been proposed for the Cu^{2+}-induced Aβ aggregation based on different Cu^{2+}:Aβ ratios [48,49]. An Aβ dimer with Cu^{2+} acting as a bridge like Aβ–Cu^{2+}–Aβ was thought to be significantly involved in the Cu-induced Aβ aggregation [50]. Similarly, an Aβ_{1-42} dimer bridged by a Cu^{2+} was also determined by Hane *et al.* [51] using single molecule atomic force spectroscopy (AFS) in combination with atomic force microscopy (AFM). It was suggested that Cu^{2+} affects the Aβ_{1-42} aggregation by increasing the binding force between the peptides. However, such Aβ–Cu^{2+}–Aβ dimers were reported to be unlikely by other studies [52]. Cu^{2+} may promote the formation of a four-coordinate Aβ dimer with a pair of His13 and His14 from two jacent Aβ monomers, which may act as a "seed" in the process of Aβ aggregation [53]. A molecular modelling study also suggested such a coordination mode for Cu^{2+} [54], and it was also reported for Zn^{2+} based on *in vitro* experiments [55]. There are some experimental structures of Aβ_{1-40}/Cu^{2+} oligomers, which exhibit well-ordered β-sheet motifs [56, 57]. However, the mechanism by which Cu^{2+} modulates the aggregation of Aβ is still missing, nor is the initialization of Aβ dimer formation involving Cu^{2+} known.

In order to investigate the roles of Cu^{2+} in Aβ_{1-42} dimerization, we performed extensive Hamiltonian replica exchange molecular dynamics (H-REMD) simulations of the Aβ_{1-42} dimer in explicit solvent with and without the presence of Cu^{2+}. In the complex of 2Aβ_{1-42}/Cu^{2+}, Cu^{2+} is coordinated by a pair of His13 and His14 from the two Aβ_{1-42} monomers, as suggested by Yeung and Axelsen [53]. Both a bonded model and a nonbonded, so-called dummy model [58], were applied to describe the interactions between Cu^{2+} and Aβ_{1-42}. Our H-REMD simulations suggest that Cu^{2+} greatly promotes the formation of β-sheet at the C-terminal regions of Aβ_{1-42}.

2 Methods

2.1 Structural Model

The initial structure of the Aβ_{1-42} dimer in complex with Cu^{2+} (2Aβ_{1-42}/Cu^{2+}) was constructed by homology modeling with distance restraints at the Cu^{2+} coordination center, one Cu^{2+} coordinated by four His residues [53]. The template was created by putting two Aβ_{1-42} monomers (PDB ID: 1Z0Q [59]) parallel at a distance of 5.5 Å. The distance restraints were based on the optimized model of Cu^{2+} coordinated with 4 imidazole rings at the B3LYP/def2-TZVP level [60–63] with D3 dispersion correction [64], as highlighted in Figure 1. Modeller v9.11 [65] was used to do the homology modelling, 100 models were generated, and the best one (Figure 1) was chosen based on the assessment by DOPE [66] and GA341 [67, 68] scores. Removing Cu^{2+} in the complex 2Aβ_{1-42}/Cu^{2+} leads to the Aβ_{1-42} dimer without Cu^{2+}, (2Aβ_{1-42}), which was simulated for comparison.

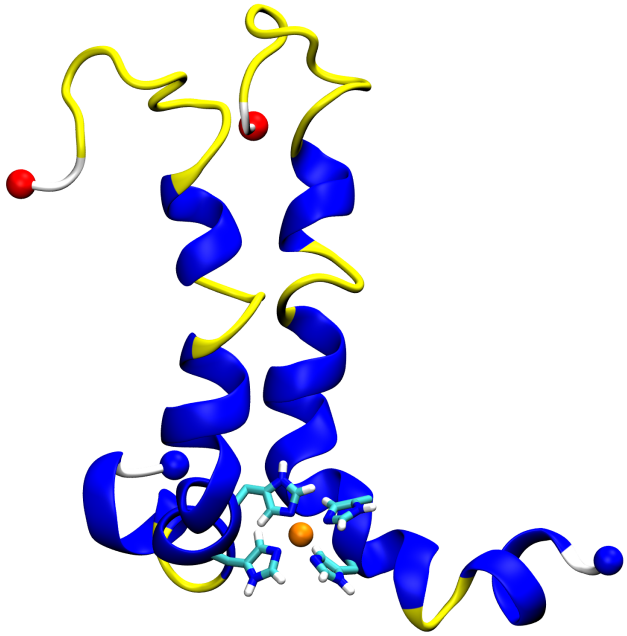

Figure 1: The initial structure of the Aβ_{1-42} dimer in complex with Cu^{2+} is shown in new cartoon, and the Cu^{2+} binding residues are shown in Corey-Pauling-Koltun (CPK) and coloured by chemical elements: cyan for carbon (C), blue for nitrogen (N), red for oxygen (O), white for hydrogen (H) and orange for Cu^{2+} atoms. The peptide color is based on secondary structure: blue for α-helix, yellow for turn and white for coil structures. The N- and C-termini are represented by blue and red beads, respectively.

2.2 Parameterization of Cu^{2+}-Aβ interactions

In this study, both a bonded and a dummy [58] models were used for Cu^{2+} binding to Aβ_{1-42}. The bonded model defines bonds, angles and torsions between the metal ion and its ligands, and van der Waals and electrostatic interactions between metal ion and ligands are added to the force field. This model has been widely used to study the interactions between metal ions and proteins [69–71]. This method attempts to define both the correct binding geometry and the correct electrostatic representation of the metal active site because simply assigning a plus two formal charge to a divalent metal ion would not describe the reality of the electronic structure of a metal ion/ligand complex [72]. The OPLS-AA/L [73,74] force field parameters for the bonded plus electrostatics model for the $(A\beta_{1-42})_2/Cu^{2+}$ complex were derived based on the calculations using QM methods. It has been shown that OPLS-AA/L produces results for Aβ in terms of helical and β-strand contents, calculated NMR J-coupling constants and chemical shifts, and radii of gyration that agree well with experimental data [75,76]. Other force fields (e.g., AMBER03, CHARMM22/CMAP) produce Aβ structures in conflict with experimental findings [75,76]. The functional form of OPLS/AA-L is given by [74]:

$$\begin{aligned} E_{MM} = & \sum_{bonds} K_r(r - r_{\text{eq}})^2 + \sum_{angles} K_\Theta(\Theta - \Theta_{\text{eq}})^2 + \\ & \sum_{dihedrals} \sum_{n=1}^{3} \frac{V_n}{2} \left[1 + \cos(n\phi)\right] + \\ & \sum_{i<j} f_{ij} \left[\frac{q_i q_j e^2}{r_{ij}} + 4\epsilon_{ij} \left(\frac{\sigma_{ij}^{12}}{r_{ij}^{12}} - \frac{\sigma_{ij}^{6}}{r_{ij}^{6}} \right) \right] \end{aligned} \tag{1}$$

K_r and K_Θ are the stretching and bending force constants, while r_{eq} and Θ_{eq} are the equilibrium bond lengths and angles, respectively. V_n is the torsional (out-of-plane) energy barrier for changing the dihedral angle, ϕ, with periodicity n. q_i and q_j are the partial charges of the interacting atoms with r_{ij} being the distance between them. ϵ_{ij} and σ_{ij} are the geometric mean values ($\epsilon_{ij} = \sqrt{\epsilon_{ii}\epsilon_{jj}}$ and $\sigma_{ij} = \sqrt{\sigma_{ii}\sigma_{jj}}$) of the van der Waals parameters of atoms i and j. Intramolecular nonbonded interactions are counted only for atoms three or more bonds apart ($f_{ij} = 1.0$); 1,4 interactions are considered but scaled down by the factor $f_{ij} = 0.5$.

The Cu^{2+} binding site was suggested by Yeung and Axelsen [53], in which Cu^{2+} is coordinated by four His residues (His13 and His14) from the two Aβ_{1-42} monomers. The system of the four imidazole rings of the four His residues in complex with Cu^{2+} was used for the QM calculations. This system was optimized at the B3LYP/def2-TZVP level [60–63] with D3 dispersion correction [64] using the Turbomole V6.3 program [78]. The force constants for bonds (K_r) and angles (K_Θ) related to Cu^{2+} were derived from QM potential

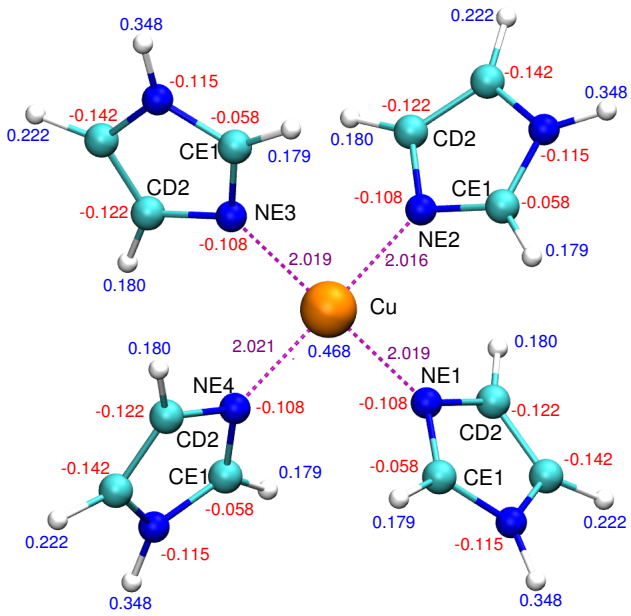

Figure 2: The fully optimized structure of the copper binding sites with the RESP charges derived at B3LYP/6-31G* level, blue and red are for positive and negative charges, respectively. The atoms involved in the bonds and angles with Cu^{2+} are also labelled. The figure was generated with VMD [77].

energy surface (PES) scans based on the fully optimized copper coordination model, while the equilibrium values of those bonds (r_{eq}) and angles (Θ_{eq}) were taken from the fully optimized geometry directly. As the geometry of the Cu^{2+} binding sites is symmetric as shown in Figure 2, we defined only one bond type for the four bonds involving Cu^{2+} (Cu^{2+}–X, X is one of the coordinating N atoms) and three angle types for the 14 angles related to Cu^{2+} (X_i–Cu–X_j and Cu–X–Y, X_i and X_j are two different atoms belonging to X, Y are atoms bound to X.). Then we performed PES scans for one bond (Cu^{2+}–NE4) and three angles (NE1–Cu^{2+}–NE2, NE1–Cu^{2+}–NE3 and Cu^{2+}–NE1–CD2) describing the bond and angle types, respectively (Figure 2). The torsional parameters V_n were neglected as commonly done in the bonded plus electrostatics model [72, 79, 80] as the coordination site with bonded Cu^{2+} is quite rigid and usually devoid of significant torsional freedom. The most widely used restrainted electrostatic potential (RESP) [81] was utilized to derive the atomic partial charges [79, 82]. Based on the fully optimized copper coordination model (Figure 2), the electrostatic potential was calculated at B3LYP/6-31G* level with Gaussian 09 [83], and

the fitting was done by antechamber [84] of AmberTools 14. Finally, we performed molecular mechanics (MM) scanning as implemented in Gromacs [85–87] using the derived parameters to reproduce the QM curves, as a validation method [88, 89].

Table 1: **OPLS-AA/L parameters for bonds and angles of the Cu^{2+} binding sites[a].**

Bonds	r_{eq} (Å)	K_r (kcal/mol·Å^2)	Bonds	r_{eq} (Å)	K_r (kcal/mol·Å^2)
Cu^{2+}–NE1	2.019	95.6	Cu^{2+}–NE2	2.016	95.6
Cu^{2+}–NE3	2.019	95.6	Cu^{2+}–NE4	2.021	95.6
Angles	Θ_{eq} (°)	K_Θ (kcal/mol·rad^2)	Angles	Θ_{eq} (°)	K_Θ (kcal/mol·rad^2)
NE1–Cu^{2+}–NE2	89.8	19.4	NE2–Cu^{2+}–NE3	89.9	19.4
NE3–Cu^{2+}–NE4	90.2	19.4	NE1–Cu^{2+}–NE4	90.1	19.4
NE1–Cu^{2+}–NE3	177.6	11.6	NE2–Cu^{2+}–NE4	178.7	11.6
Cu^{2+}–NE1–CD2	126.6	14.1	Cu^{2+}–NE2–CD2	126.3	14.1
Cu^{2+}–NE1–CE1	126.4	14.1	Cu^{2+}–NE2–CE1	126.8	14.1
Cu^{2+}–NE3–CD2	125.6	14.1	Cu^{2+}–NE4–CD2	126.5	14.1
Cu^{2+}–NE3–CE1	127.5	14.1	Cu^{2+}–NE4–CE1	126.7	14.1

a : For atom names, see Figure 2

In the nonbonded Cu^{2+} model one places a number of dummy atoms (4 or 6) around the metal ion, which are covalently connected to the metal ion in a tetrahedral or octahedral geometry, and each of the dummy atoms possesses the same partial charge [90–93]. Comparing to the bonded model, it is possible to model ligand exchange and/or interconversion between different coordination geometries with the dummy model [93]. Recently, we developed a Cu^{2+} dummy model which includes the Jahn-Teller effect [58]. It was proposed that ligand exchange existed in the folding and aggregation of Aβ_{1-42} involving Cu^{2+}, but it is not possible to distinguish between high affinity Cu^{2+} coordination and a transient small fraction of the Cu^{2+} coordinating to a single ligand [94]. Thus, the Cu^{2+} dummy model was applied for the same initial structure of the dimer shown in Figure 1 in this study.

2.3 Hamiltonian replica exchange molecular dynamics simulations

Hamiltonian replica exchange molecular dynamics (H-REMD) simulations [95, 96] were performed to improve the conformational sampling of the Aβ_{1-42} dimer. As an enhancing algorithm, it is based on executing simultaneous simulations (replicas) with different Hamiltonians (energies) of the same system and allowing exchanges at a given frequency between replicas i and j respectively at neighbouring scales m and n with a probability of [95]

$$P(X_i \leftrightarrow X_j) = \min\left[1, \exp\left(\frac{-H_m(X_j) + H_m(X_i)}{k_B T} + \frac{-H_n(X_i) + H_n(X_j)}{k_B T}\right)\right] \tag{2}$$

where H is the Hamiltonian, X are the coordinates, T is the temperature and

$$H_m(X) = \lambda_m H_{pp} + (\lambda_m)^{1/2} H_{ps} + H_{ss}(X) \tag{3}$$

where H_m is the Hamiltonian at scale m, and H_{pp}, H_{ps}, H_{ss} are the protein-protein, protein-solvent, solvent-solvent energies, respectively. λ_m is the scaling factor at scale m ($\lambda_m \leq 1.0$). Previous H-REMD tests of trpcage and a β-hairpin indicated a significantly lower computational cost and better sampling than with the temperature replica exchange algorithm [95].

Gromacs 4.6.7 simulation package [85–87] in combination with the PLUMED plugin (version 2.1) [97] were used to perform the H-REMD simulations [96] of the 2Aβ_{1-42} and 2Aβ_{1-42}/Cu^{2+} systems. The dimer was modelled with the OPLS-AA/L force field [73, 74], and it was centered in a cuboid with a dimension of 8.0×6.0×6.0 nm^3, and periodic boundary conditions were employed for the boundary treatment. The box was solvated with TIP4P explicit water molecules [98]. A sufficient number of sodium and chloride ions were added to achieve system charge neutrality while at the same time achieving a NaCl concentration of 0.150 M, which is part of the physiological milieu. Energy minimization was performed on the entire system using both the steepest descent and the conjugate gradient methods. After minimization, 500 ps of each NVT and NPT position-restrained dynamics were performed with a restraining force of 1000 kJ/mol·nm^2 on the non-hydrogen atoms of the peptide, which allowed the water molecules to equilibrate around the restrained peptide, thereby removing bad contacts and bringing the system close to equilibrium.

The final coordinates of the NPT equilibration were used as the initial coordinates for sampling without any position restraints. 24 scaling factors ranging from $\lambda_m = 1.0$ to 0.4 were generated by a geometric distribution, which were used in the H-REMD simulation of each dimer system. For the simulations of 2Aβ_{1-42} and 2Aβ_{1-42}/Cu^{2+}, each replica was subjected to 200-ns sampling in an NPT ensemble. A canonical thermostat with stochastic velocity reassignment [99] and a coupling constant of 0.5 ps was used to keep the system at a 300 K during all simulations. For the NPT simulations a Parrinello-Rahman barostat [100] with 1.0 bar pressure and 1.0 ps coupling constant was employed. Both van der Waals and Coulombic interactions were truncated at 1.2 nm, and the long-range electrostatic interactions were calculated using the Particle Mesh Ewald method [101]. The neighbour-list was updated

every 10 steps with a cut-off of 1.2 nm. The LINCS algorithm [102] was used to constrain all bond lengths during the MD simulations. The use of virtual sites for hydrogen atoms allowed the use of a 4-fs time-step. An exchange between neighbouring replicas was attempted every 2 ps, which resulted in an exchange ratio of 20-35%. The coordinates were saved every 1 ps, and the last 100-ns of the replica at λ_m=1.0 from each H-REMD simulation was utilized for further analysis.

In order to test whether ligand exchange plays a role for the Cu^{2+} coordinated dimer, we also performed an H-REMD simulation for the Aβ_{1-42} dimer in complex with the Cu^{2+} dummy model (2Aβ_{1-42}/CuDum) [58]. The initial structure for this simulation was taken from the H-REMD simulation of 2Aβ_{1-42}/Cu^{2+} at 100 ns and $\lambda = 1.0$. The protocol for the simulation of 2Aβ_{1-42}/CuDum is the same as that for the 2Aβ_{1-42} and 2Aβ_{1-42}/Cu systems, except that a 2-fs time-step was used and each of the 24 replicas was subjected to only 100-ns sampling as this simulation was started from the equilibrated 2Aβ_{1-42}/Cu^{2+} state. The exchange ratio between replicas was also around 20-35%.

2.4 Analysis

The last 100-ns sampling at $\lambda = 1.0$ of each system (100,000 frames in total) was used for all the analyses. Cluster analysis is a convenient tool to separate the conformational ensemble into clusters with similar geometry. The trajectory of each system was clustered every other frame (50,000 frames in total) using the cluster analysis method of Daura *et al.* [103]. A root mean square deviation (RMSD) cut-off of 2.0 Å between backbone atoms was used for the clustering. Root mean square fluctuation of Cα atom of each residue was calculated to describe the flexibility of the peptide. The formation of secondary structure such as α-helix and β-sheet are crucial in the studies of intrinsically disordered, fibrillogenic proteins of neurodegenerative diseases. A widely used program, DSSP [104] (dictionary of protein secondary structure), was applied to determine the secondary structure for each system. The VMD software [77] was used to visualize the peptide structures.

3 Results and Discussions

3.1 Parameterization

Firstly, we derived the force field parameters for describing the interactions between Cu^{2+} and the Aβ_{1-42} dimer as there is no standard force field for modelling metal–protein interactions. The harmonic potential, already used for metalloproteins [88, 89], is applied to bonds and angles that involve Cu^{2+}, and the force constants are derived by calculating the potential

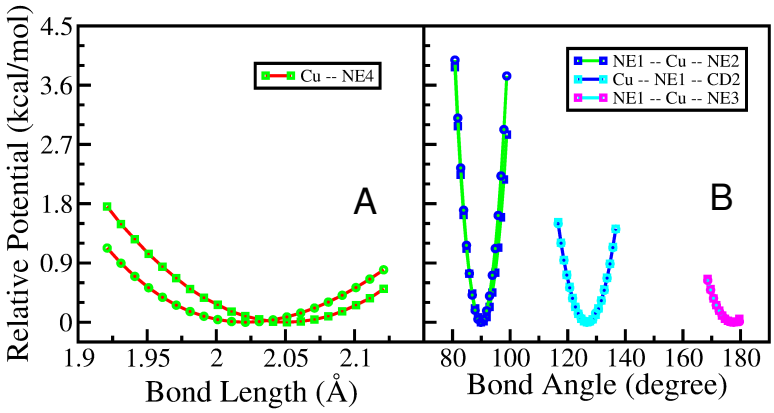

Figure 3: QM and MM potential energy curves for bond stretching (A) and angle bending (B). QM curves are shown as solid lines with circles, whereas MM curves as solid lines with squares. Different colors correspond to different bonds or angles involving Cu^{2+}.

energy profiles with QM methods. Though the harmonic oscillator approximation is widely applied in the standard force fields of proteins and other biomolecules, it can only be adopted for bonds and angles close to their equilibrium positions. Therefore, we only computed the potential energy profiles around the corresponding equilibrium positions of bonds and angles involving Cu^{2+}. The force field parameters for bonds and angles fitted to the PES from QM calculations using the least-squares method are summarized in Table 1, while the derived atomic partial charges of the Cu^{2+} binding sites using RESP method are shown in Figure 2. After geometry optimization at the B3LYP/def2-TZVP level with D3 dispersion correction, a square planar geometry for Cu^{2+} coordination sphere was observed, and the equilibrium values of Cu^{2+}–N bonds obtained from the QM optimized structure are around 2.0 Å, which are very close to previous experimental and theoretical results [40, 42, 56].

For validation, we reproduced the QM potential energy curves by using the MM method with the newly developed parameters for bonds and angles. As shown in Figure 3, the QM curves of the bond are reproduced by the MM curves within reasonable deviations close to the equilibrium value. The equilibrium value of the MM curve is increased by around 0.02 Å, and the deviations between relative MM and QM energies become larger when the bond is far from its equilibrium values. The reasons for this deviation is likely due to the harmonic approximation used. However, the MM curves of angle scanning reproduce the corresponding QM curves well. For further validation, we performed a 10-ns MD simulation of the coordinated copper complex with the newly derived parameters. The geometry of the complex was well preserved during the 10-ns simulation: the bond lengths and angles in-

volving Cu^{2+} remained near their corresponding equilibrium values and the potential energy was conserved (data not shown). We concluded that these parameters can be used to model interactions between Cu^{2+} and the Aβ_{1-42} dimer in large-scale MD simulations.

3.2 Convergence of the H-REMD simulations

One of the advantages of the H-REMD method is that good conformational sampling can be obtained in reasonable wall-clock time compared to conventional MD simulations, and it is computationally cheaper and more efficient than standard temperature REMD. For our simulations, the exchange probabilities are around 25–30% for all three systems, which guarantees good sampling. In order to further confirm the convergence of the simulations, the secondary structure contents as a function of the scaling factor λ were calculated for three different time windows: 100–130, 100–160 and 100–200 ns for 2Aβ_{1-42} and 2Aβ_{1-42}/Cu^{2+}, and for time intervals: 0–30, 0–60, 0–100 ns for 2Aβ_{1-42}/CuDum. As shown in Figure 4, the superposition of the curves for the three different time intervals suggests that the propensities of coil content have converged in the three systems. The helix propensity as a function of the amino acids in different time intervals for the three systems is shown in Figure 5. Little change is observed for the percentage of helix content for each residue as the simulation progresses. Similar results were also obtained for the other secondary structure elements. Taken together, the results confirm the convergence of the simulations. Thus, the analysis was based on the ensemble trajectory at $\lambda = 1.0$ from 100 to 200 ns for 2Aβ_{1-42} and 2Aβ_{1-42}/Cu^{2+}, and from 0 to 100 ns for 2Aβ_{1-42}/CuDum.

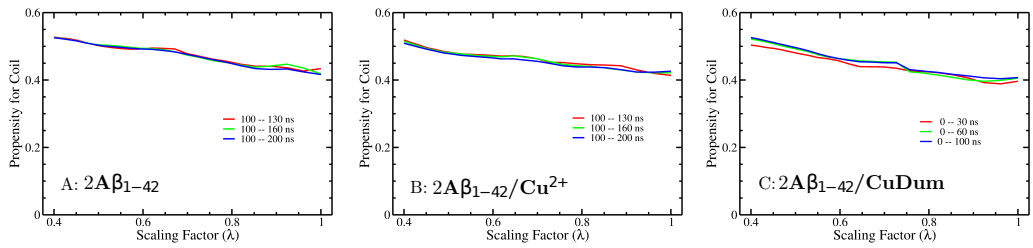

Figure 4: The propensity of coil as a function of scaling factor λ for the different time intervals 100-130, 100-160, 100-200 ns for 2Aβ_{1-42} (A), 2Aβ_{1-42}/Cu^{2+} (B), and 0-30, 0-60, 0-100 ns for 2Aβ_{1-42}/CuDum (C).

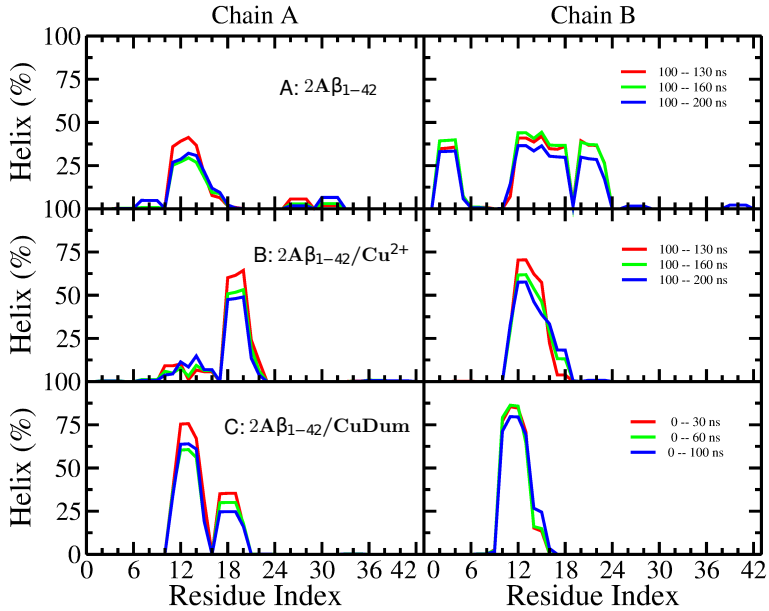

Figure 5: The helix propensity of each residue at λ=1.0 for the different time intervals and the three systems: 2Aβ_{1-42} (A), 2Aβ_{1-42}/Cu^{2+} (B) and 2Aβ_{1-42}/CuDum (C).

3.3 Effects of Cu^{2+} binding on the flexibility of Aβ_{1-42} dimer

In order to assess the conformational flexibility of the Aβ_{1-42} dimers, we performed cluster analysis and computed the root mean square fluctuations (RMSF) of individual residues for the three systems.

3.3.1 Clustering

The conformations sampled at $\lambda = 1.0$ for each of the three systems are clustered by considering only the backbone atoms. The populations of the top ten clusters are shown in Figure 6. There are less clusters (80) for 2Aβ_{1-42}/Cu^{2+} than for the other two systems (483 for 2Aβ_{1-42} and 488 for 2Aβ_{1-42}/CuDum). The most populated 2Aβ_{1-42}/Cu^{2+} cluster (55.9%) has more than four times and twice as much of the population of the 2Aβ_{1-42} (12.3%) and population of 2Aβ_{1-42}/CuDum (21.3%) clusters, respectively. Similar populations are found for all the other clusters, as shown in Figure 6. These results indicate that the bridged Cu^{2+} geometry greatly decreases the conformational flexibility of the Aβ_{1-42} dimer while the Cu^{2+} dummy model does allow for conformational flexibility.

The central conformations of the first two largest clusters of each system are shown in

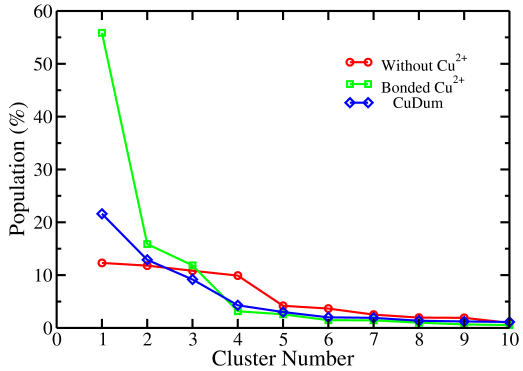

Figure 6: The populations of the top ten clusters for 2Aβ_{1-42}, 2Aβ_{1-42}/Cu^{2+} and 2Aβ_{1-42}/CuDum, respectively.

Figure 7. Generally, the most abundant residual secondary structure elements for all of the dimer conformations are turn, bend and coil structures. For the Aβ_{1-42} dimer without Cu^{2+} (2Aβ_{1-42}), two β-hairpins are observed in both chains of the most prominent cluster (Figure 7A). In chain A, the β-hairpin locates at the CHC (Phe19–Ala21) and the C-terminal polar (Asn27–Gly29) regions while it is at the CTH region (Lys28–Ile31 and Met35–Val39) of chain B. Meanwhile, there are also α- (Glu11–Phe19) and 3_{10} (Phe20–Glu22) helices sampled in chain B but none in chain A. The central conformation of the second largest cluster (Figure 7B) is quite similar to the one of the largest cluster, with an RMSD of only 3.15 Å for the backbone atoms between them. The β-hairpin in chain A is preserved while the one in chain B is gone. The helices in chain B are mostly preserved only that the 3_{10}-helix (Ala2–Phe4) appears at the N-terminal region. For the Aβ_{1-42} dimer with a bridged Cu^{2+} (2Aβ_{1-42}/Cu^{2+}), two β-hairpins are observed at the CHC (Phe19–Glu22) and central hydrophilic (Asn27–Gly29) regions as well as at the CTH region (Leu34–Val36 and Val39–Ile41) of chain B for the most dominant cluster (Figure 7C), while there is a short β-sheet (Arg5–His6) sampled at the N-terminal region of chain A, which is in contact with one of the β-hairpins in chain B. A 3_{10}-helix was sampled for both chain A (Val18–Phe20) and chain B (Val12–His14) at different positions. Two β-hairpins of 2Aβ_{1-42}/Cu^{2+} are present in the second largest cluster (Figure 7D), one is at the N-terminal region (Arg5–His6 and Gly9–Tyr10) of chain A, the other is at the CTH region (Ala30–Ile31 and Val36–Gly37) of chain B. Moreover, there are interchain β-sheets, two β-strands (Phe19–Glu22 and Ala30–Ile31) from chain B form a sheet with another strand (Leu17–Phe20) from chain A.

In the 2Aβ_{1-42}/CuDum system, the nonbonded CuDum is not stable at the coordination center but prefers to interact with negatively charged residues. CuDum is coordinated with

residues Asp1, Glu3 and Asp23 of chain A in the central structure of the largest cluster of 2Aβ_{1-42}/CuDum (Figure 7E) while it is coordinated with residue Glu11 in chain A of the second cluster (Figure 7F). Two β-hairpins appear in the most dominant cluster of 2Aβ_{1-42}/CuDum (Figure 7E), one is at the C-terminal region (Gly25–Asn27 and Met35–Gly37) of chain A while the other one is at the CHC (Phe20–Ala21) and C-terminal polar (Asn27–Lys28) regions of chain B. Furthermore, interchain β-sheets are observed at the C-terminal regions of both chain A (Val39–Val40) and chain B (Gly37–Gly38). The secondary structures of chain B formed in the second cluster of 2Aβ_{1-42}/CuDum are quite similar to chain B of the first cluster of 2Aβ_{1-42}/Cu^{2+}. The β-hairpin sampled in chain A of the first cluster of 2Aβ_{1-42}/CuDum is preserved in the second cluster, which is gone in chain A of the first cluster of 2Aβ_{1-42}/Cu^{2+}. In addition, a α-helix is sampled at the N-terminal region (Val12–Lys16) of chain A in the second cluster.

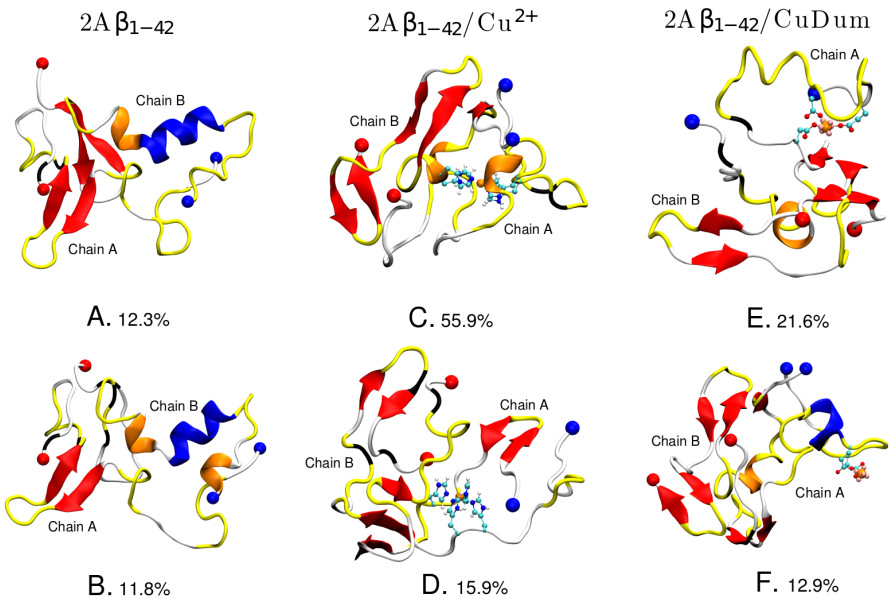

Figure 7: Central structures of the two most populated clusters for each of the three systems 2Aβ_{1-42}, 2Aβ_{1-42}/Cu^{2+} and 2Aβ_{1-42}/CuDum, respectively. The population is given below each structure, and chain A and chain B are labelled. The peptide color is based on the secondary structure: red for β-sheet, blue for α-helix, orange for 3_{10}-helix, yellow for turn, black for β-bridge and white for coil structures. The N- and C-termini are represented by blue and red beads, respectively.

3.3.2 Root mean square fluctuations

As can be seen from the root mean square fluctuation (RMSF) plots in Figure 8, the bridged Cu^{2+} greatly stabilizes Aβ_{1-42} in the 2Aβ_{1-42}/Cu^{2+} dimer, while CuDum only slightly decreases the flexibility of Aβ_{1-42} compared to the 2Aβ_{1-42} system without Cu^{2+}. For 2Aβ_{1-42}, the flexibility of the residues in chain A increases gradually from N-terminal (RMSF, ∼1.5 nm) to C-terminal (RMSF, ∼2.0 nm) regions, while the N-terminal and the CHC regions of chain B possess equivalent higher flexibility. Residues Asn27–Lys28 are least flexible in chain B. For the Aβ_{1-42} dimer with CuDum, the flexibility of chain A is similar to that in 2Aβ_{1-42}, increasing from the N- to the C-terminus only with bigger "RMSF valleys", compared to the rest of the peptide. There is one big "RMSF valley" spanning from Gly9 to Val36 of chain B, *i.e.* chain B in 2Aβ_{1-42}/CuDum is generally less flexible. The RMSF plots for chain A and chain B in 2Aβ_{1-42}/Cu^{2+} are similar to each other. The CHT region is rigid for both chains, and so is the region of His13–His14 as they are bonded to the Cu^{2+} ion. Relatively higher flexibility was observed at the N-terminal and central polar regions for both chains.

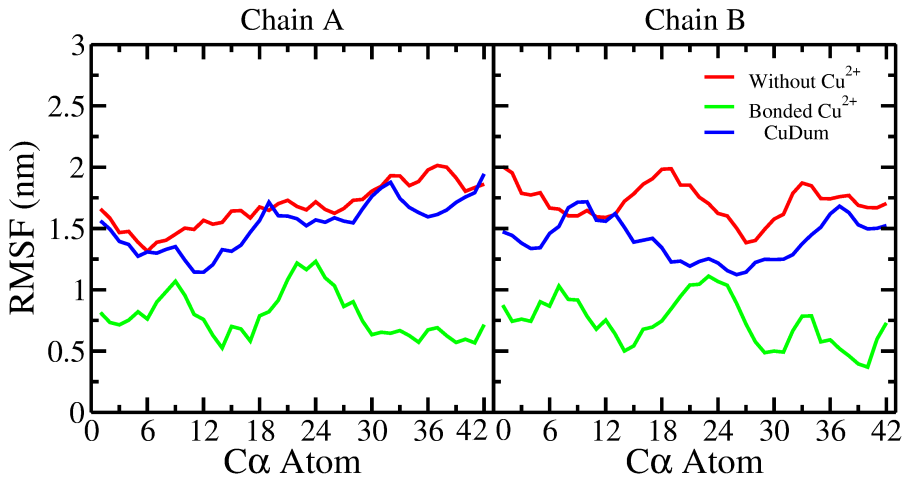

Figure 8: Average RMSF of the Cα atoms for the 2Aβ_{1-42}, 2Aβ_{1-42}/Cu^{2+} and 2Aβ_{1-42}/CuDum systems, respectively.

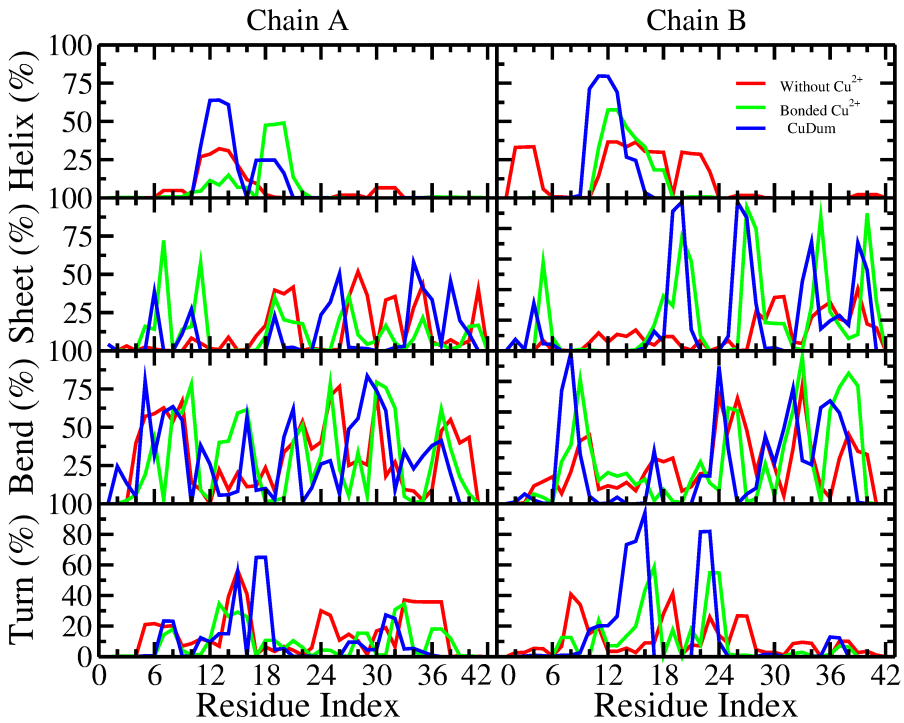

Figure 9: Averaged secondary structure content per residue for the 2Aβ_{1-42}, 2Aβ_{1-42}/Cu^{2+} and 2Aβ_{1-42}/CuDum systems, respectively. The helix content contains α-, 3_{10}- and π-helix structures, while the sheet content includes β-sheet and β-bridge structures. The coil structure is not shown.

3.4 Effects of Cu^{2+} binding on the structure of Aβ_{1-42} dimer

3.4.1 Secondary structure

The secondary structure transitions, especially the formation of β-sheets play a remarkable role in the aggregation processes and toxicity of Aβ peptides [1, 9, 105]. The propensities for secondary structure elements for the three Aβ_{1-42} dimer systems were calculated and are shown in Table 2 and Figure 9. In general, the most abundant residual secondary structure elements for all three systems are turn, bend and coil structures, especially at the N- and C-termini. More sheet contents were sampled for 2Aβ_{1-42}/Cu^{2+} (15.5%) and 2Aβ_{1-42}/CuDum (14.9%) than for 2Aβ_{1-42} (11.4%). And less helix structures were observed for 2Aβ_{1-42}/Cu^{2+} (6.3%) than for 2Aβ_{1-42} (8.1%) and 2Aβ_{1-42}/CuDum (8.2%).

As shown in Figure 9, 2Aβ_{1-42} is characterized by helical structures at the N-terminal region (Val12–His14) of chain A and at the N-terminal (Ala2–Phe4) and central (Glu11–Val18,

Phe20–Glu22) regions with probabilities around 25%. With bonded Cu^{2+}, a very localized propensity for helix structures with probabilities around 50% were determined for both chain A (Val18–Phe20) and chain B (Val12–Val18). For 2Aβ_{1-42}/CuDum, helical structures mainly appear at the N-terminal region of both chain A and chain B with rather high propensity (∼70%) and at the CHC region of chain A with lower propensity (∼25%). Furthermore, the sheet structures sampled in chain A of all the three dimer systems are more populated than in chain B with moderately high propensities. More sheet structures are observed in the CTH region of chain A of 2Aβ_{1-42} compared to 2Aβ_{1-42}/Cu^{2+} and 2Aβ_{1-42}/CuDum. However, sheet structures in chain B of both 2Aβ_{1-42}/Cu^{2+} and 2Aβ_{1-42}/CuDum are more often present than in chain B of 2Aβ_{1-42}, and there are rarely sheet structures sampled at the N-terminal and the central regions of chain A in 2Aβ_{1-42}.

Table 2: **Secondary structure propensities of in the three Aβ_{1-42} dimer systems.**

Systems	Helix (%)	Sheet (%)	Bend (%)	Turn (%)
2Aβ_{1-42}	8.1±6.2	11.4±7.5	26.7±4.3	12.3±4.8
2Aβ_{1-42}/Cu^{2+}	6.3±3.3	15.5±6.3	26.6±4.5	8.9±3.3
2Aβ_{1-42}/CuDum	8.2±3.7	14.9±3.6	25.1±5.2	11.0±3.9

3.4.2 Salt bridges

The presence of salt bridges has been suggested to be of great importance in stabilizing the structure of the Aβ_{1-42} dimer [20, 23]. At physiological pH, Aβ_{1-42} has three positively charged residues: Arg5, Lys16 and Lys28, which can form salt bridges with each of the six negatively charged residues: Asp1, Glu3, Asp7, Glu11, Glu22 and Asp23. We calculated all propensities for all possible salt bridges in 2Aβ_{1-42}, 2Aβ_{1-42}/Cu^{2+} and 1Aβ_{1-42}/CuDum systems. The populations of the intramolecular salt bridges with high probabilities >30% in at least one of the chains in the three systems are listed in Table 3. No significant intermolecular salt bridges were found in all three system, which agree with Barz and Urbanc's finding [20]. The Glu3-Arg5 salt bridge is more stable in chain A than in chain B of 2Aβ_{1-42}. With Cu^{2+} bridging the dimer (2Aβ_{1-42}/Cu^{2+}), the salt bridge is very stable in both chains. However, the stability of this salt bridge decreases in both chains when the bonded Cu^{2+} was replaced with CuDum. A turn structure centered at residue Gly25–Ser26 enables the formation of the salt bridges Glu22-Lys28 and Asp23-Lys28. The Glu22-Lys28 salt bridge is moderately stable in chain A but less stable in chain B of 2Aβ_{1-42}. It is the other way round in both 2Aβ_{1-42}/Cu^{2+} and 2Aβ_{1-42}/CuDum systems, where this salt bridge is more stable in chain B than in chain A. Meanwhile, the salt bridge Asp23-Lys28 was only sampled with

high propensity in chain B of 2Aβ_{1-42}, whereas it was hardly found when bonded Cu^{2+} or CuDum is present. Instead, residue Lys28 formed a moderately stable salt bridge with Glu11 in chain B of both 2Aβ_{1-42}/Cu^{2+} and 2Aβ_{1-42}/CuDum. Additionally, a moderately stable salt bridge of Asp1-Lys16 was found in chain A of 2Aβ_{1-42}/Cu^{2+} and 2Aβ_{1-42}/CuDum but it was missing in 2Aβ_{1-42}. However, Lys16 formed a salt bridge with Glu11 with moderate propensity in chain A of 2Aβ_{1-42}, but this salt bridge was hardly found in 2Aβ_{1-42}/Cu^{2+} and 2Aβ_{1-42}/CuDum.

In general, the propensity to form intramolecular salt bridges is reduced when a copper ion is bound to Aβ_{1-42} (2Aβ_{1-42}/Cu^{2+} or 2Aβ_{1-42}/CuDum). In particular, in 2Aβ_{1-42}/CuDum where CuDum prefers to interact with chain A, the formation of salt bridges is least pronounced (especially in chain A).

Table 3: **Population (%) of intramolecular salt bridges formed in the three Aβ_{1-42} dimer systems.**

Salt bridge	2Aβ_{1-42}		2Aβ_{1-42}/Cu^{2+}		2Aβ_{1-42}/CuDum	
	chain A	chain B	chain A	chain B	chain A	chain B
Arg5-Glu3	91.1	54.7	93.0	82.7	66.3	78.2
Lys16-Asp1	0.0	0.0	40.1	0.0	26.7	0.0
Lys16-Glu11	34.2	1.0	0.7	0.0	1.2	0.0
Lys28-Glu11	0.0	0.1	0.0	56.9	0.1	32.8
Lys28-Glu22	38.8	6.3	0.9	72.4	8.9	87.4
Lys28-Asp23	6.2	52.0	10.4	7.1	1.6	0.0

4 Conclusions

In this work, we have studied the role of the copper ion in the dimerization of Aβ_{1-42} using both a bonded model and a nonbonded model for Cu^{2+}. We first developed OPLS-AA/L force field parameters for describing the interactions within the Cu^{2+} coordination center: one copper ion coordinated by four His residues (His13 and His14) from each of the two Aβ_{1-42} peptides composing the dimer [53]. After validation, these newly developed parameters were used in the H-REMD simulation of 2Aβ_{1-42}/Cu^{2+}. The nonbonded model for Cu^{2+} we developed [58] was also applied in this study.

We found that the bonded Cu^{2+} greatly decreases the flexibility of Aβ_{1-42} in the 2Aβ_{1-42}/Cu^{2+} dimer while the nonbonded CuDum only slightly stabilizes Aβ_{1-42} compared to the 2Aβ_{1-42} system without Cu^{2+}. The differences in the flexibility of the three systems are also reflected by the populations of the most important conformational clusters. In our simulations, a propensity of around 10-15% for β-sheets and of <10% for helices were found for either

the three systems, which is close to the findings from previous experiments [9] and simulations [20, 24]. We further observed that the bridged Cu^{2+} enhances the sampling of β-sheet and disrupts the α-helix structures, which is of significant importance to the initialization of $A\beta_{1-42}$ aggregation. Specifically, Cu^{2+} stabilizes β-hairpins at the CHC and C-terminal regions of $A\beta_{1-42}$, which is consistent with our conclusions from the previous study on monomeric $A\beta_{1-42}$ with Cu^{2+}. C-terminal β-hairpins have been shown to play significant roles in the initialization of $A\beta$ aggregation [106], and may therefore be a good therapeutic target for the treatment of Alzheimer's disease [107, 108]. When using the nonbonded Cu^{2+} model during the H-REMD simulation, CuDum was not stable at the coordination center and ligand exchange was observed. Both simulations involving copper (II) revealed that Cu^{2+} binding to $A\beta_{1-42}$ reduces the propensity of $A\beta_{1-42}$ to form salt bridges.

In summary, our simulations reveal that Cu^{2+} promotes β-hairpins at the CHC and C-terminal regions in the $A\beta_{1-42}$ dimer, which may account for the enhanced toxicity of $A\beta/Cu^{2+}$ complexes. Future simulations of larger oligomers (trimers, tetramers *etc.*) are needed to further understand the roles of Cu^{2+} in the process of $A\beta$ aggregation.

5 Acknowledgements

Q.L. gratefully acknowledges the funding received towards his Ph.D. from the China Scholarship Council. The authors gratefully acknowledge the computing time granted on the supercomputers JARA-HPC at RWTH Aachen University (grant number jara0122) and JUROPA at Jülich Supercomputing Centre (grant number JICS68), as well as the HPC cluster of Heinrich-Heine University Düsseldorf.

References

[1] F. Chiti and C. M. Dobson. Protein misfolding, functional amyloid, and human disease. *Annu. Rev. Biochem.*, 75:333–366, 2006.

[2] G. M. Shankar and D. M. Walsh. Alzheimer's disease: synaptic dysfunction and Aβ. *Mol. Neurodegener.*, 4:48, 2009.

[3] Arvi Rauk. The chemistry of Alzheimer's disease. *Chem. Soc. Rev.*, 38(9):2698–2715, 2009.

[4] Karie N. Dahlgren, Arlene M. Manelli, W. Blaine Stine, Lorinda K. Baker, Grant A. Krafft, and Mary Jo LaDu. Oligomeric and fibrillar species of amyloid-β peptides differentially affect neuronal viability. *J. Biol. Chem.*, 277(35):32046–32053, 2002.

[5] Koichi Iijima, Hsin-Ping Liu, Ann-Shyn Chiang, Stephen A. Hearn, Mary Konsolaki, and Yi Zhong. Dissecting the pathological effects of human Aβ40 and Aβ42 in drosophila: A potential model for Alzheimer's disease. *Proc. Natl. Acad. Sci. U.S.A.*, 101(17):6623–6628, 2004.

[6] Marina D. Kirkitadze, Gal Bitan, and David B. Teplow. Paradigm shifts in Alzheimer's disease and other neurodegenerative disorders: The emerging role of oligomeric assemblies. *J. Neurosci. Res.*, 69(5):567–577, 2002.

[7] WL Klein, WB Stine, and DB Teplow. Small assemblies of unmodified amyloid β-protein are the proximate neurotoxin in Alzheimer's disease. *Neurobiol. Aging*, 25(5):569–580, 2004.

[8] Alex E. Roher, Michael O. Chaney, Yu-Min Kuo, Scott D. Webster, W. Blaine Stine, Lanny J. Haverkamp, Amina S. Woods, Robert J. Cotter, James M. Tuohy, Grant A. Krafft, Barry S. Bonnell, and Mark R. Emmerling. Morphology and toxicity of Aβ-(1-42) dimer derived from neuritic and vascular amyloid deposits of Alzheimer's disease. *J. Biol. Chem.*, 271(34):20631–20635, 1996.

[9] Kenjiro Ono, Margaret M. Condron, and David B. Teplow. Structure–neurotoxicity relationships of amyloid β-protein oligomers. *Proc. Natl. Acad. Sci. U.S.A.*, 106(35):14745–14750, 2009.

[10] Dominic M Walsh, Igor Klyubin, Julia V Fadeeva, William K Cullen, Roger Anwyl, Michael S Wolfe, Michael J Rowan, and Dennis J Selkoe. Naturally secreted oligomers

of amyloid β protein potently inhibit hippocampal long-term potentiation in vivo. *Nature*, 416(6880):535–539, 2002.

[11] Ganesh M Shankar, Shaomin Li, Tapan H Mehta, Amaya Garcia-Munoz, Nina E Shepardson, Imelda Smith, Francesca M Brett, Michael A Farrell, Michael J Rowan, Cynthia A Lemere, Ciaran M Regan, Dominic M Walsh, Bernardo L Sabatini, and Dennis J Selkoe. Amyloid-β protein dimers isolated directly from Alzheimer's brains impair synaptic plasticity and memory. *Nat. Med.*, 14(8):837–842, 2008.

[12] Summer L Bernstein, Nicholas F Dupuis, Noel D Lazo, Thomas Wyttenbach, Margaret M Condron, Gal Bitan, David B Teplow, Joan-Emma Shea, Brandon T Ruotolo, Carol V Robinson, et al. Amyloid-β protein oligomerization and the importance of tetramers and dodecamers in the aetiology of Alzheimer's disease. *Nat. Chem.*, 1(4):326–331, 2009.

[13] Duilio F. Raffa and Arvi Rauk. Molecular dynamics study of the beta amyloid peptide of Alzheimer's disease and its divalent copper complexes. *J. Phys. Chem. B*, 111(14):3789–3799, 2007.

[14] Olujide O Olubiyi and Birgit Strodel. Structures of the amyloid β-peptides Aβ1-40 and Aβ1-42 as influenced by pH and a D-peptide. *J. Phys. Chem. B*, 116(10):3280–3291, 2012.

[15] K Aurelia Ball, Aaron H Phillips, David E Wemmer, and Teresa Head-Gordon. Differences in β-strand populations of monomeric Aβ40 and Aβ42. *Biophys. J.*, 104(12):2714–2724, 2013.

[16] Aβ monomers transiently sample oligomer and fibril-like configurations: Ensemble characterization using a combined MD/NMR approach. *J. Mol. Biol.*, 425(18):3338–3359, 2013.

[17] Jessica Nasica-Labouze, Phuong H. Nguyen, Fabio Sterpone, Olivia Berthoumieu, Nicolae-Viorel Buchete, Sébastien Coté, Alfonso De Simone, Andrew J. Doig, Peter Faller, Angel Garcia, Alessandro Laio, Mai Suan Li, Simone Melchionna, Normand Mousseau, Yuguang Mu, Anant Paravastu, Samuela Pasquali, David J. Rosenman, Birgit Strodel, Bogdan Tarus, John H. Viles, Tong Zhang, Chunyu Wang, and Philippe Derreumaux. Amyloid β protein and Alzheimer's disease: When computer simulations complement experimental studies. *Chem. Rev.*, 115(9):3518–3563, 2015.

[18] Brigita Urbanc, L Cruz, F Ding, D Sammond, S Khare, SV Buldyrev, HE Stanley, and NV Dokholyan. Molecular dynamics simulation of amyloid β dimer formation. *Biophys. J.*, 87(4):2310–2321, 2004.

[19] Sébastien Côté, Rozita Laghaei, Philippe Derreumaux, and Normand Mousseau. Distinct dimerization for various alloforms of the amyloid-beta protein: Aβ1-40, Aβ1-42, and Aβ1-40(D23N). *J. Phys. Chem. B*, 116(13):4043–4055, 2012.

[20] Bogdan Barz and Brigita Urbanc. Dimer formation enhances structural differences between amyloid β-protein (1-40) and (1-42): An explicit-solvent molecular dynamics study. *PLoS ONE*, 7:e34345, 04 2012.

[21] Song-Ho Chong and Sihyun Ham. Atomic-level investigations on the amyloid-β dimerization process and its driving forces in water. *Phys. Chem. Chem. Phys.*, 14:1573–1575, 2012.

[22] Xiaoxia Zhu, Ram Prasad Bora, Arghya Barman, Rajiv Singh, and Rajeev Prabhakar. Dimerization of the full-length Alzheimer amyloid β-peptide (Aβ42) in explicit aqueous solution: A molecular dynamics study. *J. Phys. Chem. B*, 116(15):4405–4416, 2012.

[23] Man Hoang Viet, Phuong H. Nguyen, Son Tung Ngo, Mai Suan Li, and Philippe Derreumaux. Effect of the tottori familial disease mutation (D7N) on the monomers and dimers of Aβ40 and Aβ42. *ACS Chem. Neurosci.*, 4(11):1446–1457, 2013.

[24] Tong Zhang, Jian Zhang, Philippe Derreumaux, and Yuguang Mu. Molecular mechanism of the inhibition of EGCG on the Alzheimer Aβ1-42 dimer. *J. Phys. Chem. B*, 117(15):3993–4002, 2013.

[25] Man Hoang Viet, Phuong H. Nguyen, Philippe Derreumaux, and Mai Suan Li. Effect of the english familial disease mutation (H6R) on the monomers and dimers of Aβ40 and Aβ42. *ACS Chem. Neurosci.*, 5(8):646–657, 2014.

[26] Simon Mitternacht, Iskra Staneva, Torleif Härd, and Anders Irbäck. Comparing the folding free-energy landscapes of Aβ42 variants with different aggregation properties. *Proteins: Structure, Function, and Bioinformatics*, 78(12):2600–2608, 2010.

[27] Simon Mitternacht, Iskra Staneva, Torleif Härd, and Anders Irbäck. Monte carlo study of the formation and conformational properties of dimers of Aβ42 variants. *J. Mol. Biol.*, 410(2):357–367, 2011.

[28] Yassmine Chebaro, Ping Jiang, Tong Zang, Yuguang Mu, Phuong H. Nguyen, Normand Mousseau, and Philippe Derreumaux. Structures of Aβ17-42 trimers in isolation and with five small-molecule drugs using a hierarchical computational procedure. *J. Phys. Chem. B*, 116(29):8412–8422, 2012.

[29] Derya Meral and Brigita Urbanc. Discrete molecular dynamics study of oligomer formation by N-terminally truncated amyloid β-protein. *J. Mol. Biol.*, 425(12):2260–2275, 2013.

[30] Bogdan Barz, Olujide O. Olubiyi, and Birgit Strodel. Early amyloid β-protein aggregation precedes conformational change. *Chem. Commun.*, 50:5373–5375, 2014.

[31] Peter Faller and Christelle Hureau. Bioinorganic chemistry of copper and zinc ions coordinated to amyloid-β peptide. *Dalton Trans.*, (7):1080–1094, 2009.

[32] Peter Faller, Christelle Hureau, and Olivia Berthoumieu. Role of metal ions in the self-assembly of the Alzheimer's amyloid-β peptide. *Inorg. Chem.*, 52:12193–12206, 2013.

[33] Takashi Miura, Sayoko Mitani, Chiho Takanashi, and Nobuhiro Mochizuki. Copper selectively triggers β-sheet assembly of an N-terminally truncated amyloid β-peptide beginning with Glu3. *J. Inorg. Biochem.*, 98(1):10–14, 2004.

[34] Claire J. Sarell, Christopher D. Syme, Stephen E. J. Rigby, and John H. Viles. Copper(II) binding to amyloid-β fibrils of Alzheimer's disease reveals a picomolar affinity: Stoichiometry and coordination geometry are independent of Aβ oligomeric form. *Biochemistry*, 48(20):4388–4402, 2009.

[35] Cyril C. Curtain, Feda Ali, Irene Volitakis, Robert A. Cherny, Raymond S. Norton, Konrad Beyreuther, Colin J. Barrow, Colin L. Masters, Ashley I. Bush, and Kevin J. Barnham. Alzheimer's disease amyloid-β binds copper and zinc to generate an allosterically ordered membrane-penetrating structure containing superoxide dismutase-like subunits. *J. Biol. Chem.*, 276(23):20466–20473, 2001.

[36] Takashi Miura, Kiyoko Suzuki, Naohito Kohata, and Hideo Takeuchi. Metal binding modes of Alzheimer's amyloid β-peptide in insoluble aggregates and soluble complexes. *Biochemistry*, 39(23):7024–7031, 2000.

[37] Victor A. Streltsov, Stephen J. Titmuss, V. Chandana Epa, Kevin J. Barnham, Colin L. Masters, and Joseph N. Varghese. The structure of the amyloid-β peptide high-affinity copper II binding site in Alzheimer disease. *Biophys. J.*, 95(7):3447–3456, 2008.

[38] Simon C. Drew, Christopher J. Noble, Colin L. Masters, Graeme R. Hanson, and Kevin J. Barnham. Pleomorphic copper coordination by Alzheimer's disease amyloid-β peptide. *J. Am. Chem. Soc.*, 131(3):1195–1207, 2009.

[39] Simon C. Drew, Colin L. Masters, and Kevin J. Barnham. Alanine-2 carbonyl is an oxygen ligand in Cu^{2+} coordination of Alzheimer's disease amyloid-β peptide - relevance to N-terminally truncated forms. *J. Am. Chem. Soc.*, 131(25):8760–8761, 2009.

[40] Jorge Aí-Torres, Jean-Didier Maréchal, Luis Rodríguez-Santiago, and Mariona Sodupe. Three dimensional models of Cu^{2+}-Aβ(1-16) complexes from computational approaches. *J. Am. Chem. Soc.*, 133(38):15008–15014, 2011.

[41] Liang Xu, Xiaojuan Wang, Shengsheng Shan, and Xicheng Wang. Characterization of the polymorphic states of copper(II)-bound Aβ(1-16) peptides by computational simulations. *J. Comput. Chem.*, 34:2524–2536, 2013.

[42] Jorge Alí-Torres, Andrea Mirats, Jean-Didier Maréchal, Luis Rodríguez-Santiago, and Mariona Sodupe. 3d structures and redox potentials of Cu^{2+}-Aβ(1-16) complexes at different pH: A computational study. *J. Phys. Chem. B*, 118(18):4840–4850, 2014.

[43] Pierre Dorlet, Serge Gambarelli, Peter Faller, and Christelle Hureau. Pulse EPR spectroscopy reveals the coordination sphere of copper(II) ions in the 1-16 amyloid-β peptide: A key role of the first two N-terminus residues. *Angew. Chem. Int. Ed.*, 48(49):9273–9276, 2009.

[44] Christelle Hureau, Yannick Coppel, Pierre Dorlet, Pier Lorenzo Solari, Stŕphanie Sayen, Emmanuel Guillon, Laurent Sabater, and Peter Faller. Deprotonation of the Asp1-Ala2 peptide bond induces modification of the dynamic copper(II) environment in the amyloid-β peptide near physiological pH. *Angew. Chem. Int. Ed.*, 48:9522–9525, 2009.

[45] Héléne Eury, Christian Bijani, Peter Faller, and Christelle Hureau. Copper(II) coordination to amyloid-β: Murine versus human peptide. *Angew. Chem. Int. Ed.*, 50:901–905, 2011.

[46] Simon C. Drew and Kevin J. Barnham. The heterogeneous nature of Cu^{2+} interactions with Alzheimer's amyloid-β peptide. *Acc. Chem. Res.*, 44(11):1146–1155, 2011.

[47] Vello Tõugu, Ann Tiiman, and Peep Palumaa. Interactions of Zn(II) and Cu(II) ions with Alzheimer's amyloid-beta peptide. metal ion binding, contribution to fibrillization and toxicity. *Metallomics*, 3:250–261, 2011.

[48] David P. Smith, Giuseppe D. Ciccotosto, Deborah J. Tew, Michelle T. Fodero-Tavoletti, Timothy Johanssen, Colin L. Masters, Kevin J. Barnham, and Roberto Cappai. Concentration dependent Cu^{2+} induced aggregation and dityrosine formation of the Alzheimer's disease amyloid-β peptide. *Biochemistry*, 46(10):2881–2891, 2007.

[49] Jeppe T. Pedersen, Jesper Østergaard, Noemi Rozlosnik, Bente Gammelgaard, and Niels H. H. Heegaard. Cu(II) mediates kinetically distinct, non-amyloidogenic aggregation of amyloid-β peptides. *J. Biol. Chem.*, 286(30):26952–26963, 2011.

[50] Takashi Miura, Kiyoko Suzuki, Naohito Kohata, , and Hideo Takeuchi. Metal binding modes of Alzheimer's amyloid β-peptide in insoluble aggregates and soluble complexes. *Biochemistry*, 39(23):7024–7031, 2000.

[51] Francis Hane, Gary Tran, Simon J. Attwood, and Zoya Leonenko. Cu^{2+} affects amyloid-β (1-42) aggregation by increasing peptide-peptide binding forces. *PLoS ONE*, 8:e59005, 03 2013.

[52] Jesse W. Karr, Lauren J. Kaupp, and Veronika A. Szalai. Amyloid-β binds Cu^{2+} in a mononuclear metal ion binding site. *J. Am. Chem. Soc.*, 126(41):13534–13538, 2004.

[53] Priscilla S.-W. Yeung and Paul H. Axelsen. The crowded environment of a reverse micelle induces the formation of β-strand seed structures for nucleating amyloid fibril formation. *J. Am. Chem. Soc.*, 134(14):6061–6063, 2012.

[54] Daxiong Han, Haiyan Wang, and Pin Yang. Molecular modeling of zinc and copper binding with Alzheimer's amyloid β-peptide. *BioMetals*, 21(2):189–196, 2008.

[55] Velia Minicozzi, Francesco Stellato, Massimiliano Comai, Mauro Dalla Serra, Cristina Potrich, Wolfram Meyer-Klaucke, and Silvia Morante. Identifying the minimal copper- and zinc-binding site sequence in amyloid-β peptides. *J. Biol. Chem.*, 283(16):10784–10792, 2008.

[56] Sudhakar Parthasarathy, Fei Long, Yifat Miller, Yiling Xiao, Dan McElheny, Kent Thurber, Buyong Ma, Ruth Nussinov, and Yoshitaka Ishii. Molecular-level examination of Cu^{2+} binding structure for amyloid fibrils of 40-residue Alzheimer's β by solid-state NMR spectroscopy. *J. Am. Chem. Soc.*, 133(10):3390–3400, 2011.

[57] William A. Gunderson, Jessica Hernández-Guzmán, Jesse W. Karr, Li Sun, Veronika A. Szalai, and Kurt Warncke. Local structure and global patterning of Cu^{2+} binding in fibrillar amyloid-β [Aβ(1-40)] protein. *J. Am. Chem. Soc.*, 134(44):18330–18337, 2012.

[58] Qinghua Liao, Shina Caroline Lynn Kamerlin, and Birgit Strodel. Development and application of a nonbonded Cu^{2+} model that includes the Jahn-Teller effect. *J. Phys. Chem. Lett.*, 6(13):2657–2662, 2015.

[59] Simona Tomaselli, Veronica Esposito, Paolo Vangone, Nico A. J. van Nuland, Alexandre M. J. J. Bonvin, Remo Guerrini, Teodorico Tancredi, Piero A. Temussi, and Delia Picone. The α-to-β conformational transition of Alzheimer's Aβ-(1-42) peptide in aqueous media is reversible: A step by step conformational analysis suggests the location of β conformation seeding. *ChemBioChem*, 7(2):257–267, 2006.

[60] A. D. Becke. Density-functional exchange-energy approximation with correct asymptotic behavior. *Phys. Rev. A*, 38:3098–3100, Sep 1988.

[61] Chengteh Lee, Weitao Yang, and Robert G. Parr. Development of the colle-salvetti correlation-energy formula into a functional of the electron density. *Phys. Rev. B*, 37:785–789, Jan 1988.

[62] Florian Weigend and Reinhart Ahlrichs. Balanced basis sets of split valence, triple zeta valence and quadruple zeta valence quality for H to Rn: Design and assessment of accuracy. *Phys. Chem. Chem. Phys.*, 7:3297–3305, 2005.

[63] Florian Weigend. Accurate coulomb-fitting basis sets for H to Rn. *Phys. Chem. Chem. Phys.*, 8:1057–1065, 2006.

[64] Stefan Grimme, Jens Antony, Stephan Ehrlich, and Helge Krieg. A consistent and accurate ab initio parametrization of density functional dispersion correction (DFT-D) for the 94 elements H-Pu. *J. Chem. Phys.*, 132:154104, 2010.

[65] Andrej Šali and Tom L Blundell. Comparative protein modelling by satisfaction of spatial restraints. *J. Mol. Biol.*, 234(3):779–815, 1993.

[66] Min-yi Shen and Andrej Sali. Statistical potential for assessment and prediction of protein structures. *Protein Sci.*, 15(11):2507–2524, 2006.

[67] Francisco Melo, Roberto Sánchez, and Andrej Sali. Statistical potentials for fold assessment. *Protein Sci.*, 11(2):430–448, 2002.

[68] Bino John and Andrej Sali. Comparative protein structure modeling by iterative alignment, model building and model assessment. *Nucleic Acids Res.*, 31(14):3982–3992, 2003.

[69] Robert D. Hancock. Molecular mechanics calculations as a tool in coordination chemistry. *Prog. Inorg. Chem.*, 37:187–291, 1989.

[70] Robert D. Hancock. Molecular mechanics calculations and metal ion recognition. *Acc. Chem. Res.*, 23:253–257, 1990.

[71] Stephen C. Hoops, Kenneth W. Anderson, and Kenneth M. Merz. Force field design for metalloproteins. *J. Am. Chem. Soc.*, 113(22):8262–8270, 1991.

[72] Martin B. Peters, Yue Yang, Bing Wang, László Füsti-Molnár, Michael N. Weaver, and Kenneth M. Merz. Structural survey of zinc-containing proteins and development of the zinc AMBER force field (ZAFF). *J. Chem. Theory Comput.*, 6(9):2935–2947, 2010.

[73] William L Jorgensen, David S Maxwell, and Julian Tirado-Rives. Development and Testing of the OPLS All-Atom Force Field on Conformational Energetics and Properties of Organic Liquids. *J. Am. Chem. Soc.*, 118:11225–11236, 1996.

[74] George A. Kaminski, Richard A. Friesner, Julian Tirado-Rives, and William L. Jorgensen. Evaluation and reparametrization of the OPLS-AA force field for proteins via comparison with accurate quantum chemical calculations on peptides. *J. Phys. Chem. B*, 105(28):6474–6487, 2001.

[75] Nikolaos G. Sgourakis, Yilin Yan, Scott A. McCallum, Chunyu Wang, and Angel E. Garcia. The Alzheimer's peptides Aβ40 and 42 adopt distinct conformations in water: A combined MD/NMR study. *J. Mol. Biol.*, 368(5):1448–1457, 2007.

[76] Stacey R. Gerben, Justin A. Lemkulm, Anne M. Brown, and David R. Bevan. Comparing atomistic molecular mechanics force fields for a difficult target: a case study on the Alzheimer's amyloid β-peptide. *J. Biomol. Struct. Dyn.*, 32:1817–1832, 2014.

[77] William Humphrey, Andrew Dalke, and Klaus Schulten. VMD: Visual molecular dynamics. *J. Mol. Graph.*, 14(1):33–38, 1996.

[78] TURBOMOLE V6.3 2011, a development of University of Karlsruhe and Forschungszentrum Karlsruhe GmbH, 1989-2007, TURBOMOLE GmbH, since 2007; available from `http://www.turbomole.com`.

[79] Jan O.A. De Kerpel and Ulf Ryde. Protein strain in blue copper proteins studied by free energy perturbations. *Proteins: Struc., Func., Bioinf.*, 36:157–174, 1999.

[80] Fu Lin and Renxiao Wang. Systematic derivation of AMBER force field parameters applicable to zinc-containing systems. *J. Chem. Theory Comput.*, 6(6):1852–1870, 2010.

[81] Christopher I. Bayly, Piotr Cieplak, Wendy Cornell, and Peter A. Kollman. A well-behaved electrostatic potential based method using charge restraints for deriving atomic charges: the RESP model. *J. Phys. Chem.*, 97(40):10269–10280, 1993.

[82] LiHong Hu and Ulf Ryde. Comparison of methods to obtain force-field parameters for metal sites. *J. Chem. Theory Comput.*, 7(8):2452–2463, 2011.

[83] M. J. Frisch, G. W. Trucks, H. B. Schlegel, G. E. Scuseria, M. A. Robb, J. R. Cheeseman, G. Scalmani, V. Barone, B. Mennucci, G. A. Petersson, H. Nakatsuji, M. Caricato, X. Li, H. P. Hratchian, A. F. Izmaylov, J. Bloino, G. Zheng, J. L. Sonnenberg, M. Hada, M. Ehara, K. Toyota, R. Fukuda, J. Hasegawa, M. Ishida, T. Nakajima, Y. Honda, O. Kitao, H. Nakai, T. Vreven, J. A. Montgomery, Jr., J. E. Peralta, F. Ogliaro, M. Bearpark, J. J. Heyd, E. Brothers, K. N. Kudin, V. N. Staroverov, R. Kobayashi, J. Normand, K. Raghavachari, A. Rendell, J. C. Burant, S. S. Iyengar, J. Tomasi, M. Cossi, N. Rega, J. M. Millam, M. Klene, J. E. Knox, J. B. Cross, V. Bakken, C. Adamo, J. Jaramillo, R. Gomperts, R. E. Stratmann, O. Yazyev, A. J. Austin, R. Cammi, C. Pomelli, J. W. Ochterski, R. L. Martin, K. Morokuma, V. G. Zakrzewski, G. A. Voth, P. Salvador, J. J. Dannenberg, S. Dapprich, A. D. Daniels, O. Farkas, J. B. Foresman, J. V. Ortiz, J. Cioslowski, , and D. J. Fox. Gaussian 09 Revision A.02. Gaussian Inc. Wallingford CT 2009.

[84] Junmei Wang, Wei Wang, Peter A. Kollman, and David A. Case. Automatic atom type and bond type perception in molecular mechanical calculations. *J. Mol. Graph. Model.*, 25(2):247–260, 2006.

[85] David Van Der Spoel, Erik Lindahl, Berk Hess, Gerrit Groenhof, Alan E. Mark, and Herman J. C. Berendsen. GROMACS: Fast, flexible, and free. *J. Comput. Chem.*, 26:1701–1718, 2005.

[86] Berk Hess, Carsten Kutzner, David van der Spoel, and Erik Lindahl. GROMACS 4: Algorithms for highly efficient, load-balanced, and scalable molecular simulation. *J. Chem. Theory Comput.*, 4(3):435–447, 2008.

[87] Sander Pronk, Szilárd Páll, Roland Schulz, Per Larsson, Pär Bjelkmar, Rossen Apostolov, Michael R. Shirts, Jeremy C. Smith, Peter M. Kasson, David van der Spoel, Berk Hess, and Erik Lindahl. GROMACS 4.5: a high-throughput and highly parallel open source molecular simulation toolkit. *Bioinformatics*, 29(7):845–854, 2013.

[88] Peter Comba and Rainer Remenyi. A new molecular mechanics force field for the oxidized form of blue copper proteins. *J. Comput. Chem.*, 23:697–705, 2002.

[89] Yanyan Zhu, Yanwei Su, Xichen Li, Yan Wang, and Guangju Chen. Evaluation of amber force field parameters for copper(II) with pyridylmethyl-amine and benzimidazolylmethyl-amine ligands: A quantum chemical study. *Chem. Phys. Lett.*, 455(4–6):354–360, 2008.

[90] Yuan-Ping Pang. Novel zinc protein molecular dynamics simulations: Steps toward antiangiogenesis for cancer treatment. *J. Mol. Model.*, 5:196–202, 1999.

[91] Peter Oelschlaeger, Marco Klahn, William A. Beard, Samuel H. Wilson, and Arieh Warshel. Magnesium-cationic dummy atom molecules enhance representation of DNA polymerase β in molecular dynamics simulations: Improved accuracy in studies of structural features and mutational effects. *J. Mol. Biol.*, 366(2):687–701, 2007.

[92] Akansha Saxena and David Sept. Multisite ion models that improve coordination and free energy calculations in molecular dynamics simulations. *J. Chem. Theory Comput.*, 9(8):3538–3542, 2013.

[93] Fernanda Duarte, Paul Bauer, Alexandre Barrozo, Beat Anton Amrein, Miha Purg, Johan Åqvist, and Shina Caroline Lynn Kamerlin. Force field independent metal parameters using a nonbonded dummy model. *J. Phys. Chem. B*, 118(16):4351–4362, 2014.

[94] Christopher D. Syme, Rebecca C. Nadal, Stephen E. J. Rigby, and John H. Viles. Copper binding to the amyloid-β (aβ) peptide associated with Alzheimer's disease: Folding, coordination geometry, pH dependence, stoichiometry, and affinity of Aβ-(1-28): Insights from a range of complementary spectroscopic techniques. *J. Biol. Chem.*, 279(18):18169–18177, 2004.

[95] Lingle Wang, Richard A. Friesner, and B. J. Berne. Replica exchange with solute scaling: A more efficient version of replica exchange with solute tempering (REST2). *J. Phys. Chem. B*, 115(30):9431–9438, 2011.

[96] Giovanni Bussi. Hamiltonian replica exchange in GROMACS: a flexible implementation. *Mol. Phys.*, 112(3-4):379–384, 2014.

[97] Gareth A. Tribello, Massimiliano Bonomi, Davide Branduardi, Carlo Camilloni, and Giovanni Bussi. PLUMED2: New feathers for an old bird. *Comput. Phys. Commun.*, 185(2):604–613, 2014.

[98] William L. Jorgensen, Jayaraman Chandrasekhar, Jeffry D. Madura, Roger W. Impey, and Michael L. Klein. Comparison of simple potential functions for simulating liquid water. *J. Chem. Phys.*, 79(2):926–935, 1983.

[99] Giovanni Bussi, Davide Donadio, and Michele Parrinello. Canonical sampling through velocity rescaling. *J. Chem. Phys.*, 126(1):014101–014101–7, 2007.

[100] M. Parrinello and A. Rahman. Polymorphic transitions in single crystals: A new molecular dynamics method. *J. Appl. Phys.*, 52(12):7182–7190, 1981.

[101] Tom Darden, Darrin York, and Lee Pedersen. Particle mesh Ewald: An N·log(N) method for Ewald sums in large systems. *J. Chem. Phys.*, 98(12):10089, 1993.

[102] Berk Hess, Henk Bekker, Herman J. C. Berendsen, and Johannes G. E. M. Fraaije. LINCS: A linear constraint solver for molecular simulations. *J. Comput. Chem.*, 18:1463–1472, 1997.

[103] Xavier Daura, Karl Gademann, Bernhard Jaun, Dieter Seebach, Wilfred F. van Gunsteren, and Alan E. Mark. Peptide folding: When simulation meets experiment. *Angew. Chem. Int. Ed.*, 38:236–240, 1999.

[104] Wolfgang Kabsch and Christian Sander. Dictionary of protein secondary structure: Pattern recognition of hydrogen-bonded and geometrical features. *Biopolymers*, 22(12):2577–2637, 1983.

[105] Deborah J. Tew, Stephen P. Bottomley, David P. Smith, Giuseppe D. Ciccotosto, Jeffrey Babon, Mark G. Hinds, Colin L. Masters, Roberto Cappai, and Kevin J. Barnham. Stabilization of neurotoxic soluble β-sheet-rich conformations of the Alzheimer's disease amyloid-β peptide. *Biophys. J.*, 94(7):2752–2766, 2008.

[106] Chun Wu, Megan M. Murray, Summer L. Bernstein, Margaret M. Condron, Gal Bitan, Joan-Emma Shea, and Michael T. Bowers. The structure of Aβ42 C-terminal fragments probed by a combined experimental and theoretical study. *J. Mol. Biol.*, 387(2):492–501, 2009.

[107] Erica A. Fradinger, Bernhard H. Monien, Brigita Urbanc, Aleksey Lomakin, Miao Tan, Huiyuan Li, Sean M. Spring, Margaret M. Condron, Luis Cruz, Cui-Wei Xie, George B. Benedek, and Gal Bitan. C-terminal peptides coassemble into Aβ42 oligomers and protect neurons against Aβ42-induced neurotoxicity. *Proceed. Natl. Acad. Sci. U.S.A.*, 105(37):14175–14180, 2008.

[108] Qin Nie, Xiao-guang Du, and Mei-yu Geng. Small molecule inhibitors of amyloid β peptide aggregation as a potential therapeutic strategy for Alzheimer's disease. *Acta Pharm. Sinic.*, 32(5):545–551, 2011.

5 Conclusions

In this thesis, we investigated by means of computer simulations, the effect of Cu^{2+} ions and environmental pH on the conformation and dimerization of the Aβ peptide. The role of these two external factors in the aggregation of Aβ peptide has already been demonstrated experimentally. However, the details of the molecular process is far from being understood. The elucidation of the Cu^{2+} coordination to Aβ peptides is essential to understand its role in the aggregation of the Aβ peptide. Some models have been proposed for the Aβ_{1-16}/Cu^{2+} complexes, based on experimental [76,77,79] and computational [74, 75,133] studies, but the mechanism of how Cu^{2+} modulates Aβ aggregation is still not clear. We used the enhanced sampling, made possible by H-REMD simulations [134, 136], to provide information about conformational transitions of Aβ peptide folding and aggregation upon Cu^{2+} binding and pH changes.

In our first study, we developed a set of OPLS-AA/L force field parameters to model the interactions between Aβ_{1-42} and Cu^{2+} as rigid bonds, coordinated by the amine and carbonyl groups of Asp1, His6 and His13 as suggested by Drew *et al.* [76]. After validation, the new parameters were applied to the H-REMD simulations of Aβ_{1-42}/Cu^{2+}. We also carried out H-REMD simulations for Aβ_{1-42} without Cu^{2+} at different pH values (5.3, 6.0, 7.4), to compare the effects of Cu^{2+} binding and acidic pH values on Aβ_{1-42} folding. The most abundant secondary structures sampled for all the four systems (A$\beta_{1-42}^{5.3,0}$, A$\beta_{1-42}^{6.0,1-}$, A$\beta_{1-42}^{6.9,Cu}$ and A$\beta_{1-42}^{7.4,3-}$) are bends, turns and random coils. Although the metal binding region of Aβ_{1-42} is rigidified upon Cu^{2+} binding, the conformational flexibility of the other regions of Aβ_{1-42} is increased, while decreasing pH values also enhance the conformational flexibility of Aβ_{1-42}. Moreover, more β-sheet structures were sampled for Aβ_{1-42}/Cu^{2+} binding and at low pH. Thus, we conclude that both Cu^{2+} binding and a mildly acidic pH accelerate the formation of β-sheets in Aβ_{1-42}, which may promote Aβ peptide aggregation.

For a more realistic modelling of the Cu^{2+} ion used in MD simulations, in the second study we developed a dummy model for Cu^{2+} (CuDum). A dummy model is able to allow for ligand exchange and interconversion between different metal coordination spheres, but bonded model is not. CuDum was able to reproduce both the Jahn-Teller effect and the experimental hydration free energy of Cu^{2+}. Our model was also able to maintain the stable coordination geometries of metalloproteins during MD simulations without assigning

artificial bonds between metal center and ligands. Furthermore, a dummy model for Zn^{2+}, based on a previous proposed model [183], was also derived (ZnDum). Our models were able to reproduce both the square planar Cu^{2+} and tetrahedral Zn^{2+} geometries in the metal binding region of the amyloid-β peptide, Aβ_{1-16}, and the Cu-Zn superoxide dismutase (CuZnSOD). The comparison between Aβ_{1-16}/CuDum and Aβ_{1-16}/ZnDum revealed a lower binding affinity for ZnDum, which is in agreement with experimental findings [4,184]. Two independent 100-ns MD simulations of CuZnSOD further confirmed that it is possible to apply two dummy models together without artificial repulsion between the two metal centers. Thus, the novel dummy models of Cu^{2+} and Zn^{2+} developed in this work will be of great importance for future studies investigating the interaction between proteins and metal ions.

Furthermore, the role of copper ion in the dimerization of Aβ_{1-42} was investigated in our third study, wherein both a bonded and a nonbonded model for Cu^{2+} were used. We developed OPLS-AA/L force field parameters for the bonded model to describe the interactions within the Cu^{2+} coordination center: one copper ion coordinated by four His residues (His13 and His14) from each of the two Aβ_{1-42} peptides composing the dimer [185]. These newly developed parameters were then used in the H-REMD simulation of 2Aβ_{1-42}/Cu^{2+}. The nonbonded model for Cu^{2+} we developed [186] was also applied in this study. We found that the bonded Cu^{2+} greatly decreases the flexibility of Aβ_{1-42} in the 2Aβ_{1-42}/Cu^{2+} dimer, while the nonbonded CuDum only slightly stabilizes Aβ_{1-42} compared to the Aβ_{1-42} dimer system without Cu^{2+}. Moreover, a propensity of around 10-15% of β-sheets and <10% of helices were observed for either of the three systems, close to which were shown in previous experiments [15] and simulations [187,188]. Cu^{2+} promotes the formation of β-hairpins at the CHC and C-terminal regions of Aβ_{1-42}, being consistent with our previous study on monomeric Aβ_{1-42} with Cu^{2+}. When using the nonbonded Cu^{2+} model during the H-REMD simulation, CuDum was not stable at the coordination center and ligand exchange was observed. Both simulations involving copper (II) revealed that Cu^{2+} binding to Aβ_{1-42} is able to reduce the propensity of Aβ_{1-42} to form salt bridges in the dimer system. In short, our simulations reveal that Cu^{2+} promotes β-hairpins formation in the CHC and C-terminal regions in the dimerization of Aβ_{1-42}, partially accounting for the enhanced toxicity of Aβ/Cu^{2+} complexes. Future simulations of bigger oligomers (trimers, tetramers *etc.*) are needed to further understand the roles of Cu^{2+} during Aβ aggregation.

Our results on the effects of Cu^{2+} binding and pH value on the Aβ_{1-42} folding, and the roles of Cu^{2+} in the dimerization of Aβ_{1-42} reveals crucial information regarding the protein-ion interaction at atomistic resolution and the role of Cu^{2+} in the early aggregation of Aβ_{1-42} peptide of extreme relevance to its toxicity. Future computational studies in combination with experiments focused on elucidating the conformations of Aβ_{1-42}

oligomers in complex with Cu^{2+} will provide invaluable information regarding the molecular details leading to their toxicity. Moreover, our novel dummy model for Cu^{2+} was shown to successfully model ligand exchange, and can be used in future studies of the aggregation of Aβ peptide involving Cu^{2+} and also other folded copper proteins, without the rigid constraints used in the models used by others thus far.

Bibliography

[1] Alzheimer's Association. 2015 Alzheimer's disease facts and figures. *Alzheimers Dement.*, 11(3):332–384, 2015.

[2] Liesi E Hebert, Jennifer Weuve, Paul A Scherr, and Denis A Evans. Alzheimer disease in the United States (2010–2050) estimated using the 2010 census. *Neurol.*, 80(19):1778–1783, 2013.

[3] Arvi Rauk. The chemistry of Alzheimer's disease. *Chem. Soc. Rev.*, 38(9):2698–2715, 2009.

[4] Kasper P. Kepp. Bioinorganic chemistry of Alzheimer's disease. *Chem. Rev.*, 112(10):5193–5239, 2012.

[5] World Health Organization et al. *Dementia: a public health priority.* World Health Organization, 2012.

[6] JA Hardy and GA Higgins. Alzheimer's disease: the amyloid cascade hypothesis. *Science*, 256(5054):184–185, 1992.

[7] John Hardy and Dennis J. Selkoe. The amyloid hypothesis of Alzheimer's disease: Progress and problems on the road to therapeutics. *Science*, 297(5580):353–356, 2002.

[8] Peter Faller and Christelle Hureau. Bioinorganic chemistry of copper and zinc ions coordinated to amyloid-β peptide. *Dalton Trans.*, 21:1080–1094, 2009.

[9] Peter Faller, Christelle Hureau, and Olivia Berthoumieu. Role of metal ions in the self-assembly of the Alzheimer's amyloid-β peptide. *Inorg. Chem.*, 52:12193–12206, 2013.

[10] Murray Coles, Wendy Bicknell, Andrew A. Watson, David P. Fairlie, , and David J. Craik. Solution structure of amyloid β-peptide(1-40) in a water-micelle environment. is the membrane-spanning domain where we think it is? *Biochemistry*, 37(31):11064–11077, 1998.

[11] Simona Tomaselli, Veronica Esposito, Paolo Vangone, Nico A. J. van Nuland, Alexandre M. J. J. Bonvin, Remo Guerrini, Teodorico Tancredi, Piero A. Temussi, and Delia Picone. The α-to-β conformational transition of Alzheimer's Aβ-(1-42) peptide in aqueous media is reversible: A step by step conformational analysis suggests the location of β conformation seeding. *ChemBioChem*, 7(2):257–267, 2006.

[12] Orlando Crescenzi, Simona Tomaselli, Remo Guerrini, Severo Salvadori, Anna M. D'Ursi, Piero Andrea Temussi, and Delia Picone. Solution structure of the Alzheimer amyloid β-peptide (1-42) in an apolar microenvironment. *Eur. J. Biochem.*, 269(22):5642–5648, 2002.

[13] William Humphrey, Andrew Dalke, and Klaus Schulten. VMD: Visual molecular dynamics. *J. Mol. Graph.*, 14(1):33–38, 1996.

[14] Liming Hou, Haiyan Shao, Yongbo Zhang, Hua Li, Nanda K. Menon, Elizabeth B. Neuhaus, John M. Brewer, In-Ja L. Byeon, Dale G. Ray, Michael P. Vitek, Takashi Iwashita, Ronald A. Makula, Alan B. Przybyla, , and Michael G. Zagorski. Solution NMR studies of the Aβ(1-40) and Aβ(1-42) peptides establish that the Met35 oxidation state affects the mechanism of amyloid formation. *J. Am. Chem. Soc.*, 126(7):1992–2005, 2004.

[15] Kenjiro Ono, Margaret M. Condron, and David B. Teplow. Structure–neurotoxicity relationships of amyloid β-protein oligomers. *Proc. Natl. Acad. Sci. U.S.A.*, 106(35):14745–14750, 2009.

[16] Kenjiro Ono, Margaret M. Condron, and David B. Teplow. Effects of the English (H6R) and Tottori (D7N) familial Alzheimer disease mutations on amyloid β-protein assembly and toxicity. *J. Biol. Chem.*, 285(30):23186–23197, 2010.

[17] Yilin Yan and Chunyu Wang. Aβ42 is more rigid than Aβ40 at the C terminus: Implications for Aβ aggregation and toxicity. *J. Mol. Biol.*, 364(5):853–862, 2006.

[18] Nikolaos G. Sgourakis, Yilin Yan, Scott A. McCallum, Chunyu Wang, and Angel E. Garcia. The Alzheimer's peptides Aβ40 and 42 adopt distinct conformations in water: A combined MD/NMR study. *J. Mol. Biol.*, 368(5):1448–1457, 2007.

[19] Noel D. Lazo, Marianne A. Grant, Margaret C. Condron, Alan C. Rigby, and David B. Teplow. On the nucleation of amyloid β-protein monomer folding. *Protein Sci.*, 14(6):1581–1596, 2005.

[20] Wei Chen, Normand Mousseau, and Philippe Derreumaux. The conformations of the amyloid-β (21-30) fragment can be described by three families in solution. *J. Chem. Phys.*, 125(8):084911, 2006.

[21] Yassmine Chebaro, Normand Mousseau, and Philippe Derreumaux. Structures and thermodynamics of Alzheimer's amyloid-β Aβ(16-35) monomer and dimer by replica exchange molecular dynamics simulations: Implication for full-length Aβ fibrillation. *J. Phys. Chem. B*, 113(21):7668–7675, 2009.

[22] Duilio F. Raffa and Arvi Rauk. Molecular dynamics study of the beta amyloid peptide of Alzheimer's disease and its divalent copper complexes. *J. Phys. Chem. B*, 111(14):3789–3799, 2007.

[23] Olujide O Olubiyi and Birgit Strodel. Structures of the amyloid β-peptides Aβ_{1-40} and Aβ_{1-42} as influenced by pH and a D-peptide. *J. Phys. Chem. B*, 116(10):3280–3291, 2012.

[24] Yuji Sugita and Yuko Okamoto. Replica-exchange molecular dynamics method for protein folding. *Chem. Phys. Lett.*, 314(1-2):141–151, 1999.

[25] David J. Rosenman, Christopher R. Connors, Wen Chen, Chunyu Wang, and Angel E. García. Aβ monomers transiently sample oligomer and fibril-like configurations: Ensemble characterization using a combined MD/NMR approach. *J. Mol. Biol.*, 425(18):3338–3359, 2013.

[26] Jessica Nasica-Labouze, Phuong H. Nguyen, Fabio Sterpone, Olivia Berthoumieu, Nicolae-Viorel Buchete, Sébastien Coté, Alfonso De Simone, Andrew J. Doig, Peter Faller, Angel Garcia, Alessandro Laio, Mai Suan Li, Simone Melchionna, Normand Mousseau, Yuguang Mu, Anant Paravastu, Samuela Pasquali, David J. Rosenman, Birgit Strodel, Bogdan Tarus, John H. Viles, Tong Zhang, Chunyu Wang, and Philippe Derreumaux. Amyloid β protein and Alzheimer's disease: When computer simulations complement experimental studies. *Chem. Rev.*, 115(9):3518–3563, 2015.

[27] Michael R. Nichols, Melissa A. Moss, Dana Kim Reed, Wen-Lang Lin, Rajendrani Mukhopadhyay, Jan H. Hoh, , and Terrone L. Rosenberry. Growth of β-amyloid(1-40) protofibrils by monomer elongation and lateral association. characterization of distinct products by light scattering and atomic force microscopy. *Biochemistry*, 41(19):6115–6127, 2002.

[28] Sidhartha M. Chafekar, Frank Baas, and Wiep Scheper. Oligomer-specific Aβ toxicity in cell models is mediated by selective uptake. *Biochim. Biophys. Acta (BBA) - Mol. Basis Dis.*, 1782(9):523–531, 2008.

[29] Masafumi Sakono and Tamotsu Zako. Amyloid oligomers: formation and toxicity of Aβ oligomers. *FEBS J.*, 277:1348–1358, 2010.

[30] Iryna Benilova, Eric Karran, and Bart De Strooper. The toxic Aβ oligomer and Alzheimer's disease: an emperor in need of clothes. *Nat. Neurosci.*, 15:349–357, 2012.

[31] Rakez Kayed and Cristian A Lasagna-Reeves. Molecular mechanisms of amyloid oligomers toxicity. *J. Alzheimers Dis.*, 33:S67–S78, 2013.

[32] F. Chiti and C. M. Dobson. Protein misfolding, functional amyloid, and human disease. *Annu. Rev. Biochem.*, 75:333–366, 2006.

[33] Deborah J. Tew, Stephen P. Bottomley, David P. Smith, Giuseppe D. Ciccotosto, Jeffrey Babon, Mark G. Hinds, Colin L. Masters, Roberto Cappai, and Kevin J. Barnham. Stabilization of neurotoxic soluble β-sheet-rich conformations of the Alzheimer's disease amyloid-β peptide. *Biophys. J.*, 94(7):2752–2766, 2008.

[34] Robin Roychaudhuri, Mingfeng Yang, Minako M. Hoshi, and David B. Teplow. Amyloid β-protein assembly and Alzheimer disease. *J. Biol. Chem.*, 284(8):4749–4753, 2009.

[35] Wolfgang Hoyer, Caroline Grönwall, Andreas Jonsson, Stefan Stähl, and Torleif Härd. Stabilization of a β-hairpin in monomeric Alzheimer's amyloid-β peptide inhibits amyloid formation. *Proceed. Natl. Acad. Sci. U.S.A*, 105(13):5099–5104, 2008.

[36] Liping Yu, Rohinton Edalji, John E. Harlan, Thomas F. Holzman, Ana Pereda Lopez, Boris Labkovsky, Heinz Hillen, Stefan Barghorn, Ulrich Ebert, Paul L. Richardson, Laura Miesbauer, Larry Solomon, Diane Bartley, Karl Walter, Robert W. Johnson, Philip J. Hajduk, and Edward T. Olejniczak. Structural characterization of a soluble amyloid β-peptide oligomer. *Biochemistry*, 48(9):1870–1877, 2009.

[37] Mahiuddin Ahmed, Judianne Davis, Darryl Aucoin, Takeshi Sato, Shivani Ahuja, Saburo Aimoto, James I Elliott, William E Van Nostrand, and Steven O Smith. Structural conversion of neurotoxic amyloid-β_{1-42} oligomers to fibrils. *Nat. Struct. Mol. Biol.*, 17(5):561–567, 2010.

[38] William M. Tay, Danting Huang, Terrone L. Rosenberry, and Anant K. Paravastu. The Alzheimer's amyloid-β(1-42) peptide forms off-pathway oligomers and fibrils that are distinguished structurally by intermolecular organization. *J. Mol. Biol.*, 425(14):2494–2508, 2013.

[39] Ryan K. Spencer, Hao Li, and James S. Nowick. X-ray crystallographic structures of trimers and higher-order oligomeric assemblies of a peptide derived from Aβ_{17-36}. *J. Am. Chem. Soc.*, 136(15):5595–5598, 2014.

[40] Eric Hayden and David Teplow. Amyloid β-protein oligomers and Alzheimer's disease. *Alzheimer's Res. Ther.*, 5(6):60, 2013.

[41] Hideyo Inouye, Paul E Fraser, and Daniel A Kirschner. Structure of β-crystallite assemblies formed by Alzheimer β-amyloid protein analogues: analysis by x-ray diffraction. *Biophys. J.*, 64(2):502–519, 1993.

[42] Thorsten Lührs, Christiane Ritter, Marc Adrian, Dominique Riek-Loher, Bernd Bohrmann, Heinz Döbeli, David Schubert, and Roland Riek. 3D structure of Alzheimer's amyloid-β(1-42) fibrils. *Proceed. Natl. Acad. Sci. U.S.A*, 102(48):17342–17347, 2005.

[43] Oleg N. Antzutkin, John J. Balbach, Richard D. Leapman, Nancy W. Rizzo, Jennifer Reed, and Robert Tycko. Multiple quantum solid-state NMR indicates a parallel, not antiparallel, organization of β-sheets in Alzheimer's β-amyloid fibrils. *Proceed. Natl. Acad. Sci. U.S.A.*, 97(24):13045–13050, 2000.

[44] Aneta T. Petkova, Yoshitaka Ishii, John J. Balbach, Oleg N. Antzutkin, Richard D. Leapman, Frank Delaglio, and Robert Tycko. A structural model for Alzheimer's β-amyloid fibrils based on experimental constraints from solid state NMR. *Proceed. Natl. Acad. Sci. U.S.A.*, 99(26):16742–16747, 2002.

[45] Robert Tycko. Insights into the amyloid folding problem from solid-state NMR. *Biochemistry*, 42(11):3151–3159, 2003.

[46] Aneta T. Petkova, Wai-Ming Yau, , and Robert Tycko. Experimental constraints on quaternary structure in Alzheimer's β-amyloid fibrils. *Biochemistry*, 45(2):498–512, 2006.

[47] Anant K. Paravastu, Richard D. Leapman, Wai-Ming Yau, and Robert Tycko. Molecular structural basis for polymorphism in Alzheimer's β-amyloid fibrils. *Proceed. Natl. Acad. Sci. U.S.A*, 105(47):18349–18354, 2008.

[48] Wei Qiang, Wai-Ming Yau, Yongquan Luo, Mark P. Mattson, and Robert Tycko. Antiparallel β-sheet architecture in Iowa-mutant β-amyloid fibrils. *Proceed. Natl. Acad. Sci. U.S.A.*, 109(12):4443–4448, 2012.

[49] Jun-Xia Lu, Wei Qiang, Wai-Ming Yau, Charles D. Schwieters, Stephen C. Meredith, and Robert Tycko. Molecular structure of β-amyloid fibrils in Alzheimer's disease brain tissue. *Cell*, 154(6):1257–1268, 2013.

[50] Yiling Xiao, Buyong Ma, Dan McElheny, Sudhakar Parthasarathy, Fei Long, Minako Hoshi, Ruth Nussinov, and Yoshitaka Ishii. Aβ(1-42) fibril structure illuminates self-recognition and replication of amyloid in Alzheimer's disease. *Nat. Struct. Mol. Biol.*, 22:499–505, 2015.

[51] Matthias Schmidt, Alexis Rohou, Keren Lasker, Jay K. Yadav, Cordelia Schiene-Fischer, Marcus Fändrich, and Nikolaus Grigorieff. Peptide dimer structure in an Aβ(1-42) fibril visualized with cryo-EM. *Proceed. Natl. Acad. Sci. U.S.A.*, 112(38):11858–11863, 2015.

[52] Muralidhar L Hegde, P Bharathi, Anitha Suram, Chitra Venugopal, Ramya Jagannathan, Pankaj Poddar, Pullabhatla Srinivas, Kumar Sambamurti, Kosagisharaf Jagannatha Rao, Janez Scancar, et al. Challenges associated with metal chelation therapy in Alzheimer's disease. *J. Alzheimers Dis.*, 17(3):457, 2009.

[53] Craig S. Atwood, Richard C. Scarpa, Xudong Huang, Robert D. Moir, Walton D. Jones, David P. Fairlie, Rudolph E. Tanzi, and Ashley I. Bush. Characterization of copper interactions with Alzheimer amyloid β peptides. *J. Neurochem.*, 75:1219–1233, 2000.

[54] Jesse W. Karr and Veronika A. Szalai. Cu(II) binding to monomeric, oligomeric, and fibrillar forms of the Alzheimer's disease amyloid-β peptide. *Biochemistry*, 47(17):5006–5016, 2008.

[55] Luc Guilloreau, Luminita Damian, Yannick Coppel, Honoré Mazarguil, Mathias Winterhalter, and Peter Faller. Structural and thermodynamical properties of Cu^{II} amyloid-β16/28 complexes associated with Alzheimer's disease. *J.Biol. Inorg. Chem.*, 11:1024–1038, 2006.

[56] William Garzon-Rodriguez, Anatoly K. Yatsimirsky, and Charles G. Glabe. Binding of Zn(II), Cu(II), and Fe(II) ions to Alzheimer's Aβ peptide studied by fluorescence. *Bioorg. Med. Chem. Lett.*, 9(15):2243–2248, 1999.

[57] Dianlu Jiang, Lijie Men, Jianxiu Wang, Yi Zhang, Sara Chickenyen, Yinsheng Wang, , and Feimeng Zhou. Redox reactions of copper complexes formed with different β-amyloid peptides and their neuropathalogical relevance. *Biochemistry*, 46(32):9270–9282, 2007.

[58] Cyril C. Curtain, Feda Ali, Irene Volitakis, Robert A. Cherny, Raymond S. Norton, Konrad Beyreuther, Colin J. Barrow, Colin L. Masters, Ashley I. Bush, and Kevin J. Barnham. Alzheimer's disease amyloid-β binds copper and zinc to generate an allosterically ordered membrane-penetrating structure containing superoxide dismutase-like subunits. *J. Biol. Chem.*, 276:20466–20473, 2001.

[59] Anna K. Tickler, Danielle G. Smith, Giuseppe D. Ciccotosto, Deborah J. Tew, Cyril C. Curtain, Darryl Carrington, Colin L. Masters, Ashley I. Bush, Robert A. Cherny, Roberto Cappai, John D. Wade, and Kevin J. Barnham. Methylation of the imidazole side chains of the Alzheimer disease amyloid-β peptide results in abolition of superoxide dismutase-like structures and inhibition of neurotoxicity. *J. Biol. Chem.*, 280:13355–13363, 2005.

[60] David P. Smith, Danielle G. Smith, Cyril C. Curtain, John F. Boas, John R. Pilbrow, Giuseppe D. Ciccotosto, Tong-Lay Lau, Deborah J. Tew, Keyla Perez, John D. Wade, Ashley I. Bush, Simon C. Drew, Frances Separovic, Colin L. Masters, Roberto Cappai, and Kevin J. Barnham. Copper-mediated amyloid-β toxicity is associated with an intermolecular histidine bridge. *J. Biol. Chem.*, 281:15145–15154, 2006.

[61] Francis Hane, Gary Tran, Simon J. Attwood, and Zoya Leonenko. Cu^{2+} affects amyloid-β (1-42) aggregation by increasing peptide-peptide binding forces. *PLoS ONE*, 8:e59005, 03 2013.

[62] Teresa Kowalik-Jankowska, Monika Ruta, Kornelia Wiśniewska, and Leszek Lankiewicz. Coordination abilities of the 1-16 and 1-28 fragments of β-amyloid peptide towards copper(II) ions: a combined potentiometric and spectroscopic study. *J. Inorg. Biochem.*, 95(4):270–282, 2003.

[63] Lanying Q. Hatcher, Lian Hong, William D. Bush, Tessa Carducci, and John D. Simon. Quantification of the binding constant of copper(II) to the amyloid-beta peptide. *J. Phys. Chem. B*, 112(27):8160–8164, 2008.

[64] Claire J. Sarell, Christopher D. Syme, Stephen E. J. Rigby, and John H. Viles. Copper(II) binding to amyloid-β fibrils of Alzheimer's disease reveals a picomolar affinity: Stoichiometry and coordination geometry are independent of Aβ oligomeric form. *Biochemistry*, 48(20):4388–4402, 2009.

[65] T. Hamaguchi, K. Ono, and M. Yamada. Anti-amyloidogenic therapies: strategies for prevention and treatment of Alzheimer's disease. *Cell. Mol. Life Sci.*, 63(13):1538–1552, 2006.

[66] Małgorzata Rózga, Magdalena Sokołowska, AnnaMaria Protas, and Wojciech Bal. Human serum albumin coordinates Cu(II) at its N-terminal binding site with 1 pM affinity. *J. Biol. Inorg. Chem.*, 12(6):913–918, 2007.

[67] Peter Faller. Copper and zinc binding to amyloid-β: Coordination, dynamics, aggregation, reactivity and metal-ion transfer. *ChemBioChem*, 10(18):2837–2845, 2009.

[68] Yifat Miller, Buyong Ma, and Ruth Nussinov. Metal binding sites in amyloid oligomers: Complexes and mechanisms. *Coord. Chem. Rev.*, 256(19-20):2245–2252, 2012.

[69] Séverine Zirah, Sergey A. Kozin, Alexey K. Mazur, Alain Blond, Michel Cheminant, Isabelle Ségalas-Milazzo, Pascale Debey, and Sylvie Rebuffat. Structural changes of region 1-16 of the Alzheimer disease amyloid β-peptide upon zinc binding and in vitro aging. *J. Biol. Chem.*, 281(4):2151–2161, 2006.

[70] Elena Gaggelli, Anna Janicka-Klos, Elzbieta Jankowska, Henryk Kozlowski, Caterina Migliorini, Elena Molteni, Daniela Valensin, Gianni Valensin, and Ewa Wieczerzak. NMR studies of the Zn^{2+} interactions with rat and human β-amyloid (1-28) peptides in water-micelle environment. *J. Phys. Chem. B*, 112(1):100–109, 2008.

[71] Velia Minicozzi, Francesco Stellato, Massimiliano Comai, Mauro Dalla Serra, Cristina Potrich, Wolfram Meyer-Klaucke, and Silvia Morante. Identifying the minimal copper- and zinc-binding site sequence in amyloid-β peptides. *J. Biol. Chem.*, 283:10784–10792, 2008.

[72] Christopher D. Syme, Rebecca C. Nadal, Stephen E. J. Rigby, and John H. Viles. Copper binding to the amyloid-β (aβ) peptide associated with Alzheimer's disease: Folding, coordination geometry, pH dependence, stoichiometry, and affinity of Aβ-(1-28): Insights from a range of complementary spectroscopic techniques. *J. Biol. Chem.*, 279(18):18169–18177, 2004.

[73] Yu Lu, Michel Prudent, Liang Qiao, Manuel A. Mendez, and Hubert H. Girault. Copper(I) and copper(II) binding to β-amyloid 16 (Aβ16) studied by electrospray ionization mass spectrometry. *Metallomics*, 2:474–479, 2010.

[74] Jorge Alí-Torres, Jean-Didier Maréchal, Luis Rodríguez-Santiago, and Mariona Sodupe. Three dimensional models of Cu^{2+}-Aβ(1-16) complexes from computational approaches. *J. Am. Chem. Soc.*, 133(38):15008–15014, 2011.

[75] Jorge Alí-Torres, Andrea Mirats, Jean-Didier Maréchal, Luis Rodríguez-Santiago, and Mariona Sodupe. 3d structures and redox potentials of Cu^{2+}-Aβ(1-16) complexes at different pH: A computational study. *J. Phys. Chem. B*, 118(18):4840–4850, 2014.

[76] Simon C. Drew, Christopher J. Noble, Colin L. Masters, Graeme R. Hanson, and Kevin J. Barnham. Pleomorphic copper coordination by Alzheimer's disease amyloid-β peptide. *J. Am. Chem. Soc.*, 131(3):1195–1207, 2009.

[77] Simon C. Drew, Colin L. Masters, and Kevin J. Barnham. Alanine-2 carbonyl is an oxygen ligand in Cu^{2+} coordination of Alzheimer's disease amyloid-β peptide–relevance to N-terminally truncated forms. *J. Am. Chem. Soc.*, 131(25):8760–8761, 2009.

[78] Simon C. Drew and Kevin J. Barnham. The heterogeneous nature of Cu^{2+} interactions with Alzheimer's amyloid-β peptide. *Acc. Chem. Res.*, 44(11):1146–1155, 2011.

[79] Pierre Dorlet, Serge Gambarelli, Peter Faller, and Christelle Hureau. Pulse EPR spectroscopy reveals the coordination sphere of copper(II) ions in the 1-16 amyloid-β peptide: A key role of the first two N-terminus residues. *Angew. Chem. Int. Ed.*, 48(49):9273–9276, 2009.

[80] Héléne Eury, Christian Bijani, Peter Faller, and Christelle Hureau. Copper(II) coordination to amyloid-β: Murine versus human peptide. *Angew. Chem. Int. Ed.*, 50:901–905, 2011.

[81] Yuji Yoshiike, Kentaro Tanemura, Ohoshi Murayama, Takumi Akagi, Miyuki Murayama, Shinji Sato, Xiaoyan Sun, Nobuo Tanaka, and Akihiko Takashima. New insights on how metals disrupt amyloid β-aggregation and their effects on amyloid-β cytotoxicity. *J. Biol. Chem.*, 276(34):32293–32299, 2001.

[82] Emily House, Joanna Collingwood, Ayesha Khan, Olga Korchazkina, Guy Berthon, and Christopher Exley. Aluminium, iron, zinc and copper influence the in vitro formation of amyloid fibrils of $A\beta_{42}$ in a manner which may have consequences for metal chelation therapy in Alzheimer's disease. *J. Alzheimers Dis.*, 6(3):291–301, 2004.

[83] Bakthisaran Raman, Tadato Ban, Kei-ichi Yamaguchi, Miyo Sakai, Tomoji Kawai, Hironobu Naiki, and Yuji Goto. Metal ion-dependent effects of clioquinol on the fibril growth of an amyloid β peptide. *J. Bio. Chem.*, 280(16):16157–16162, 2005.

[84] Jungki Ryu, Koyeli Girigoswami, Chanki Ha, Sook Hee Ku, and Chan Beum Park. Influence of multiple metal ions on β-amyloid aggregation and dissociation on a solid surface. *Biochemistry*, 47(19):5328–5335, 2008.

[85] Vello Tõugu, Ann Karafin, Kairit Zovo, Roger S. Chung, Claire Howells, Adrian K. West, and Peep Palumaa. Zn(II)- and Cu(II)-induced non-fibrillar aggregates of amyloid-β (1-42) peptide are transformed to amyloid fibrils, both spontaneously and under the influence of metal chelators. *J. Neurochem.*, 110(6):1784–1795, 2009.

[86] Massimo Innocenti, Emanuele Salvietti, Martina Guidotti, Angela Casini, Silvano Bellandi, Maria Luisa Foresti, Chiara Gabbiani, Andrea Pozzi, Paolo Zatta, and Luigi Messori. Trace copper (II) or zinc (II) ions drastically modify the aggregation behavior of amyloid-β_{1-42}: an AFM study. *J. Alzheimers Dis.*, 19(4):1323–1329, 2009.

[87] Xudong Huang, Craig S. Atwood, Robert D. Moir, Mariana A. Hartshorn, Rudolph E. Tanzi, and Ashley I. Bush. Trace metal contamination initiates the apparent auto-aggregation, amyloidosis, and oligomerization of Alzheimer's Aβ peptides. *J. Biol. Inorg. Chem.*, 9(8):954–960, 2004.

[88] F. Ricchelli, D. Drago, B. Filippi, G. Tognon, and P. Zatta. Aluminum-triggered structural modifications and aggregation of β-amyloids. *Cell. Mol. Life Sci.*, 62(15):1724–1733, 2005.

[89] Cristina Rodríguez-Rodríguez, Natalia Sánchez de Groot, Albert Rimola, Ángel Álvarez-Larena, Vega Lloveras, José Vidal-Gancedo, Salvador Ventura, Josep Vendrell, Mariona Sodupe, and Pilar González-Duarte. Design, selection, and characterization of thioflavin-based intercalation compounds with metal chelating properties for application in Alzheimer's disease. *J. Am. Chem. Soc.*, 131(4):1436–1451, 2009.

[90] Christine Talmard, Rodrigue Leuma Yona, and Peter Faller. Mechanism of zinc(II)-promoted amyloid formation: Zinc(II) binding facilitates the transition from the partially α-helical conformer to aggregates of amyloid β protein(1-28). *J. Biol. Inorg. Chem.*, 14(3):449–455, 2009.

[91] Jin Zou, Katsushi Kajita, and Naoki Sugimoto. Cu^{2+} inhibits the aggregation of amyloid β-peptide(1-42) in vitro. *Angew. Chem. Int. Ed.*, 40(12):2274–2277, 2001.

[92] Emily House, Matthew Mold, Joanna Collingwood, Alex Baldwin, Steven Goodwin, and Christopher Exley. Copper abolishes the β-sheet secondary structure of preformed amyloid fibrils of amyloid-β_{42}. *J. Alzheimers Dis.*, 18(4):811–817, 2009.

[93] David P. Smith, Giuseppe D. Ciccotosto, Deborah J. Tew, Michelle T. Fodero-Tavoletti, Timothy Johanssen, Colin L. Masters, Kevin J. Barnham, and Roberto Cappai. Concentration dependent Cu^{2+} induced aggregation and dityrosine formation of the Alzheimer's disease amyloid-β peptide. *Biochemistry*, 46(10):2881–2891, 2007.

[94] Xiao-Hui Yang, Han-Chang Huang, Lin Chen, Wei Xu, and Zhao-Feng Jiang. Coordinating to three histidine residues: Cu(II) promotes oligomeric and fibrillar amyloid-β peptide to precipitate in a non-β aggregation manner. *J. Alzheimers Dis.*, 18(4):799–810, 2008.

[95] Sangmi Jun, Joel R. Gillespie, Byong kyu Shin, and Sunil Saxena. The second Cu(II)-binding site in a proton-rich environment interferes with the aggregation of amyloid-β(1-40) into amyloid fibrils. *Biochemistry*, 48(45):10724–10732, 2009.

[96] Genevieve M. J. A. Klug, Dusan Losic, Supundi, S. Subasinghe, Marie-Isabel Aguilar, Lisandra L. Martin, and David H. Small. β-amyloid protein oligomers induced by metal ions and acid pH are distinct from those generated by slow spontaneous ageing at neutral pH. *Eur. J. Biochem.*, 270(21):4282–4293, 2003.

[97] Jeppe T. Pedersen, Kaare Teilum, Niels H. H. Heegaard, Jesper Østergaard, Hans-Werner Adolph, and Lars Hemmingsen. Rapid formation of a preoligomeric peptide-metal-peptide complex following copper(II) binding to amyloid β peptides. *Angew. Chem. Int. Ed.*, 50(11):2532–2535, 2011.

[98] K. Garai, P. Sengupta, B. Sahoo, and S. Maiti. Selective destabilization of soluble amyloid β oligomers by divalent metal ions. *Biochem. Biophys. Res. Commun.*, 345(1):210 – 215, 2006.

[99] K. Garai, B. Sahoo, S. K. Kaushalya, R. Desai, , and S. Maiti. Zinc lowers amyloid-β toxicity by selectively precipitating aggregation intermediates. *Biochemistry*, 46(37):10655–10663, 2007.

[100] Dun-Sheng Yang, JoAnne McLaurin, Kefeng Qin, David Westaway, and Paul E. Fraser. Examining the zinc binding site of the amyloid-β peptide. *Eur. J. Biochem.*, 267(22):6692–6698, 2000.

[101] Takashi Miura, Kiyoko Suzuki, Naohito Kohata, and Hideo Takeuchi. Metal binding modes of Alzheimer's amyloid β-peptide in insoluble aggregates and soluble complexes. *Biochemistry*, 39(23):7024–7031, 2000.

[102] Kiyoko Suzuki, Takashi Miura, and Hideo Takeuchi. Inhibitory effect of copper(II) on zinc(II)-induced aggregation of amyloid β-peptide. *Biochem. Biophys. Res. Commun.*, 285(4):991–996, 2001.

[103] Chanki Ha, Jungki Ryu, , and Chan Beum Park. Metal ions differentially influence the aggregation and deposition of Alzheimer's β-amyloid on a solid template. *Biochemistry*, 46(20):6118–6125, 2007.

[104] Matthew Mold, Larissa Ouro-Gnao, Beata M Wieckowski, and Christopher Exley. Copper prevents amyloid-β_{1-42} from forming amyloid fibrils under near-physiological conditions in vitro. *Sci. Rep.*, 3:1256, 2013.

[105] Jesse W. Karr, Lauren J. Kaupp, and Veronika A. Szalai. Amyloid-β binds Cu^{2+} in a mononuclear metal ion binding site. *J. Am. Chem. Soc.*, 126(41):13534–13538, 2004.

[106] Claire J. Sarell, Shane R. Wilkinson, and John H. Viles. Substoichiometric levels of Cu^{2+} ions accelerate the kinetics of fiber formation and promote cell toxicity of amyloid-β from Alzheimer disease. *J. Biol. Chem.*, 285(53):41533–41540, 2010.

[107] Jeppe T. Pedersen, Jesper Østergaard, Noemi Rozlosnik, Bente Gammelgaard, and Niels H. H. Heegaard. Cu(II) mediates kinetically distinct, non-amyloidogenic aggregation of amyloid-β peptides. *J. Biol. Chem.*, 286(30):26952–26963, 2011.

[108] Venus Singh Mithu, Bidyut Sarkar, Debanjan Bhowmik, Muralidharan Chandrakesan, Sudipta Maiti, and Perunthiruthy K Madhu. Zn^{++} binding disrupts the Asp^{23}-Lys^{28} salt bridge without altering the hairpin-shaped cross-β structure of $A\beta_{42}$ amyloid aggregates. *Biophys. J.*, 101(11):2825–2832, 2011.

[109] Sudhakar Parthasarathy, Fei Long, Yifat Miller, Yiling Xiao, Dan McElheny, Kent Thurber, Buyong Ma, Ruth Nussinov, and Yoshitaka Ishii. Molecular-level examination of Cu^{2+} binding structure for amyloid fibrils of 40-residue Alzheimer's β by solid-state NMR spectroscopy. *J. Am. Chem. Soc.*, 133(10):3390–3400, 2011.

[110] William A. Gunderson, Jessica Hernández-Guzmán, Jesse W. Karr, Li Sun, Veronika A. Szalai, and Kurt Warncke. Local structure and global patterning of Cu^{2+} binding in fibrillar amyloid-β [Aβ(140)] protein. *J. Am. Chem. Soc.*, 134(44):18330–18337, 2012.

[111] Gözde Eskici and Paul H. Axelsen. Copper and oxidative stress in the pathogenesis of Alzheimer's disease. *Biochemistry*, 51:6289–6311, 2012.

[112] P Murali Doraiswamy and Anne E Finefrock. Metals in our minds: therapeutic implications for neurodegenerative disorders. *Lancet Neurol.*, 3(7):431–434, 2004.

[113] Mark A Smith, Akihiko Nunomura, Xiongwei Zhu, Atsushi Takeda, and George Perry. Metabolic, metallic, and mitotic sources of oxidative stress in Alzheimer disease. *Antioxid. Redox Signal.*, 2(3):413–420, 2000.

[114] X. Zhu, B. Su, X. Wang, M.A. Smith, and G. Perry. Causes of oxidative stress in Alzheimer disease. *Cell. Mol. Life Sci.*, 64(17):2202–2210, 2007.

[115] Christelle Hureau and Peter Faller. Aβ-mediated ROS production by Cu ions: Structural insights, mechanisms and relevance to Alzheimer's disease. *Biochimie*, 91(10):1212–1217, 2009.

[116] D Allan Butterfield, Aaron M Swomley, and Rukhsana Sultana. Amyloid β-peptide (1–42)-induced oxidative stress in Alzheimer disease: importance in disease pathogenesis and progression. *Antioxid. Redox. Signal.*, 19(8):823–835, 2013.

[117] Xudong Huang, Math P. Cuajungco, Craig S. Atwood, Mariana A. Hartshorn, Joel D. A. Tyndall, Graeme R. Hanson, Karen C. Stokes, Michael Leopold, Gerd Multhaup, Lee E. Goldstein, Richard C. Scarpa, Aleister J. Saunders, James Lim, Robert D. Moir, Charles Glabe, Edmond F. Bowden, Colin L. Masters, David P. Fairlie, Rudolph E. Tanzi, and Ashley I. Bush. Cu(II) potentiation of Alzheimer aβ neurotoxicity: Correlation with cell-free hydrogen peroxide production and metal reduction. *J. Biol. Chem.*, 274(52):37111–37116, 1999.

[118] Carlos Opazo, Xudong Huang, Robert A. Cherny, Robert D. Moir, Alex E. Roher, Anthony R. White, Roberto Cappai, Colin L. Masters, Rudolph E. Tanzi, Nibaldo C. Inestrosa, and Ashley I. Bush. Metalloenzyme-like activity of Alzheimer's disease β-amyloid: Cu-dependent catalytic conversion of dopamine, cholesterol, and biological reducing agents to neurotoxic H_2O_2. *J. Biol. Chem.*, 277:40302–40308, 2002.

[119] Luc Guilloreau, Sarah Combalbert, Alix Sournia-Saquet, Honoré Mazarguil, and Peter Faller. Redox chemistry of copper–amyloid-β: The generation of hydroxyl radical in the presence of ascorbate is linked to redox-potentials and aggregation state. *ChemBioChem*, 8(11):1317–1325, 2007.

[120] William R Markesbery and Mark A Lovell. Damage to lipids, proteins, DNA, and RNA in mild cognitive impairment. *Arch. Neurol.*, 64(7):954–956, 2007.

[121] John H. Viles. Metal ions and amyloid fiber formation in neurodegenerative diseases. copper, zinc and iron in Alzheimer's, Parkinson's and prion diseases. *Coord. Chem. Rev.*, 256(19-20):2271–2284, 2012.

[122] William R Markesbery. Oxidative stress hypothesis in Alzheimer's disease. *Free Radic. Biol. Med.*, 23(1):134–147, 1997.

[123] Stefan I Liochev. The mechanism of "fenton-like" reactions and their importance for biological systems. A biologist's view. *Met. Ions Biol. Syst.*, 36:1–39, 1998.

[124] Rodolfo Gómez-Balderas, Duilio F. Raffa, Gail A. Rickard, Patrick Brunelle, , and Arvi Rauk. Computational studies of Cu(II)/Met and Cu(I)/Met binding motifs relevant for the chemistry of Alzheimer's disease. *J. Phys. Chem. A*, 109(24):5498–5508, 2005.

[125] Gail A. Rickard, Rodolfo Gomez-Balderas, Patrick Brunelle, Duilio F. Raffa, , and Arvi Rauk. Binding affinities for models of biologically available potential Cu(II) ligands relevant to Alzheimer's disease: an ab initio study. *J. Phys. Chem. A*, 109(37):8361–8370, 2005.

[126] Duilio F Raffa, Rodolfo Gómez-Balderas, Patrick Brunelle, Gail A Rickard, and Arvi Rauk. Ab initio model studies of copper binding to peptides containing a His–His sequence: relevance to the β-amyloid peptide of Alzheimer's disease. *J. Bio. Inorg. Chem.*, 10(8):887–902, 2005.

[127] Duilio F Raffa, Gail A Rickard, and Arvi Rauk. Ab initio modelling of the structure and redox behaviour of copper (I) bound to a His–His model peptide: relevance to the β-amyloid peptide of Alzheimer's disease. *J. Biol. Inorg. Chem.*, 12(2):147–164, 2007.

[128] A. D. Becke. Density-functional exchange-energy approximation with correct asymptotic behavior. *Phys. Rev. A*, 38:3098–3100, Sep 1988.

[129] Chengteh Lee, Weitao Yang, and Robert G. Parr. Development of the colle-salvetti correlation-energy formula into a functional of the electron density. *Phys. Rev. B*, 37:785–789, Jan 1988.

[130] V. Minicozzi, S. Morante, G. C. Rossi, F. Stellato, N. Christian, and K. Jansen. The role of metals in amyloid aggregationexperiments and ab initio simulations. *Int. J. Quantum Chem.*, 108:1992–2015, 2008.

[131] Yong Jiao, , and Pin Yang. Mechanism of copper(II) inhibiting Alzheimer's amyloid β-peptide from aggregation: a molecular dynamics investigation. *J. Phys. Chem. B*, 111(26):7646–7655, 2007.

[132] Daxiong Han, Haiyan Wang, and Pin Yang. Molecular modeling of zinc and copper binding with Alzheimer's amyloid β-peptide. *BioMetals*, 21(2):189–196, 2008.

[133] Liang Xu, Xiaojuan Wang, Shengsheng Shan, and Xicheng Wang. Characterization of the polymorphic states of copper(II)-bound Aβ(1-16) peptides by computational simulations. *J. Comput. Chem.*, 34:2524–2536, 2013.

[134] Giovanni Bussi. Hamiltonian replica exchange in GROMACS: a flexible implementation. *Mol. Phys.*, 112(3-4):379–384, 2014.

[135] Sébastien Côté, Vincent Binette, Evgeniy S Salnikov, Burkhard Bechinger, and Normand Mousseau. Probing the huntingtin 1-17 membrane anchor on a phospholipid bilayer by using all-atom simulations. *Biophys. J.*, 108(5):1187–1198, 2015.

[136] Lingle Wang, Richard A. Friesner, and B. J. Berne. Replica exchange with solute scaling: A more efficient version of replica exchange with solute tempering (REST2). *J. Phys. Chem. B*, 115(30):9431–9438, 2011.

[137] Daniel A. Beard and Hong Qian. *Chemical Biophysics: Quantitative Analysis of Cellular Systems.* Cambridge University Press, UK, 2008.

[138] Laurent Capolungo Mohammed Cherkaoui. *Atomistic and Continuum Modeling of Nanocrystalline Materials: Deformation Mechanisms and Scale Transition.* Springer, 2009.

[139] Leach A.R. *Molecular modelling: principles and applications.* Pearson Prentice Hall, Harlow, GB, 2001.

[140] Jensen F. *Introduction to Computational Chemistry.* John Wiley & Sons Ltd, UK, 2007.

[141] Adri C. T. van Duin, Siddharth Dasgupta, Francois Lorant, , and William A. Goddard III. ReaxFF: A reactive force field for hydrocarbons. *J. Phys. Chem. A*, 105:9396–9409, 2001.

[142] Jay W. Ponder, Chuanjie Wu, Pengyu Ren, Vijay S. Pande, John D. Chodera, Michael J. Schnieders, Imran Haque, David L. Mobley, Daniel S. Lambrecht, Jr. Robert A. DiStasio, Martin Head-Gordon, Gary N. I. Clark, Margaret E. Johnson, and Teresa Head-Gordon. Current status of the AMOEBA polarizable force field. *J. Phys. Chem. B*, 114:2549–2564, 2010.

[143] Jr. A. D. MacKerell, D. Bashford, M. Bellott, Jr. R. L. Dunbrack, J. D. Evanseck, M. J. Field, S. Fischer, J. Gao, H. Guo, S. Ha, D. Joseph-McCarthy, L. Kuchnir, K. Kuczera, F. T. K. Lau, C. Mattos, S. Michnick, T. Ngo, D. T. Nguyen, B. Prodhom, III W. E. Reiher, B. Roux, M. Schlenkrich, J. C. Smith, R. Stote, J. Straub, M. Watanabe, J. Wiórkiewicz-Kuczera, D. Yin, , and M. Karplus. All-atom empirical potential for molecular modeling and dynamics studies of proteins. *J. Phys. Chem. B*, 102(18):3586–3616, 1998.

[144] Jay W Ponder and David A Case. Force fields for protein simulations. *Adv. Protein Chem.*, 66:27–85, 2003.

[145] Alexander D. Mackerell. Empirical force fields for biological macromolecules: Overview and issues. *J. Comput. Chem.*, 25(13):1584–1604, 2004.

[146] Chris Oostenbrink, Alessandra Villa, Alan E Mark, and Wilfred F Van Gunsteren. A biomolecular force field based on the free enthalpy of hydration and solvation:

The GROMOS force-field parameter sets 53A5 and 53A6. *J. Comput. Chem.*, 25(13):1656–1676, 2004.

[147] Viktor Hornak, Robert Abel, Asim Okur, Bentley Strockbine, Adrian Roitberg, and Carlos Simmerling. Comparison of multiple Amber force fields and development of improved protein backbone parameters. *Proteins: Struct., Funct., Bioinf.*, 65(3):712–725, 2006.

[148] Olgun Guvench and Jr. MacKerell, AlexanderD. *Comparison of Protein Force Fields for Molecular Dynamics Simulations*, volume 443 of *Methods Molecular Biology*. 2008.

[149] Nathan Schmid, Andreas P Eichenberger, Alexandra Choutko, Sereina Riniker, Moritz Winger, Alan E Mark, and Wilfred F van Gunsteren. Definition and testing of the GROMOS force-field versions 54A7 and 54B7. *Eur. Biophys. J.*, 40(7):843–856, 2011.

[150] K. Vanommeslaeghe, E. Hatcher, C. Acharya, S. Kundu, S. Zhong, J. Shim, E. Darian, O. Guvench, P. Lopes, I. Vorobyov, and A. D. Mackerell. CHARMM general force field: A force field for drug-like molecules compatible with the CHARMM all-atom additive biological force fields. *J. Comput. Chem.*, 31(4):671–690, 2010.

[151] Wenbo Yu, Xibing He, Kenno Vanommeslaeghe, and Alexander D. MacKerell. Extension of the CHARMM general force field to sulfonyl-containing compounds and its utility in biomolecular simulations. *J. Comput. Chem.*, 33(31):2451–2468, 2012.

[152] Junmei Wang, Romain M. Wolf, James W. Caldwell, Peter A. Kollman, and David A. Case. Development and testing of a general amber force field. *J. Comput. Chem.*, 25(9):1157–1174, 2004.

[153] Pengfei Li, Benjamin P. Roberts, Dhruva K. Chakravorty, and Kenneth M. Merz. Rational design of particle mesh Ewald compatible Lennard-Jones parameters for +2 metal cations in explicit solvent. *J. Chem. Theory Comput.*, 9(6):2733–2748, 2013.

[154] Pengfei Li and Kenneth M. Merz. Taking into account the ion-induced dipole interaction in the nonbonded model of ions. *J. Chem. Theory Comput.*, 10(1):289–297, 2014.

[155] Yuan-Ping Pang. Novel zinc protein molecular dynamics simulations: Steps toward antiangiogenesis for cancer treatment. *J. Mol. Model.*, 5:196–202, 1999.

[156] Peter Oelschlaeger, Marco Klahn, William A. Beard, Samuel H. Wilson, and Arieh Warshel. Magnesium-cationic dummy atom molecules enhance representation of DNA polymerase β in molecular dynamics simulations: Improved accuracy in studies of structural features and mutational effects. *J. Mol. Biol.*, 366(2):687–701, 2007.

[157] Fu Lin and Renxiao Wang. Systematic derivation of AMBER force field parameters applicable to zinc-containing systems. *J. Chem. Theory Comput.*, 6(6):1852–1870, 2010.

[158] Martin B. Peters, Yue Yang, Bing Wang, László Füsti-Molnár, Michael N. Weaver, and Kenneth M. Merz. Structural survey of zinc-containing proteins and development of the zinc AMBER force field (ZAFF). *J. Chem. Theory Comput.*, 6(9):2935–2947, 2010.

[159] Raúl Mera-Adasme, Keyarash Sadeghian, Dage Sundholm, and Christian Ochsenfeld. Effect of including torsional parameters for histidine-metal interactions in classical force fields for metalloproteins. *J. Phys. Chem. B*, 118(46):13106–13111, 2014.

[160] Christopher I. Bayly, Piotr Cieplak, Wendy Cornell, and Peter A. Kollman. A well-behaved electrostatic potential based method using charge restraints for deriving atomic charges: the resp model. *J. Phys. Chem.*, 97(40):10269–10280, 1993.

[161] Wendy D. Cornell, Piotr Cieplak, Christopher I. Bayly, and Peter A. Kollman. Application of resp charges to calculate conformational energies, hydrogen bond energies, and free energies of solvation. *J. Am. Chem. Soc.*, 115(21):9620–9631, 1993.

[162] Loup Verlet. Computer "Experiments" on classical fluids. i. thermodynamical properties of lennard-jones molecules. *Phys. Rev.*, 159(1):98–103, 1967.

[163] R.W Hockney, S.P Goel, and J.W Eastwood. Quiet high-resolution computer models of a plasma. *J. Comput. Phys.*, 14(2):148–158, 1974.

[164] William C. Swope, Hans C. Andersen, Peter H. Berens, and Kent R. Wilson. A computer simulation method for the calculation of equilibrium constants for the formation of physical clusters of molecules: Application to small water clusters. *J. Chem. Phys.*, 76(1):637–649, 1982.

[165] H. J. C. Berendsen, J. P. M. Postma, W. F. van Gunsteren, A. DiNola, and J. R. Haak. Molecular dynamics with coupling to an external bath. *J. Chem. Phys.*, 81(8):3684–3690, 1984.

[166] Giovanni Bussi, Davide Donadio, and Michele Parrinello. Canonical sampling through velocity rescaling. *J. Chem. Phys.*, 126(1):014101, 2007.

[167] Shūichi Nosé. A molecular dynamics method for simulations in the canonical ensemble. *Mol. Phys.*, 52(2):255–268, 1984.

[168] William G. Hoover. Canonical dynamics: Equilibrium phase-space distributions. *Phys. Rev. A*, 31(3):1695–1697, 1985.

[169] M. Parrinello and A. Rahman. Polymorphic transitions in single crystals: A new molecular dynamics method. *J. Appl. Phys.*, 52(12):7182–7190, 1981.

[170] Shuichi Nosé and M.L. Klein. Constant pressure molecular dynamics for molecular systems. *Mol. Phys.*, 50(5):1055–1076, 1983.

[171] P. P. Ewald. Die berechnung optischer und elektrostatischer gitterpotentiale. *Annalen der Physik*, 369(3):253–287, 1921.

[172] Tom Darden, Darrin York, and Lee Pedersen. Particle mesh Ewald: An N·log(N) method for Ewald sums in large systems. *J. Chem. Phys.*, 98(12):10089–10092, 1993.

[173] Ulrich Essmann, Lalith Perera, Max L. Berkowitz, Tom Darden, Hsing Lee, and Lee G. Pedersen. A smooth particle mesh Ewald method. *J. Chem. Phys.*, 103(19):8577–8593, 1995.

[174] R. W. Hockney and J. W Eastwood. *Computer simulation using particles.* New York:McGraw-Hill, 1981.

[175] Brock A. Luty, Ilario G. Tironi, and Wilfred F. van Gunsteren. Lattice-sum methods for calculating electrostatic interactions in molecular simulations. *J. Chem. Phys.*, 103(8):3014–3021, 1995.

[176] HJC Berendsen, JR Grigera, and TP Straatsma. The missing term in effective pair potentials. *J. Phys. Chem.*, 91(24):6269–6271, 1987.

[177] William L. Jorgensen, Jayaraman Chandrasekhar, Jeffry D. Madura, Roger W. Impey, and Michael L. Klein. Comparison of simple potential functions for simulating liquid water. *J. Chem. Phys.*, 79(2):926–935, 1983.

[178] Michael W. Mahoney and William L. Jorgensen. A five-site model for liquid water and the reproduction of the density anomaly by rigid, nonpolarizable potential functions. *J. Chem. Phys.*, 112(20):8910, 2000.

[179] William L Jorgensen, David S Maxwell, and Julian Tirado-Rives. Development and testing of the OPLS all-atom force field on conformational energetics and properties of organic liquids. *J. Am. Chem. Soc.*, 118:11225–11236, 1996.

[180] George A. Kaminski, Richard A. Friesner, Julian Tirado-Rives, and William L. Jorgensen. Evaluation and reparametrization of the OPLS-AA force field for proteins via comparison with accurate quantum chemical calculations on peptides. *J. Phys. Chem. B*, 105(28):6474–6487, 2001.

[181] Xavier Daura, Karl Gademann, Bernhard Jaun, Dieter Seebach, Wilfred F. van Gunsteren, and Alan E. Mark. Peptide folding: When simulation meets experiment. *Angew. Chem. Int. Ed.*, 38:236–240, 1999.

[182] John Marelius, Karin Kolmodin, Isabella Feierberg, and Johan Åqvist. Q: a molecular dynamics program for free energy calculations and empirical valence bond simulations in biomolecular systems. *J. Mol. Graph. Model.*, 16(4-6):213–225, 1998.

[183] Fernanda Duarte, Paul Bauer, Alexandre Barrozo, Beat Anton Amrein, Miha Purg, Johan Åqvist, and Shina Caroline Lynn Kamerlin. Force field independent metal parameters using a nonbonded dummy model. *J. Phys. Chem. B*, 118(16):4351–4362, 2014.

[184] Nanditha G Nair, George Perry, Mark A Smith, and V Prakash Reddy. NMR studies of zinc, copper, and iron binding to histidine, the principal metal ion complexing site of amyloid-β peptide. *J. Alzheimers Dis.*, 20(1):57–66, 2010.

[185] Priscilla S.-W. Yeung and Paul H. Axelsen. The crowded environment of a reverse micelle induces the formation of β-strand seed structures for nucleating amyloid fibril formation. *J. Am. Chem. Soc.*, 134(14):6061–6063, 2012.

[186] Qinghua Liao, Shina Caroline Lynn Kamerlin, and Birgit Strodel. Development and application of a nonbonded Cu^{2+} model that includes the Jahn-Teller effect. *J. Phys. Chem. Lett.*, 6(13):2657–2662, 2015.

[187] Bogdan Barz and Brigita Urbanc. Dimer formation enhances structural differences between amyloid β-protein (1-40) and (1-42): An explicit-solvent molecular dynamics study. *PLoS ONE*, 7:e34345, 04 2012.

[188] Tong Zhang, Jian Zhang, Philippe Derreumaux, and Yuguang Mu. Molecular mechanism of the inhibition of EGCG on the Alzheimer Aβ1-42 dimer. *J. Phys. Chem. B*, 117(15):3993–4002, 2013.